Geochemical Constraints for Mechanisms of Planetary Differentiation and Volatile Depletion

Dhaliwal, Jasmeet Kaur

2016

UNIVERSITY OF CALIFORNIA, SAN DIEGO

Geochemical Constraints for Mechanisms of Planetary Differentiation and Volatile Depletion

A dissertation submitted in partial satisfaction of the requirements
for the degree Doctor of Philosophy

in

Earth Sciences

by

Jasmeet Kaur Dhaliwal

Committee in charge:

Professor James Day, Chair
Professor Catherine Constable
Professor David Hilton
Professor David Stegman
Professor Mark Thiemens

2016

The dissertation of Jasmeet Kaur Dhaliwal is approved and it is acceptable in quality and form for publication on microfilm and electronically:

Chair

University of California, San Diego

2016

DEDICATION

To the memory of Kamal Kaur Dhaliwal and all that she could have been

To Gurkiran Singh Dhaliwal in the pursuit of a bright and creative future.

EPIGRAPH

Education is the most powerful weapon which you can use to change the world

Nelson Mandela

TABLE OF CONTENTS

Signature Page……………………………………………………………………...iii

Dedication……………………………………………………………………………..iv

Epigraph..…………………………………………………………………………....v

Table of Contents…………………………..……………………………………vi

List of Figures……………………………………..………………………vii

List of Tables…………………………………………………………...……..ix

Acknowledgements……………………………………………………………x

Vita……………………………………………………………………..…xiv

Abstract of the Dissertation…..……………………………………………...…...xv

Chapter 1: Introduction……………………………………………..……………….1

Chapter 2: Early metal-silicate differentiation during planetesimal formation revealed by Acapulcoite and Lodranite meteorites ……………………..…………..21

Chapter 3: Highly siderophile element abundance and Os isotope evidence for primary metal-silicate signatures in eucrite meteorites……..…………..…………..…93

Chapter 4: Volatile element loss during planetary magma ocean phases .………….132

Chapter 5: Conclusions……………. ...…………………..………………………195

LIST OF FIGURES

Figure 1.1 Mineral-Melt Partition Coefficients …………………………………...13

Figure 1.2 Chondrite Relative Abundances of HSE in Terrestrial Materials………...14

Figure 1.3 Chondrite Evolution Curve of the ^{187}Os/^{188}Os ratio since 4.56 Ga…...….15

Figure 1.4 Rayleigh Distillation of Zn and Zn Isotopic Ratios………………………16

Figure 2.1: Metal and and troilite abundances in acapulcoites, lodanites……………60

Figure 2.2: Back-scattered electron images……………….……………….………...61

Figure 2.3: Second set of back-scattered electron images.…………….…………….62

Figure 2.4: Photomicrographs in plane-polarized and cross-polarized light.……......63

Figure 2.5: Mineral chemistry compositions………….………….…..…..………...64

Figure 2.6: Average HSE abundances for FeNi metal grains and sulfide grains…....65

Figure 2.7: CI chondrite normalized Fe/Mg versus Ca/Mg and……………………..66

Figure 2.8: Trace multi-element plot for acapulcoite-lodranites.……..…….…….…67

Figure 2.9: CI chondrite normalized rare earth element (REE) abundances.…......…68

Figure 2.10: Oxygen isotope plot for acapulcoites and lodranites.…….…….……..69

Figure 2.11: HSE relative abundances for acapulcoite and lodranite meteorites...…70

Figure 2.12: The ^{187}Re/^{188}Os and ^{187}Os/^{188}Os ratios…………….…………..…....71

Figure 2.13: REE in acapulcoites with modeled compositions of residual liquids.....72

Figure 2.14: Adaptation of model by Chabot and Jones (2003) …………..…….…73

Figure 2.15: The Pd/Os and Pt/Os ratios of the sample set.…………..…………..…74

Figure 2.S1: Reflected light photomicrograph of the Acapulco meteorite.………….75

Figure 2.S2: Reflected light photomicrograph map of transitional meteorite..….......76

Figure 2.S3: Reflected light photomicrograph map of lodranite GRA 95209…….......77

Figure 3.1: Nickel versus Co concentrations for eucrite samples..…..……………..…118

Figure 3.2: Nickel versus Os concentrations for eucrite amples..…...……………......119

Figure 3.3: HSE relative abundances for eucrite samples...………...……………...120

Figure 3.4: Second set of HSE relative abundances for eucrite samples..............…121

Figure 3.5: ^{187}Re/^{188}Os versus ^{187}Os/^{188}Os for eucrite samples...……….…..……….....122

Figure 3.6: Osmium isotope ratios versus Os concentrations for eucrite samples.....123

Figure 3.7: HSE relative abundances for the subset of pristine eucrites...…......……124

Figure 3.8: Pt/Os versus Ir/Os in eucrite samples...………....…..….. .....…..….....125

Figure 4.1: Zinc isotope versus Zn abundance data for lunar samples...……….......163

Figure 4.2: The modeled crystal zinc isotopic composition and concentration...…..164

Figure 4.3: The Maxwell-Boltzmann distributions of zinc and volatile elements.....165

Figure 4.S1: Schematic diagrams of the two models presented …………………...179

Figure 4.S2: The ~ 1:1 relation observed between the surface and LMO ……….....180

Figure 4.S3: Schematic after Nishimura (2012) showing……………...………...…181

LIST OF TABLES

Table 2.1: Average mineral compositions of acapulcoites and lodranites…………...78

Table 2.2: Highly siderophile element abundances in FeNi and FeS grains …..........80

Table 2.3: Whole-rock major-element abundances in achondrite meteorite………....81

Table 2.4: Whole-rock trace-element abundances (in ppm) ………..……………..82

Table 2.5: Oxygen isotope data for acapulcoites and lodranites ……….………….....84

Table 2.6: Rhenium-osmium isotopes and highly siderophile element abundances...85

Table 3.1: Ni and Co abundances in eucrite meteorites (in ppm) …….………….126

Table 3.2 Re-Os isotope and HSE abundance data for eucrite meteorite…..………127

Table 4.S1: LMO Crystallization Input Parameters…….……………………..…182

Table 4.S2: Zn abundances in mineral phases in lunar mare basalt samples……….183

Table 4.S3: LMO Crystallization Input Parameters for *in situ* Partition ………..…..184

Table 4.S4: Constants for Equilibrium Fractionation at 2400 K…………………...185

Table 4.S5: Results for Hydrodynamic Escape Modeling of Zn………………..…186

ACKNOWLEDGEMENTS

I am thankful for the support of my parents and family in my academic pursuits: to my mother for instilling in me an appreciation for both breadth and depth in education, my father for helping me realize the luxury of studying by electric light well into the night, my brothers, Gurkiran and Kavinder, for humoring my bookishness and space-related presents (mostly the Moon globe), Akira for being the newest light in our life, and Rajii for becoming such an important and loving member of the family. I am fortunate to have had the unconditional support of my partner, Ned, who ensures that I always laugh more often than not, even when I worry about potentially miscounted Teflon beakers or exploding Carius tubes. I would further like to thank my Massiji, Dhanwant, for her emotional support through the years, my Mamajis, Jasdev and Hardial, for encouraging me to pursue the sciences yet appreciating my interest in the arts, Amina for such a warm smile, enthusiasm and friendship, and Zorawar for reminding me of the childhood fascination for outer space that we all grew up with. Last, but certainly not least, I would like to thank my Naniji for inspring me to value learning, as she raised her children and taught herself to read both Punjabi and English, and continues to always have a book in her hand.

I am immensely grateful to Professor James Day for his guidance in this undertaking, particularly his patience and forgiveness over the years, and for teaching me the value of careful laboratory measurements and observational data, despite my juvenile excitement over crash-bang dynamic modeling studies. I greatly appreciate his belief in me, for recognizing my enthusiasm for things extraterrestrial and letting it guide a biologist and linguist into the realm of planetary science, thus expanding my academic horizons more than I ever dreamed possible. I further value the high standards that James sets for himself and his students; learning to be a detail-oriented and careful scientist with clear communication skills will serve me well in the years to come.

I would further like to acknowledge my thesis committee: Dr. Catherine Constable for inspiring discussion on statistics and earth science modeling, and for common-sense truths and grounding; Dr. David Hilton for cheerful and enlightening conversations regarding the scientific significance of lab measurements, especially given the limitations of cosmochemsitry; Dr. David Stegman for his unique and open-minded views on the pursuit of scientific research, and candid sense of humor; and Dr. Mark Thiemens for encouraging me to explore the intricacies of physical chemistry and that even the most complicated topics are never fully out of reach.

I would further like to thank collaborators I have had the good fortune to learn from and work with: Dr. Frederic Moynier for all things moderately-volatile and zinc, Dr. Francis McCubbin for his knowledge of mineralogy and ever interesting discussions, Dr. Larry Taylor for his attention to petrographic detail and musings on science, and Dr. Kim Tait for being an inspiration—I have always thought museum curators are the coolest! I would also like to acknowledge Dr. Simone Marchi for his guidance, support and advice in my search for a postdoc—I'm very hopeful that we'll be able to collaborate in the future.

Lab work is a special calling, and I am much obliged to my lab-mates over the years for all the camaraderie and cooperation, even with so many time-sensitive tasks and competition for hot-plate space. In particular, I would like to thank Brad for so many hilarious jokes, a great capacity for teamwork and coordination, and his patient friendship that have all been integral to our success in graduate school. My introduction to and experience in geochemistry and geology would also not have been complete without the company and knowledge of the GRD M.S. students and Earth Science undergraduates; thank you for teaching me what I needed to learn, and for the privilege of TA-ing in your classes and trying to return the favor.

The SIO community is an essential part of any graduate experience here, and I am so thankful for having the support of everyone in the office: Adam, Anne, Azzure, Christine, Denise, Gayle, Gilbert, Jan, Jessica, Laura, Maureen McGreevy, Maureen (her holiness), Megan, Monica, Olivia, Tina and Wayne. Thank you to my fellow graduate students for such wonderful friendship, especially the cohorts of 2011 and 2013, there are too many to name and I would not want to leave anyone out.

Finally, I owe a great debt of gratitude to Mr. Michael Cook for being the greatest teacher, always challenging and questioning me, teaching me that complacency and cutting corners is never an option, reminding me to remain grounded, that valuing family and respecting our elders is always in fashion, and for his confidence in my abilities that I have carried with me since first-year Latin almost two decades ago.

Chapter 2, in full, is a reprint of material in preparation for submission to *Geochimca et Cosmochima Acta*, 2016, Dhaliwal, Jasmeet K; Day, James M.D.; Corder, Chistopher, A.; Tait, Kim; Marti, Kurt; Assayag, Nelly; Cartigny, Pierre; Rumble, Doug III; Taylor, Lawrence. The dissertation author was the primary investigator and author of this paper. Figures 2.2 – 2.4 and 2.S1-2.S3 are copyrighted material from Corder (2015) and used with permission. The text in sections 2.2.3, 2.2.4, 2.2.6, 2.3.1, 2.3.2 and 2.3.5 is primarily sourced from Corder (2015) and used with permission in this thesis as a reprint of the submitted manuscript.

Chapter 4, in full, is a reprint of material submitted to *Icarus*, 2016, Dhaliwal, Jasmeet K.; Day, James M. D.; Moynier, Frederic. The dissertation author was the primary investigator and author of this paper.

VITA

2002 – 2006	Bachelor of Arts: Integrative Biology, Spanish & Portuguese University of California, Berkeley
2009 – 2010	Master in Public Health: Environmental Health Sciences University of California, Los Angeles
2011 – 2012	Master of Science: Earth Sciences University of California, San Diego
2012 – 2013	NSF GK-12 Fellow, Scripps Institution of Oceanography University of California, San Diego
2013	Lunar Exploration Intern Lunar and Planetary Institute, Houston, TX
2015	Planetary Summer Science School: Plumes Lead Jet Propulsion Laboratory, Pasadena, CA
2016	Doctor of Philosophy: Earth Sciences University of California, San Diego

ABSTRACT OF THE DISSERTATION

Geochemical Constraints for Mechanisms of Planetary Differentiation and Volatile Depletion

by

Jasmeet Kaur Dhaliwal
Doctor of Philosophy in Earth Sciences
University of California, San Diego, 2016

Professor James Day, Chair

The evolution of the terrestrial planets involved a range of complex processes, including accretion, core formation, post-core formation accretion, mantle

differentiation and volatile depletion. The earliest processes of accretion and core formation have largely been overprinted on Earth and Mars, but can be investigated using geochemical measurements of extraterrestrial materials. Highly siderophile elements (HSE; Os, Ir, Ru, Rh, Pt, Pd, Re, Au) preferentially partition into metal phases and are therefore powerful tracers for examining mechanisms of core formation on partially differentiated bodies, and differentiation and post-core formation late accretion on fully differentiated planetesimals. Chapter 2 examines the partially-melted, primitive acapulcoite and lodranite meteorites for insight into metal segregation and metal-sulfide partitioning. This work examines the effects of sulfur on HSE partitioning during the earliest stages of core formation, and allows identification of samples that may have derived near the nascent core of the acapulcoite-lodranite parent body. Chapter 3 consists of detailed measurements of the HSE and Os isotopes in eucrite meteorites, revealing new insight into metal-silicate and differentiation of the Asteroid-4 Vesta. These data are used to identify pristine eucrite samples that may represent the first natural examples of metal-silicate signatures of primary planetary differentiation in the Solar System. The fourth chapter transitions to volatile depletion, and investigates the potential for volatile loss using a model of magma ocean differentiation and constraints from zinc abundance and isotope data in lunar samples. The models constructed demonstrate that the lunar zinc signature, which reflects wholesale volatile depletion from the Moon, can be explained by surface volatile depletion and subsequent homogenization in a magma ocean. The continuum from

core formation, to metal-silicate differentiation and late accretion, to volatile loss provides an overview of planet formation through detailed measurements and analysis of these fundamental mechanisms that occurred during terrestrial planet evolution in the Solar System.

Chapter 1:

Introduction

The existence of the planets has long fascinated the human imagination, from the times of the Greeks, to Galileo's discovery of Saturn, and the Apollo missions that allowed us to set foot on the Moon. As with stars, understanding the evolution and formation of planets touches on the curiosity of Earth's origins and place in the Solar System. Planetary evolution is a complex process that begins with coagulation of dust, 'pebble' accretion (e.g., Lambrechts & Johansen, 2012), and ultimately accretion in which smaller planetesimals coalesce to form a larger body, resulting in collisional heating and melting of precursor material (e.g., Halliday & Kleine, 2006), often associated with complex planetary dynamics (Gomes et al., 2005; Tsiganis et al., 2005). Ultimately, accretionary melting leads to the segregation of molten iron-nickel metal and sulfide from the associated silicates; on a large scale, the metal pools together and migrates to the center of a planetary body due to the low velocity of melt migration being counteracted by the distance melt must travel (Moskovitz & Gaidos, 2011). These processes result in core-formation, after which the molten silicate mantle gradually crystallizes. The mantle then partially melts to form the crust, which is subject to the effects of late accretion (e.g., Walker, 2009; Day et al., 2016).

The unique evolutionary history of Earth that led to it becoming a habitable planet is of great interest, and this includes considerations of generation of a geodynamo (Loper, 1978), plate tectonics (Wilson, 1968) and the retention of volatile species to form its oceans and atmosphere (Kasting and Catling, 2003; Zahnle et al., 2007). However, crustal recycling on Earth has led to overprinting of primary terrestrial signatures, making meteorites and lunar samples valuable for identifying and understanding mechanisms in the evolution of planets, acting as 'witnesses' to these processes. This work consists of three chapters that individually aim to examine poorly understood aspects of planet formation: early metal segregation during core formation; metal-silicate partitioning during mantle differentiation; and the depletion of volatiles from rocky planetary bodies. Chapters 2 and 3 describe detailed geochemical measurements on meteorite samples, and the fourth utilizes geochemical data from lunar samples as a key constraint for a magma ocean model of planetary differentiation. The major geochemical measurements and constraints in this dissertation are trace element partitioning, that of rare-earth elements (REE) in silicates and highly siderophile elements (HSE) in metals, the ^{187}Re-^{187}Os chronometer to provide time constraints, and Zn isotopic ratios, which are used to track volatile depletion and inventories of planets

1.2 Examples of Key Geochemical Measurements

This thesis employs a range of geochemical constraints to examine fundamental processes during planet formation. While not exhaustive, the examples of methods used below consider the use of rare earth elements, highly siderophile elements and Os isotope ratios, and Zn abundances and isotopic compositions.

1.1.1 Rare Earth Elements

Trace elements exhibit different partitioning behavior and can be used to evaluate the degree of partial melting and major mineral phases that were present during partial melting. The rare earth elements (REE), which consist of 14 elements on the periodic table from La to Lu (Pm does not have a stable isotope), are particularly valuable tracers of silicate petrogenesis (e.g., Hess, 1989). This suite of elements is largely trivalent (except Eu and Ce), and their solid-melt partition coefficients generally increase from La to Lu. The partition coefficients ($D_{solid\text{-}melt}$) for the REE are specific for each element and silicate mineral phase (e.g., olivine, orthopyroxene, etc.), and $D_{solid\text{-}melt} > 1$ means 'compatibility' in the mineral phase while a $D_{solid\text{-}melt} < 1$ represents 'incompatibility.' The light rare earth elements (LREE: La, Ce, Pr, Nd, Sm, Eu, and Gd) are more incompatible during melting than the heavy rare earth elements (HREE: Tb, Dy, Ho, Er, Tm, Yb, and Lu), evident in the lower LREE partition coefficients for mafic mineral phases (**Figure 1.1**). For example, during low degrees of partial melting, the LREE rapidly partition into the melt and exhibit strong enrichments in subsequent crystallization products; these effects are less marked for higher degrees of partial melting as incompatible elements become more enriched in the melt and depleted in the residue. The partitioning behavior of the REE during melting therefore results in inter-element fractionation patterns that can be used to trace the melting history of a rock from its source reservoir.

1.1.2 The Highly Siderophile Elements and Osmium Isotope Ratios

The highly siderophile elements (HSE), which consist of the platinum-group elements (PGE: Os, Ir, Ru, Rh, Pt, Pd), Re and Au, preferentially partition into liquid metal and sulfide compared to silicate melts (Barnes et al., 1985), and exhibit inter-element fractionation because Os, Ir and Ru are more compatible in metal phases than the other HSE (Mungall & Brenan, 2014). These elements are therefore used to trace liquid metal segregation from silicate phases during core formation (e.g., Walker, 2009); on a small scale, this is evident in metals pools and networks in primitive extraterrestrial samples (e.g., McCoy et al., 1997). The HSE can also be used to trace metal-sulfide partitioning because their affinity for metal phases is affected by the sulfur content of the melt (Chabot & Jones, 2003). This inter-element partitioning is further affected by oxygen fugacity and temperature (e.g., Mann et al., 2012), and primary planetary materials should exhibit noticeable, and in many cases, unique inter-element fractionation patterns. Samples from differentiated planetary bodies, including the Earth, that exhibit chondritic relative abundances (i.e. limited inter-element fractionation) among the HSE are classically interpreted to be indicative of contamination from chondritic impactors, which overprints the primary HSE patterns (**Figure 1.2**).

In addition to HSE abundances and inter-element fractionation, the Re-Os isotope system is important for tracing early core formation (e.g. for iron meteorites, Smoliar et al., 1998; Shirey & Walker 1998), the long-term evolution of planetary mantles (Walker, 2009; Day et al., 2016) and chondritic impact contributions to samples (e.g., Norman et al., 2002). The beta decay of ^{187}Re to ^{187}Os has a half-life of 41.6 Ga (Selby et al., 2007), and since Re is less compatible than Os, the long term ^{187}Os/^{188}Os of a differentiated planetary body evolves to more variable compositions compared with the present-day, evolved value for chondrite materials of ~0.126 to 0.128. This is evident in **Figure 1.3** (after Harvey & Day, 2016; Day et al., 2016), which shows the evolution of chondrite Os-isotope compositions, as well as more radiogenic ratios (e.g., +10 and +20 γ_{Os}), which result from differentiation and slight enrichments in ^{187}Re in planetary crusts (compared to Os) and its subsequent decay to ^{187}Os. This evolution assumes an Solar System initial ^{187}Os/^{188}Os = 0.09531 and ^{187}Re/^{188}Os$_{chondrite}$ = 0.40186 and is described by the following equation: $^{187}\text{Os}/^{188}\text{Os}_{(t)} = {}^{187}\text{Os}/^{188}\text{Os}_{(initial)} + {}^{187}\text{Re}/^{188}\text{Os}_{(chondrite)}(e^{\lambda(4568000000)} - e^{\lambda t})$. Osmium isotopic ratios greater than ~0.128 are considered *supra-chondritic* because they reflect the radioactive decay of elevated Re concentrations in silicate reservoirs. In the case of primary and radiogenic Os isotope signatures from a differentiated planetesimal, these measurements are valuable tracers of Re-Os partitioning during core-formation and differentiation. In addition to observations of chondrite relative abundances of the HSE in differentiated planetary materials, chondritic Os isotope ratios are sensitive indicators of impact addition (e.g., Norman et al., 2002; Day et al., 2010; Goderis et al., 2016) and can be used to differentiate 'pristine' samples from impact-contaminated samples.

1.1.3 Zinc Abundances and Isotopic Ratios

The terrestrial planets are relatively depleted in volatiles compared with most chondritic materials, but quantifying the history of the outgassing and loss of species such as H_2 and CO_2 can be challenging. The moderately volatile elements, defined as those with 50% condensation temperatures between 704K and 1290K (Lodders, 2003), also exhibit differences between volatile-rich reservoirs such as the Earth, compared to the more volatile depleted Moon. One of the most faithful tracers of volatile depletion in planetary materials is the moderately volatile element, Zn, which has five major isotopes and does not fractionate during magmatic differentiation. Enrichment in the heavy isotopes of Zn (^{66}Zn and ^{68}Zn) compared to the lighter isotopes (^{64}Zn) is indicative of evaporative volatile loss. The magnitude of this effect is typically reported as δ^{X}Zn (expressed in per mille [‰] as $\delta^{X}\text{Zn} = ([^{X}\text{Zn}/^{64}\text{Zn})_{\text{sample}} /[^{X}\text{Zn}/^{64}\text{Zn}]_{\text{JMC-Lyon}} - 1) \times 1000$, where ^{X}Zn equals either ^{66}Zn, ^{67}Zn, ^{68}Zn or ^{70}Zn) and values > 0 indicate enrichment of ^{66}Zn compared to ^{64}Zn. Volatile loss of zinc can be modeled by Rayleigh distillation, which describes the progressive loss of Zn abundances and enrichment in δ^{66}Zn values as a result of evaporative fractionation (**Figure 1.4a**).

The marked heavy zinc isotopic enrichment in some planetary materials reflects their volatile inventories, and the variation (or lack thereof) in δ^{66}Zn among samples from the same parent body provide insight into the scale and mechanisms of volatile depletion (**Figure 1.4b**). This is evident for the Earth and Mars, which both exhibit limited fractionation, where δ^{66}Zn = ~0.3‰ is the typical chondritic value and reflects no fractionation. The average δ^{66}Zn value for terrestrial lavas is δ^{66}Zn of +0.28 ±0.05‰ (Chen et al., 2013), and the average signature of martian basalts is δ^{66}Zn = +0.25 ±0.03‰ (Paniello et al., 2012). This contrasts with the bulk signature of the lunar mantle, δ^{66}Zn = +1.4 ±0.5‰ (2 s.d.; Kato et al., 2015), as derived from measurements on low- and high-Ti mare basalts. The limited range of δ^{66}Zn indicates large-scale melting and volatile loss on the Moon (Paniello et al., 2012; Day & Moynier, 2014; Kato et al., 2015), which is valuable for examining volatile depletion during lunar differentiation, and can be extended to understanding the volatile inventories on other low-mass planetesimals in the Solar System.

1.3 Meteorite Samples

A major theme of this work is that meteorites can be used to ascertain fundamental mechanisms and primary signatures on their parent bodies, the planetesimal(s) from which they presumably derived; this is also the case for lunar samples, which reveal the compositional and melting history of the Moon, and a recent review is provided in Day (2015). The chondrite meteorites are the most primitive specimens of the early Solar System, and precursor material for the fully differentiated terrestrial planets and both undifferentiated and differentiated planetesimals (Brearley & Jones, 1998). This assertion is based on compositional similarities between the Sun and the Ivuna chondrite specimen (and other CI, Chondrite Ivuna, type chondrite samples; Anders & Grevesse, 1989), and the presence of calcium-aluminum-inclusions (CAI), which are thought to have condensed from the early nebula (Brearley and Jones, 1998). Simple progression from dust to chondrites to differentiated materials appears to be an oversimplification, however, since the crystallization ages for chondrite parent bodies can be later than those for differentiated bodies such as the angrite and eucrite parent bodies (Bizarro et al., 2005; Kleine et al., 2009), and the precursor material for Earth and other terrestrial bodies may deviate from chondrite compositions (e.g., Becker et al., 2006). Despite these caveats, the chondrites are still considered the most primitive meteorites because they have experienced limited to no melting or differentiation. On the other hand the primitive acapulcoite and lodranite achondrites, which show evidence of segregation of iron-nickel-sulfur (Fe-Ni-S) and silicates, exhibit metal pooling and segregation, likely represent a microcosm of nascent core formation.

1.4 Thesis Chapters

1.4.1 Chapter 2 – Early metal-silicate differentiation during planetesimal formation revealed by Acapulcoite and Lodranite meteorites

The second chapter of this dissertation focuses on petrographic and geochemical analyses of a suite of acapulcoite and lodranite meteorites, which are partially-melted, primitive achondrites and represent natural experiments of metal-sulfide partitioning. The aim is to characterize metal segregation behavior in these samples, both on the basis of visual examination of polished 10 μm thick sections of rock, and trace element abundances, particularly of the HSE. These samples have not been thoroughly examined before, yet they have the potential to reveal fundamental processes acting during planetesimal core formation (e.g., Day et al., 2016). The absolute HSE abundances and inter-element fractionation trends are powerful tracers of metal segregation, a process that is captured by the acapulcoite and lodranite meteorites. This partitioning is further affected by temperature, pressure, oxygen fugacity and liquid sulfur content (e.g., Jones and Drake, 1986; Chabot and Jones, 2003; Wade and Wood, 2005; Mann et al., 2012), which are relevant to the low-mass, reduced conditions on the acapulcoite-lodranite parent body. The data in this chapter reveal fundamental metal-silicate HSE partitioning trends in the presence of variable amounts of sulfur, with progressive depletions in Pt and then Pd with increased degrees of partial melting of chondrite-like precursor material.

1.4.2 Chapter 3 – Highly siderophile element abundance and Os isotope evidence for primary metal-silicate signatures in eucrite meteorites

The third chapter consists of detailed measurements the HSE and osmium isotopes in eucrite meteorites. Based on oxygen isotope ratios (Greenwood et al., 2005; Scott et al., 2009), which reflect wholesale silicate melting and mixing on planetesimals and result in unique values for distinct parent bodies, the eucrites are linked to the howardite and diogenite meteorites. Together, these meteorites form the howardite-eucrite-diogenite (HED) clan and are considered to originate from Asteroid-4 Vesta (and the Vestoid family; Binzel & Xu, 1993). The HED parent body is a fully differentiated planetesimal and is therefore an important end-member in understanding the evolution of the larger terrestrial planets (McSween et al., 2013). This work focuses on the *unbrecciated* eucrites, which have often been considered to be free from impact contamination, and identifying the most *pristine* of these samples. The HSE are valuable for examining exogenous impact contributions; samples that reflect primary metal-silicate mechanisms retain unique HSE inter-element fractionations, but those that have witnessed impact contamination exhibit unfractionated, chondrite-relative abundances of HSE. These *pristine* eucrites also reveal primary mantle differentiation signatures of the HED parent body, which include strong fractionation between Ir and Os, where the latter is strongly depleted relative to the other HSE. The pristine eucrites yielded primary signatures of mantle differentiation and likely reveal the nature of silicate mantles prior to post-core formation late accretion.

1.4.3 Chapter 4 – Volatile element loss during planetary magma ocean phases

The fourth chapter examines the timing and mechanism of volatile depletion on the Moon and extends it to consideration of volatile depletion of smaller planetesimals that may have served as precursor material for larger planets. This work consists of a joint Rayleigh distillation and Assimilation Fractional Crystallization model (AFC; DePaolo, 1981; Nishimura, 2012), where the former is quantifies isotopic fractionation during volatilization and the latter describes isotopic mixing between an assimilant and a crystallizing reservoir. The model is able to predict the bulk zinc isotopic enrichment signature of the Moon, as measured in lunar mare basalt samples. This demonstrates that concurrent evaporative fractionation of volatiles on the surface during a magma ocean phase is a valid explanation for bulk lunar volatile depletion, and can be extended to other planetary bodies. Chapter 4 further explores mechanism of volatile loss, particularly in the case of the heavier, moderately-volatile elements like zinc, and concludes that the effects of hydrodynamic escape are negligible. The major implication is that planetary magma oceans, or molten magma regions on smaller bodies, may contribute to the 'drying out' of rocky bodies, but that loss of volatiles from the atmosphere requires mechanisms like atmospheric blowoff in the case of larger bodies such as the Moon.

1.5 Scientific Significance

The remaining chapters of this dissertation consider various aspects of the evolution of planets from the accretion of chondritic precursors to the differentiation and crystallization of a magma ocean. The geochemistry that underlies these chapters highlights the value and diverse application of careful and detailed laboratory measurements, as tracers of metal-sulfide partitioning, a recorder of primary and vestigial processes, and as a constraint for magmatic mixing models. This work can be applied and extended to quantifying several effects: light elements such as sulfur in planetary cores; heterogeneous differentiation of small, reduced planetesimals; and large-scale mixing on the assimilation of planetary surface signatures into the deep interior. The implications for Earth are broad, and can be extended to better understand the oxidation of the mantle during core formation, the influence of mantle heterogeneity on volatile outgassing to the atmosphere, and the composition and retention of volatiles that eventually allowed this planet to harbor life.

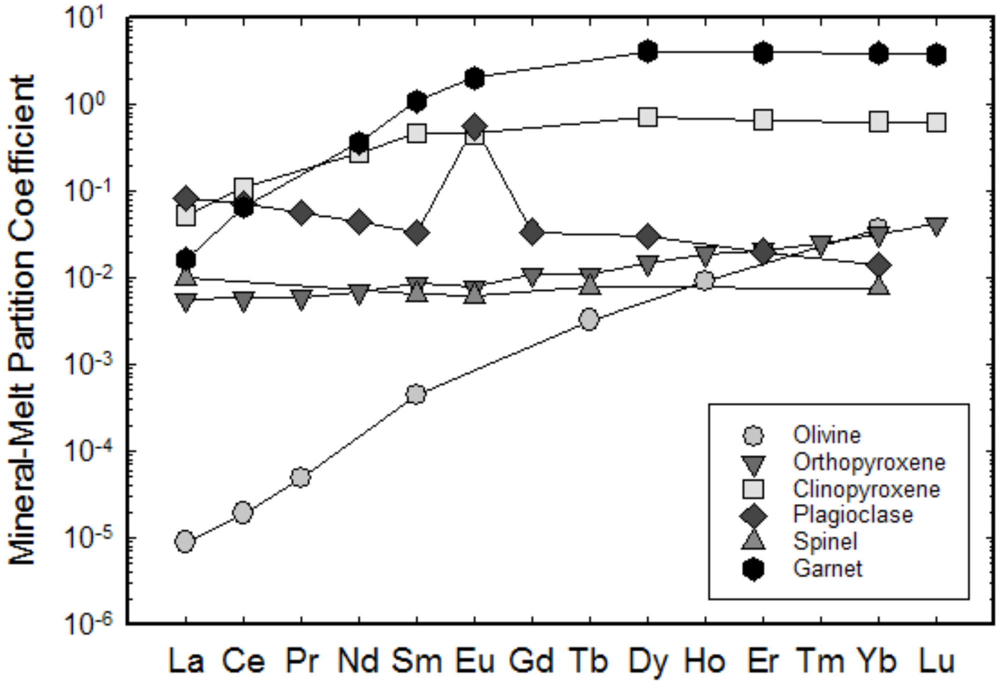

Figure 1.1 Mineral-Melt Partition Coefficients for Rare Earth Elements
The solid-melt partition coefficients for the REE in mafic mineral phases show the increasing compatibility of the heavy REE (HREE) compared to the light REE (LREE). The partition coefficient data are from a compilation by White (2009) and references therein.

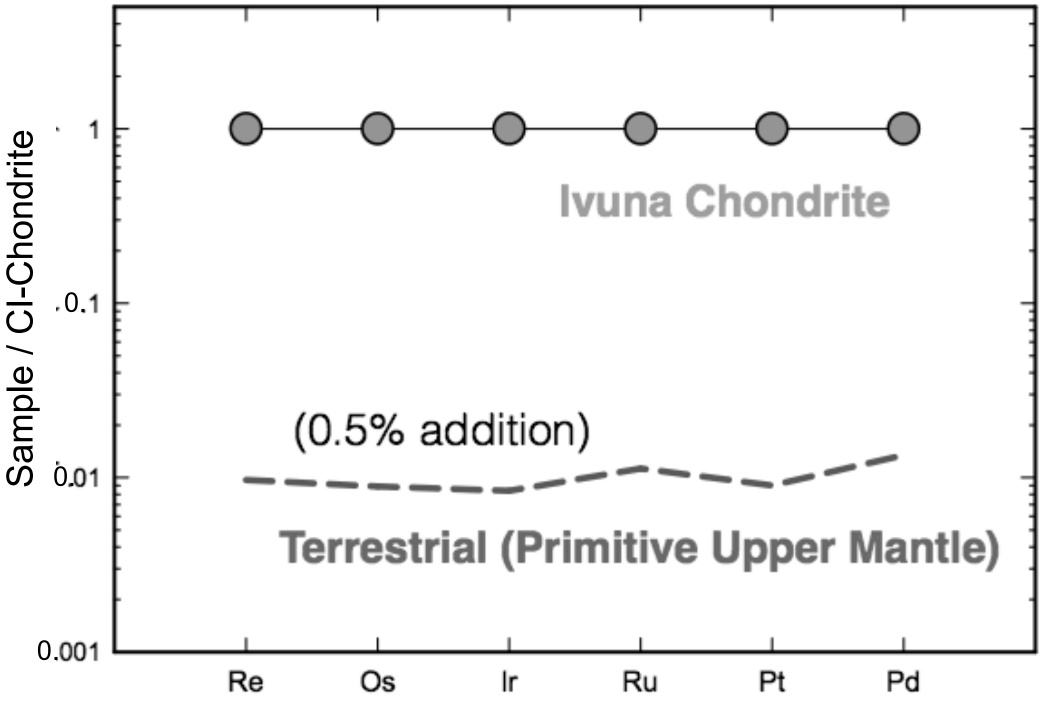

Figure 1.2 Chondrite Relative Abundances of HSE in Terrestrial Materials
The HSE abundances in the terrestrial primitive upper mantle (Becker et al, 2006) are relatively unfractionated, similar to those measured in the Ivuna chondrite (CI chondrite composition; Horan et al., 2003). This indicates that primary and fractionated HSE signatures in terrestrial mantle materials have been overprinted by ~0.5 % chondritic impact addition (e.g., Kimura et al., 1974; Chou, 1978).

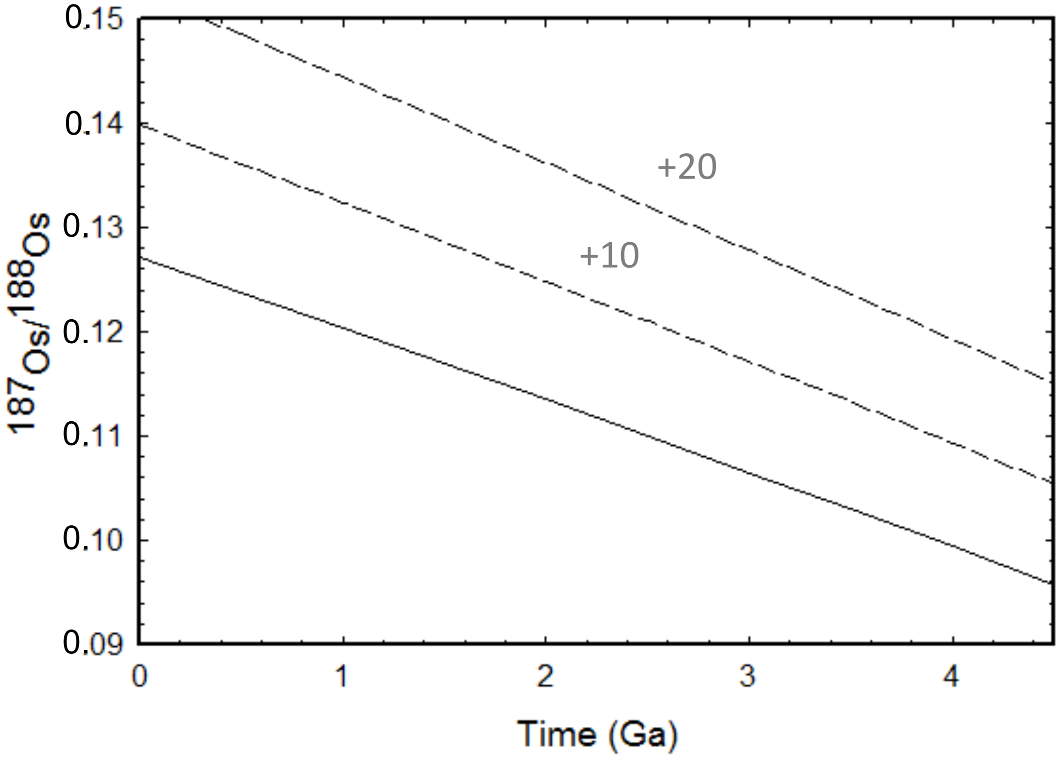

Figure 1.3 Chondrite Evolution Curve of the ^{187}Os/^{188}Os ratio since 4.56 Ga
Plot shows the evolution of the chondrite Os-isotope ratio from an initial ^{187}Os/^{188}Os = 0.09531 and an average ^{187}Re/^{188}Os = 0.40186 for chondrites to the present-day, evolved value of ^{187}Re/^{188}Os = ~0.127 (after Harvey and Day, 2016). The dotted lines above show enrichments of +10 and +20 γ_{Os}, which describes the percentage difference between evolved, radiogenic samples and the average chondritic composition at that time.

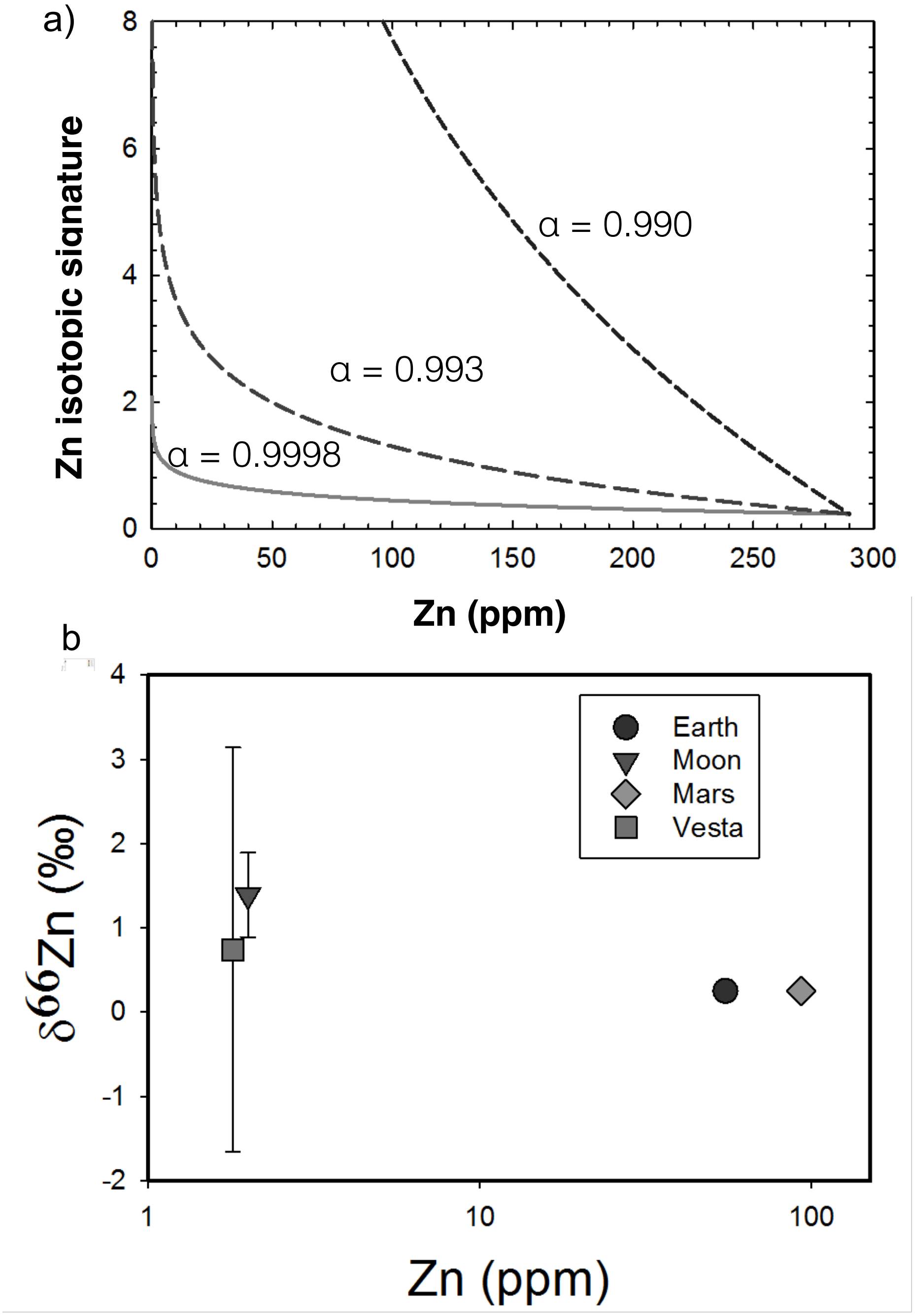

Figure 1.4 Rayleigh Distillation of Zn and Zn Isotopic Ratios in Planetary Materials (a) Modeling of Rayleigh distillation for theoretical fractionation factors, α = 0.990 for ZnS and α = 0.993 for $ZnCl_2$, which are two possible phases present in lunar samples. The value α = 0.9998 approaches unity and has been previously used to model lunar zinc compositions in mare basalts (Day and Moynier, 2014). (b) Zinc abundances and isotope ratios in the terrestrial planets (data from Paniello et al., 2012a, 2012b).

References

Anders, E., & Grevesse, N. (1989). Abundances of the elements: Meteoritic and solar. *Geochimica et Cosmochimica acta*, *53*, 197-214.

Barnes, S. J., Naldrett, A. J., & Gorton, M. P. (1985). The origin of the fractionation of platinum-group elements in terrestrial magmas. *Chemical Geology*, *53*, 303-323.

Becker, H., Horan, M. F., Walker, R. J., Gao, S., Lorand, J. P., & Rudnick, R. L. (2006). Highly siderophile element composition of the Earth's primitive upper mantle: constraints from new data on peridotite massifs and xenoliths. *Geochimica et Cosmochimica Acta*, *70*, 4528-4550.

Binzel, R. P. & Xu, S., (1993). Chips off of asteroid 4 Vesta: Evidence for the parent body of basaltic achondrite meteorites. *Science, 260,* 186–191.

Bizzarro, M., Baker, J. A., Haack, H., & Lundgaard, K. L. (2005). Rapid timescales for accretion and melting of differentiated planetesimals inferred from ^{26}Al-^{26}Mg chronometry. *The Astrophysical Journal Letters*, *632*, L41.

Brearley, A. J., & Jones, R. H. (1998). Chondritic meteorites. *Reviews in mineralogy and geochemistry*, *36*, 3-1.

Chabot, N. L., & Jones, J. H. (2003). The parameterization of solid metal-liquid metal partitioning of siderophile elements. *Meteoritics & Planetary Science*, *38*, 1425-1436.

Chen, H., Savage, P. S., Teng, F. Z., Helz, R. T., & Moynier, F. (2013). Zinc isotope fractionation during magmatic differentiation and the isotopic composition of the bulk Earth. *Earth and Planetary Science Letters*, *369*, 34-42.

Chou, C. L. (1978). Fractionation of siderophile elements in the Earth's upper mantle. In *Lunar and Planetary Science Conference Proceedings, 9*, 219-230.

Day, J. M. D., Walker, R. J., James, O. B., Puchtel, I. S., (2010). Osmium isotope and highly siderophile element systematics of the lunar crust. *Earth and Planetary Science Letters, 289,* 595–605.

Day, J.M.D., Brandon, A. D., & Walker, R. J. (2016). Highly siderophile elements in Earth, Mars, the Moon, and asteroids. *Reviews in Mineralogy and Geochemistry*, *81*, 161-238.

Day, J.M.D., Corder, C. A., Rumble, D., Assayag, N., Cartigny, P., & Taylor, L. A. (2015). Differentiation processes in FeO-rich asteroids revealed by the achondrite Lewis Cliff 88763. *Meteoritics & Planetary Science*, *50*, 1750-1766.

Day, J.M.D., & Moynier, F. (2014). Evaporative fractionation of volatile stable isotopes and their bearing on the origin of the Moon. *Philosophical Transactions of the Royal Society of London A: Mathematical, Physical and Engineering Sciences*, *372*, 20130259.

DePaolo, D. J. (1981). Trace element and isotopic effects of combined wallrock assimilation and fractional crystallization. *Earth and planetary science letters*, *53*, 189-202.

Goderis, S., Brandon, A. D., Mayer, B., & Humayun, M. (2016). Ancient impactor components preserved and reworked in martian regolith breccia Northwest Africa 7034. *Geochimica et Cosmochimica Acta*, *191*, 203-215.

Gomes, R., Levison, H. F., Tsiganis, K., & Morbidelli, A. (2005). Origin of the cataclysmic Late Heavy Bombardment period of the terrestrial planets. *Nature*, *435*, 466-469.

Greenwood, R. C., Franchi, I. A., Jambon, A., & Buchanan, P. C. (2005). Widespread magma oceans on asteroidal bodies in the early solar system. *Nature*, *435*, 916-918.

Halliday, A.N. & Kleine, T., (2006). Meteorites and the timing, mechanisms, and conditions of terrestrial planet accretion and early differentiation. In *Meteorites and the Early Solar System II*, 775-801.

Harvey, J. & Day, J.M.D. (2016). Highly Siderophile and Strongly Chalcophile Elements in High Temperature Geochemistry and Cosmochemistry. Mineralogical Society of America & Geochemical Society.

Hess, P. C. (1989). *Origins of igneous rocks*. Harvard University Press.

Horan, M. F., Walker, R. J., Morgan, J. W., Grossman, J. N., & Rubin, A. E. (2003). Highly siderophile elements in chondrites. *Chemical Geology*, *196*, 27-42.

Jones, J. H., & Drake, M. J. (1986). Geochemical constraints on core formation in the Earth. *Nature, 322*, 221-228.

Kasting, J. F., & Catling, D. (2003). Evolution of a habitable planet. *Annual Review of Astronomy and Astrophysics*, *41*, 429-463.

Kato, C., Moynier, F., Valdes, M. C., Dhaliwal, J. K., & Day, J. M. D. (2015). Extensive volatile loss during formation and differentiation of the Moon. *Nature communications*, *6*, 7617, doi:10.1038/ncomms8617.

Kimura, K., Lewis, R. S., & Anders, E. (1974). Distribution of gold and rhenium between nickel-iron and silicate melts: implications for the abundance of siderophile elements on the Earth and Moon. *Geochimica et Cosmochimica Acta*, *38*, 683-701.

Kleine, T., Touboul, M., Bourdon, B., Nimmo, F., Mezger, K., Palme, H., Jacobsen, S.B., Yin, Q.Z. & Halliday, A. N. (2009). Hf–W chronology of the accretion and early evolution of asteroids and terrestrial planets. *Geochimica et Cosmochimica Acta*, *73*, 5150-5188.

Lambrechts, M., & Johansen, A. (2012). Rapid growth of gas-giant cores by pebble accretion. *Astronomy & Astrophysics*, *544*, A32.

Lodders, K. (2003). Solar system abundances and condensation temperatures of the elements. *The Astrophysical Journal*, *591*, 1220-1247.

Loper, D. E. (1978). The gravitationally powered dynamo. *Geophysical Journal International*, *54*, 389-404.

Mann, U., Frost, D. J., Rubie, D. C., Becker, H., & Audétat, A. (2012). Partitioning of Ru, Rh, Pd, Re, Ir and Pt between liquid metal and silicate at high pressures and high temperatures-Implications for the origin of highly siderophile element concentrations in the Earth's mantle. *Geochimica et Cosmochimica Acta*, *84*, 593-613.

McCoy, T. J., Keil, K., Muenow, D. W., & Wilson, L. (1997). Partial melting and melt migration in the acapulcoite-lodranite parent body. *Geochimica et Cosmochimica Acta*, *61*, 639-650.

McSween Jr, H. Y., Mittlefehldt, D. W., Beck, A. W., Mayne, R. G., & McCoy, T. J., (2010). HED meteorites and their relationship to the geology of Vesta and the Dawn mission. In *The Dawn Mission to Minor Planets 4 Vesta and 1 Ceres* (pp. 141-174). Springer New York.

Moskovitz, N., & Gaidos, E. (2011). Differentiation of planetesimals and the thermal consequences of melt migration. *Meteoritics & Planetary Science*, *46*, 903-918.

Mungall, J. E., & Brenan, J. M. (2014). Partitioning of platinum-group elements and Au between sulfide liquid and basalt and the origins of mantle-crust fractionation of the chalcophile elements. *Geochimica et Cosmochimica Acta*, *125*, 265-289.

Nishimura, K. (2012). A mathematical model of trace element and isotopic behavior during simultaneous assimilation and imperfect fractional crystallization. *Contributions to Mineralogy and Petrology*, *164*, 427-440.

Norman, M. D., Bennett, V. C., & Ryder, G. (2002). Targeting the impactors: siderophile element signatures of lunar impact melts from Serenitatis. *Earth and Planetary Science Letters*, *202*, 217-228.

Paniello, R. C., Day, J. M.D., & Moynier, F. (2012). Zinc isotopic evidence for the origin of the Moon. *Nature*, *490*, 376-379.

Scott, E. R., Greenwood, R. C., Franchi, I. A., & Sanders, I. S., (2009). Oxygen isotopic constraints on the origin and parent bodies of eucrites, diogenites, and howardites. *Geochimica et Cosmochimica Acta, 73*, 5835–5853.

Selby, D., Creaser, R.A., Stein, H.J., Markey, R.J., & Hannah, J.L. (2007). Assessment of the ^{187}Re decay constant by cross calibration of Re-Os molybdenite and U-Pb zircon chronometers in magmatic ore systems. *Geochimica et Cosmochimica Acta*, *71,* 1999-2013.

Shirey, S. B., & Walker, R. J. (1998). The Re-Os isotope system in cosmochemistry and high-temperature geochemistry. *Annual Review of Earth and Planetary Sciences*, *26*, 423-500.

Smoliar, M. I., Walker, R. J., & Morgan, J. W. (1996). Re-Os ages of group IIA, IIIA, IVA, and IVB iron meteorites. *Science*, *271*, 1099.

Tsiganis, K., Gomes, R., Morbidelli, A., & Levison, H. F. (2005). Origin of the orbital architecture of the giant planets of the Solar System. *Nature*, *435*, 459-461.

Wade, J., & Wood, B. J. (2005). Core formation and the oxidation state of the Earth. *Earth and Planetary Science Letters*, *236*, 78-95.

Walker, R. J. (2009). Highly siderophile elements in the Earth, Moon and Mars: update and implications for planetary accretion and differentiation. *Chemie der Erde-Geochemistry*, *69*, 101-125.

White, W. M. (2013). *Geochemistry*. John Wiley & Sons.

Wilson, J. T. (1968). Static or Mobile Earth - Current Scientific Revolution. *Proceedings of the American Philosophical Society, 112,* 309-320.

Zahnle, K., Arndt, N., Cockell, C., Halliday, A., Nisbet, E., Selsis, F., & Sleep, N. H. (2007). Emergence of a habitable planet. In *Geology and Habitability of Terrestrial Planets* (2007), pp. 35-78.

Chapter 2:

Early metal-silicate differentiation during planetesimal formation revealed by Acapulcoite and Lodranite meteorites

Abstract

In order to establish the role and expression of silicate-metal fractionation in early planetesimal bodies, we have conducted a highly siderophile element (HSE: Os, Ir, Ru, Pt, Pd, Re) abundance and Re-Os isotope study of acapulcoite-lodranite meteorites. These data are reported with petrography, mineral chemistry, bulk-rock major and trace element geochemistry, oxygen isotopes (Corder, 2015), highly siderophile elements and osmium isotopes for Acapulco, Allan Hills (ALHA) 81187, Meteorite Hills (MET) 01195, Northwest Africa (NWA) 2871, NWA 4833, NWA 4875, NWA 7474 and two examples of transitional acapulcoite-lodranites, Elephant Moraine (EET) 84302 and Graves Nunataks (GRA) 95209. These data confirm previous studies indicating that these meteorites are likely linked to the same parent body and exhibit limited degrees (<2 to 7%) of silicate melt removal. New HSE and osmium isotope data support broadly chondritic relative and absolute abundances of these element in acapulcoites, lower absolute abundances in lodranites and elevated

(>2 × CI chondrite) HSE abundances in transitional acapulcoite-lodranites (EET 84302, GRA 95209). All of the meteorites define chondritic Re/Os with measured ^{187}Os/^{188}Os ratios of 0.1271 ± 0.0040 (2 SD). These characteristics imply that the precursor material of the acapulcoites and lodranites was broadly chondritic in composition and experienced subsequent variable Fe-Ni-S melting to form lodranites and transitional acapulcoite-lodranites. There is considerable variation in the absolute abundance of the HSE, both among samples and between aliquots of the same sample, consistent with both inhomogeneous distribution of HSE-rich metal, and of heterogeneous melting and incomplete mixing on the acapulcoite-lodranite parent body. Oxygen isotope data for acapulcoite-lodranites are consistent with inhomogeneous melting and mixing of accretion components from different nebular sources, and do not form a well-defined mass-dependent fractionation line. Modeling of HSE inter-element fractionation confirms increased degrees of melting in the Fe-Ni-S system, where lower S contents in the melt resulted in lower Pt/Os and Pd/Os ratios, as observed in lodranites. The transitional meteorites, EET 84302 and GRA 95209, exhibit the most elevated HSE abundances and do not follow modelled Pt/Os and Pd/Os partitioning trends. We interpret this to reflect metal melt pooling into these samples, suggesting that they may originate deeper within the acapulcoite-lodranite parent body, closer to the nascent core. Petrographic examination of transitional samples reveals the most extensive melting, pooling and networking of metal grains among these meteorites. Overall, our results show that metal-sulfide-silicate partitioning in primitive, partially melted achondrites follows a predictable sequence of limited partial melting and melt pooling that can lead to significant HSE inter-element fractionation effects.

2.1 Introduction

Metal-silicate segregation is a fundamental process in the evolution of differentiated planetary bodies, leading to the formation of metal cores and silicate mantles and crusts, in some cases, quite early in Solar System history (e.g., Jones & Drake, 1986; Righter & Drake, 1996; Rushmer et al., 2000; Kleine et al., 2002; Righter, 2003). Understanding of core formation processes is important for assessing the present distribution of elements within planetary bodies, including the behavior of siderophile (e.g., Fe, W) and highly siderophile elements (HSE: Os, Ir, Ru, Rh, Pt, Pd, Au, Re; cf., Brenan et al., 2016; Day et al., 2016), in addition to light elements (e.g., Poirier, 1994), and volatile element inventories that may be affected by core formation processes (Righter, 2003). By definition, fully differentiated bodies such as Earth or Mars, do not retain information on the earliest stages of core formation and metal-silicate differentiation. Improved knowledge of the way in which metal-silicate differentiation processes were operative early in their evolution would be valuable for understanding the timing and nature of core formation processes.

Within the available collection of meteorites, there are a number of ‘primitive’ achondrites that reflect intermediate compositions between undifferentiated ordinary, carbonaceous and enstatite chondrites, and differentiated achondrites, and so have the potential to yield information on early metal-silicate differentiation. These primitive achondrites include ureilites, brachinites, winonaites-IAB-IIICD iron meteorites, and the acapulcoite-lodranite meteorites (e.g., Weisberg et al., 2006; Day, 2015). Of these samples, acapulcoites and lodranites have experienced the least apparent metal and silicate melt-loss and have compositions most similar to chondrites. These features of acapulcoites and lodranites makes them useful analogs for understanding early core-formation processes in planetesimals, as they preserve the earliest stages of metal segregation and, possibly, metal accumulation. Acapulcoite-lodranite meteorites are characterized by early-formation ages (^{182}Hf-^{182}W model ages of ~4563 ± 1 Ma; Touboul et al., 2009) and represent metamorphic to incipient melts from primitive chondritic precursors, with similar mineralogy, mineral compositions, thermal histories and exposure ages, indicating their genesis on the same parent body (McCoy et al., 1996; 1997a,b; Mittlefehldt et al., 1996; Weigel et al., 1999). Refractory lithophile and siderophile element abundances in acapulcoites have previously been suggested to be most similar to those in CI chondrites (Rubin, 2007), but measurements of C and N isotope ratios of graphite grains in the archetype meteorite, Acapulco, indicate distinct source compositions of precursor material (El Goresy et al., 1995, 2005), as well as incomplete homogenization on the acapulcoite-lodranite parent body, including within condensing FeNi grains.

The range of oxygen isotopic compositions in acapulcoite and lodranite meteorites (Clayton and Mayeda, 1996; Greenwood et al., 2012), is also consistent with incomplete differentiation and mixing in the parent body (McCoy et al., 2006; c.f. winonaites, Hunt et al., 2016), and may also be explained by aqueous alteration prior to metamorphism (Greenwood et al., 2012). These observations are evidence for a protracted thermal history, resulting in the preservation of different degrees of partial melting and temperature regimes. Acapulcoites experienced lower temperatures of equilibration than lodranites, with only FeNi-FeS cotectic melting, and so these meteorites generally retain chondritic modal abundances of troilite and plagioclase. In contrast, lodranites experienced larger degrees of partial melting and show evidence of both FeNi-FeS cotectic melting and silicate melting, including more extensive melt migration and associated troilite depletion (McCoy et al., 1997) (**Figure 1**). Estimated thermal conditions experienced by lodranites for silicate melting are in the range of ~1050 to 2000°C (~5-20% partial melting, 300 MPa), compared to acapulcoites, at around ~950 to 1000°C (<1-3% partial melting, ~10-40 MPa; McCoy et al., 1996; 1997), suggesting an unidetermined parent body with a radius between ~ 35 to 100 km based on Hf-W and Pb-Pb closure temperatures and ages (Touboul et al., 2009).

Here we apply the first detailed study of Re-Os isotopes and HSE abundances in acapulcoite and lodranite meteorites to investigate early metal-silicate equilibrium processes in planetesimal bodies. Acapulcoites and lodranites represent attractive targets for Re-Os isotope and HSE abundance analysis for several reasons. First, acapulcoites have been suggested to represent high-grade metamorphic rocks in which partial melting in the Fe-Ni-S system occurred (Palme et al., 1981; Mittlefehldt et al., 1996), whereas lodranites are considered residues after partial melting, and the removal of Fe, Ni-FeS and basaltic partial melts (Bild & Wasson, 1976; McCoy et al., 1997a). These modes-of-origin, combined with the mineralogy of acapulcoites and lodranites, allow estimation of the modal abundances of metal and sulfide phases (Mittlefehldt et al., 1996; Rubin, 2007); this makes them ‘natural experiments’ of HSE fractionation during the initial phases of planetary differentiation. Second, the number of recognized acapulcoites and lodranites has increased dramatically in the past two decades, with many finds from the Antarctic that appear petrographically ‘fresh’ (e.g., low limonite contents; Rubin, 2007), and are therefore likely to be faithful recorders of primary signatures of the acapulcoite-lodranite parent body.

The new ^{187}Re-^{187}Os and HSE data are complemented by petrography, mineral chemistry, oxygen isotope systematics and bulk-rock major- and trace-element compositions. Study of the HSE in planetary materials is a particularly powerful tool for investigating processes of metal-silicate equilibrium and accretion (e.g., Day et al., 2016), and this method has already been widely applied to chondrites (e.g., Horan et al., 2003; Fischer-Godde et al., 2011) and primitive achondrites (Rankenburg et al., 2007; 2008; Day et al., 2009; 2012). We use the new data to examine the processes of metal-silicate differentiation during the earliest stages of planetary melting to ascertain core-formation processes on planetesimals and primitive achondrite parent bodies (e.g., Goodrich et al., 1987), which has implications for accretion mechanisms relevant to planet formation.

2.2 Samples and methods

2.2.1 Samples

One hundred and forty meteorites with affinities to the acapulcoite-lodranite clan are listed in the Meteoritical Bulletin (accessed November, 2016). Of these, however, there are several examples of paired meteorites (e.g., Meteorite Hills [MET] 01195 is paired with MET 01198 and MET 01244), and examples of meteorites identified as acapulcoites or lodranites, but that are in fact other meteorite types (e.g., ureilite Miller Range 091004; Day et al., 2017). Additionally, of the Antarctic meteorite finds, a large fraction (~60%) of the acapulcoites and lodranites found have masses less than 20 g. Due to these restrictions, we focused on examination of larger samples, for which sufficient material was available for study (~0.5 g per sample). For the acapulcoites, we examined, Acapulco, two antarctic acapulcoites (Allan Hills [ALHA] 81187, Meteorite Hills [MET] 01195) and Northwest Africa (NWA) 2871. The 'type' sample, Acapulco, is a fall that was rapidly recovered, resulting in little to no terrestrial weathering, with a total original mass of 1914 g (Graham, 1978). Lodranites studied were all from the northwest African desert region (NWA 4833; NWA 4875; NWA 7474), and two transitional acapulcoite-lodranites (Elephant Moraine [EET] 84302; Graves Nunataks [GRA] 95209) were also examined. Although GRA 95209 is classified as a lodranite, we consider it to be a transitional acapulcoite-lodranite, consistent with prior studies (Mittlefehldt and Lindstrom, 1998; McCoy et al., 2006; Mittlefehldt, 2007).

2.2.2 Petrography and mineral chemistry

Polished, 10 μm thick sections of Acapulco, ALHA 81187, 7, MET 01195, 33, EET 84302, 28 and GRA 95209, 218 were examined for petrographic characteristics using a *Nikon POL* light microscope. These sections were then used to obtain major- and minor-element mineral compositions using a *Cameca* SX-100 electron microprobe (EMP) at the University of Tennessee, using an acceleration potential of 15 keV and a 1 μm beam size. Beam currents were 30 nA for olivine, pyroxene and spinel grains, 20 nA for metal and sulfide grains, and 10 nA for feldspar grains. Detection limits for silicate and spinel grains were <0.03 wt. % for SiO_2, TiO_2, Al_2O_3, MgO, CaO, and Na_2O, <0.04 wt. % for K_2O, V_2O_3, and Cr_2O_3, <0.05 wt. % for Cr_2O_3, MnO, FeO, and P_2O_5, <0.06 wt. % for NiO, and <0.1 wt. % for BaO. For analyses of metal and sulfide grains, the detection limits were <0.03 wt. % for Si, P, Mg, Al, and Ti, <0.04 wt. % for S, Fe, Cr, Mn, and Mg, and <0.05 wt. % for Co and Ni.

Highly siderophile element (HSE) abundances in metal and sulfide phases were determined in Acapulco, MET 01195, 33, GRA 95209, 218 and NWA 7474 using a *New Wave Research UP213* (213 nm) laser-ablation system coupled to a *Thermo Scientific iCAP Q* Inductively Coupled Plasma-Mass Spectrometer (ICP-MS) at the *Scripps Isotope Geochemistry Laboratory (SIGL)*. Analyses were done using spots with a 150 μm beam diameter, a laser repetition rate of 5 Hz, and a photon fluence of 3.5 J/cm^2. Ablation took place in a 3 cm^3 cell. The cell was flushed with

He-gas to enhance production and transport of fine aerosols, and was mixed with an Ar carrier-gas flow of ~1 L/min before reaching the torch. Oxide production, based on UO/U was less than 0.05%. Each analysis consisted of ~60 s data collection. Backgrounds on the sample gas were collected for ~20 s followed by ~40 s of laser ablation. Washout time between analyses was >120 s. Data were collected in time-resolved mode so effects of inclusions, mineral zoning and possible penetration of the laser beam to underlying phases could be evaluated. Plots of counts per second versus time were examined for each analysis, and integration intervals for the gas background and the sample analysis were selected. Standardization was performed using iron meteorite in-house standards Filomena, Hoba and Coahuila for siderophile element abundances, and the USGS sulfide standard, MASS-1.

2.2.3 Whole-rock sample preparation

Whole rock meteorite specimens were split and hand-ground into fine powders using an agate mortar and pestle (Corder, 2015). The mortar and pestle was cleaned between each sample using purified quartz sand and through rinsing was performed before and after the quartz sand abrasion, using ultra-pure water (18.2 MΩ). Fusion crusts were removed from the crushed aliquots prior to homogenization of powders. Metal-rich samples were difficult to fully homogenize due to resistance to powdering and potential for metal smearing on the mortar and pestle. This effect likely resulted in ‘nuggeting’ effects, evident in different HSE abundances across repeat analyses of the same sample.

2.2.4 Whole-rock major and trace-element analyses

Major and trace element analyses were performed on 40 mg sample aliquots, by weighing them into Parr Bomb vessels with 4 mL of Optima 29N HF and 1 mL of Teflon Distilled (TD) 15.7M HNO_3. The samples, along with standards and total procedural blanks were then digested at 170°C for >72 hours in a convection oven. Resulting clear solutions were dried down and then subject to two purification steps using TD HNO_3 in order to remove fluoride compounds that may cause measurement interferences. Stock solutions were prepared and doped with In, prior to making diluted solutions for trace-element (4000 × dilution) and major-element (40,000 × dilution) determinations. Major- and trace-elements were measured using a *ThermoScientific iCAP Q* ICP-MS in normal, low-resolution mode at the *SIGL* and were performed in an identical manner to results presented in Day et al. (2015; 2017). For major- and trace-elements, reproducibility of the reference materials was generally better than 6% RSD (Corder, 2015)

2.2.5 Rhenium-osmium isotope and HSE abundance analysis

Homogenised powder aliquots of acapulcoite-lodranites, standards (see Day et al., 2015; 2016b) and total analytical blanks were digested in sealed borosilicate Carius tubes, with isotopically enriched multi-element spikes (^{99}Ru, ^{106}Pd, ^{185}Re, ^{190}Os, ^{191}Ir, ^{194}Pt), and a 1:2 mixture of multiply Teflon distilled 12M HCl and purged 15.7M HNO_3 (expunged of Os by treatment with H_2O_2). Samples were digested to a maximum temperature of 270˚C in an oven for 96 hours. Osmium was triply extracted from the acid using CCl_4 and then back-extracted into HBr (Cohen & Waters, 1996), prior to purification by multiple micro-distillation (Birck et al., 1997). Rhenium and the other HSE were recovered and purified from the residual solutions using standard anion exchange separation techniques. Isotopic compositions of Os were measured in negative-ion mode on a *ThermoScientific* Triton thermal ionisation mass spectrometer at the *SIGL*. Rhenium, Pd, Pt, Ru and Ir were measured using a *Cetac Aridus II* desolvating nebuliser coupled to a *ThermoScientific iCAP Q* ICP-MS. Offline corrections for Os involved an oxide correction, an iterative fractionation correction using ^{192}Os/^{188}Os = 3.08271, a ^{190}Os spike subtraction, and finally, an Os blank subtraction. Precision for ^{187}Os/^{188}Os, determined by repeated measurement of the UMCP Johnson-Matthey standard was better than ±0.2% (2 SD; 0.11390 ±20; n = 5). Measured Re, Ir, Pt, Pd and Ru isotopic ratios for sample solutions were corrected for mass fractionation using the deviation of the standard average run on the day over the natural ratio for the element. External reproducibility on HSE analyses using the *iCAP Q* ICP-MS was better than 0.5% for 0.5 ppb solutions and all reported values are blank corrected. The total procedural blanks analyzed with samples had ^{187}Os/^{188}Os = 0.32 ± 0.24, with quantities (in picograms) of 1.8 ± 1.3 [Re], 30 ± 20 [Pd], 90 ± 20 [Pt], 9 ± 5 [Ru], 10 ± 9 [Ir] and 4 ± 3 [Os] (n = 3; all errors are 1 SD). These blanks resulted in negligible corrections to samples (<0.5%).

2.2.6 Oxygen isotope analyses

Oxygen isotope analyses of acapulcoite-lodranite meteorites were performed at the Institut de Physique du Globe-Paris (Corder, 2015) using identical methods to those described in Day et al. (2015). Silicate grains were pulverized under alcohol in a tungsten-carbide mortar and pestle, ultrasonicated in dilute HCl at room temperature for 240 s to remove weathering products, washed with MilliQ water, dried, and then separated into magnetic and non-magnetic fractions. Measurement was done using BrF_5 fluorination using a CO_2 laser coupled to a dual inlet mass spectrometer (*ThemoFinnigan* Delta V). Non-magnetic fractions of the meteorite samples were analyzed using laser fluorination along with San Carlos olivine and garnet standard UWG-2 (Valley et al. 1995). Oxygen isotopic ratios ($^{X}O/^{16}O$, where X = ^{18}O or ^{17}O) are measured versus international standard, V-SMOW, and expressed in δ notation, according to the following equation: $\delta^{X}O = 1000 \times ((^{X}O/^{16}O)/(^{X}O/^{16}O_{std})-1)$. From the delta notation values, $\Delta^{17}O$ (in per mil, representing deviation from the terrestrial fractionation line: $\Delta^{17}O = \delta^{17}O - ((\delta^{18}O/1000 + 1) \wedge 0.524 - 1) \times 1000)$ was then calculated. Values of $\delta^{18}O$ were normalized to UWG-2 garnet with $\delta^{18}O = 5.75‰$. Measurement of the San Carlos olivine and UWG-2 garnet standard aliquots that were measured gave (in per mil) uncertainties on $\delta^{17}O = \pm 0.09$, on $\delta^{18}O = \pm 0.17$, and for $\Delta^{17}O = -0.004 \pm 0.018$ (2 SD; n = 18). In-run uncertainties for individual measurements were <0.06‰ for $\delta^{17}O$ and <0.03‰ for $\delta^{18}O$.

2.3 Results

2.3.1 Petrography

Acapulcoites and lodranites can be broadly described as having a granular texture with moderate to high amounts of FeNi metal and subordinate troilite FeS. Silicate grains are typically ≤ 1 mm in maximum dimension in EET 84302 and MET 01195, ≤ 0.7 mm in GRA 95209, and ≤ 0.5 mm in Acapulco and ALHA 81187. Studied samples display variable degrees of textural equilibration, with EET 84302 as the most equilibrated meteorite, ALHA 81187 and Acapulco as the least equilibrated, and GRA 95209 and MET 01195 as moderately equilibrated. The meteorites contain low-Ca pyroxene, high-Ca pyroxene, plagioclase, olivine, FeNi metal, FeS metal, and chromite as major mineral phases, except for EET 84302, which lacks chromite in the samples that we examined. Acapulco, MET 01195, and ALHA 81187 also contain schreibersite as a minor mineral phase. Our petrographic results agree well with previously published petrography for acapulcoite-lodranites (e.g., Palme et al. 1981, Zipfel et al. 1995, McCoy et al. 1996, McCoy et al. 1997a, McCoy et al. 2006, Mittlefehldt et al. 1996; Corder 2015). Below, we describe the samples in approximately increasing order of partial melting. The modal percentages of FeNi metal and sulfide grains observed in thin sections are provided in *Table S9*.

The Acapulco meteorite displays a range of grain sizes (≤ 0.5 mm) and shapes (most often subhedral to euhedral) with silicate grains often creating 120° triple junctions (**Figure 2**, see also *Figure S1*), in agreement with previous studies (Palme et al. 1981; Zipfel et al. 1995) and possibly indicative of heterogeneous thermal disturbances after primary crystallization (Min et al., 2003). Many of the silicates in the meteorite poikilitically enclose smaller grains of other major mineral phases. This is evident in feldspars that enclose smaller (~20-40 μm) rounded grains of olivine and/or pyroxene minerals. Pyroxene and olivine grains are poikilitic whereas FeNi metal and troilite occur as coarse (≤ 0.5 mm) irregularly shaped grains, and as swarms of tiny (≤ 15 μm) blebs (*Figure S1*). There is remarkable similarity in the sizes of these swarms, which average ~150 × 75 μm, although some are smaller or larger, but never longer than 300 μm in any one dimension. The swarms have remarkably well defined boundaries within their silicate hosts and we interpret them to reflect annealed grain boundaries. The sample of Acapulco that we studied included a patch (~1 mm) of fusion crust, which could potentially differ in composition from bulk rock as a result of terrestrial alteration. While Terrestrial weathering was difficult to identify in reflected light, it is likely minimal since Acapulco is a fall and is reported to have been recovered within an hour of impact (Graham, 1978).

Acapulcoite ALHA 81187 contains a finer grained granular texture than Acapulco (**Figure 2.2**). The sample is relatively unequilibrated, containing subhedral silicate grains up to 0.5 mm in diameter, with most up to 0.25 mm in diameter, and large quantities of anhedral metallic grains (FeNi metal and lesser amounts of FeS, troilite) up to 0.5 mm in the longest dimension. Large grains of troilite are often adjacent to large FeNi metal grains, but large FeNi metal grains do not always have adjoining FeS grains. Notable features found in ALHA 81187 are remnants of small (~0.25 mm radius) layered globular structures (**Figure 2.3a**) of FeNi metal. Chromite is smaller in grain size than the other major mineral phases, with the largest grain measuring about 0.3 mm in the long dimension. In plane-polarized and cross-polarized light, the polished section of ALHA 81187, 7 appears dark because of the ubiquity of an opaque and poorly reflective material (possibly carbon) that exists interstitially (**Figure 2.4c,d**). This darkening may be a result of reduced conditions, as has been previously suggested by Yugami et al. (1995).

Moderately equilibrated acapulcoite MET 01195 contains the same major mineral phases as Acapulco and ALHA 81187, and also displays a similar granular texture (**Figures 2.2** and **2.3**). Silicate grain sizes approach 0.8 mm in a few cases, but mostly remain between 0.1 and 0.4 mm, with abundant 120° triple junctions. Terrestrial weathering is present throughout the sample as rust colored alteration along grain boundaries and within fractures in silicates. Iron-nickel metal, troilite, and chromite grains in MET 01195 have a few major morphological differences from the other acapulcoites. Iron-nickel metal grains are generally larger in size, with the largest measuring ~1.5 × 0.5 mm. The largest metal grain adjoins a large chromite grain that measures ~1.2 × 0.5 mm. The majority of FeNi grains are anhedral to subhedral, with the longest dimensions spanning 0.1-0.5 mm. Chromite generally remains ≤ ~0.1 mm in the long dimension. Iron-sulfide metals grains are typically ~50-250 µm in size, but are also present as tiny micron-scale blebs within silicates or in interstitial spaces. In many instances FeS grains adjoin FeNi grains. In reflected light, a few narrow (≤ 50 µm wide, discontinuous bifurcating veins can extend up to 3 mm in length) veins of grey weathered material (likely iron oxide) occur. In some FeNi grains, short “splashes” of dark carbonaceous material are associated with the metal (**Figure 2.3**).

The transitional acapulcoite-lodranite EET 84302 is the most equilibrated of the acapulcoite-lodranites in this study and displays the coarsest granoblastic texture (**Figure 2.2**, see also *Figure 2.S2*). The polished section, EET 84302, 28, was previously studied by Yugami et al. (1998), Takeda et al. (1994) and Corder (2015). Silicate grain sizes are variable (≤ 1 mm, with most in the range of ~0.2-0.5 mm) and abundant 120° triple junctions are visible. Silicate grains are euhedral to subhedral, often with one or more fractures, and rarely display undulatory extinction, which is indicative of shock. The polished section exhibits terrestrial weathering effects, evident in the rust colored alteration along grain boundaries and intergranular fractures; however, EET 84302, 28 is also noticeably less weathered than ALHA 81187, 7 and MET 01195, 33. Takeda et al. (1994) reported dusty cores in EET 84302 orthopyroxene grains, and we confirm this observation along with a modified observation that the cores’ dusty appearance is associated with well-defined (often ~0.1-0.3 mm in the long dimension) swarms of tiny (µm-scale) metallic blebs, much like those found in Acapulco. FeNi metal dominantly occurs as large ‘pooled’ grains that can be connected by narrow metallic ‘arms’; the large, elongate grains can be up to ~2 mm in length. Troilite is also present in the sample, but is less common and has a smaller (≤ 0.1 mm) grain sizes than the FeNi metal.

Graves Nunataks 95209, the single ‘lodranite’ (considered ‘transitional’ in this study) for which we obtained a polished section (,218; **Figure 2.3**), is a moderately coarse grained granoblastic and metal-rich stone that displays many of the same petrologic characteristics as the acapulcoites described above. McCoy et al. (2006) studied the meteorite in detail and described three different lithologies present – “prominent metal veins, the metal-poor regions, and the matrix that serves as the host for the other two lithologies and is the dominant lithology.” Our results are similar to those of McCoy et al. (2006), with the exception that they reported a maximum silicate size of 2 mm while in this study the maximum silicate grain size observed is 0.8 mm in the longest dimension. Most silicate grains are ≤0.5 mm. This likely suggests textural heterogeneity within GRA 95209 that has been reported previously (Mittlefehldt and Lindstrom 1998, McCoy et al. 2006). Examination in reflect light reveals narrow grey weathered veins thought to be iron oxide (≤40 μm wide, often mm-scale in length with one vein measuring 6 mm long) and similarly sized counterpart veins of FeNi metal with and without troilite (*Figure 2.S3*). Some of these FeNi metal grains are hosts to graphite rosettes (cf., McCoy et al., 2006). There is also a significant decrease in the number of FeNi grains in proximity to a large weathered vein (*Figure 2.S3*).

2.3.2 Major- and minor-element mineral chemistry

All five acapulcoite-lodranites examined for major- and minor-element mineral chemistry are similar in composition (**Table 2.1**), with no examples of zoning of silicate grains observed in any of the samples. This relationship is reflected in the limited ranges in pyroxene and plagioclase compositions for the meteorites; low-Ca pyroxene grains exhibit a range in Cr_2O_3 contents (0.28 wt.% in Acapulco to 0.91 wt.% in ALHA 81187). (**Figure 2.5**). The olivine grains within the meteorites have low CaO contents (<0.03 wt.%), and a limited range of forsterite (Fo) contents among the meteorites (e.g., Clayton & Mayeda, 1988; McCoy, 1994). The errors reported for the mineral data are 1 SD, unless otherwise noted.

As the archetypal acapulcoite, Acapulco contains olivine grains with an average forsterite (Fo) content of 88.4 ± 0.1 (*n* = 12) where forsterite is the Mg-rich end-member of olivine. The feldspars have anorthite and albite compositions of $An_{15.7 \pm 0.4}Ab_{80.5 \pm 0.3}$ (*n* = 13), which reflect their Ca and Na content, respectively. The pyroxens are described by their wollastonite (Ca-rich end-member) and enstatite (Mg-rich end-member) contents, with the low-Ca pyroxene average of $Wo_{1.7 \pm 0.3}En_{86.9 \pm 1.2}$ (*n* = 13), and high-Ca pyroxene average of $Wo_{44.8 \pm 1.1}En_{50.5 \pm 0.6}$ (*n* = 5). Acapulco also contains chromites with Cr# (where Cr# = Cr/(Cr+Al) × 100) of 87.8 ±0.5 (*n* = 16), FeNi metal grains with 87.3 ±6.1 wt. % Fe (*n* = 24), and troilite with 36.7 ±0.4 wt. % S (*n* = 12). Our data agrees well with the published data for the Acapulco meteorite (Palme et al. 1981; Zipfel et al. 1995; Corder, 2015).

Acapulcoite ALH 81187, 7 contains olivines of $Fo_{95.8 \pm 0.1}$ (*n* = 7), feldspars of $An_{19.4 \pm 0.7}Ab_{79.0 \pm 0.7}$ (*n* = 6), low-Ca pyroxenes of $Wo_{3.1 \pm 0.5}En_{90.5 \pm 1.3}$ (*n* = 10), and high-Ca pyroxenes of $Wo_{43.1 \pm 0.9}En_{54.1 \pm 0.6}$ (*n* = 6). Allan Hills 81187 also contains chromite grains with Cr# of 87.2 ±1.8 (*n* = 5), FeNi metal grains with 93.0 ±0.5 wt. % Fe (*n* = 18), troilite with 37.2 ±0.4 wt. % S (*n* = 6), and schreibersite grains with 43.1 ±6.0 wt. % Fe (*n* = 7). Mittlefehldt et al. (1996) and McCoy et al. (1996) published mineral chemistry data for ALHA 81187, and the datasets presented here and in those studies are in good agreement (Corder, 2015).

The relatively texturally equilibrated acapulcoite MET 01195, 33 contains olivine grains of $Fo_{91.3 \pm 0.1}$ (*n* = 7), feldspars of $An_{16.9 \pm 0.6}Ab_{79.9 \pm 0.4}$ (*n* = 8), low-Ca pyroxenes of $Wo_{1.7 \pm 0.4}En_{89.5 \pm 0.5}$ (*n* = 7), and high-Ca pyroxenes of $Wo_{43.6 \pm 0.9}En_{52.4 \pm 0.8}$ (*n* = 8). Meteorite Hills 01195 also contains chromite grains with Cr# of 86.3 ±0.2 (*n* = 9), FeNi metal grains with 87.6 ±6.0 wt. % Fe (*n* = 13), troilite with 36.6 ±0.2 wt. % S (*n* = 12), and schreibersite grains with 35.5 ±1.0 wt. % Fe (*n* = 5). Rubin (2007) reported data for MET 01195 olivine grains, low-Ca pyroxenes, and chromite grains and our data is in agreement for the same mineral phases (Corder, 2015).

Transitional acapulcoite-lodranite EET 84302, 28 contains olivines of $Fo_{91.7 \pm 0.1}$ (*n* = 7), feldspars of $An_{23.8 \pm 0.9}Ab_{74.4 \pm 0.7}$ (*n* = 9), low-Ca pyroxenes of $Wo_{1.8 \pm 0.3}En_{90.0 \pm 0.4}$ (*n* = 7), and high-Ca pyroxenes of $Wo_{44.3 \pm 1.3}En_{52.2 \pm 1.2}$ (*n* = 7). It also contains FeNi metal grains with 92.7 ±0.4 wt. % Fe (*n* = 9), troilite grains with 36.5 ±0.1 wt. % S (*n*

= 6), and schreibersite with 53.7 ±3.9 wt. % Fe (*n* = 6). Mittlefehldt et al. (1996) reported data for EET 84302 olivine grains, low-and high-Ca pyroxenes, and feldspars and McCoy et al. (1997a) reported data for olivines and low- and high-Ca pyroxenes; our data agrees well with both published studies (Corder, 2015).

The transitional meteorite, GRA 95209, 218 contains olivines of $Fo_{92.9 \pm 0.1}$ (*n* = 8), feldspars of $An_{18.7 \pm 0.8}Ab_{79.5 \pm 0.8}$ (*n* = 8), low-Ca pyroxenes of $Wo_{3.1 \pm 0.5}En_{89.6 \pm 0.6}$ (*n* = 8), and high-Ca pyroxenes of $Wo_{42.2 \pm 0.2}En_{54.1 \pm 0.2}$ (*n* = 7). Graves Nunataks 95209 also contains chromite grains with Cr# of 91.7 ±1.3 (*n* = 13), FeNi metal grains with 92.0 ±0.6 wt. % Fe (*n* = 9), and troilite with 36.7 ±0.8 wt. % S (*n* = 11), which agrees with previously published data (Mittlefehldt & Lindstrom 1998; McCoy et al. 2006; Corder, 2015).

2.3.3 Highly siderophile element abundances of metal and sulfide grains

Highly siderophile element abundances were measured in individual metal and sulfide grains in Acapulco, MET 01195, GRA 95209 and NWA 7474 using LA-ICP-MS and are reported in **Table 2.2**. The data reveal that FeNi metal grains have, on average, 20 to 300 times greater HSE abundances than associated troilite grains. FeNi metal grains in the meteorites show similar patterns to the bulk rock, with high Os and Ir contents and low Pd contents (**Figure 2.6**). The most elevated HSE abundances occur in the FeNi metal grains of NWA 7474, at ~40 × CI chondrite abundances of Os and Ir, ~20-30 × CI chondrite abundances for Re, Ru, Rh, Pt and Au, and ~8 × CI chondrite abundances for Pd. Troilite grains in the meteorites have relatively low and variable HSE abundances. Repeat analyses of the troilite grains in Acapulco demonstrate that they have strong enrichment in Pd (~3 × CI chondrite abundances), but this feature is not exhibited in troilite grains from MET 01195 or GRA 95209.

2.3.4 Whole-rock major- and trace-element abundances

Lodranite meteorites have more variable major element abundances than acapulcoite meteorites in the samples that we analyzed (**Table 2.3**, after Corder, 2015). While Mg (13.6 ± 3.2 wt.%, 1 SD), Ti (0.08 ± 0.02 wt.%, 1 SD) and Mn (0.25 ± 0.03 wt.%, 1 SD) have relatively invariant absolute concentrations (≤ ~20% variation) within the meteorites, ratios of (Na, Fe, Al, P, Ca, Cr, Co, Ni)/Mg are highly variable within lodranites compared with acapulcoite meteorites (**Figure 2.7**).

Trace-element abundances were analyzed in the eight different acapulcoite-lodranite meteorites and are reported in **Table 2.4** (Corder, 2015) and **Figures 2.8** and **2.9**. Samples show broadly flat, CI chondrite-like patterns, with the notable exceptions of Cs, Rb, Ba, Th and U. The desert meteorite NWA 4875 displays negative Zr and Hf anomalies that are more pronounced than the rest of the acapulcoite-lodranite meteorites. The CI-normalized Zr/Hf ratio of the meteorite is elevated (Zr/Hf = 1.33), whereas the rest of the group displays Zr/Hf closer to unity (average Zr/Hf = 1.01 ± 0.06).

Acapulcoite and lodranite meteorites analyzed in this study exhibit variable REE patterns, with a range of abundances from ~0.3 to ~3 × CI chondrite abundances (**Figure 2.9**). Acapulco, ALHA 81187, MET 01195 and NWA 2871 have broadly flat patterns for the middle (MREE; e.g., Sm) to heavy REE (HREE; e.g., Yb), but Acapulco is characterized by light REE (LREE) enrichment (La/Yb = 2.7). NWA 2871 (La/Yb = 2.8) and NWA 4833 (La/Yb = ~6) both show similar LREE enrichment to Acapulco but, as with the other lodranites, NWA 2871 has generally lower absolute REE abundances than acapulcoites and strong depletion in the MREE/HREE. This is reflected in the generally lower Ho/Yb ratios for lodranites (~0.26-0.3), compared with acapulcoites (≥0.3). Seven out of the eight meteorites exhibit positive Eu anomalies (Eu/Sm ratios between 1.0 and 2.2). MET 01195, the single acapulcoite-lodranite with a negative Eu anomaly, has an Eu/Sm ratio of 0.88. A general trend among the samples is that the acapulcoites exhibit the highest and most chondrite-like REE patterns, the transitional samples have lower REE abundances and comparable REE patterns, and the most partially melted lodranites have the lowest REE abundances and more fractionated patterns.

2.3.5 Oxygen isotopes

The samples analyzed in this study show agreement with oxygen isotope measurements from prior studies (**Table 2.5**; Mayeda and Clayton, 1980; Clayton & Mayeda, 1992; McCoy et al., 1993; Clayton et al., 1996; Greenwood et al., 2012, 2016). The $\delta^{17}O$ values range from -0.64 to +1.31 ‰, with an average of +0.47 ± 0.54

‰ (1 SD), and the $\delta^{18}O$ values range from +1.27 to + 4.02 ‰, with an average of +2.90 ± 0.87 ‰ (1 SD). The acapulcoite-lodranite meteorites form a distinct array on an oxygen three-isotope diagram (**Figure 2.10**) that lies between the slope 1 (Young & Russel; Y&R) and carbonaceous chondrite anhydrous mineral (CCAM) lines, and reflects an intermediate, primordial oxygen isotope composition; these reference lines represent primordial variation in oxygen isotopes of Solar System materials (Greenwood et al., 2012).

2.3.6 Rhenium-osmium isotope systematics and HSE abundances

New whole rock HSE abundances and ^{187}Re-^{187}Os systematics for acapulcoite-lodranites are reported in **Table 2.6**. The HSE concentrations of the measured acapulcoite and lodranite samples range from approximately 0.1 to 10 times CI chondrite values (**Figure 2.11**) and the $^{187}Os/^{188}Os$ ratios are broadly chondritic, ranging between 0.1242 and 0.1315 (Chondritic range = 0.120-0.132; Walker et al., 2002; Fischer-Godde et al., 2010; Day et al., 2016). Acapulcoite samples (ALHA 81187, MET 01195, NWA 2871, Acapulco) generally cluster closer to chondritic abundances, while the lodranites (NWA 4833, NWA 4875, NWA 7474) exhibit greater variability in HSE abundances. The transitional meteorites, EET 84302 and GRA 95209, exhibit the highest, ‘supra-chondritic’ abundances of the sample suite. This is consistent with the concept that the two samples have similar melting and partitioning histories, intermediate between acapulcoites and lodranites (McCoy et al., 2006). The majority of samples have broadly flat HSE abundance profiles, with pronounced down-turns in Pd, similar to what is observed in individual metal grain analyses (**Figure 2.6**). However, Acapulco exhibits Pd enrichments and this aliquot is likely enriched in sulfides, making it distinct from the other acapulcoite and lodranite meteorite samples.

Fractionation of the HSE within samples is evident for the majority of samples, with elevated Pt/Os ratios in acapulcoites and acapulcoites-lodranites, and lower Pd/Os ratios in lodranite samples. The acapulcoite and acapulcoite-lodranite samples exhibit higher Pt/Os ratios (Pt/Os = 1.86 ± 0.04; *n* = 5, excluding Acapulco; all errors are 1 SD) compared to lodranite samples (Pt/Os = 1.26 ± 0.32; *n* = 3). Ratios of Pd/Os are higher for the acapulcoites (Pd/Os = 0.90 ± 0.15; *n* = 3, excluding Acapulco), compared to the lodranites and acapulcoites-lodranite samples (Pd/Os = 0.51 ± 0.13; *n* = 5). A notable exception to this is the Acapulco meteorite, which exhibits elevated Pd abundances, with Pd/Os = 1.87 ± 0.39 (*n* = 2), and lower Pt/Os = 1.39 ± 0.01; (*n* = 2). There is limited fractionation between Ir and Os, with an Ir/Os = 1.01 ± 0.13 (*n* = 9).

In ^{187}Re/^{188}Os-^{187}Os/^{188}Os space, samples exhibit some scatter around the 4.56 Ga iron meteorite reference isochron (**Figure 2.12**). They exhibit chondritic ^{187}Os/^{188}Os compositions, but range in ^{187}Re/^{188}Os, indicating open-system behavior of Re (e.g., Hyde et al., 2014; Day et al., 2016). The Re* values, which are calculated Re abundances assuming chondritic ^{187}Os/^{188}Os at the time of crystallization (e.g., Day et al., 2010), deviate significantly from the measured Re concentrations, particularly for samples that exhibit heterogeneity in ^{187}Re/^{187}Os ratios across different aliquot digestions (Acapulco, EET 84302, NWA 4875, NWA 7474). This is also observed for some iron meteorite groups (e.g., Morgan et al., 1995).

2.4 Discussion

New results for the acapulcoites and lodranites that we studied confirm and extend the petrography and mineral chemistry observations previously made for these samples (Palme et al. 1981, Zipfel et al. 1995, McCoy et al. 1996, McCoy et al. 1997a, McCoy et al. 2006, Mittlefehldt et al. 1996; Corder, 2015). In the following discussion, we focus on the behavior of the HSE in the acapulcoites and lodranites to better understand melting processes during planetary formation and to examine the mechanisms by which early metal-silicate segregation occurred on planetary bodies.

2.4.1 Alteration and open system behavior

We recognize at least three different lines of evidence for alteration and open system behavior in the acapulcoites and lodranites that are largely attributable to terrestrial alteration. Nonetheless, we conclude that these effects are not responsible for the HSE abundances and inter-element fractionations of these elements that are observed in the meteorites. The first line of evidence is obvious petrographic evidence for alteration. Rust coloration along grain boundaries and silicate fractures observed in EET 84302, ALHA 81187 and MET 01195 are indicative of terrestrial weathering.

The oxidation of iron is likely related to the high metal and sulfide content in these rocks, which makes them susceptible to alteration in the terrestrial environment.

The second line of evidence is the behavior of trace elements known to be subject to disturbance through alteration. Two desert samples, NWA 4833 and NWA 4875, exhibit notable Ba enrichments (~100 ppm) and elevated U contents, which are typically observed for hot desert meteorites (e.g., Barrat et al., 1999; Crozaz et al., 2003). Depletions in Cs and Rb are observed for all samples, which may be a primary feature of the acapulcoite-lodranite meteorites, but some meteorites, such as NWA 4833 and ALHA 81187, exhibit slightly higher Cs and Rb contents, which may be a result of weathering and exterior contamination (Biswas et al., 1980). Slight enrichments in Sr are also observed for all meteorites, which may reflect contamination during terrestrial residence time (Crozaz et al., 2003). The elevated LREE patterns in NWA 4833 may be related to terrestrial alteration, since desert weathering leads to REE mobilization (e.g. Mittlefehldt & Lindstrom, 1991; Crozaz et al., 2003), but Acapulco, which is a fresh fall, shows a similar effect suggesting these may be primary characteristics of the samples. Desert weathering may also explain the unusual character of one of the aliquots of NWA 2871, which exhibits unusual enrichments in La and Ce (CI-normalized La/Ce = 1.29). An alternative explanation for elevated LREE in Acapulco could be phosphate content, which constitutes up to 1.6 modal % (percentage by mineral mode) of this meteorite (Palme et al., 1981); this may also be valid for other samples that exhibit LREE enrichments (e.g. MET 01195).

A third line of evidence for alteration and open-system behavior comes from the Re-Os isotope system. The majority of samples exhibit combined ^{187}Re/^{188}Os-^{187}Os/^{188}Os systematics that deviate from the 4.56 reference isochron (**Figure 2.12**), which is defined by iron meteorites that crystallized within the first 40 Ma of Solar System formation (Smoliar et al., 1996). In the case that precursor material for the acapulcoite-lodranite meteorites had uniform initial ^{187}Os/^{188}Os ratios, the range in ^{187}Re/^{188}Os ratios, and the differences between measured Re abundances and calculated Re* values indicate open-system behavior, as has been recognized previously for partially differentiated ureilites, brachinites, and other achondrite meteorites (Rankenburg et al., 2007; Van Acken et al., 2012; Riches et al., 2012; Day et al., 2012; 2016; Hyde et al., 2014).

The acapulcoite and lodranite samples generally show Re* values that are higher than the measured abundances (**Table 2.6**), indicating Re loss (or Os gain). The transitional meteorites, EET 84302 and GRA 95209, exhibit Re abundances higher than Re* values that could be related to the metal-rich nature of these samples, which may have resulted in localized Re enrichments in the surrounding silicate matrix. Most notably, one aliquot of EET 84203 with a much lower Re* value compared to measured Re also exhibits a ^{187}Re/^{188}Os ratio that strongly deviates from the reference isochron (**Figure 2.12**), indicating open-system behavior and Re gain (or possibly Os loss). During metal segregation, Ir and Os exhibit similar partitioning behavior and thus the small range of Ir/Os ratios that approach unity (Ir/Os_{avg} = 1.01 ± 0.13; n = 9, 1 SD) reflects limited mobilization of Os. The mobilization of Re is therefore a more probable explanation for the differences in Re* values and measured Re concentrations; this mechanism is further supported by Re/Os = 0.08 ± 0.05 (1 SD) and $^{187}Re/^{188}Os$ = 0.387 ± 0.25 (n = 9, 1 SD), for which the error is ~60% of the mean value, indicating significant variability among samples.

The differences in Re/Os between different aliquots of samples (e.g., NWA 4875, EET 84302) suggest localized mobilization on a small scale (sub-cm to millimetric), rather than wholesale loss or gain of Re from bulk meteorites; this could be the result of weathering of metals, oxides and sulfides leading to Re depletions (Hyde et al., 2014). The primary host phases for the HSE in the meteorites are metals and sulfides, which are particularly susceptible to aqueous alteration, as observed for chondrite meteorites (Horan et al., 2003; Fischer-Godde et al., 2011); Re enrichments are also associated with altered sulfide phases such as marcasite (Hyde et al., 2014). Similar to brachinites ($^{187}Os/^{188}Os$ = 0.1280 ± 0.0030, n = 6, 1 SD; Day et al., 2012), the limited and chondritic range of $^{187}Os/^{188}Os$ for acapulcoite and lodranite meteorites (0.1271 ± 0.0020, *n* = 9; 1 SD) suggests that Re mobilization occurred during terrestrial weathering and alteration, and is not indicative of open-system behavior on the acapulcoite-lodranite parent body.

2.4.2 Origin of acapulcoite-lodranite meteorites

The acapulcoites and lodranites are considered to come from the same parent body (e.g., Clayton and Mayeda, 1996, 1999; McCoy et al., 1996, 1997a,b; Mittlefehldt et al., 1996; Weigel et al., 1999), which is supported by the measurements of mineral compositions, trace element abundances and oxygen isotope ratios on samples made in this study. The petrological data exhibits similar high-Ca and low-Ca pyroxene, feldspar and chromite compositions among samples; the range of forsterite content in olivine grains is limited ($Fo_{88.4} – Fo_{95.8}$) and is similar to that of winonaites (**Figure 2.5**; Goodrich et al., 2011). Furthermore, samples unaffected by open-system behavior and alteration exhibit trace element patterns that are similar.

Oxygen isotopes are important indicators of genetic links between meteorites and measurements from this study show close agreement with prior studies (**Table 2.5**; Mayeda and Clayton, 1980; Clayton et al., 1992; McCoy et al., 1993; Clayton et al., 1996; Greenwood et al., 2012, 2016) and yield an average $\Delta^{17}O$ value for acapulcoite lodranites of = -1.04 ± 0.28 (2 SD), with a range of -0.791 to -1.305 ‰. The acapulcoite-lodranite array is more variable than that exhibited for the differentiated howardite-eucrite-diogenite meteorites or angrite meteorites, which have average values of $\Delta^{17}O$ = -0.24 ± 0.01‰ (2 SD) and $\Delta^{17}O$ = - 0.07 ± 0.01‰ (2 SD), respectively (Greenwood et al., 2012), and define their own mass-dependent fractionation lines (**Figure 2.10b**). The variable $\Delta^{17}O$ composition of the acapulcoite-lodranite group has been interpreted to reflect primary variability in the chondrite precursor material (Greenwood et al., 2012), which has also been observed in the range of C and N isotopes in graphite phases that generally occur within kamacite grains (El Goresy et al., 2005). These data are consistent with incomplete melting and a lack of wholesale homogenization on the acapulcoite-lodranite parent body, compared to the fully differentiated angrite and HED parent bodies. This is also observed for the brachinite meteorites (Day et al., 2012) and likely reflects the 'primitive' and limited melting on the brachinite and acapulcoite-lodranite parent bodies.

2.4.3 Petrological evidence for metal melt segregation and pooling

The early process of metal segregation in the acapulcoite-lodranite meteorites is evident in the pooling of metal that is clearly indicated by the transitional meteorite samples, with metal vein networks up to ~4 mm in EET 84302 and thin metal veins ~2 mm in GRA 95209 (*Figures 2.S2* and *2.S3*). The thin section of GRA 95209 in this study (218) has more matrix than metal, but prior work has revealed metal veins up to 1 cm in width for this sample McCoy et al. (2006). Extensive metal pooling and draining networks indicate Fe-Ni-S melting and segregation from silicate phases, as is considered to have occurred during core-formation on planetesimals. A deep origin and metal intrusion for GRA 95209 have been suggested (McCoy et al., 2006), and so the transitional acapulcoite-lodranite meteorites may reflect metal ponding and sinking within the acapulcoite-lodranite parent body. Regions of pooled metal and FeNi veins have also been observed for other acapulcoite-lodranite samples (e.g., McCoy et al., 1996, 1997a,b; Zipfel et al., 1995; Rubin et al., 2007), including Acapulco, MET

01195 and ALHA 81187 (this study). This indicates that the acapulcoite-lodranite meteorites, and the continuum from acapulcoite to transitional acapulcoite-lodranite to lodranite, are important for examining early mechanisms of metal segregation, including pooling and draining of metal out of silicate regions, as well as metal infiltration into deeper source regions.

2.4.4 Partial melting of silicates

With the exception of terrestrial alteration effects (e.g., NWA 4833, NWA 4875), the REE patterns of the acapulcoite-lodranite meteorites largely reflect chondritic relative abundances and, therefore suggest limited partial melting and melt-solid segregation in the silicate system. The acapulcoites exhibit higher concentrations of the REE than lodranites that are close to chondrite absolute abundances, indicative of a general lack of silicate melting, as noted in prior studies (McCoy et al., 1997). The lodranites and transitional meteorites have lower absolute REE abundances and more fractionated CI chondrite normalized REE patterns, which can be explained by silicate melting and migration out of the source regions for these meteorites (McCoy et al., 1997). The majority of samples, except MET 01195, show positive Eu anomalies (higher relative abundance of Eu compared to the other REE) that are generally associated with plagioclase content; the positive Eu anomaly is minimal for EET 84302, but noticeable for GRA 95209 and NWA 2871, indicating that plagioclase migration for these samples was inefficient (e.g., Floss, 2000).

The general trend for REE abundances in the acapulcoite-lodranite meteorites is progressive depletion associated with loss of silicate phases, which was greatest for the lodranite meteorites. This is supported by partial melt modeling that we adopted from our previous work (e.g., Day et al., 2017) (**Figure 2.13**) from an initial CI chondrite composition (McDonough and Sun, 1995), which exhibits similar patterns to the acapulcoite-lodranite meteorites, with increased degrees of partial melting resulting in decreased REE abundances and more fractionated REE patterns in the residues. Because of the uncertainties surrounding the LREE enrichments in acapulcoites and lodranites, we focus our estimates of partial melting on the HREE, which are generally less susceptible to alteration. Based on our partial melting calculations, we find that the acapulcoites have experienced less than 2% silicate melt loss (by mass), whereas the lodranites (e.g., NWA 4833) have experienced up to 7% silicate melt loss, assuming a CI chondrite starting composition. The elevated REE abundances observed for Acapulco and MET 01195, and to a lesser degree for NWA 2871 and ALHA 81187, may be a result of phosphate content, such as REE-rich merrillite or apatite phases (Floss, 2000).

2.4.5 Metal-sulfide partitioning of the HSE

The inter-element fractionation observed amongst the HSE in the acapulcoite-lodranite meteorites may be primarily attributed to metal-sulfide partitioning during incipient melting and migration. This is particularly evident in the decreasing Pt/Os and Pd/Os ratios in the transition from acapulcoites to lodranites. A possible explanation for this may be differential metal-silicate and metal-sulfide partitioning of the HSE, which is supported by experimental studies.

The relative compatibilities of the HSE between silicate solid and melt are Os > Ir > Ru > Pt > Pd > Re (Pearson et al., 2004; Brenan et al., 2003, 2005; Becker et al. 2006; Fischer-Godde et al., 2011; Day et al., 2016). This order also reflects their general affinity for metal, where $D^{met/sil\ melt}$ is the metal-silicate melt partition coefficient and higher $D^{met/sil\ melt}$ values reflect a greater affinity for the metal phase. For example, partitioning experiments between metal and silicate at 1400°C yielded $D^{met/sil\ melt} \sim 10^4$ for Re at IW -1, $D^{met/sil\ melt} \sim 10^3$ to $\sim 10^7$ for Pd at IW -2, $D^{met/sil\ melt} \sim 10^9$ (up to 10^{12}) for Ir at IW -1 (O'Neill et al., 1995; Brenan et al. 2003; 2016). Experimental work on Fe-HSE alloys with synthetic peridotite melts by Mann et al. (2012) indicates increasing metal-silicate partition coefficients with decreasing oxygen fugacity, most notably for Ir, Re and Ru, and decreasing $D^{metal/silicate}$ at higher temperatures and pressures. At the peridotite liquidus and IW -2, the partition coefficients range from $\sim 10^{11.5}$ to $10^{6.5}$, with Ir > Pt ~ Ru > Re > Pd (Mann et al., 2012). The partition coefficients for Os is similar to Ir (e.g. Barnes et al., 1985), and this value reduces to $D^{met/sil\ melt} \sim 10^7$ at the fayalite-magnetite-quartz redox buffer, FMQ (O'Neill et al., 1995; Hart and Ravizza, 1996). Experimental data therefore suggests extremely siderophile behavior of Os, Ir, Ru and Pt at the low oxygen fugacity conditions of the acapulcoite-lodranite meteorites, with possibly increased metal partitioning at the lower temperatures experienced by the acapulcoites.

The lower Pd/Os, Pt/Os and Pt/Ru ratios among the lodranites, compared to the acapulcoites, may reflect the effect of increasing temperatures, which significantly decreases the metal-silicate partition coefficients of palladium and platinum (e.g. Mann et al., 2012). An alternative explanation may be that higher degrees of partial melting in lodranite source regions led to the extraction of Pt and Pd into the migrating melt, which may have been further affected by the sulfur content of the melt (e.g. Chabot and Jones, 2003). This assertion appears to be supported by overall troilite depletions observed in lodranites compared to the nearly-chondritic abundances of troilite typical of acapulcoites (McCoy et al., 1993). Preferential sulfur partitioning of Pd is implicated by whole rock and *in situ* analyses of Acapulco, which exhibits an elevated Pd/Os ratio in the bulk rock and significantly Pd-enriched sulfide grains. These distinct sulfide compositions are consistent with decreased metal-silicate partition coefficients of sulfur with decreasing oxygen fugacity conditions (Rose-Weston et al., 2009), suggesting immiscible sulfur-rich phases during Fe-Ni-S melting at fO_2 ~ IW -2 on the acapulcoite-lodranite parent body.

The inter-element fractionation for Pd/Os and Pt/Os among the acapulcoite-lodranite meteorites can be modeled using a solid metal-liquid metal parametrization for the partitioning of siderophile elements in the presence of sulfur (Chabot and Jones, 2003). This is shown in **Figure 2.14**, where the partition coefficient for Pd (represented by 1/D) is largely unchanged with greater amounts of sulfur (as mole fraction) in the melt versus Os, Ir and Pt, which exhibit increasingly siderophile behavior. We assume an initial CI chondrite HSE composition, and metallic partition coefficients (D_0) and element specific constants (β) from Chabot and Jones (2003) to model the expected concentrations of Pd, Pt, Ir, Os after partial melting and melt migration in metal-rich residues; our models are similar to those of Rankenburg et al. (2008) and Day et al. (2012; 2017) for ureilite and brachinite meteorites. With progressive metal melt removal, we find that the Pd/Os and Pt/Os ratios decrease in a solid residue (**Figure 2.15**). This may have occurred from the migration of liquid metal from acapulcoite source regions, and subsequent melting of the remaining solid composition that resulted in the acapulcoite-lodranite and lodranite meteorites.

The model replicates the Pt/Os and Pd/Os ratios observed in the acapulcoite and lodranite samples, but the intermediate, acapulcoite-like Pt/Os ratios (~1.8) and lodranite-like Pd/Os ratios (~ 0.5) ratios observed in the transitional meteorites (EET 84302 and GRA 95209) are more difficult to explain using these models; this issue is similar to that previously observed brachinite-like achondrite meteorites with high Pt/Os (NWA 6077; Zag(b); Day et al., 2012). We suggest two possibilities to explain the compositions of these meteorites. First, they could be explained by the more rapid depletion of Pd compared to Pt in solid metal residues, such as through an initial loss of Pd during the removal of Pd-rich sulfide melt, followed by Pt loss with increased silicate melting and sulfide removal. Evidence for this process is suggested by the large metal grains and networks observed in these samples, which presumably reflect the increased degrees of Fe-Ni-S melting, but with less silicate melting than the more evolved lodranite meteorites. It is also supported by the high Pd contents in sulfide grains from the Acapulco meteorite. Relative exhaustion of Pd by these processes may have led to a change in Pd in later formed sulfide grains in some of the transitional acapulcoite-lodranites and lodranites (e.g., **Figure 2.6**). Alternatively, these meteorites may reflect metal melt pooling (core formation). Residues depleted in Pt and Pd relative to Os result in complementary metal-sulfide melts enriched in Pt and Pd relative to Os. In either case, the highest HSE concentrations are observed in these acapulcoite-lodranite meteorites, EET 84302 and GRA 95209, and ratios may reflect enriched precursor material or regions of trapped, interstitial metal rich in HSEs, including intrusions from distant source regions (e.g. McCoy et al., 2006) prior to the large-scale melt migration and troilite depletion hypothesized for the lodranites.

Measurements of the HSE reveal inter-element fractionation trends in the Pt/Os and Pd/Os that can be explained by the control of sulfur during progressive metal-sulfide partitioning, which builds on prior work (e.g., McCoy et al., 2006) to examine early metal segregation mechanisms during core-formation. This observation is supported by experimental studies of HSE partitioning under conditions of low pressure and oxygen fugacity. Planetesimals that accreted to form the larger, terrestrial bodies may have experienced melting histories similar to the acapulcoite-lodranite meteorites. This is supported by the fact that some differentiated bodies are older than chondrite parent-body materials by about one million years (Bizzarro et al., 2005) and may represent intermediate or precursor material for larger bodies. The metal segregation evident in acapulcoite-lodranite meteorites may therefore be analogous to early accretion on the Earth, prior to large-scale metal ponding and core-formation.

2.5 Conclusions

Acapulcoites and lodranite meteorites capture the very early, transitional period between melting of chondrite-like precursors and core-formation and are therefore valuable for ascertaining planetary evolution. New oxygen isotope data, combined with petrology and geochemistry confirm previous conclusions that acapulcoite-lodranites likely derive from a single parent body that was accreted from isotopically heterogenous precursor materials that never fully mixed or equilibrated (e.g., Clayton and Mayeda, 1996; McCoy et al., 1996; 1997a,b; Mittlefehldt et al., 1996; Weigel et al., 1999; Greenwood et al., 2012). Nonetheless, thermal metamorphism on the acapulcoite-lodranite parent body led to limited (2-7%) silicate partial melting and more significant Fe-Ni-S melting and melt segregation.

Our study of acapulcoite and lodranite meteorites is consistent with previous studies that characterize the partial melting history of these samples in the Fe-Ni-S system (with limited silicate melting), incomplete large-scale mixing on the acapulcoite-lodranite parent body, and genetic links that suggest a similar origin for these meteorites The new HSE and Os-isotope data in this study reveals important links between the acapulcoites and lodranites with other primitive achondrites, such as ureilites and brachinites (Rankenburg et al., 2007, 2008; Day et al., 2012), but also reveals the unique metal-sulfide partitioning and metal segregation behavior of these samples as they transition from low degrees of melting in acapulcoites to transitional acapulcoite-lodranites with elevated HSE to the troilite depleted lodranites. Samples of transitional acapulcoite-lodranites with high Pt/Os and low Pd/Os ratios may derive from multi-stage S-depleted metal melting, or from deeper within the parent body that the acapulcoites and lodranites, at the base of metal ponding and in proximity to the nascent core. Our results support models of Fe-Ni-S melt-solid partitioning observed for iron meteorites (e.g., Chabot & Jones, 2003) and may have implications for understanding early core segregation on the fully differentiated terrestrial planets.

Acknowledgements

We thank the Meteorite Working Group and Royal Ontario Museum for provision of acapulcoite and lodranite samples. US Antarctic meteorite samples are recovered by the Antarctic Search for Meteorites (ANSMET) program which has been funded by NSF and NASA, and characterized and curated by the Department of Mineral Sciences of the Smithsonian Institution and Astromaterials Curation Office at NASA Johnson Space Center. Support for this work came from NASA Cosmochemistry and Emerging Worlds (NNX12AH75G & NNX15AL74G to JMDD and NNX11AG586 to LAT).

Chapter 2, in full, is a reprint of material in preparation for submission to *Geochimca et Cosmochima Acta*, 2016, Dhaliwal, Jasmeet K; Day, James M.D.; Corder, Chistopher, A.; Tait, Kim; Marti, Kurt; Assayag, Nelly; Cartigny, Pierre; Rumble, Doug III; Taylor, Lawrence. The dissertation author was the primary investigator and author of these this paper. Figures 2.2 – 2.4 and 2.S1-2.S3 are copyrighted material from Corder (2015) and used with permission. The text in sections 2.2.3, 2.2.4, 2.2.6, 2.3.1, 2.3.2 and 2.3.5 is primarily sourced from Corder (2015) and used with permission in this thesis as a reprint of the submitted manuscript.

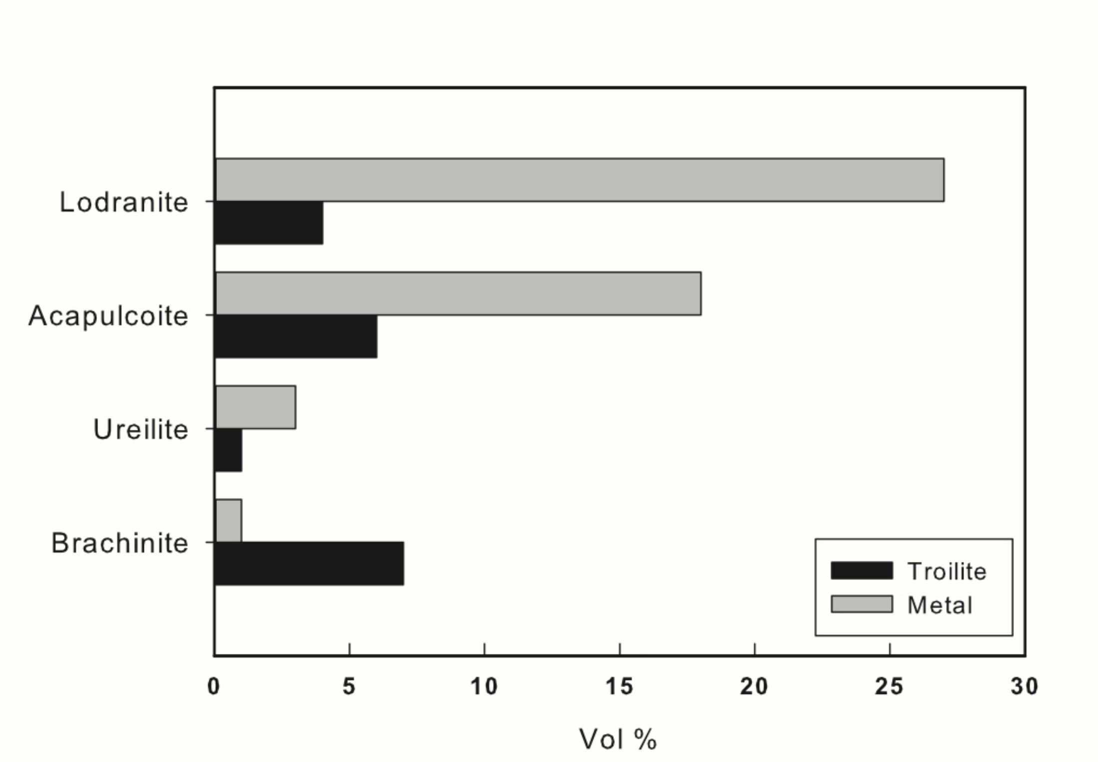

Figure 2.1: Metal and and troilite abundances in acapulcoites, lodanites, ureilites and brachinites. Data from Goodrich et al, 1987; Nehru et al., 1992; Mittlefehldt, 1996; McCoy et al. (1996, 1997) and Rubin, 2007.

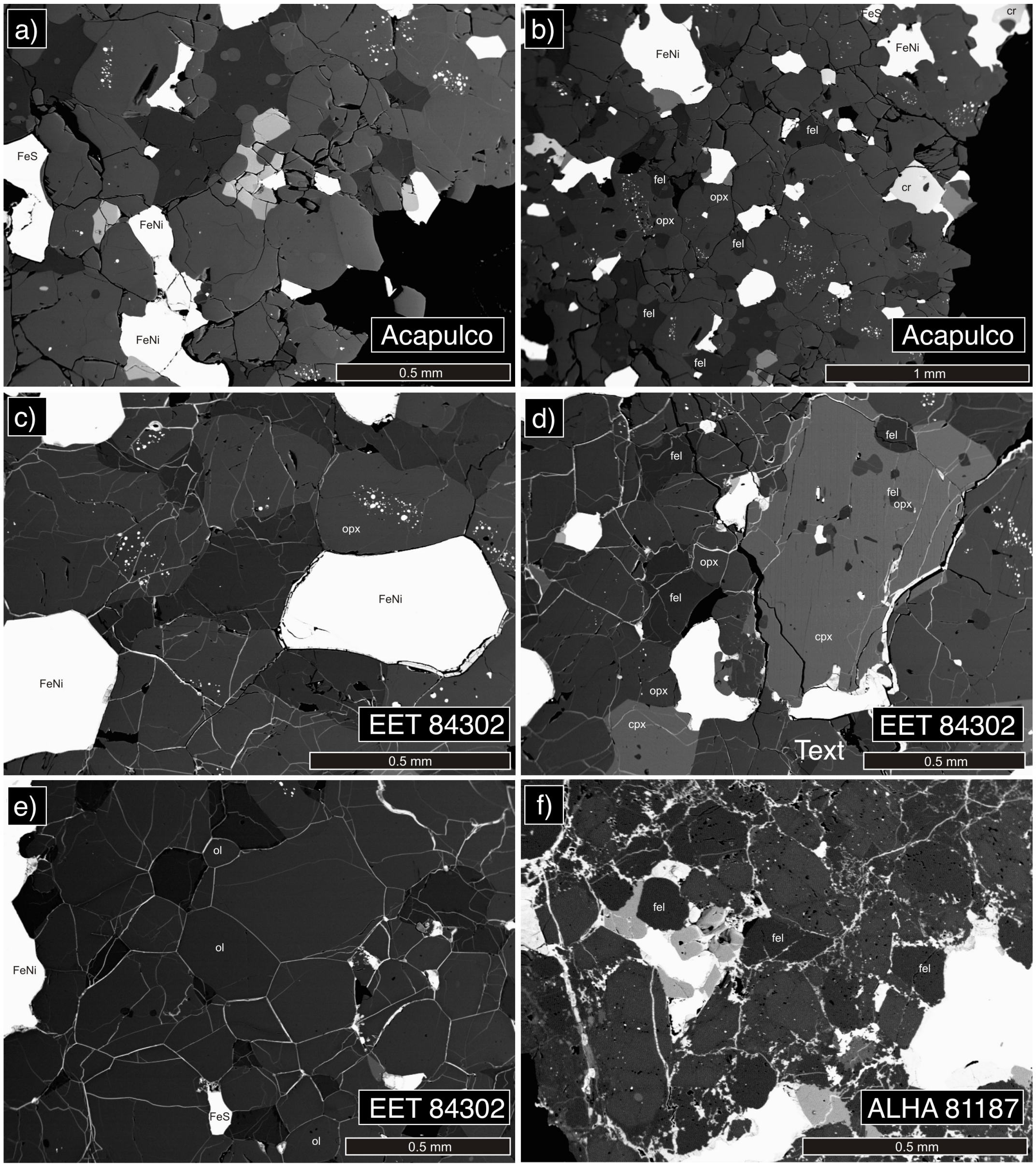

Figure 2.2: Back-scattered electron images of areas of (a), (b) Acapulco; (c)-(e) EET 84302, 28; (f) ALHA 81187, after Corder (2015). In (a) and (b), the granoblastic, poikilitic texture of Acapulco is visible, exhibiting abundant 120° triple junctions. Also visible are well-defined swarms of metallic blebs, as well as coarse metal grains. Panels (c)-(e) shows the granoblastic texture in EET 84302, 28. Like Acapulco, EET 84302, 28 also contains swarms of metallic blebs. Panel (f) shows the granoblastic texture and more weathered nature of ALHA 81187, 7. The mottled appearance of intergranular material, as well as the silicates in (f) are due to weathering. Abbreviations: FeNi = iron-nickel metal, FeS = iron-sulfide (troilite), fel = feldspar, cr = chromite, opx = orthopyroxene, cpx = clinopyroxene, ol = olivine.

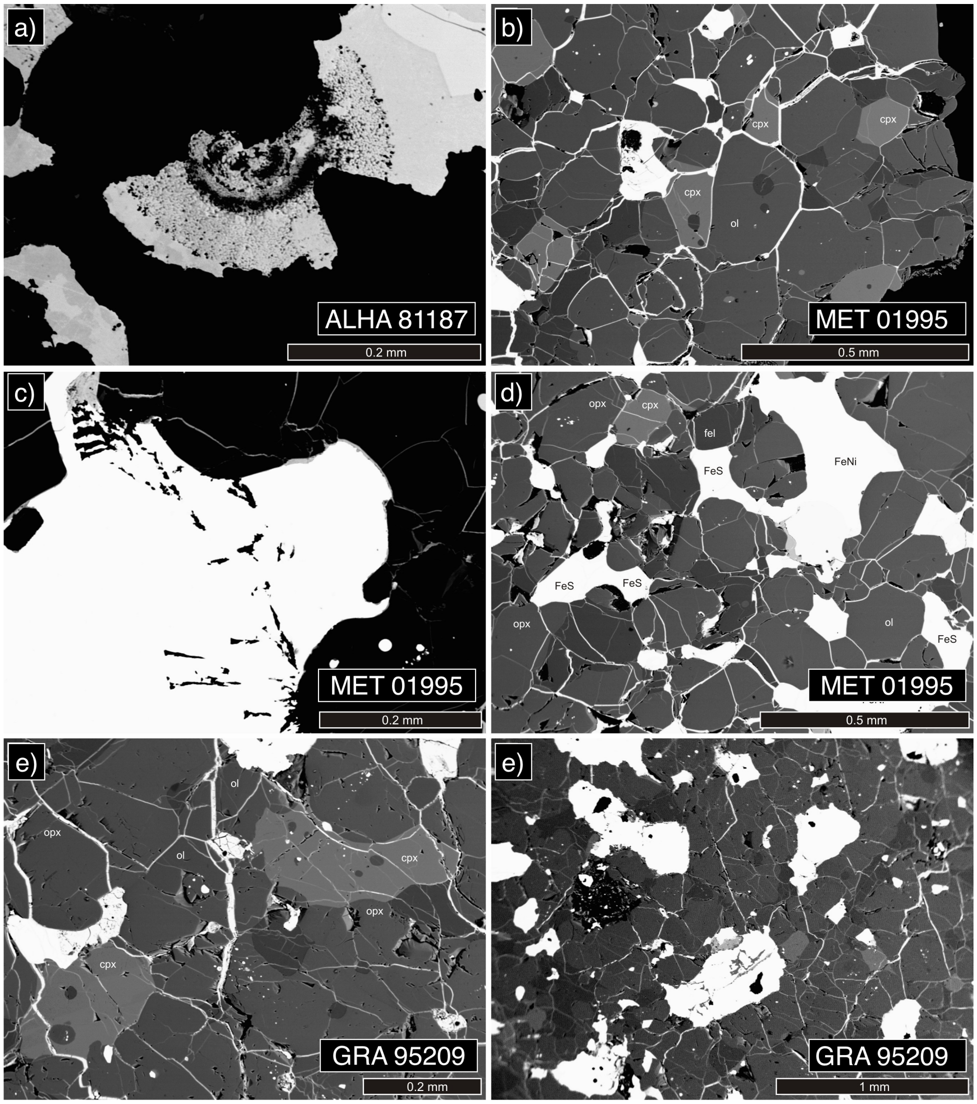

Figure 2.3: Second set of back-scattered electron images of portions of (a) ALHA 81187, 7; (b)-(d) MET 01195, 33; (e), (f) GRA 95209, 218, after Corder (2015). Frame (a) displays a remnant of a layered globular structures in ALHA 81187. The structure is largely composed of FeNi metal, as well as tiny structures that appear iridescent in reflected light and may be phosphates. The granoblastic, sometimes poikilitic, metal-rich texture of MET 01195, 33 is presented in (b) and (d). Frame (b) also shows veins of weathered material that completely surround silicate grains. In (c), a MET 01195, 33 FeNi metal grain contains carbon (small elongate black areas within the large white FeNi grain). Images (e) and (f), display textures in GRA 95209, 218. Abbreviations: FeNi = iron-nickel metal, FeS = iron-sulfide metal, fel = feldspar, opx = orthopyroxene, cpx = clinopyroxene, ol = olivine.

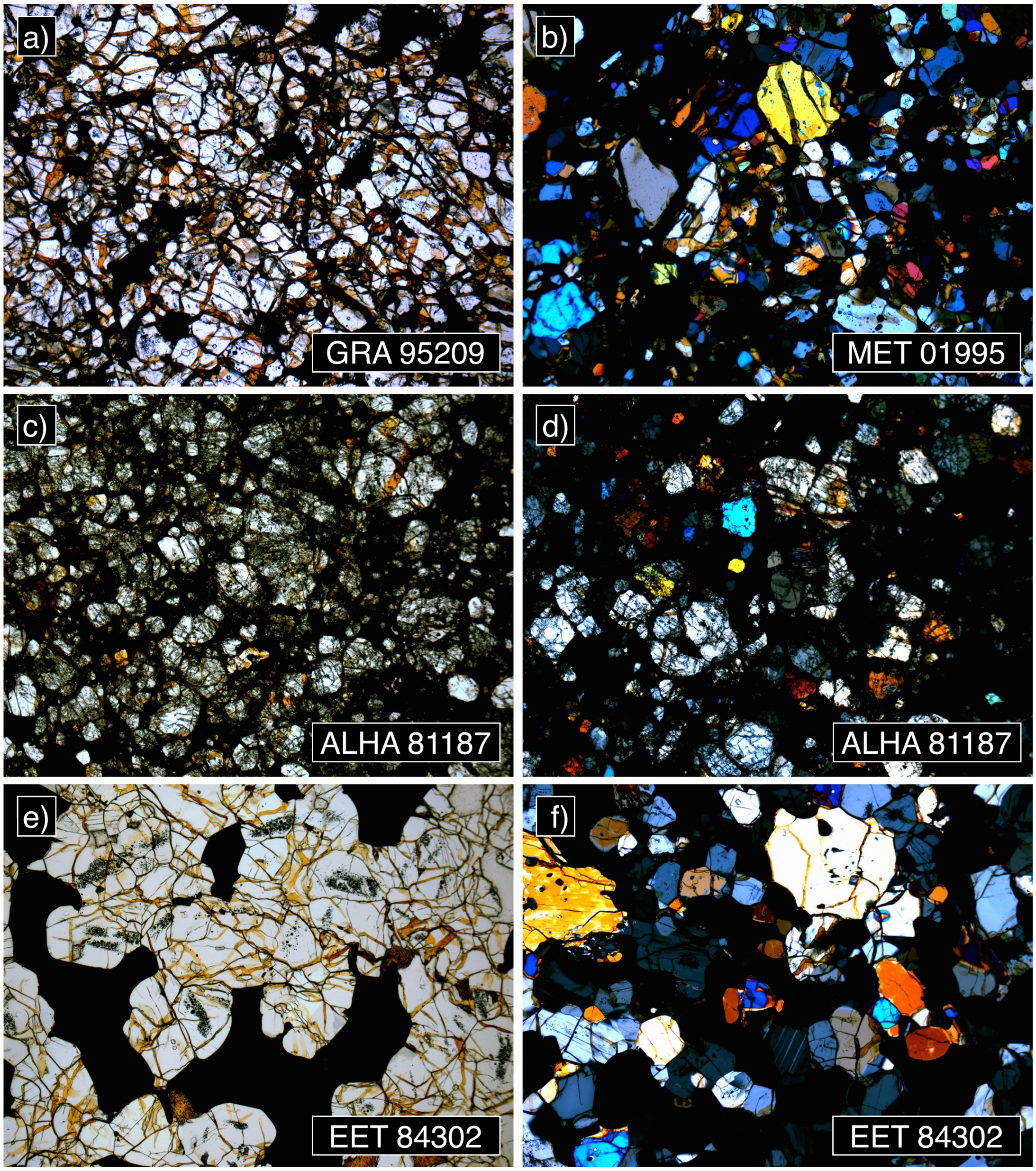

Figure 2.4: Photomicrographs in plane-polarized (a, c, and e) and cross-polarized (b, d, and f) light of a) GRA 95209, b) MET 01195, c) and d) ALHA 81187, and e) and f) EET 84302, after Corder (2015). Each photomicrograph was taken at 5× magnification and has a field of view 1.95 mm × 2.60 mm.

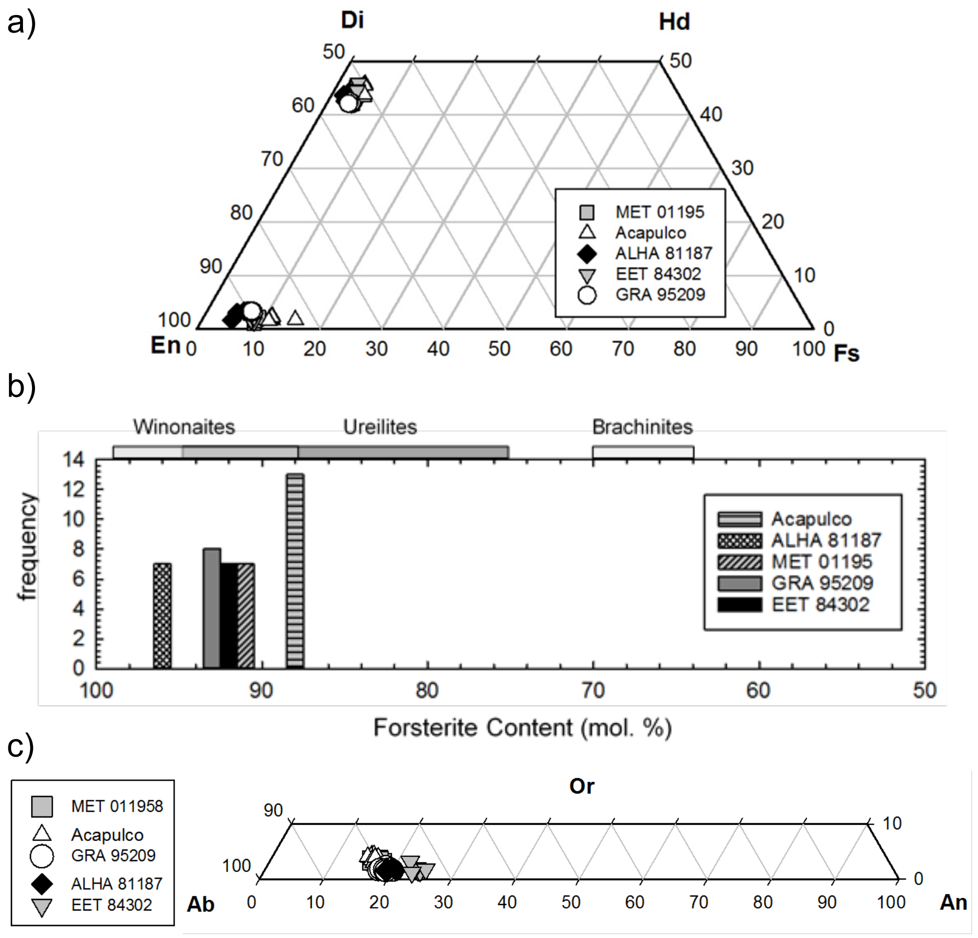

Figure 2.5: Mineral chemistry compositions for (a) Pyroxene quadrilateral showing low-Ca and high-Ca pyroxene compositions, (b) forsterite contents for olivine and (c) plagioclase compositions for Acapulco, ALHA 81187, MET 01195, EET 84302 and GRA 95209, after Corder (2015). Limited variation is evident for pyroxene and plagioclase compositions between the meteorites, and fosterite content of olivine grains plot in the range of other primitive achondrites, winonaites and ureilites (from Mittlefehldt, 2007 and Day et al., 2012). The end-members on these plots are (a) Di (diopside, MgCa end-member), En (enstatite, Mg-rich), Hd (hedenbergite, FeCa end-member), and Fs (ferrosilite, Fe-rich); (b) forsterite (Fo, Mg-rich end-member); (c) Or (orthoclase, K-rich), Ab (albite, Na-rich) and An (anorthite, Ca-rich).

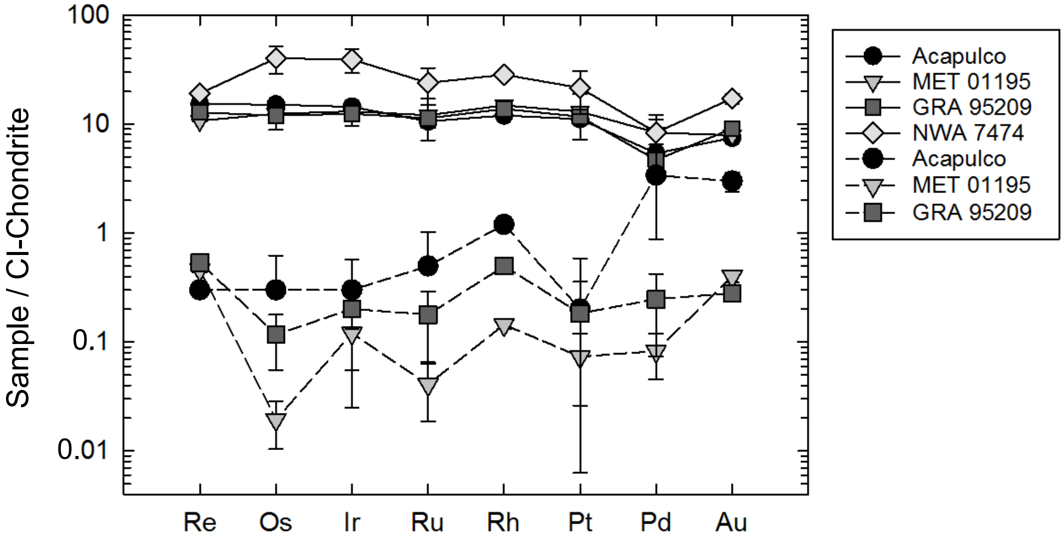

Figure 2.6: Average HSE abundances for FeNi metal grains (solid lines) and sulfide grains (dotted lines) normalized to CI chondrite in Acapulco, MET 01195, GRA 95209 and NWA 7474 obtained by LA-ICP-MS. CI chondrite normalization from Day et al. (2016).

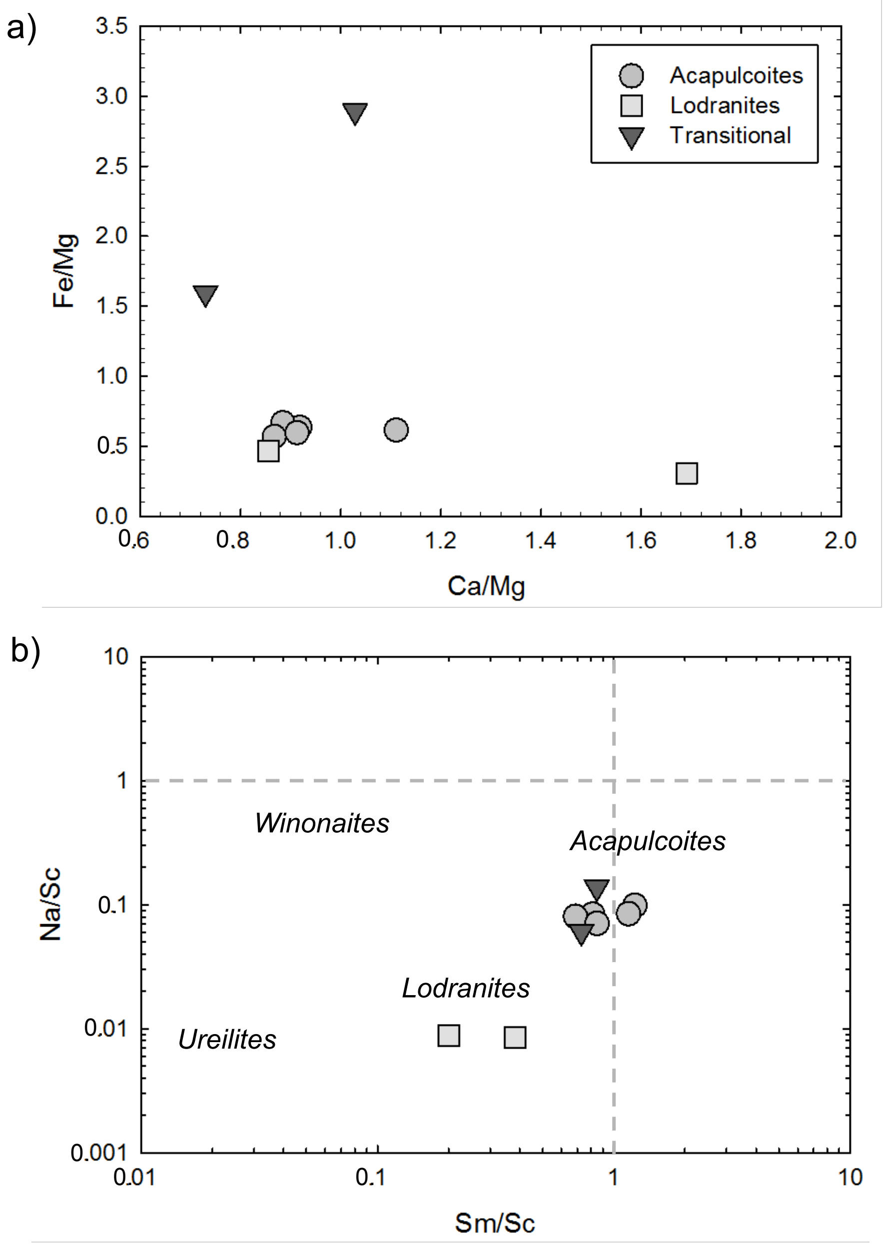

Figure 2.7: CI chondrite normalized (a) Fe/Mg versus Ca/Mg and (b) Na/Sc versus Sm/Sc diagram for acapulcoite and lodranite meteorites, compared with other meteorite groups, after Shearer et al. (2008). CI chondrite normalization data from McDonough & Sun (1995).

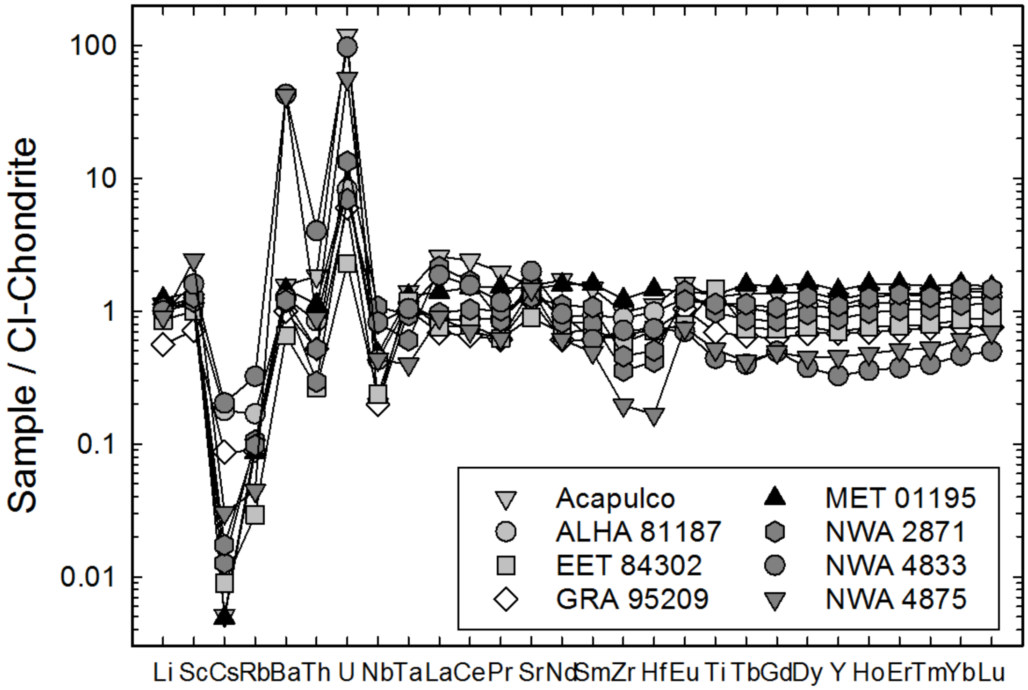

Figure 2.8: Trace multi-element plot for acapulcoite-lodranites normalized to CI chondrite Ivuna after Corder (2015). Samples plotted with circles are acapulcoites, samples plotted with diamonds are lodranites, and EET 84302 – a transitional acapulcoite-lodranite – is plotted with stars. CI chondrite normalization from McDonough & Sun (1995).

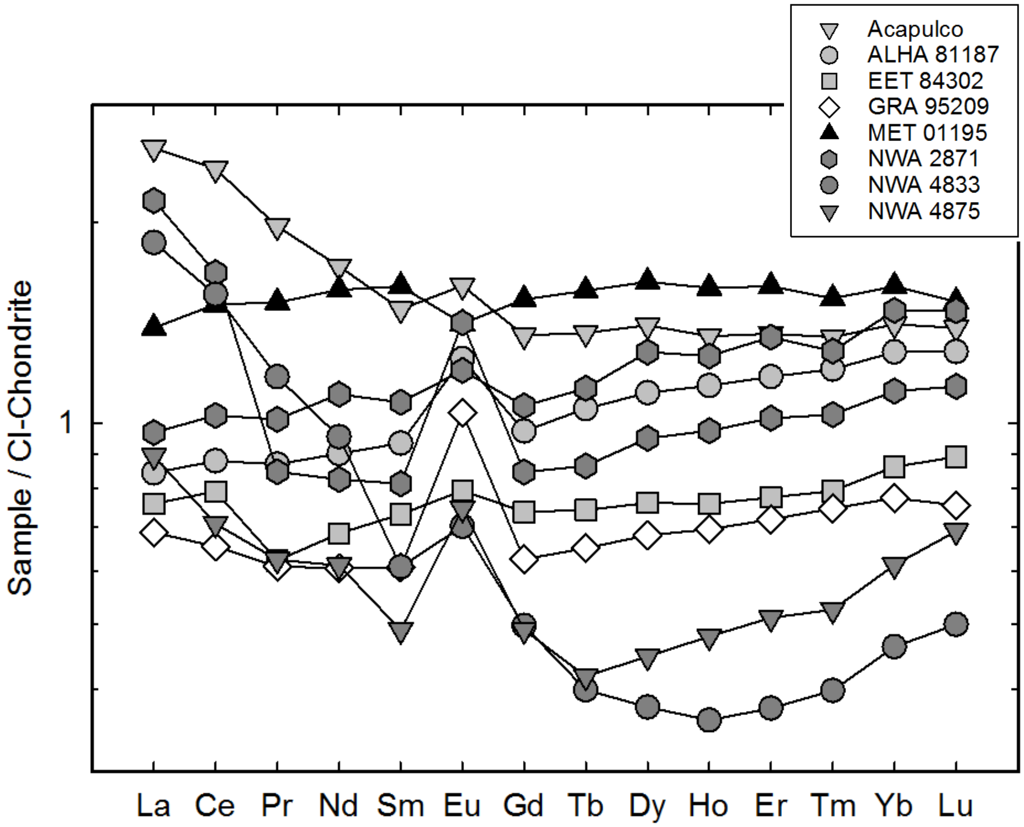

Figure 2.9: CI chondrite normalized rare earth element (REE) abundances for acapulcoite-lodranite meteorites analyzed in this study (Corder, 2015). CI chondrite normalization from McDonough & Sun (1995).

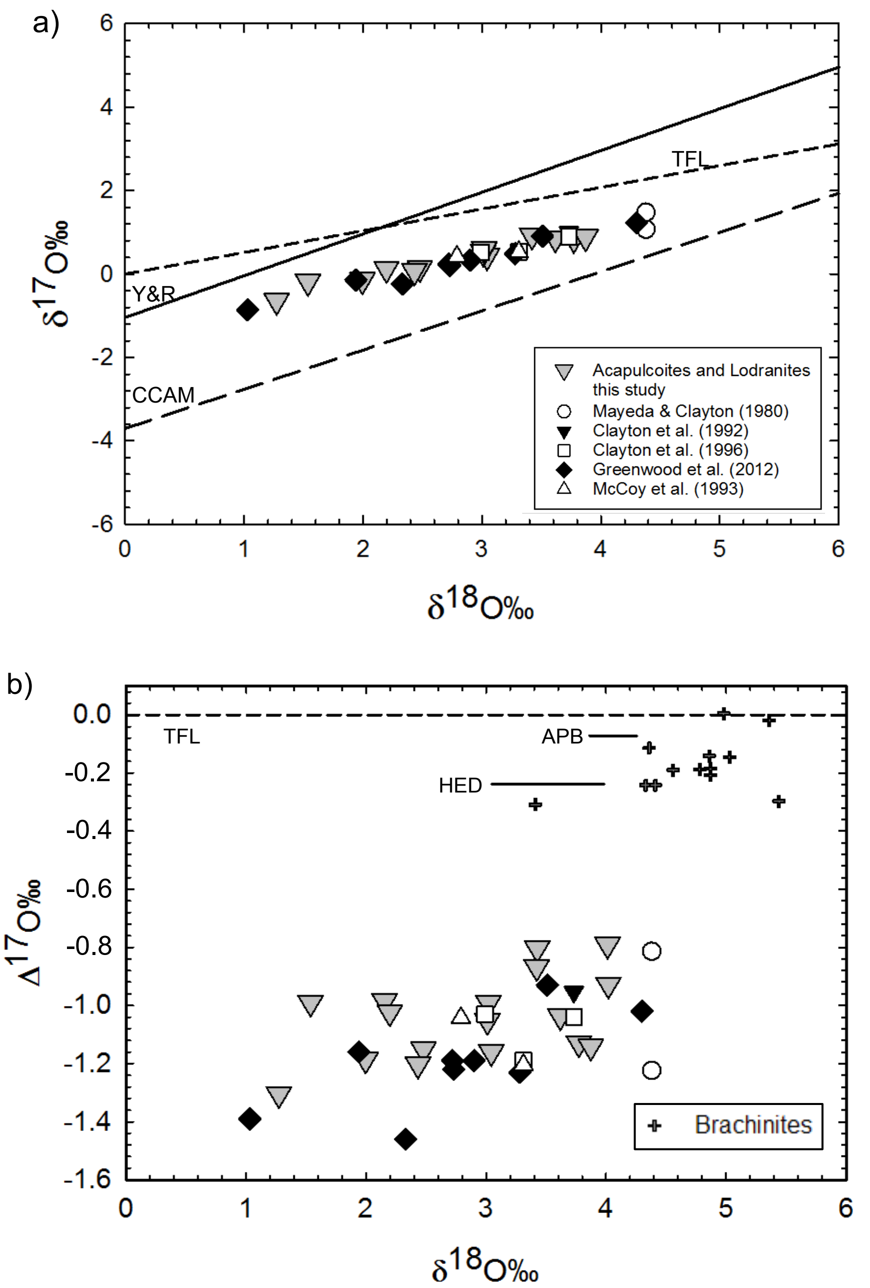

Figure 2.10: Oxygen isotope plot for acapulcoites and lodranites. (a) δ^{17}O versus δ^{18}O for acapulcoite-lodranite meteorites, which plot between the 'Y&R' (Young & Russell, 1998) and 'CCAM' (Carbonaceous Chondrite Anhydrous Mineral) lines and (b) Δ^{17}O versus δ^{18}O for acapulcoite-lodranite meteorites (same legend as **9a**) and brachinites (crosses; data from Day et al., 2012) with the angrite parent body (APB), howardite-eucrite-diogenite (HED) and terrestrial fractionation lines (TFL; Greenwood et al., 2012).

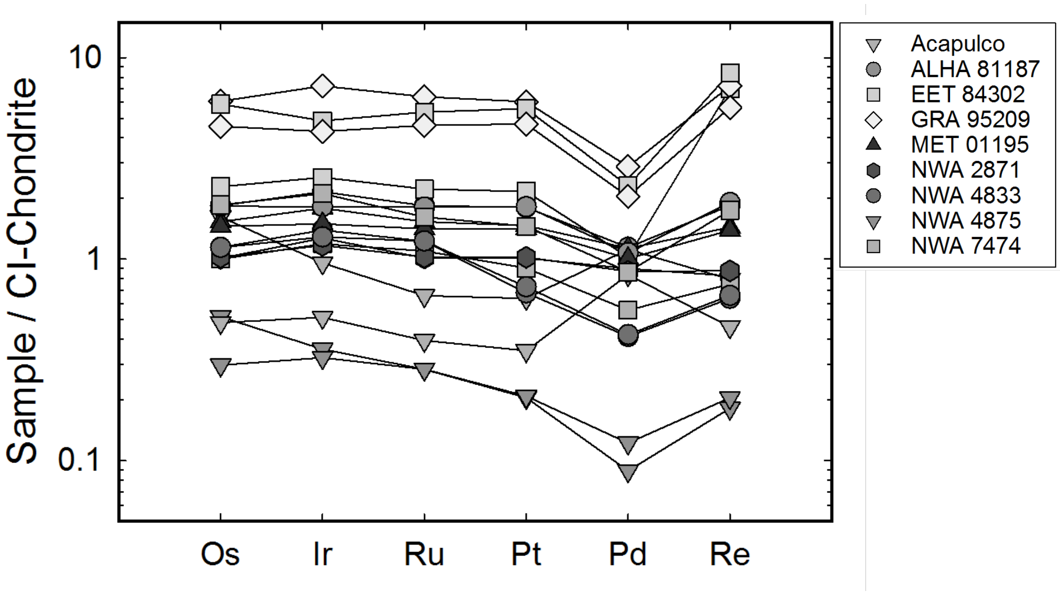

Figure 2.11: HSE abundances for acapulcoite and lodranite meteorites normalized to CI chondrite; normalization data from Horan et al. (2003).

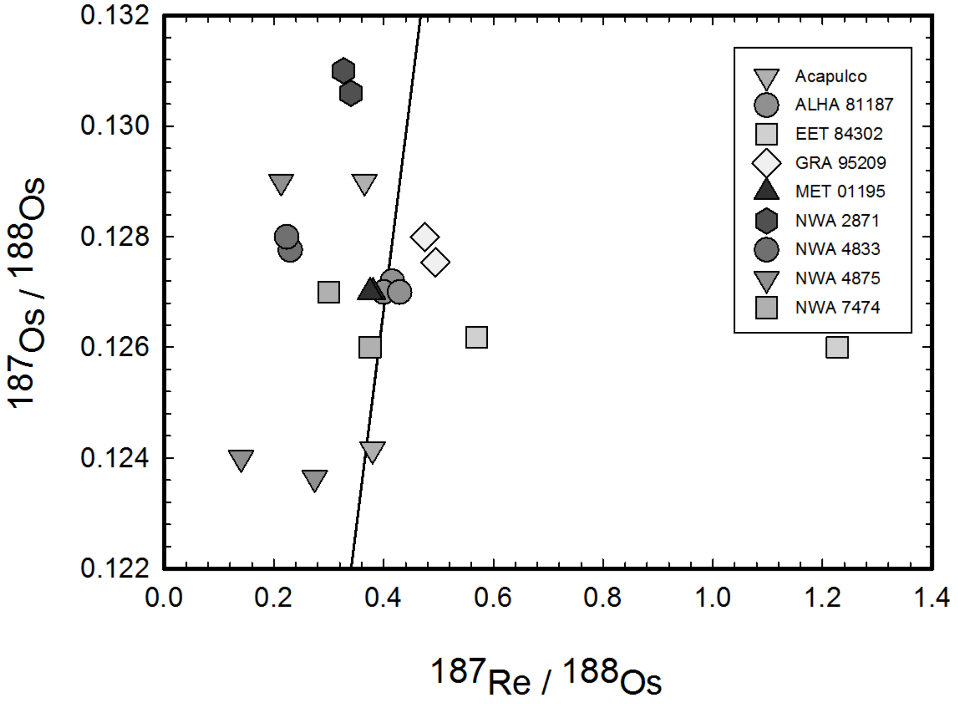

Figure 2.12: The ^{187}Re/^{188}Os and ^{187}Os/^{188}Os ratios of acapulcoite and lodranite samples plotted with the 4.56 Ga iron meteorite reference isochron (Smoliar et al., 1996).

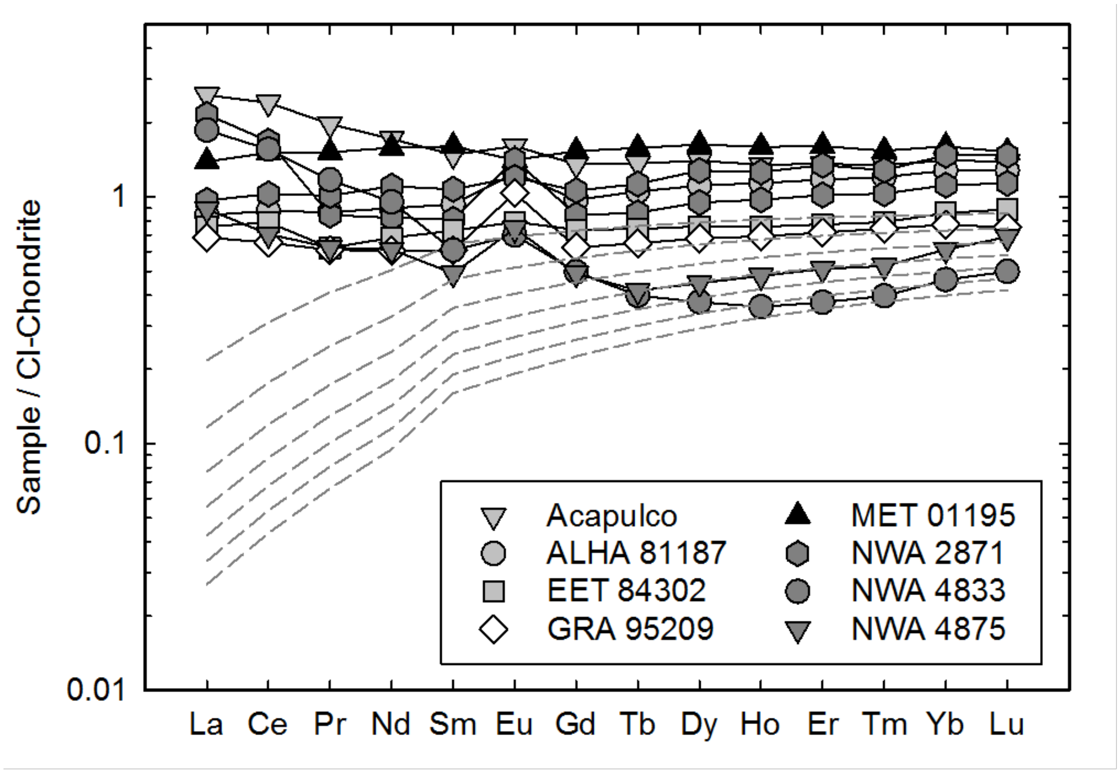

Figure 2.13: REE in acapulcoites with modeled compositions of residual liquids for 1 to 7 % partial melting, assuming an initial CI-chondrite composition (McDonough and Sun, 1995), partition coefficients from Sun and Liang (2014) and Suhr et al. (1998) and modal mineralogy from Day et al. (2017).

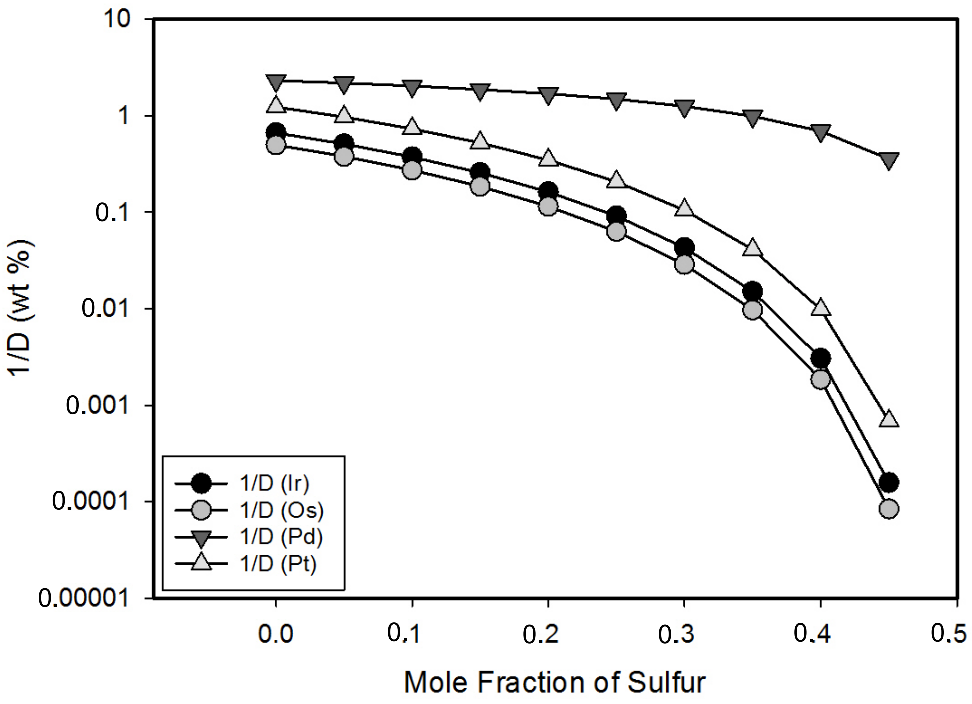

Figure 2.14: Adaptation of model by Chabot and Jones (2003) that shows the effect of the mole fraction of sulfur in the melt and the inverse of the solid metal-liquid metal partition coefficient (1/D) for Ir, Os, Pd, Pt.

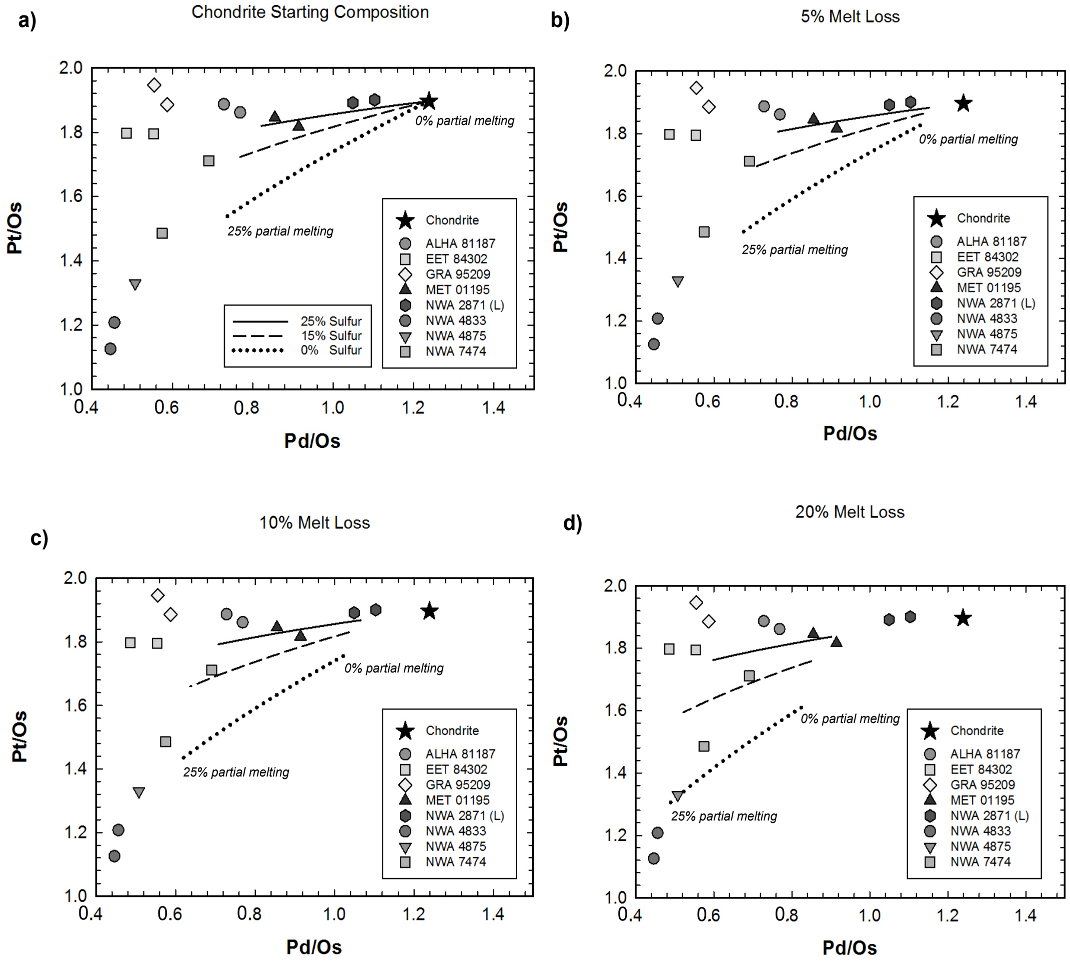

Figure 2.15: The Pd/Os and Pt/Os ratios of the sample set (with the exception of Acapulco and one split of NWA 4875) with models of melt loss using the parameterization of Chabot and Jones (2003) for the solid metal residue for 0 to 25 % melting with variable sulfur content: 0% S (dotted); 15% S (dashed); 25% S (solid).

Supplementary Material

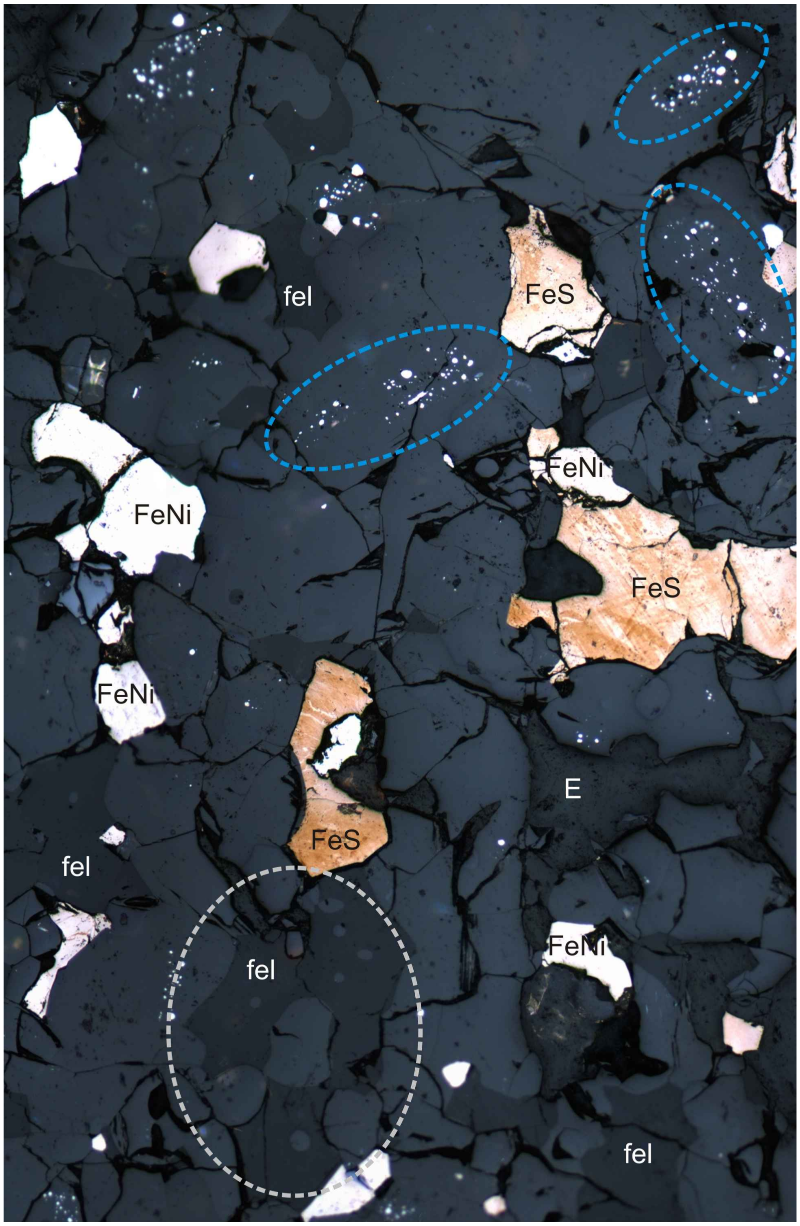

Figure 2.S1: Reflected light photomicrograph of the Acapulco meteorite after Corder (2015). Field of view is 1.93 mm × 1.27 mm. Blue dashed ovals surround well-defined swarms of FeNi metal blebs and the grey dashed oval highlights feldspars poikilitically enclosing olivines and/or pyroxenes. Abbreviations: FeNi – iron-nickel metal, FeS = iron-sulfide metal, fel = feldspar, E = epoxy resin.

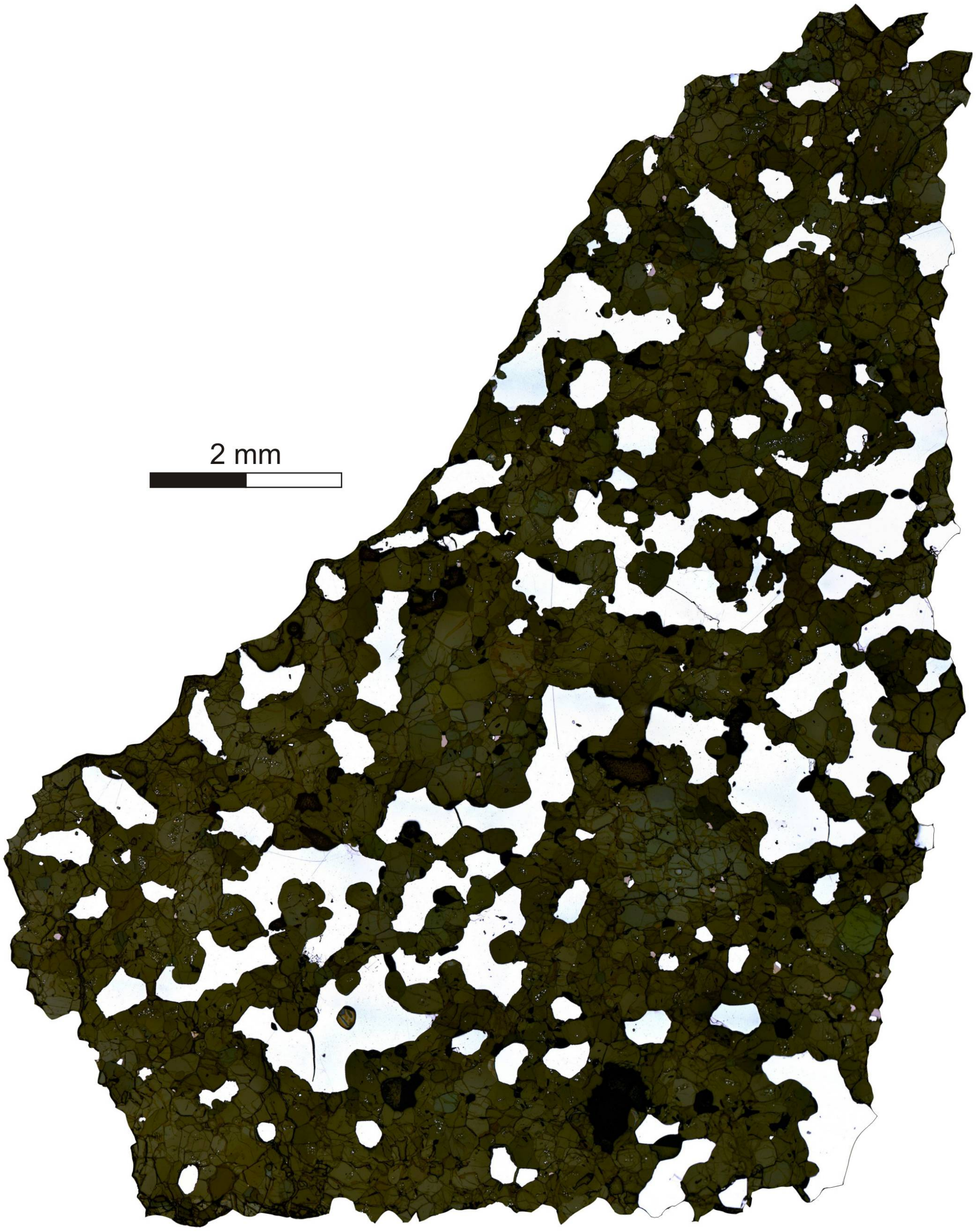

Figure 2.S2: Reflected light photomicrograph map of transitional meteorite EET 84302, 28 after Corder (2015). This meteorite serves as a particularly useful demonstration of the migration of metal in primitive meteorites – the FeNi metal in this sample appears to have "pooled" into large anhedral grains.

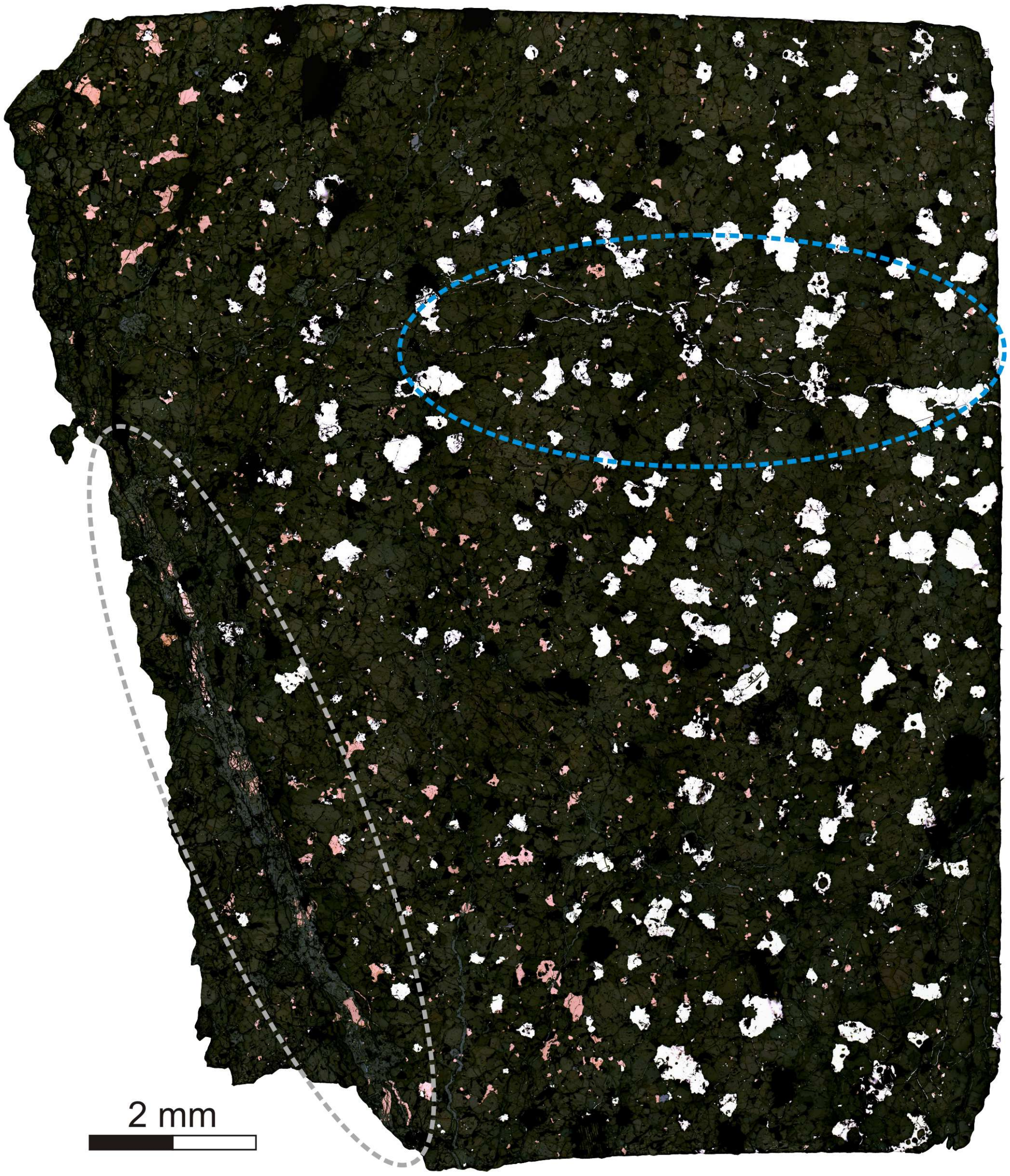

Figure 2.S3: Reflected light photomicrograph map of lodranite GRA 95209 (section 218) demonstrating behavior of metal migration in primitive meteorites, after Corder (2015). The gray dashed oval highlights the ~10 × 3 mm weathered vein with non-weathered sections of FeS demonstrating mass movement of metallic material on the meteorite's parent body. The weathered portions likely existed as primary metallic material before weathering. The blue dashed oval highlights a region with smaller unweathered veins of FeNi metal. Both type of vein suggest melt migration processes were active on the meteorite's parent body. Moreover, the decrease of still-primary FeNi grains near the large weathered vein (gray dashed oval) suggests that the FeNi in this region was migrating away via the large vein.

Table 2.1: Average mineral compositions of acapulcoites and lodranites

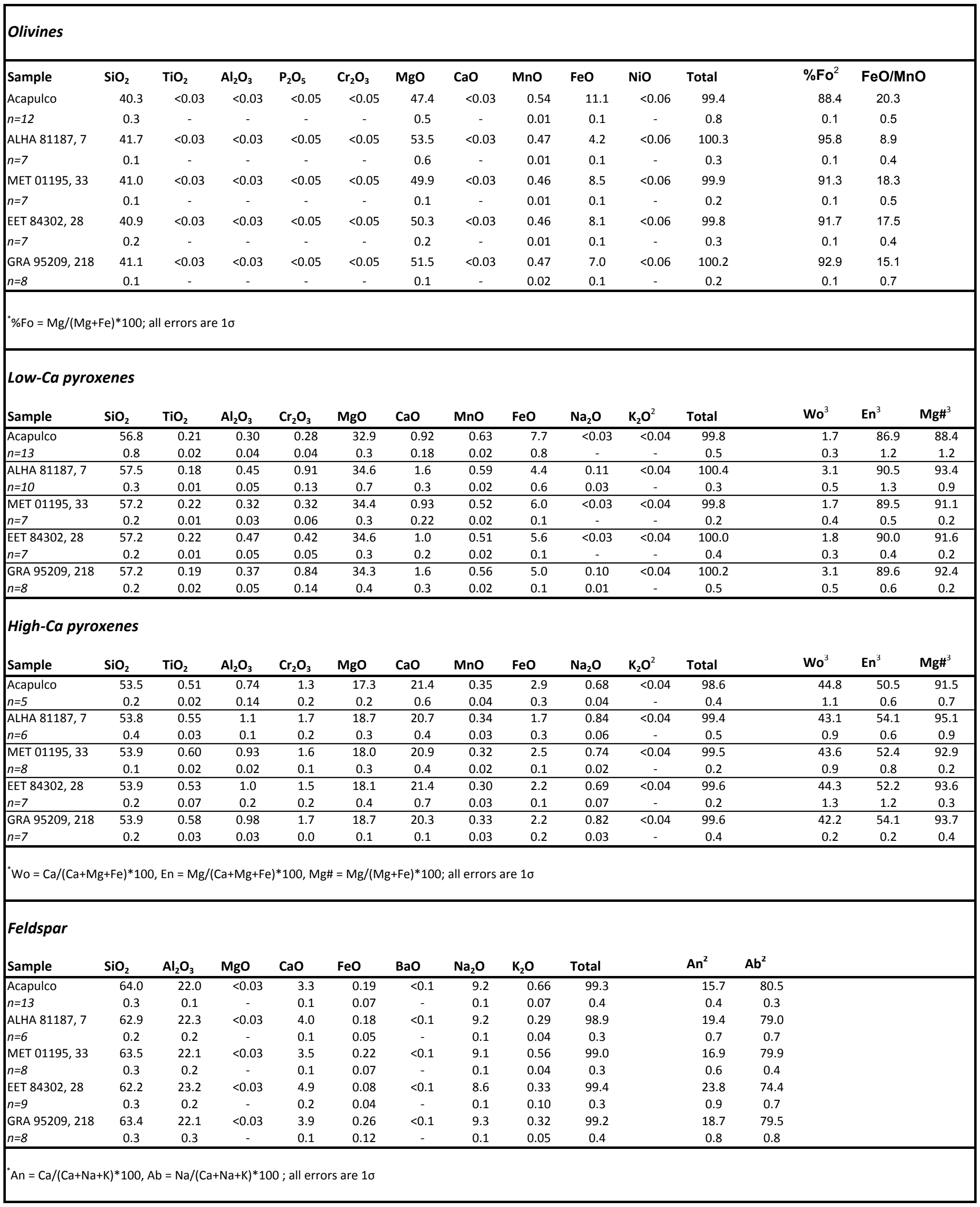

Olivines

Sample	SiO_2	TiO_2	Al_2O_3	P_2O_5	Cr_2O_3	MgO	CaO	MnO	FeO	NiO	Total	%Fo[2]	FeO/MnO
Acapulco	40.3	<0.03	<0.03	<0.05	<0.05	47.4	<0.03	0.54	11.1	<0.06	99.4	88.4	20.3
n=12	0.3	-	-	-	-	0.5	-	0.01	0.1	-	0.8	0.1	0.5
ALHA 81187, 7	41.7	<0.03	<0.03	<0.05	<0.05	53.5	<0.03	0.47	4.2	<0.06	100.3	95.8	8.9
n=7	0.1	-	-	-	-	0.6	-	0.01	0.1	-	0.3	0.1	0.4
MET 01195, 33	41.0	<0.03	<0.03	<0.05	<0.05	49.9	<0.03	0.46	8.5	<0.06	99.9	91.3	18.3
n=7	0.1	-	-	-	-	0.1	-	0.01	0.1	-	0.2	0.1	0.5
EET 84302, 28	40.9	<0.03	<0.03	<0.05	<0.05	50.3	<0.03	0.46	8.1	<0.06	99.8	91.7	17.5
n=7	0.2	-	-	-	-	0.2	-	0.01	0.1	-	0.3	0.1	0.4
GRA 95209, 218	41.1	<0.03	<0.03	<0.05	<0.05	51.5	<0.03	0.47	7.0	<0.06	100.2	92.9	15.1
n=8	0.1	-	-	-	-	0.1	-	0.02	0.1	-	0.2	0.1	0.7

[*] %Fo = Mg/(Mg+Fe)*100; all errors are 1σ

Low-Ca pyroxenes

Sample	SiO_2	TiO_2	Al_2O_3	Cr_2O_3	MgO	CaO	MnO	FeO	Na_2O	K_2O[2]	Total	Wo[3]	En[3]	Mg#[3]
Acapulco	56.8	0.21	0.30	0.28	32.9	0.92	0.63	7.7	<0.03	<0.04	99.8	1.7	86.9	88.4
n=13	0.8	0.02	0.04	0.04	0.3	0.18	0.02	0.8	-	-	0.5	0.3	1.2	1.2
ALHA 81187, 7	57.5	0.18	0.45	0.91	34.6	1.6	0.59	4.4	0.11	<0.04	100.4	3.1	90.5	93.4
n=10	0.3	0.01	0.05	0.13	0.7	0.3	0.02	0.6	0.03	-	0.3	0.5	1.3	0.9
MET 01195, 33	57.2	0.22	0.32	0.32	34.4	0.93	0.52	6.0	<0.03	<0.04	99.8	1.7	89.5	91.1
n=7	0.2	0.01	0.03	0.06	0.3	0.22	0.02	0.1	-	-	0.2	0.4	0.5	0.2
EET 84302, 28	57.2	0.22	0.47	0.42	34.6	1.0	0.51	5.6	<0.03	<0.04	100.0	1.8	90.0	91.6
n=7	0.2	0.01	0.05	0.05	0.3	0.2	0.02	0.1	-	-	0.4	0.3	0.4	0.2
GRA 95209, 218	57.2	0.19	0.37	0.84	34.3	1.6	0.56	5.0	0.10	<0.04	100.2	3.1	89.6	92.4
n=8	0.2	0.02	0.05	0.14	0.4	0.3	0.02	0.1	0.01	-	0.5	0.5	0.6	0.2

High-Ca pyroxenes

Sample	SiO_2	TiO_2	Al_2O_3	Cr_2O_3	MgO	CaO	MnO	FeO	Na_2O	K_2O[2]	Total	Wo[3]	En[3]	Mg#[3]
Acapulco	53.5	0.51	0.74	1.3	17.3	21.4	0.35	2.9	0.68	<0.04	98.6	44.8	50.5	91.5
n=5	0.2	0.02	0.14	0.2	0.2	0.6	0.04	0.3	0.04	-	0.4	1.1	0.6	0.7
ALHA 81187, 7	53.8	0.55	1.1	1.7	18.7	20.7	0.34	1.7	0.84	<0.04	99.4	43.1	54.1	95.1
n=6	0.4	0.03	0.1	0.2	0.3	0.4	0.03	0.3	0.06	-	0.5	0.9	0.6	0.9
MET 01195, 33	53.9	0.60	0.93	1.6	18.0	20.9	0.32	2.5	0.74	<0.04	99.5	43.6	52.4	92.9
n=8	0.1	0.02	0.02	0.1	0.3	0.4	0.02	0.1	0.02	-	0.2	0.9	0.8	0.2
EET 84302, 28	53.9	0.53	1.0	1.5	18.1	21.4	0.30	2.2	0.69	<0.04	99.6	44.3	52.2	93.6
n=7	0.2	0.07	0.2	0.2	0.4	0.7	0.03	0.1	0.07	-	0.2	1.3	1.2	0.3
GRA 95209, 218	53.9	0.58	0.98	1.7	18.7	20.3	0.33	2.2	0.82	<0.04	99.6	42.2	54.1	93.7
n=7	0.2	0.03	0.03	0.0	0.1	0.1	0.03	0.2	0.03	-	0.4	0.2	0.2	0.4

[*] Wo = Ca/(Ca+Mg+Fe)*100, En = Mg/(Ca+Mg+Fe)*100, Mg# = Mg/(Mg+Fe)*100; all errors are 1σ

Feldspar

Sample	SiO_2	Al_2O_3	MgO	CaO	FeO	BaO	Na_2O	K_2O	Total	An[2]	Ab[2]
Acapulco	64.0	22.0	<0.03	3.3	0.19	<0.1	9.2	0.66	99.3	15.7	80.5
n=13	0.3	0.1	-	0.1	0.07	-	0.1	0.07	0.4	0.4	0.3
ALHA 81187, 7	62.9	22.3	<0.03	4.0	0.18	<0.1	9.2	0.29	98.9	19.4	79.0
n=6	0.2	0.2	-	0.1	0.05	-	0.1	0.04	0.3	0.7	0.7
MET 01195, 33	63.5	22.1	<0.03	3.5	0.22	<0.1	9.1	0.56	99.0	16.9	79.9
n=8	0.3	0.2	-	0.1	0.07	-	0.1	0.04	0.3	0.6	0.4
EET 84302, 28	62.2	23.2	<0.03	4.9	0.08	<0.1	8.6	0.33	99.4	23.8	74.4
n=9	0.3	0.2	-	0.2	0.04	-	0.1	0.10	0.3	0.9	0.7
GRA 95209, 218	63.4	22.1	<0.03	3.9	0.26	<0.1	9.3	0.32	99.2	18.7	79.5
n=8	0.3	0.3	-	0.1	0.12	-	0.1	0.05	0.4	0.8	0.8

[*] An = Ca/(Ca+Na+K)*100, Ab = Na/(Ca+Na+K)*100 ; all errors are 1σ

Table 2.1: Average mineral compositions of acapulcoites and lodranites (continued)

Chromite

Sample	**SiO_2**	**TiO_2**	**Al_2O_3**	**V_2O_3**	**Cr_2O_3**	**MgO**	**CaO**	**MnO**	**FeO**	**NiO[2]**	**Total**	**Cr#[3]**	**Mg#[3]**
Acapulco	0.07	1.2	5.8	0.57	62.7	6.5	<0.03	1.3	21.2	<0.06	99.5	87.8	35.4
n=16	0.02	0.0	0.3	0.03	0.5	0.6	-	0.2	0.6	-	0.6	0.5	2.7
ALHA 81187, 7	0.07	0.64	6.4	0.54	64.8	9.6	<0.03	2.9	15.1	<0.06	100.0	87.2	52.9
n=5	0.01	0.26	1.0	0.08	0.7	1.1	-	0.8	1.0	-	0.3	1.8	4.5
MET 01195, 33	0.07	1.1	6.8	0.53	63.5	8.6	<0.03	1.3	18.0	<0.06	99.8	86.3	45.9
n=9	0.01	0.0	0.1	0.02	0.4	0.3	-	0.3	0.5	-	0.3	0.2	1.6
GRA 95209, 218	0.06	1.0	3.8	0.53	62.8	1.7	<0.03	1.4	26.5	<0.06	97.8	91.7	10.1
n=13	0.01	0.1	0.6	0.07	0.6	0.8	-	0.3	1.0	-	0.3	1.3	4.4

[*] Cr# = Cr/(Cr+Al)*100, Mg# = Mg/(Mg+Fe)*100 ; all errors are 1σ

FeNi Metal

Sample	**Modal**	**Fe**	**Ni**	**S**	**Co**	**P**	**Si**	**Mn[2]**	**Mg**	**Al**	**Ti**	**Total**	**Ni/Co**
Acapulco	11%	90.7	7.6	-	0.58	-	-	-	-	-	-	99.0	**13.8**
n=16, kam.		1.3	1.3	-	0.14	-	-	-	-	-	-	0.5	
		80.5	17.9	-	0.33	-	-	-	-	-	-	98.8	**57.7**
n=8, taen.		6.2	6.1	-	0.05	-	-	-	-	-	-	0.4	
ALHA 81187, 7	6%	93.0	5.8	<0.04	0.48	<0.03	<0.03	<0.04	<0.03	<0.03	<0.03	99.3	12.0
n=18, kam.		0.5	0.2	-	0.02	-	-	-	-	-	-	0.4	
MET 01195, 33	*7%*	91.2	6.9	-	0.46	-	-	-	-	-	-	98.6	15.0
n=9, kam.		0.6	0.2	-	0.04	-	-	-	-	-	-	0.5	
		79.4	19.3	-	0.25	-	-	-	-	-	-	99.1	82.3
n=4, taen.		3.8	3.9	-	0.05	-	-	-	-	-	-	0.1	
EET 84302, 28	20%	92.7	5.7	<0.04	0.46	0.1	<0.03	<0.04	<0.03	<0.03	<0.03	99.0	12.3
n=9		0.4	0.4	-	0.03	0.0	-	-	-	-	-	0.5	
GRA 95209, 218	4%	92.0	6.1	<0.04	0.43	<0.03	<0.03	<0.04	<0.03	<0.03	<0.03	98.6	14.3
n=9		0.6	0.1	-	0.02	-	-	-	-	-	-	0.5	

[*] kam. = kamacite ; taen. = taenite ; all errors are 1σ

FeS Metal

Sample	**Modal**	**S**	**Fe**	**Co**	**Ni**	**P**	**Si**	**Mn[2]**	**Mg**	**Al**	**Ti**	**Cr[2]**	**Total**
Acapulco	1.9%	36.7	62.4	<0.05	<0.05	<0.03	<0.03	<0.04	<0.03	<0.03	<0.03	n.a.	99.2
n=12		0.4	0.3	-	-	-	-	-	-	-	-	-	0.5
ALHA 81187, 7	1.9%	37.2	62.7	<0.05	<0.05	<0.03	<0.03	<0.04	<0.03	<0.03	<0.03	n.a.	99.9
n=6		0.4	0.3	-	-	-	-	-	-	-	-	-	0.3
MET 01195, 33	4.0%	36.6	62.5	<0.05	<0.05	<0.03	<0.03	<0.04	<0.03	<0.03	<0.03	n.a.	99.1
n=12		0.2	0.1	-	-	-	-	-	-	-	-	-	0.3
EET 84302, 28	1.0%	36.5	62.3	<0.05	<0.05	<0.03	<0.03	<0.04	<0.03	<0.03	<0.03	n.a.	98.9
n=6		0.1	0.1	-	-	-	-	-	-	-	-	-	0.1
GRA 95209, 218	2.4%	36.7	62.7	<0.05	<0.05	<0.03	<0.03	<0.04	<0.03	<0.03	<0.03	n.a.	99.4
n=11		0.8	0.3	-	-	-	-	-	-	-	-	-	0.9

* n.a. = not analyzed ; all errors are 1σ

Schribersite

Sample	**Fe**	**Ni**	**P**	**S**	**Co**	**Si**	**Mn[2]**	**Mg**	**Al**	**Ti**	**Total**
ALHA 81187, 7	43.1	41.6	15.2	<0.04	0.08	<0.03	<0.04	<0.03	<0.03	<0.03	100.0
n=7	6.0	5.9	0.1	-	0.02	-	-	-	-	-	0.4
MET 01195, 33	35.5	49.5	15.2	<0.04	<0.05	<0.03	<0.04	<0.03	<0.03	<0.03	100.4
n=5	1.0	0.9	0.1	-	-	-	-	-	-	-	0.2
EET 84302, 28	53.7	31.1	15.4	<0.04	0.12	<0.03	<0.04	<0.03	<0.03	<0.03	100.4
n=6	3.9	3.8	0.0	-	0.01	-	-	-	-	-	0.1

Table 2.2: Highly siderophile element abundances in FeNi and FeS grains (μ g g-1)

Sample		Re	Os	Ir	Ru	Rh	Pt	Pd	Au
Acapulco									
	Metal Avg.	0.584	6.950	6.202	6.743	1.567	9.671	3.106	1.312
	(n =7)	0.05	0.90	0.54	1.35	0.29	0.87	1.11	0.30
	Sulfide Avg.	0.011	0.132	0.125	0.332	0.159	0.211	1.953	0.530
	(n = 8)	0.03	0.32	0.28	0.52	0.16	0.39	2.52	0.60
MET 01195									
	Metal Avg.	0.407	5.742	5.625	7.701	1.947	11.360	4.779	1.385
	(n =10)	0.15	3.66	3.43	4.97	1.06	5.83	3.77	0.58
	Sulfide Avg.	0.018	0.009	0.052	0.026	0.019	0.064	0.047	0.070
	(n = 5)	0.02	0.01	0.06	0.02	0.01	0.05	0.04	0.05
GRA 95209									
	Metal Avg.	0.488	5.504	5.344	7.214	1.806	10.207	2.675	1.593
	(n =8)	0.04	0.52	0.67	0.94	0.25	1.35	0.27	0.10
	Sulfide Avg.	0.020	0.054	0.086	0.113	0.065	0.159	0.141	0.049
	(n = 6)	0.01	0.06	0.07	0.11	0.08	0.18	0.17	0.04
NWA 7474									
	Metal Avg.	0.726	18.529	16.857	15.227	3.729	18.740	4.784	3.009
	(n =7)	0.34	11.30	9.83	8.90	2.18	9.10	2.67	1.94

Table 2.3: Whole-rock major-element abundances in achondrite meteorite samples (in wt. %)

Sample	Acapulco	ALHA 81187	MET 01195	NWA 2871 (L)	NWA 2871 (S)	EET 84302	GRA 95209	NWA 4833	NWA 4875
	Parr Bomb	Parr Bomb	Parr Bomb	Parr Bomb	Parr Bomb	Parr Bomb	Parr Bomb	Parr Bomb	Parr Bomb
Mass (mg)	39.46	39.75	38.29	39.59	14.81	38.64	38.69	39.66	39.22
Na	0.61	0.49	0.60	0.48	0.46	0.31	0.51	0.07	0.11
Mg	13.20	13.25	13.41	12.48	13.99	11.98	7.74	18.23	18.05
Fe	15.71	16.58	15.48	13.34	15.64	35.84	41.98	15.94	10.44
Al	1.10	0.95	1.08	0.99	0.79	0.81	0.80	0.17	0.16
P	0.20	0.11	0.10	0.08	0.22	0.18	0.30	0.05	0.05
Ca	1.16	1.12	1.43	1.04	1.22	0.84	0.76	1.49	2.93
Ti	0.09	0.08	0.10	0.07	0.11	0.10	0.06	0.05	0.05
Mn	0.29	0.24	0.23	0.23	0.26	0.23	0.19	0.27	0.27
Cr	0.46	0.35	0.48	0.22	0.54	1.49	0.15	0.38	0.39
Co	0.38	0.69	0.44	0.34	0.39	1.57	1.83	0.32	0.10
Ni	0.50	0.64	0.47	0.34	0.38	1.48	1.80	0.35	0.10

Table 2.4: Whole-rock trace-element abundances (in ppm) in acapulcoites and lodranites, total procedural blanks (TPB) and standards (BHVO-2, BCR-2, BIR-1)

	Acapulco	ALHA 81187	MET 01195	NWA 2871 (L)	NWA 2871 (S)	EET 84302	GRA 95209	NWA 4833	NWA 4875
Li	1.68	1.50	1.87	1.57	1.59	1.29	0.84	1.50	1.36
Sc	7.15	6.79	8.23	6.97	7.50	5.93	4.25	9.46	14.45
Ti	558.35	505.80	586.23	430.27	500.35	646.92	305.52	193.38	226.60
V	70.53	59.30	80.21	55.74	89.70	154.09	32.97	92.53	114.53
Cu	72.55	19.55	46.36	49.32	56.01	36.89	37.90	38.19	17.69
Zn	175.14	101.58	171.56	11.79	21.39	224.70	40.44	112.26	104.78
Ga	4.48	6.34	6.52	4.59	6.52	14.49	8.24	3.64	1.53
Ge	3.68	11.52	7.60	7.09	11.12	32.36	40.19	6.60	2.27
Rb	0.22	0.39	0.20	0.24	0.22	0.07	0.20	0.74	0.10
Sr	11.22	10.39	10.64	11.58	9.25	6.51	8.75	14.44	10.55
Y	1.93	1.64	2.25	1.37	1.72	1.10	1.07	0.51	0.71
Zr	3.72	3.39	4.69	1.36	1.75	2.21	2.54	2.73	0.75
Nb	0.05	0.10	0.11	0.20	0.26	0.06	0.05	0.20	0.10
Sn	0.56	0.50	0.48	0.44	0.54	0.65	1.71	0.48	0.31
Cs	0.00	0.03	0.00	0.00	0.00	0.00	0.02	0.04	0.01
Ba	3.75	3.01	3.52	2.83	2.89	1.57	2.39	103.54	101.10
La	0.61	0.20	0.33	0.51	0.23	0.18	0.16	0.44	0.21
Ce	1.48	0.54	0.92	1.03	0.63	0.48	0.40	0.96	0.43
Pr	0.18	0.08	0.14	0.08	0.09	0.06	0.06	0.11	0.06
Nd	0.79	0.41	0.72	0.38	0.51	0.31	0.28	0.44	0.28
Sm	0.22	0.14	0.24	0.12	0.16	0.11	0.09	0.09	0.07
Eu	0.09	0.07	0.08	0.08	0.07	0.04	0.06	0.04	0.04
Gd	0.27	0.19	0.31	0.17	0.21	0.15	0.12	0.10	0.10
Tb	0.05	0.04	0.06	0.03	0.04	0.03	0.02	0.01	0.02
Dy	0.35	0.27	0.40	0.23	0.31	0.19	0.17	0.09	0.11
Ho	0.07	0.06	0.09	0.05	0.07	0.04	0.04	0.02	0.03
Er	0.22	0.19	0.26	0.16	0.22	0.12	0.11	0.06	0.08
Tm	0.03	0.03	0.04	0.03	0.03	0.02	0.02	0.01	0.01
Yb	0.23	0.21	0.26	0.18	0.24	0.14	0.12	0.07	0.10
Lu	0.03	0.03	0.04	0.03	0.04	0.02	0.02	0.01	0.02
Hf	0.12	0.10	0.15	0.04	0.05	0.07	0.07	0.08	0.02
Ta	0.02	0.02	0.02	0.01	0.01	0.02	0.01	0.01	0.01
Th	0.05	0.02	0.03	0.01	0.02	0.01	0.02	0.12	0.03
U	0.89	0.06	0.07	0.05	0.10	0.02	0.04	0.72	0.42

Table 2.4: Whole-rock trace-element abundances (in ppm) in acapulcoites and lodranites, total procedural blanks (TPB) and standards (BHVO-2, BCR-2, BIR-1) (continued)

	TBP (n=4)		BHVO-2 (n=3)		BCR-2 (n=3)		BIR-1 (n=2)	
	Avg.	**RSD**	**Avg.**	**RSD**	**Avg.**	**RSD**	**Avg.**	**RSD**
Li	0.02	42%	4.69	3%	8.4	2%	3.3	5%
Sc	0.08	6%	31.77	4%	28.4	4%	43.1	6%
Ti	0.45	110%	16339.40	5%	11541.4	6%	5573.3	8%
V	0.35	130%	317.38	6%	355.4	7%	318.0	9%
Cu	0.31	62%	128.13	5%	17.6	7%	115.2	8%
Zn	1.37	13%	104.11	5%	112.0	5%	66.7	8%
Ga	0.00	60%	22.10	5%	19.5	5%	15.4	7%
Ge	0.01	17%	1.64	6%	1.5	8%	1.2	10%
Rb	0.01	69%	9.95	3%	43.2	3%	0.2	4%
Sr	0.02	69%	403.82	3%	296.4	3%	108.2	5%
Y	0.00	121%	25.83	3%	30.3	3%	15.2	5%
Zr	0.06	57%	170.31	3%	159.4	3%	14.6	5%
Nb	0.00	25%	18.03	2%	10.5	3%	0.5	5%
Sn	0.28	19%	1.84	6%	2.1	7%	0.8	4%
Cs	0.00	117%	0.10	3%	1.0	2%	0.0	4%
Ba	0.03	71%	139.21	2%	599.5	2%	6.8	4%
La	0.01	167%	15.13	2%	21.1	1%	0.6	0%
Ce	0.04	169%	37.20	2%	44.8	1%	1.9	1%
Pr	0.00	156%	5.33	3%	5.8	1%	0.4	3%
Nd	0.00	156%	24.35	3%	24.3	1%	2.3	4%
Sm	0.00	42%	6.04	3%	5.5	1%	1.1	4%
Eu	0.00	63%	2.06	3%	1.8	2%	0.5	5%
Gd	0.00	145%	6.21	2%	5.9	2%	1.6	4%
Tb	0.00	104%	0.92	3%	0.9	2%	0.3	4%
Dy	0.00	87%	5.29	3%	5.4	2%	2.5	4%
Ho	0.00	94%	0.97	3%	1.1	1%	0.6	4%
Er	0.00	112%	2.53	3%	3.1	1%	1.6	4%
Tm	0.00	107%	0.33	3%	0.4	2%	0.2	4%
Yb	0.00	120%	1.99	3%	2.8	2%	1.6	4%
Lu	0.00	103%	0.27	3%	0.4	1%	0.2	4%
Hf	0.00	85%	4.34	3%	4.1	1%	0.6	4%
Ta	0.00	48%	1.13	2%	0.7	2%	0.0	4%
Th	0.00	77%	1.24	5%	5.0	1%	0.0	1%
U	0.00	25%	4.06	3%	13.8	2%	0.1	5%

Table 2.5: Oxygen isotope data for acapulcoites and lodranites

Sample	**δ^{17}O**	1 stdev	**δ^{18}O**	1 stdev	**Δ^{17}O**	source
Acapulcoites						
Acapulco	1.310	0.025	4.012	0.023	-0.791	*this study*
	1.176	0.040	4.019	0.021	-0.928	*this study*
	0.990	0.058	3.425	0.016	-0.803	*this study*
Acapulco (pyx)	1.070		4.380			*Mayeda & Clayton (1980)*
Acapulco (plag)	1.480		4.380		-0.814	*Mayeda & Clayton (1980)*
Acapulco	1.000		3.730		-0.954	*Clayton et al. (1992)*
Acapulco	0.900		3.730		-1.040	*Clayton et al. (1996)*
Acapulco	0.91	0.09	3.51	0.16	−0.93	Greenwood et al. (2012)
ALHA 81187	0.143	0.027	2.154	0.021	-0.985	*this study*
	-0.185	0.036	1.537	0.025	-0.990	*this study*
ALHA 81187	0.520		2.990		-1.030	*Clayton et al. (1996)*
ALHA 81187	−0.14	0.06	1.94	0.16	−1.16	Greenwood et al. (2012)
ALHA 81187*	0.24	0.03	2.72	0.09	−1.19	Greenwood et al. (2012)
ALHA 81187	0.42		2.79		-1.042	McCoy et al. (1993
MET 01195	0.523	0.025	3.010	0.022	-1.053	*this study*
	0.590	0.024	3.019	0.020	-0.991	*this study*
NWA 2871 (l)	0.845	0.041	3.772	0.013	-1.130	*this study*
	0.886	0.031	3.872	0.008	-1.141	*this study*
NWA 2871 (s)	0.858	0.056	3.618	0.009	-1.037	*this study*
NWA 2871	1.23	0.05	4.3	0.06	−1.02	Greenwood et al. (2012)
NWA 2871*	0.49	0.02	3.28	0.06	−1.23	Greenwood et al. (2012)
Acapulcoite-Lodranites						
EET 84302	0.923	0.034	3.421	0.008	-0.868	*this study*
	0.433	0.045	3.043	0.006	-1.160	*this study*
EET 84302	0.530		3.310		-1.190	*Clayton et al. (1996)*
EET 84302	0.21	0.05	2.73	0.1	−1.22	Greenwood et al. (2012)
EET 84302*	0.33	0.09	2.9	0.28	−1.19	Greenwood et al. (2012)
EET 84302	0.53		3.31		-1.204	McCoy et al. (1993)
GRA 95209	-0.638	0.039	1.273	0.012	-1.305	*this study*
GRA 95209	−0.86	0.15	1.03	0.31	−1.39	Greenwood et al. (2012)
GRA 95209*	−0.24	0.03	2.33	0.03	−1.46	Greenwood et al. (2012)
Lodranites						
NWA 4833	0.146	0.075	2.478	0.025	-1.151	*this study*
	-0.141	0.043	1.995	0.024	-1.186	*this study*
NWA 4875	0.071	0.031	2.432	0.009	-1.203	*this study*
	0.128	0.058	2.197	0.024	-1.023	*this study*

*EATG residue

Table 2.6: Rhenium-osmium isotopes and highly siderophile element abundances (in ng g-1) for acapulcoites and lodranites

Sample	Mass (g)	Re	Re*	Os	Ir	Ru	Pt	Pd	^{187}Re/^{188}O	±2σ	^{187}Os/^{188}Os	±2σ	DOs[1]
Acapulcoites													
Acapulco	0.099	30.2	38	399.5	411.9	419.2	557.2	637.4	0.033		0.12869	0.00031	308
Acapulco	0.059	17.6	18	222.8	221.0	251.5	306.6	477.2	0.380	0.002	0.12415	0.00007	-10
ALHA 81187	0.099	70.3	78	848.9	930.8	1174	1580	652.6	0.400		0.12743	0.00004	6
ALHA 81187	0.075	72.7	77	843.2	784.6	1155	1591	614.1	0.416	0.009	0.12719	0.00003	-8
MET 01195	0.121	54.9	65	706.1	771.6	977.3	1283	645.7	0.375		0.12725	0.00001	24
MET 01195	0.070	53.0	61	670.7	644.8	902.3	1238	573.5	0.381	0.007	0.12700	0.00006	17
NWA 2871 (L)	0.132	31.4	48	463.8	547.5	646.2	881.7	511.9	0.327		0.13147	0.00006	104
NWA 2871 (L)	0.055	33.3	48	472.2	504.4	653.4	893.2	495.5	0.340	0.005	0.13060	0.00007	85
Acapulcoite-Lodranites													
EET 84302	0.043	268	95	1054	1097	1421	1892	584	1.227		0.12660	0.00005	-654
EET 84302	0.060	320	241	2713	2096	3425	4876	1318	0.569	0.028	0.12618	0.00005	-140
Lodranites													
GRA 95209	0.048	276	259	2800	3120	4078	5280	1644	0.476		0.12751	0.00003	-52
GRA 95209	0.092	216	195	2103	1855	2944	4094	1167	0.494	0.022	0.12754	0.00001	-67
NWA 4833	0.136	24.3	50	527.0	600.5	782.5	593.2	235.2	0.223		0.12801	0.00002	152
NWA 4833	0.096	25.1	49	526.8	555.1	783.7	636.1	240.4	0.230	0.005	0.12776	0.00009	144
NWA 4875	0.048	6.9	20	237.7	153.8	180.6	179.1	50.7	0.141		0.12427	0.00044	179
NWA 4875	0.195	7.8	11	137.1	139.4	181.0	182.3	69.6	0.274	0.001	0.12364	0.00010	68
NWA 7474 (I)	0.126	28.6	42	460.1	512.6	699.7	787.5	317.9	0.300		0.12695	0.00004	80
NWA 7474 (II)	0.093	66.5	75	856.6	911.0	1032.3	1272.6	492.4	0.375		0.12580	0.00007	10

[1] DOs (after Fischer-Godde et al. 2010) refers to the combined deviation in the determined ^{187}Os/^{188}Os and ^{187}Re/^{188}Os for a given chondrite sample from the IIIA iron meteorite reference isochron, DOs = 10^4 (^{187}Os/^{188}Os$_{chondrite}$ (0.09524 + 0.07887 × ^{187}Re/^{188}Os$_{chondrite}$)), ^{187}Os/^{188}Os$_{chondrite}$ and ^{187}Re/^{188}Os$_{chondrite}$ are the values determined for chondrites, 0.09524 is the initial ^{187}Os/^{188}Os and 0.07887 is the slope of the IIIA iron meteorite isochron (Smoliar et al., 1996).

References

Barnes, S. J., Naldrett, A. J., & Gorton, M. P. (1985). The origin of the fractionation of platinum-group elements in terrestrial magmas. *Chemical Geology*, *53*, 303-323.

Barrat, J. A., Gillet, P., Lesourd, M., Blichert-Toft, J., & Poupeau, G. R. (1999). The Tatahouine diogenite: Mineralogical and chemical effects of sixty-three years of terrestrial residence. *Meteoritics & Planetary Science*, *34*, 91-97.

Becker, H., Horan, M. F., Walker, R. J., Gao, S., Lorand, J. P., & Rudnick, R. L. (2006). Highly siderophile element composition of the Earth's primitive upper mantle: constraints from new data on peridotite massifs and xenoliths. *Geochimica et Cosmochimica Acta*, *70*, 4528-4550.

Bild, R.W. & Wasson, J.T. (1976). The Lodran meteorite and its relationship to the ureilites. *Mineralogical Magazine, 40*, 721-735.

Birck, J. L., Barman, M. R., & Capmas, F. (1997). Re-Os isotopic measurements at the femtomole level in natural samples. *Geostandards newsletter*, *21*, 19-27.

Biswas, S., Ngo, H. T., & Lipschutz, M. E. (1980). Trace element contents of selected Antarctic meteorites. I. Weathering effects and ALH A77005, A77257, A77278 and A77299. *Zeitschrift für Naturforschung A*, *35*, 191-196.

Bizzarro, M., Baker, J. A., Haack, H., & Lundgaard, K. L. (2005). Rapid timescales for accretion and melting of differentiated planetesimals inferred from ^{26}Al-^{26}Mg chronometry. *The Astrophysical Journal Letters*, *632*, L41.

Brenan, J. M., McDonough, W. F., & Dalpe, C. (2003). Experimental constraints on the partitioning of rhenium and some platinum-group elements between olivine and silicate melt. *Earth and Planetary Science Letters*, *212*, 135-150.

Brenan, J. M., McDonough, W. F., & Ash, R. (2005). An experimental study of the solubility and partitioning of iridium, osmium and gold between olivine and silicate melt. *Earth and Planetary Science Letters*, *237*, 855-872.

Brenan, J. M., Bennett, N. R., & Zajacz, Z. (2016). Experimental results on fractionation of the highly siderophile elements (HSE) at variable pressures and temperatures during planetary and magmatic differentiation. *Reviews in Mineralogy and Geochemistry*, *81*, 1-87.

Chabot, N. L., & Jones, J. H. (2003). The parameterization of solid metal-liquid metal partitioning of siderophile elements. *Meteoritics & Planetary Science*, *38*, 1425-1436.

Clayton, R. N., & Mayeda, T. K. (1988). Formation of ureilites by nebular processes. *Geochimica et Cosmochimica Acta*, *52*, 1313-1318.

Clayton, R. N., Mayeda, T. K., & Nagahara, H. (1992). Oxygen isotope relationships among primitive achondrites. In *Lunar and Planetary Science Conference*, *23*, 231-232.

Clayton, R. N., & Mayeda, T. K. (1996). Oxygen isotope studies of achondrites. *Geochimica et Cosmochimica Acta*, *60*, 1999-2017.

Clayton, R. N., & Mayeda, T. K. (1999). Oxygen isotope studies of carbonaceous chondrites. *Geochimica et Cosmochimica Acta*, *63*, 2089-2104.

Cohen, A. S., & Waters, F. G. (1996). Separation of osmium from geological materials by solvent extraction for analysis by thermal ionisation mass spectrometry. *Analytica Chimica Acta*, *332*, 269-275.

Corder, C. A. (2015). Primitive and differentiated achondrite meteorites and partial melting in the early Solar System.

Crozaz, G., Floss, C., & Wadhwa, M. (2003). Chemical alteration and REE mobilization in meteorites from hot and cold deserts. *Geochimica et Cosmochimica Acta*, *67*, 4727-4741.

Day, J.M.D. (2015). Planet formation processes revealed by meteorites. Geology Today, 31, 12-20.

Day, J.M.D., Ash, R.D., Liu, Y., Bellucci, J.J., Rumble III, D., McDonough, W.F., Walker, R.J. & Taylor, L.A., 2009. Early formation of evolved asteroidal crust. *Nature, 457*, 179-182.

Day, J.M.D, Walker, R.J., Ash, R.D., Liu, Y., Rumble, D., Irving, A.J., Goodrich, C.A., Tait, K., McDonough, W.F. & Taylor, L.A. (2012). Origin of felsic achondrites Graves Nunataks 06128 and 06129, and ultramafic brachinites and brachinite-like achondrites by partial melting of volatile-rich primitive parent bodies. *Geochimica et Cosmochimica Acta*, *81*, 94-128.

Day, J.M.D., Corder, C. A., Rumble, D., Assayag, N., Cartigny, P., & Taylor, L. A. (2015). Differentiation processes in FeO-rich asteroids revealed by the achondrite Lewis Cliff 88763. *Meteoritics & Planetary Science*, *50*, 1750-1766.

Day, J.M.D., Brandon, A. D., & Walker, R. J. (2016). Highly siderophile elements in Earth, Mars, the Moon, and asteroids. *Reviews in Mineralogy and Geochemistry*, *81*, 161-238.

Day, J.M.D., Waters, C. L., Schaefer, B. F., Walker, R. J., & Turner, S. (2016b). Use of Hydrofluoric Acid Desilicification in the Determination of Highly Siderophile Element Abundances and Re-Pt-Os Isotope Systematics in Mafic-Ultramafic Rocks. *Geostandards and Geoanalytical Research*, *40*, 49-65.

Day, J.M.D., Corder, C.A., Cartigny, P., Steele, A.M., Assayag, N., Rumble, D. & Taylor, L.A. (2017). A carbon-rich region in Miller Range 091004 and implications for ureilite petrogenesis. *Geochemica et Cosmochimica Acta,* **in press**.

El Goresy, A. E., Zinner, E., & Marti, K. (1995). Survival of isotopically heterogeneous graphite in a differentiated meteorite. *Nature, 373*, 496-499.

El Goresy, A., Zinner, E., Pellas, P., & Caillet, C. (2005). A menagerie of graphite morphologies in the Acapulco meteorite with diverse carbon and nitrogen isotopic signatures: implications for the evolution history of acapulcoite meteorites. *Geochimica et cosmochimica acta*, *69*, 4535-4556.

Fischer-Gödde, M., Becker, H., & Wombacher, F. (2010). Rhodium, gold and other highly siderophile element abundances in chondritic meteorites. *Geochimica et Cosmochimica Acta*, *74*, 356-379.

Fischer-Gödde, M., Becker, H., & Wombacher, F. (2011). Rhodium, gold and other highly siderophile elements in orogenic peridotites and peridotite xenoliths. *Chemical Geology*, *280*, 365-383.

Floss, C. (2000). Complexities on the acapulcoite-lodranite parent body: Evidence from trace element distributions in silicate minerals. *Meteoritics & Planetary Science, 35*, 1073-1085.

Goodrich, C. A., Jones, J. H., & Berkley, J. L. (1987). Origin and evolution of the ureilite parent magmas: multi-stage igneous activity on a large parent body. *Geochimica et Cosmochimica Acta*, *51*, 2255-2273.

Goodrich, C. A., Kita, N. T., Spicuzza, M. J., Valley, J. W., Zipfel, J., Mikouchi, T., & Miyamoto, M. (2011). The Northwest Africa 1500 meteorite: Not a ureilite, maybe a brachinite. *Meteoritics & Planetary Science*, *45*, 1906-1928.

Graham, A.L. (1978). The Meteoritical Bulletin No. 55. In *Meteoritics, 13*, 327-352.

Greenwood, R. C., Franchi, I. A., Gibson, J. M., & Benedix, G. K. (2012). Oxygen isotope variation in primitive achondrites: The influence of primordial, asteroidal and terrestrial processes. *Geochimica et Cosmochimica Acta*, *94*, 146-163.

Greenwood, R. C., Burbine, T. H., Miller, M. F., & Franchi, I. A. (2016). Melting and differentiation of early-formed asteroids: The perspective from high precision oxygen isotope studies. *Chemie der Erde-Geochemistry*, **in press**.

Hart, S. R., & Ravizza, G. E. (1996). Os partitioning between phases in lherzolite and basalt. *Earth Processes: Reading the Isotopic Code*, 123-134.

Horan, M. F., Walker, R. J., Morgan, J. W., Grossman, J. N., & Rubin, A. E. (2003). Highly siderophile elements in chondrites. *Chemical Geology*, *196*, 27-42.

Hunt, A.C., Benedix, G.K., Hammond, S.J., Bland, P.A., Rehkämper, M., Kreissig, K. & Strekopytov, S. (2016). A geochemical study of the winonaites: Evidence for limited partial melting and constraints on the precursor composition. *Geochimica et Cosmochimica Acta*.

Hyde, B. C., Day, J.M.D., Tait, K. T., Ash, R. D., Holdsworth, D. W., & Moser, D. E. (2014). Characterization of weathering and heterogeneous mineral phase distribution in brachinite Northwest Africa 4872. *Meteoritics & Planetary Science*, *49*, 1141-1156.

Jones, J. H., & Drake, M. J. (1986). Geochemical constraints on core formation in the Earth. *Nature, 322*, 221-228.

Kleine, T., Münker, C., Mezger, K., & Palme, H. (2002). Rapid accretion and early core formation on asteroids and the terrestrial planets from Hf–W chronometry. *Nature*, *418*, 952-955.

Mann, U., Frost, D. J., Rubie, D. C., Becker, H., & Audétat, A. (2012). Partitioning of Ru, Rh, Pd, Re, Ir and Pt between liquid metal and silicate at high pressures and high temperatures-Implications for the origin of highly siderophile element concentrations in the Earth’s mantle. *Geochimica et Cosmochimica Acta*, *84*, 593-613.

Mayeda, T. K., & Clayton, R. N. (1980). Oxygen isotopic compositions of aubrites and some unique meteorites. In *Lunar and Planetary Science Conference Proceedings*, 11, 1145-1151.

McCoy, T. J., Keil, K., Clayton, R. N., & Mayeda, T. K. (1993). Classificational parameters for acapulcoites and lodranites: The cases of FRO 90011, EET 84302 and ALH A81187/84190. In *Lunar and Planetary Science Conference*, 24, 945-946.

McCoy, T. J. (1994). Partial melting of the acapulcoite-lodranite meteorite parent body. Ph.D. Thesis, University of Hawaii at Manoa.

McCoy, T.J., Keil, K., Clayton, R.N., Mayeda, T.K., Bogard, D.D., Garrison, D.H., Huss, G.R., Hutcheon, I.D. & Wieler, R., (1996). A petrologic, chemical, and isotopic study of Monument Draw and comparison with other acapulcoites: Evidence for formation by incipient partial melting. *Geochimica et Cosmochimica Acta*, *60*, 2681-2708.

McCoy, T. J., Carlson, W. D., Nittler, L. R., Stroud, R. M., Bogard, D. D., & Garrison, D. H. (2006). Graves Nunataks 95209: A snapshot of metal segregation and core formation. *Geochimica et Cosmochimica Acta*, *70*, 516-531.

McDonough, W. F., & Sun, S. S. (1995). The composition of the Earth. *Chemical geology*, *120*, 223-253.

Mittlefehldt, D.W. (2007). Achondrites. *Treatise on Geochemistry, I,* 1-40.

Min, K., Farley, K. A., Renne, P. R., & Marti, K. (2003). Single grain (U–Th)/He ages from phosphates in Acapulco meteorite and implications for thermal history. *Earth and Planetary Science Letters*, *209*, 323-336.

Mittlefehldt, D.W., & Lindstrom, M. M. (1991). Generation of abnormal trace element abundances in Antarctic eucrites by weathering processes. *Geochimica et Cosmochimica Acta*, *55*, 77-87.

Mittlefehldt, D. W., Lindstrom, M. M., Bogard, D. D., Garrison, D. H., & Field, S. W. (1996). Acapulco-and Lodran-like achondrites: Petrology, geochemistry, chronology, and origin. *Geochimica et Cosmochimica Acta*, *60*, 867-882.

Mittlefehldt, D. W., & Lindstrom, M. M. (1998). Petrology and geochemistry of lodranite GRA 95209. *Meteoritics and Planetary Science Supplement*, *33*, A111.

Morgan, J. W., Horan, M. F., Walker, R. J., & Grossman, J. N. (1995). Rheniumum concentration and isotope systematics in group IIAB iron meteorites. *Geochimica et Cosmochimica Acta*, *59*, 2331-2344.

Nehru, C. E., Prinz, M., Weisberg, M. K., Ebihara, M., Clayton, R. N., & Mayeda, T. K. (1992). Brachinites: A new primitive achondrite group. *Meteoritics*, *27*, 267.

O'Neill, H. S. C., Dingwell, D. B., Borisov, A., Spettel, B., & Palme, H. (1995). Experimental petrochemistry of some highly siderophile elements at high temperatures, and some implications for core formation and the mantle's early history. *Chemical Geology*, *120*, 255-273.

Palme, H., Schultz, L., Spettel, B., Weber, H. W., Wänke, H., Michel-Levy, M. C., & Lorin, J. C. (1981). The Acapulco meteorite: chemistry, mineralogy and irradiation effects. *Geochimica et Cosmochimica Acta*, *45*, 727-752.

Pearson, D. G., Irvine, G. J., Ionov, D. A., Boyd, F. R., & Dreibus, G. E. (2004). Re–Os isotope systematics and platinum group element fractionation during mantle melt extraction: a study of massif and xenolith peridotite suites. *Chemical Geology*, *208*, 29-59.

Poirier, J. P. (1994). Light elements in the Earth's outer core: a critical review. *Physics of the earth and planetary interiors*, *85*, 319-337.

Rankenburg, K., Brandon, A. D., & Humayun, M. (2007). Osmium isotope systematics of ureilites. *Geochimica et Cosmochimica Acta*, *71*, 2402-2413.

Rankenburg, K., Humayun, M., Brandon, A. D., & Herrin, J. S. (2008). Highly siderophile elements in ureilites. *Geochimica et Cosmochimica Acta*, *72*, 4642-4659.

Riches, A. J., Day, J.M.D., Walker, R. J., Simonetti, A., Liu, Y., Neal, C. R., & Taylor, L. A. (2012). Rhenium–osmium isotope and highly-siderophile-element abundance systematics of angrite meteorites. *Earth and Planetary Science Letters*, *353*, 208-218.

Righter, K., & Drake, M. J. (1996). Core formation in Earth's moon, Mars, and Vesta. *Icarus*, *124*, 513-529.

Righter, K. (2003). Metal-Silicate Partitioning of Siderophile Elements and Core Formation in the Early Earth. *Annual Review of Earth and Planetary Sciences*, *31*, 135-174.

Righter, K., Humayun, M., & Danielson, L. (2008). Partitioning of palladium at high pressures and temperatures during core formation. *Nature Geoscience*, *1*, 321-323.

Rose-Weston, L., Brenan, J. M., Fei, Y., Secco, R. A., & Frost, D. J. (2009). Effect of pressure, temperature, and oxygen fugacity on the metal-silicate partitioning of Te, Se, and S: Implications for earth differentiation. *Geochimica et Cosmochimica Acta*, *73*, 4598-4615.

Rubin, A. E., Trigo-Rodríguez, J. M., Huber, H., & Wasson, J. T. (2007). Progressive aqueous alteration of CM carbonaceous chondrites. *Geochimica et Cosmochimica Acta*, *71*, 2361-2382.

Rushmer, T., Minarik, W. G., & Taylor, G. J. (2000). Physical processes of core formation. *Origin of the Earth and Moon*, *1*, 227-243.

Shearer, C.K., Burger, P.V., Neal, C.R., Sharp, Z., Borg, L.E., Spivak-Birndorf, L., Wadhwa, M., Papike, J.J., Karner, J.M., Gaffney, A.M. & Shafer, J. (2008). Letter. A unique glimpse into asteroidal melting processes in the early solar system from the Graves Nunatak 06128/06129 achondrites. *American Mineralogist*, *93*, 1937-1940.

Smoliar M. I., Walker R. J. & Morgan J. W. (1996) Re–Os ages of group IIA, IIIA, IVA and IVB iron meteorites. *Science, 271*, 1099–1102.

Suhr, G., Seck, H.A., Shimizu, N., Günther, D., & Jenner, G. (1998). Infiltration of refractory melts into the lowermost oceanic crust: evidence from dunite- and gabbro-hosted clinopyroxenes in the Bay of Islands Ophiolite. *Contributions to Mineralogy and Petrology, 131*, 136–154.

Sun, C., & Liang, Y. (2014). An assessment of subsolidus re-equilibration on REE distribution among mantle minerals olivine, orthopyroxene, clinopyroxene, and garnet in peridotites. *Chemical Geology 372*, 80–91.

Takeda, H., Mori, H., Hiroi, T., & Saito, J. (1994). Mineralogy of new Antarctic achondrites with affinity to Lodran and a model of their evolution in an asteroid. *Meteoritics*, *29*, 830-842.

Touboul, M., Kleine, T., Bourdon, B., Van Orman, J. A., Maden, C., & Zipfel, J. (2009). Hf–W thermochronometry: II. Accretion and thermal history of the acapulcoite–lodranite parent body. *Earth and Planetary Science Letters*, *284*, 168-178.

Van Acken, D., Brandon, A. D., & Lapen, T. J. (2012). Highly siderophile element and osmium isotope evidence for postcore formation magmatic and impact processes on the aubrite parent body. *Meteoritics & Planetary Science*, *47*, 1606-1623.

Walker, R. J., Horan, M. F., Morgan, J. W., Becker, H., Grossman, J. N., & Rubin, A. E. (2002). Comparative ^{187}Re-^{187}Os systematics of chondrites: Implications regarding early solar system processes. *Geochimica et Cosmochimica Acta*, *66*, 4187-4201.

Weigel, A., Eugster, O., Koeberl, C., Michel, R., Krähenbühl, U., & Neumann, S. (1999). Relationships among lodranites and acapulcoites: Noble gas isotopic abundances, chemical composition, cosmic-ray exposure ages, and solar cosmic ray effects. *Geochimica et cosmochimica acta*, *63*, 175-192.

Weisberg, M. K., McCoy, T. J., & Krot, A. N. (2006). Systematics and evaluation of meteorite classification. *Meteorites and the early solar system II*, 19-52.

Young, E. D., & Russell, S. S. (1998). Oxygen reservoirs in the early solar nebula inferred from an Allende CAI. *Science*, *282*(5388), 452-455.

Yugami, K., Miyamoto, M., & Takeda, H. (1995). The similar reduction processes of primitive achondrites from different parent bodies. *Meteoritics*, *30*, 605.

Yugami, K., Takeda, H., Kojima, H., & Miyamoto, M. (1998). Modal mineral abundances and the differentiation trends in primitive achondrites. *Antarctic meteorite research*, *11*, 49.

Zipfel, J., Palme, H., Kennedy, A. K., & Hutcheon, I. D. (1995). Chemical composition and origin of the Acapulco meteorite. *Geochimica et Cosmochimica Acta*, *59*, 3607-36

Chapter 3:

Highly siderophile element abundance and Os isotope evidence for primary metal-silicate signatures in eucrite meteorites

Abstract

Highly siderophile element (HSE: Os, Ir, Ru, Pt, Pd, Re), Ni and Co abundances and Os isotope ratios in a suite of eucrite meteorites provide robust means for determining rocks formed during crystallization on their parent body (pristine samples) versus those affected by later impact contamination. The criteria for pristine lunar rocks is applied to the eucrite meteorites to identify the most pristine eucrite samples; these include low Ni concentrations, low absolute HSE abundances and non-chondritic Os isotope ratios. These new data provide greater precision compared to previous studies of siderophile elements in eucrite meteorites and demonstrate that impact contamination can occur even in ostenisbly unbrecciated and petrologically primary samples. The samples that are free from impact contamination include both previously identified unbrecciated samples, as well as other types of eucrite meteorites. Eucrites characterized as pristine are valuable for examining early metal-silicate differentiation on the howardite-eucrite-

diogenite (HED) parent body, widely held to be the asteroid, Vesta. These samples reveal marked Os abundance depletions that result in elevated Ir/Os signatures; this fractionation seems to be a primary feature of differentiation and persists even among impact contaminated eucrites as well as within diogenite meteorites. Fractionation of Ir/Os is of particular interest since Ir and Os generally exhibit similar partitioning during metal-silicate melting, and may indicate that effects of low oxygen fugacity and low pressure are required during metal-silicate differentiation within the HED parent body. The new data also indicates distinct HSE fractionations, particularly in Ru and Pt, among eucrite samples with minimal to moderate impact contamination. These partitioning trends may reflect heterogeneous melting and metal-silicate differentiation on the HED parent body, which is supported by the small mass of the parent planetesimal and a shorter-lived magma ocean event compared to the Earth or the Moon. Pristine eucrites therefore represent natural experiments of metal-silicate partitioning on a fully differentiated planetesimal, with important implications for understanding the early evolution of the terrestrial planets.

3.1 Introduction

There is obvious evidence for the complete differentiation of planets into cores, mantle and crusts, but the geochemical signatures expected for metal-silicate equilibration have not been found, despite nearly-exhaustive analyses of samples from a wide range of planetary bodies (e.g., Day et al., 2007; 2012; 2016; Brandon et al., 2012; Dale et al., 2012; Riches et al., 2012; van Acken et al., 2012; Day & Walker, 2015). Core formation is predicted to efficiently strip the highly siderophile elements (HSE: Re, Os, Ir, Ru, Pt, Rh, Pd, Au) from planetary mantles due to the high metal-silicate partition coefficients (>10^4) typical of these elements at relatively low pressures and temperatures (Jones & Drake, 1986; Borisov & Palme, 1997). Furthermore, the process of metal-silicate separation is predicted to lead to significant fractionations of the HSE from one another (e.g., Mann et al., 2012), although the magnitude and sense of inter-element fractionation is not known. Instead, samples measured from differentiated bodies, including Earth, the Moon, Mars and differentiated asteroids, all show evidence for additions of broadly chondritic HSE-rich materials to their mantles after silicate equilibrium. This feature is known as 'late accretion' and has been recognized to account for between 0.02 and <0.8 mass addition to planets after the final phases of core growth (Kimura et al., 1974; Chou, 1978; Walker, 2009; Day et al., 2016).

In this study, we have targeted the last known samples for which we might reasonably expect to observe primary metal-silicate signatures; the unbrecciated eucrites. Eucrite meteorites are basaltic and cumulate melts with some of the earliest crystallization ages in the Solar System that are as early as two million years after the formation of the earliest solids, calcium aluminium inclusions (CAIs - ^{53}Mn-^{53}Cr dating and absolute Pb-Pb dates; Lugmair and Shukolyukov, 1998; Trinquier et al., 2008; Amelin, 2008). Eucrites are genetically linked by oxygen isotopes to the diogenite and howardite meteorites, forming the HED (howardite-eucrite-diogenite) meteorite clan (Wiechert et al., 2004; Greenwood et al., 2005; Scott et al., 2009; Day et al., 2012). HED meteorites are considered to derive from the Vestan asteroid family based on remote sensing spectra (McCord et al., 1970; Binxel and Xu, 1993; McSween et al., 2013).

Asteroid-4 Vesta, and the Vestoids, represent fully differentiated, low-mass, atmosphere-free planetesimals(s) that are part of the continuum of rocky planets, including Earth, Moon and Mars. The HED meteorites are therefore valuable for examining key steps in planetary formation and evolution because they originate from a planetesimal unaffected by complete and later overprinting effects.

Through comprehensive geochemical analyses, we have sought to characterize the 'pristine' eucrite samples, with geochemical compositions that may reflect primary mantle differentiation of the eucrite parent body. To identify these samples, we use criteria analagous to that for lunar rocks (Warren and Wasson, 1977); the lunar samples are similar to eucrites in their low siderophile element concentrations. The criteria for pristine crustal lunar rocks have been defined as: (1) low bulk-rock siderophile abundances; $< 3 \times 10^{-4} \times$ chondrite abundances; (2) low incompatible element concentrations; (3) coarse granularity, > 3mm; (4) ancient ages, >4.2 Ga; (5) phase homogeneity; (6) non-radiogenic $^{87}Sr/^{88}Sr$; (7) cumulate textures, and (8) low Ni/Co ratios in FeNi metals (Warren and Wasson, 1977; Ryder et al., 1980; Warren 2009; Day et al., 2010). Some of these criteria, namely low incompatible element concentrations, coarse granularity and phase homogeneity, are not applicable to the eucrite meteorites, and even more ancient ages might be expected for some of the eucrites. For example, the cumulate and basaltic eucrites show variable incompatible element abundances, fine-grained basaltic textures, and primary crystallization features with heterogeneous mineral phases. Nonetheless, criterion including low Ni/Co ratios and low abundances of siderophile elements are key tracers for understanding impactor contamination. This work focuses on this concept and present new measurements of siderophile element abundances, Ni and Co, the highly siderophile elements (HSE: Os, Ir, Ru, Pt, Pd, Re) and ^{187}Os/^{188}Os ratios to ascertain the contributions from impact addition to a suite of unbrecciated eucrites.

The moderately siderophile elements, Ni and Co, are subject to metal-silicate partitioning during core segregation and planetary differentiation, but are also incorporated into the silicate phase. In the terrestrial mantle, these elements are present at ~0.2 × CI-chondrite abundances, and their metal-silicate partitioning behavior is further controlled by oxygen fugacity, temperature and pressure conditions (Chou, 1978). Impactor material is typically rich in Fe-Ni metal and therefore samples that have experienced impact contamination often exhibit elevated Ni/Co ratios because of the addition of Ni. This metric has been previously used to compare lunar polymict breccias (subject to impact mixing) and pristine lunar rocks, where the latter exhibit Ni/Co ratio < 2 (Ryder et al., 1980). The Ni content has also been used to examine the degree of brecciation in HED meteorites, particularly the howardites, and indicate highly diverse Ni concentrations even in ‘breccias’ (Warren et al., 2009). Warren et al. (2009) also showed that variable and sometimes low siderophile contents occurred in polymict eucrites, suggesting that multiple impacts on the HED parent body were required to significantly enrich siderophile element inventories. This criterion of Ni content (< 1 ppm) is applied to the HED meteorites for preliminary identification of pristine eucrite samples, followed by detailed analyses of HSE abundances and Os-isotope ratios to identify specimens with the most primitive (i.e., late-accretion/impact contamination free) signatures.

The HSE are more strongly siderophile than Ni and Co, with metal-silicate partition coefficients of more than 10^4 (e.g., Day et al., 2016), and are more efficiently extracted into metal phases during core formation. Differentiated planets therefore exhibit significantly depleted HSE abundances as observed in planetary mantle materials, ~0.007 – 0.008 × CI-chondrite for the Earth and Mars, and ~0.0002 × CI-chondrite in the Moon (Day et al., 2016). The HSE also exhibit differences in partitioning behavior, with relative compatibilities between metal-silicate being Os > Ir > Ru > Pt > Pd > Re (Day et al., 2016; Brenan et al., 2016); this partitioning should yield inter-element fractionation trends in planetary mantle materials. However, there is limited inter-element HSE fractionation observed in terrestrial, martian or lunar samples, and their absolute HSE abundances are more than those predicted by partitioning experiments, with upper limits of ~10^{-4} × CI-chondrite at 60 GPa to ~10^{-7} × CI-chondrite at 5 GPa (Mann et al., 2012). This discrepancy indicates that additional processes are required to elevate the estimated HSE abundances to the observed values, such as the late accretion of chondritic impactors (e.g., Chou, 1978; Walker, 2009). The process of impact addition can explain both elevated absolute HSE abundances, and the over-printing of primary inter-element HSE fractionation signatures with unfractionated, chondritic relative abundances.

The new work presented herein complements and significantly extends prior siderophile element analyses in HED meteorites (Warren et al., 2009), HSE measurements of diogenites (Day et al., 2012) and eucrites and diogenites (Dale et al., 2012). These latter studies of eucrites and diogenites suggested that late accretion was concurrent with the later stages of planetesimal differentiation. The diogenites, however, exhibit a wide range of HSE abundances and inter-element fractionation, indicative of the unique mechanisms of metal-silicate differentiation and heterogeneous late accretion to the HED parent body (Day et al., 2012). The extremely low absolute HSE abundances and non-chondritic fractionation patterns among the HSE in some diogenite samples are thought to reflect primary signatures from metal segregation and core formation on Vesta. The second chapter further examines this hypothesis using measurements on unbrecciated eucrites. The results of this study have ramifications for understanding primary signatures of magmatic evolution (e.g. Mandler and Elkins-Tanton, 2013) and volatile inventories (e.g. Paniello et al., 2012; Sarafian et al., 2013), as well as of the impact history of Asteroid-4 Vesta and the implications this has for potential dynamo formation (Fu et al., 2012). Ultimately, the new results show for the first time, evidence of a pristine 'pre-late accretion' metal-silicate differentiation signature in the early Solar System.

3.2 Samples and Methods

3.2.1 Samples

Twelve Antarctic eucrite finds: Allan Hills (ALHA) 81001, Bates Nunatak (BTN) 00300, Cumulus Hills (CMS) 04049, Elephant Terrane (EET) 90020, Graves Nunataks (GRA) 98098, Grosvenor Range (GRO) 95533, Lewis Cliffs (LEW) 85305, Pecora Escarpment (PCA) 82502, PCA 91245, Queen Alexandra Range (QUE) 97014, QUE 97053, GRO 06049; twelve Saharan desert finds: Agoult, Sayh al Uhaymir (SaU) 562, Northwest Africa (NWA) 1000, NWA 1666, NWA 1836, NWA 1918, NWA 1923, NWA

2362, NWA 5232, NWA 5356, NWA 5601, NWA 5612, four falls: Bereba, Millbillillie, Pasamonte and Stannern, and two finds from France (Bouvante and Juvinas), were analyzed in this study, for a total study of 30 individual meteorites.

3.2.2 Sample Preparation & Analytical Techniques

All samples were weighed and photographed when received from their various sources (Meteorite Working Group, Royal Ontario Museum, J.-A. Barrat [Brest, France], T. Kleine [Muenster, Germany]). An initial small chip (~100 mg) was prepared for major and trace element analysis by being broken off and weighed. This fragment was then ground in an alumina-silicate ceramic mortar and pestle to make a homogenized powder. The alumina-silicate ceramic mortar and pestle was cleaned using a fresh and ultrapure 1N HCl solution, and thoroughly cleaned with quartz sand and ultra-pure water between each preparation of individual samples. The quartz sand was made at the *Scripps Isotope Geochemistry Laboratory (SIGL)* from acid leached quartz Carius tubes; the sand used to clean the dedicated mortar and pestle was the last and cleanest grind. Powders for subsequent HSE analyses were made from a second, larger chip (typically ~1.2 g).

Trace element digestions for Ni and Co involved ~40 mg of sample powder directly weighed into Teflon Parr Bomb vessels; a mixture of 4 ml HF and 1 ml HNO_3 was added to each vessel and the samples were digested at 170°C for 72 hours. This method was employed because it ensures complete digestion of the most refractory mineral phases. Samples were then evaporated to dryness and further digested in 1 ml HNO_3 twice to eliminate any organic compounds from the samples and to remove fluorides. A 1 ppm In solution was added to the final stock solutions; these were then diluted and analyzed using a *Thermo-Scientific* iCAP-Q inductively coupled plasma mass spectrometer (ICP-MS) in normal mode at the *SIGL* using methods outlined in Dhaliwal et al. (in review).

The full methods and procedures for HSE abundance and Os isotope analyses are identical to those of Day et al. (2010; 2012). For most samples, the highly siderophile element analyses comprised two separate digestions, except where total aliquots were limited or single analyses were deemed sufficient. The initial Carius Tube (CT) ‘reconnaissance’ digestion consisted of a ~0.2 to 0.3 g aliquot, which was used to determine the HSE concentrations in the samples. This preliminary data was then used to determine the optimal amount of spike required for the second digestion of larger (0.6-1g) aliquots. Some of the optimally spiked digestions were done using an *Anton Parr* High Pressure Asher (HPA) using high-purity quartz vessels, but because of reuse of the tubes and resultant elevated total analytical blanks in some sample sets, many final analyses were CT digestions (see **Table 3.2**). Samples were prepared with isotopically enriched multi-element spikes (^{99}Ru, ^{106}Pd, ^{185}Re, ^{190}Os, ^{191}Ir, ^{194}Pt), and appropriate quantities of a 1:2 mixture of multiply Teflon distilled HCl and HNO_3 that was purged with H_2O_2 to remove Os. Samples in CT were digested to a maximum temperature of 270˚C in an oven for 72 hours and samples digested in the HPA were digested at >150 bar at 300˚C for 6 hours. Osmium was triply extracted from the acid using CCl_4 and then back-extracted into HBr (Cohen & Waters, 1996), prior to purification by micro-distillation (Birck et al., 1997). Rhenium and the other HSE were recovered and purified from the residual solutions using standard anion exchange separation techniques. Measurement protocols were identical to those described previously (Day et al., 2016b). Isotopic compositions of Os were measured in negative-ion mode on a *ThermoScientific* Triton thermal ionisation mass spectrometer at the SIGL. Rhenium, Pd, Pt, Ru and Ir were measured using an *Cetac* Aridus II desolvating nebuliser coupled to a *ThermoScientific* iCAP q ICP-MS. Offline corrections for Os involved an oxide correction, an iterative fractionation correction using $^{192}Os/^{188}Os = 3.08271$, a ^{190}Os spike subtraction, and finally, an Os blank subtraction.

Precision for $^{187}Os/^{188}Os$, determined by repeated measurement of the UMCP Johnson-Matthey standard was better than ±0.2% (2 St. Dev.; 0.11390 ±20; n = 5). Measured Re, Ir, Pt, Pd and Ru isotopic ratios for sample solutions were corrected for mass fractionation using the deviation of the standard average run on the day over the natural ratio for the element. External reproducibility on HSE analyses using the iCAP q was better than 0.5% for 0.5 ppb solutions and all reported values are blank corrected. The total procedural blank run with the samples had $^{187}Os/^{188}Os = 0.28 \pm 0.12$, with quantities (in picograms) of 5 ±3 [Re], 38 ±18 [Pd], 15 ±10 [Pt], 52 ±26 [Ru], 8 ±6 [Ir] and 0.001 ±0.001 [Os] (*n* = 10). All concentrations and isotopic compositions are blank-corrected using blank contributions measured for individually prepared experimental batches, resulting in a range of calculated uncertainties for samples. For small aliquants, the associated uncertainties relating to blank additions are large, and in many cases, these uncertainties exceed analytical uncertainties. Because of the proportionally large relative uncertainties in Re blank contributions, the value Re* is also reported; this is the concentration of Re calculated assuming chondritic ^{187}Os/^{188}Os at the assumed time of sample crystallization. Total procedural blanks range from 2-87%, 0.1-71%, 0.1-64%, 0.1-~100%, 0.1-92% and 0.1-84% of total measured Re, Pd, Pt, Ru, Ir and Os, respectively. The high values for blank contributions reflect analytical difficulties in detection for the extremely low HSE concentrations in several eucrite meteorites, which resulted in incomplete data collection, particularly in the case of Pd concentrations.

3.3 Results

3.3.1 Siderophile Elements

A previous, detailed study of siderophile concentrations in HED meteorites yielded low Ni concentrations for unbrecciated eucrites, < 30 ppm (Warren et al., 2009). The measurements of Ni in this study have lower analytical uncertainty (< 1 %), and these more precise data are valuable for examining eucrite samples for evidence of impact contamination (**Table 3.1**). The significant enrichments in Ni concentration in some samples compared to Co concentrations (**Figure 3.1**) demonstrate the effects of impact contamination in some samples. The samples in this plot are categorized according to their Ni content: very low (< 1 ppm); low (1-5 ppm); intermediate (5-10 ppm) and high (> 10 ppm). Extremely low Ni contents are predicted in a Vestan mantle assuming metal-silicate partitioning expressed by models (Righter & Drake, 1996).

The samples with the lowest Ni are unbrecciated eucrites: CMS 04049, QUE 97014, PCA 91245, GRO 95533, EET 90020 and BTN 00300; desert meteorite, NWA 5356; and two finds: Bouvante and one aliquot of Juvinas. Low Ni concentrations (1–

5ppm) are obsereved in unbrecciated samples: LEW 85305, QUE 97053, GRA 98098, and ALHA 81001; desert meteorites: Agoult, NWA 1918, NWA 1836, NWA 1923, NWA 2362, and NWA 5617; and falls: Millbillillie, Stannern, and Bereba. Prior analyses of Agoult and Millbillillie yielded 6 ppm and ~1 ppm, respectively (Warren et al., 2009). Pasamonte and NWA 1000 are classified as 'low' Ni, but have abundances close to 5 ppm Ni, which is the lower limit for 'intermediate' Ni contents. The intermediate Ni content meteorites are PCA 82502, NWA 1666 and SaU 562; prior analysis of PCA 82502 yielded 18 ppm (Warren et al., 2009), but we obtained 8.5 ppm. The eucrites with the elevated Ni contents, >> 10 ppm are the brecciated eucrite, GRO 06059, two desert meteorites, NWA 5232, NWA 5601 and one aliquot of Juvinas (II). These Ni content categories are further used to group and analyze the HSE abundance and Os isotope data in subsequent sections.

3.3.2 Highly siderophile element abundances and osmium isotope ratios

Highly siderophile element concentrations in the eucrites range from about 10^{-6} to 0.1 × CI chondrite (**Table 3.2**). The Ni and Os concentrations seem to be correlated (**Figure 3.2**) and the HSE relative abundances exhibit variable inter-element fractionation patterns (**Figures 3.3, 3.4**). For greater clarity of viewing, the plots are grouped according to their Ni content, which reveals similarity in HSE patterns between meteorite samples from each group. The samples in **Figure 3.3** are those with the lowest Ni concentrations (< 1 ppm) (**Figure 3.3a**), low Ni content (1 ppm < [Ni] < 5 ppm; **Figure 3.3b**) and all samples with < 5 ppm Ni for which complete HSE abundance data could not be obtained

(**Figure 3.3c**). The intermediate Ni content samples are shown in **Figure 3.4a** and those with the highest Ni are presented in **Figure 3.4b**.

Most samples exhibit significant Os depletions compared to Ir and the other HSE. While measured abundances for Ir, Ru, Pt, Pd, Re are likely upper limits on actual HSE concentrations and have been, in some cases, heavily blank corrected, we do not consider analytical issues to be the cause of low Os/Ir in some samples. This is due to the fact that the higher average blank abundance for Ir relative to Os would be expected to lead to an opposite effect. Furthermore, previous studies have shown similarly low Os/Ir for some eucrite and diogenite meteorites (Dale et al., 2012; Day et al., 2012). Among samples with < 5 ppm Ni, the elevated Ir/Os ratio is not observed for EET 90020, NWA 5356, BTN 00300 and one aliquot of CMS 04049, as well as NWA 5617, which also exhibit elevated absolute HSE abundances (**Figure 3.3**). Samples with intermediate Ni content (**Figure 3.4a**) that also show Os depletions are PCA 82502, Juvinas (II) and one aliquot of SaU 562; the Ir/Os fractionation is less marked for these samples and they also exhibit higher HSE abundances than lower Ni samples. The highest Ni concentration samples, including brecciated eucrite, GRO 06059, and howardite, Kapoeta, exhibit chondritic HSE patterns, ranging from ~10^{-3} to 10^{-1} × CI chondrite (**Figure 3.4b**).

The ^{187}Os/^{188}Os isotope ratios for the complete sample suite ranges from 0.1030 to 0.815 (**Table 3.2**). The Os isotope ratios versus Os concentrations (pg/g) for ^{187}Os/^{188}Os in the range of 0.1 to 0.45 are shown in **Figure 3.6**, along with the Ni content category of the samples. Eucrite samples with lower contents of Ni trend toward enriched and radiogenic values $^{187}Os/^{188}Os > 0.127$ (i.e., the chondritic value; Shirey & Walker, 1998), as well as lower Os concentrations. This is most notable for CMS 04049, which has the most radiogenic measured Os isotopic composition of all samples ($^{187}Os/^{188}Os = 0.8147$), and a mixing line between this sample and a CI chondrite initial may explain the Os isotope compositions of non-pristine eucrite samples. Similar mixing trajectories have been used previously for lunar crustal and mare basalt samples to explore the degree of impact contamination in samples (Day et al., 2010; Day & Walker, 2015). The intermediate and high Ni content samples generally approach the chondritic $^{187}Os/^{188}Os$ value and exhibit higher Os abundances (>100 pg/g) than pristine and low Ni samples, confirming an impact contamination signature.

Measured $^{187}Re/^{188}Os$ ratios are highly variable in the studied eucrites and span several orders of magnitude (**Figure 3.5**). They deviate strongly from the 4.56 Ga iron meteorite reference isochron (Smoliar et al.,1996), which is not expected given the very early crystallization ages of the eucrites. These elevated $^{187}Re/^{188}Os$ values indicate open-system behavior. The Re* value, which is a calculation based on a chondritic $^{187}Os/^{188}Os$ at the time of crystallization, are similar to, but not equivalent to the measured Re concentrations. This result is strongly indicative of open-system behavior, either through mobilization of Re or Os, or through neutron fluence effects (e.g., Day et al., 2010).

3.3.3 Impact Contamination Effects

Nickel concentrations, which are elevated in impact contaminated materials, provide an important baseline for interpreting the HSE concentrations and Os isotope ratios. A further advantage to this analysis is that samples with similar HSE relative abundances group together, and may indicate shared mechanisms of metal-silicate differentiation and/or impact addition. This section highlights the unique aspects of eucrite samples with similar Ni concentrations, and therefore comparable levels of pristinity or impact contamination.

The very low [Ni] samples, except for PCA 91245, show relative depletions in Os and Ir (**Figure 3.3a**). The meteorites, QUE 97014, PCA 91245 and GRO 95533, have Pd depletions while EET 90020 and NWA 5356 exhibit Pd enrichments. The replicate of NWA 5356 shows a strong Ir depletion and a small Pd enrichment not observed in the initial analysis, and probably reflects heterogeneity in metal phases in the sample. Pecora Escarpment (PCA) 91245 also exhibits a depletion in Ru, which is also observed in some of the low [Ni] samples, NWA 2362, NWA 2362 (rep) and NWA 1000 (**Figure 3.3b**).

The low [Ni] samples in **Figure 3.3b** show similar trends with Ir/Os ratios > 1 and Pd relative depletions in most samples. Pasamonte and NWA 1918 do not show marked fractionation between Os and Ir. Enrichments in Pt (mainly relative to Pd) are observed in all samples except Pasamonte and Bereba. The low [Ni] samples in **Figure 3.3b** have more variable trends, most notably a strong Os enrichment in NWA 1923. Both analyses of NWA 5617 exhibit the highest HSE concentrations, an Ir/Os ratio ~1 and Pt depletions, but variable Pd and Re trends that probably reflect sample heterogeneity. Except for Os and Re, NWA 1923 and Millbillillie show limited fractionation in the other HSE, and may therefore reflect a limited chondritic component.

The intermediate [Ni] samples and one aliquot of NWA 5601 (rep) are shown in **Figure 3.4a**, including those with 'incomplete' HSE data (NWA 1666, rep), and two diogenite samples from a prior study (MET 00424, NWA 1877; Day et al., 2012). There are strong Os depletions for low concentration samples (Juvinas and SaU 562, rep), but the overall fractionation between Ir and Os is less marked compared to samples with lower Ni concentrations. Ru is depleted in NWA 1666 (rep) and NWA 5601 and enriched in NWA 1666 and SaU 562 (rep). Both analyses of SaU 562 exhibit Pt depletions while Juvinas and NWA 5601 show Pt enrichments. The differences in HSE abundances observed between aliquots for SaU 562 and NWA 1666 indicate sample heterogeneity.

The HSE data for howardite, Kapoeta, and eucrite samples with high Ni content (>8 ppm; except for NWA 5601 (rep)), are presented in **Figure 3.4b**. The brecciated eucrite, GRO 06059, and Kapoeta aliquots are included as a point of comparison for samples that have definitively witnessed impact addition. A chondritic component is evident in the relatively unfractionated HSE patterns for these high [Ni] samples. A single analysis of NWA 5601, and both analyses of NWA 5232, show similar patterns (assuming the missing Pd abundances are similar to the other HSE), and likely reflect a late accretion component that overprinted primary HSE abundances and fractionation patterns.

The two digestions of NWA 5601 (**Figure 3.4a,b**) are useful points of comparison because they yield both chondritic relative abundances (NWA 5601) and visible fractionations among the HSE (NWA 5601, rep). Such sample heterogeneity supports incomplete mixing of late accretion impactors to the HED parent body, where NWA 5601 (rep) experienced partial impact addition, but retained a Pt enrichment that may reflect a primary feature of metal-silicate segregation. The eucrite samples in **Figure 3.6** therefore represent a continuum of late accretion, in which incomplete mixing with a chondritic component may result in HSE fractionation patterns that reflect both the primary mantle signature and impact contamination.

3.4 Discussion

3.4.1 Eucrite Pristinity

Herein, we focus on two geochemical indicators of impact contamination that can be used to ascertain eucrite 'pristinity': low Ni and low absolute HSE abundances. The Ni concentration in eucrite samples is valuable as a 'first-order' criterion of impact contamination, and is easier to quantify in samples since it exhibits higher abundances (Ni ~ ppm versus HSE ~ ppb). In this context, we argue that samples with both the lowest [Ni] concentrations and the lowest HSE abundances are perhaps the most pristine and represent primitive HED mantle signatures of metal-silicate differentiation.

Under these criteria, the following eucrites, which have < 1 ppm Ni and < 10 ppt Os, are pristine: CMS 04049, Bouvante, QUE 97014, GRO 95533, NWA 5356 and BTN 00300. Additional pristine samples include LEW 85305 and QUE 97053, which have < 10 ppt Os, but exhibit slightly higher Ni contents (1 < [Ni] <1.5 ppm). The very elevated

HSE abundances in ‘unbrecciated’ eucrites, PCA 82502, EET 90020 and SaU 562, suggest that these samples have witnessed impact addition and therefore do not represent primary signatures of the HED parent body. The Ni concentration criterion of < 1 ppm for ‘pristine’ eucrites differs from Ni concentrations previously measured in pristine, unbrecciated and cumulate eucrites and defined as ~3 ± 3 ppm (Warren et al., 2009).

Eucrites with intermediate characteristics between ‘pristine’ (<1 ppm Ni) and high Ni (>10 ppm) samples, include NWA 1918, Millbillillie and ALHA 81001, which have [Os] ~10 ppt and [Ni] < 2 ppm. These samples may also be pristine, or subject to minimal impact addition, especially based on prior definitions (Warren et al., 2009). Similar reasoning can be applied to Stannern and Bereba, which have < 10 ppt Os and Ni content between 2 and 3 ppm. Northwest Africa (NWA) 1000, NWA 1836 and GRA 98098 have Os concentrations < 50 ppt, as well as low Ni content, < 5 ppm, again indicating minimal disturbance from impact addition. The eucrite samples with Os concentrations between 50 and 500 ppt have likely witnessed impact addition and consist of Agoult, Pasamonte, one aliquot of NWA 1923 ([Os] ~193 ppt) and NWA 2362 (average [Os] ~ 81 ppt, n = 2). Two separate aliquots of Juvinas were measured in this study, and indicate marked sample heterogeneity, likely due to inhomogeneous impactor contamination, because the aliquot with low Ni content showed high Os concentrations, and the sample with high [Ni] had a low Os abundance. The remainder of the eucrite samples show Os concentrations > 1 ppb, which are comparable to the brecciated eucrite, GRO 06059, and howardite, Kapoeta, and therefore indicative of significant impact addition.

The variability in HSE patterns among the eucrite samples with intermediate [Ni] is like the data for the diogenite samples with low HSE concentrations, which may, at least partially, reflect primary HSE signatures from metal-silicate partitioning during core-formation (Day et al., 2012). They suggest that the contributions from impact material, either concurrent with or after core-formation, may be variable and subject to localized mixing, in the absence of a long-lived magma ocean (Day et al., 2012). This heterogeneity is also evident on a smaller scale in the Juvinas meteorite, which likely results from incomplete mixing of impactor material with the bulk rock, and may be observed in other eucrite samples over multiple analyses. Given the size of the HED parent body and potentially limited mixing within a short-lived magma ocean, several repeat measurements on pristine eucrites are needed to ascertain primary HED mantle signatures.

3.4.2 Open-system behavior of Re and/or Os

Measurements of ^{187}Re/^{188}Os in eucrite samples exhibit significant variability and are similar to the dispersion of Re-Os isotope signatures observed in a recent study on lunar mare basalt samples (Day and Walker, 2015). In a plot of ^{187}Re/^{188}Os versus ^{187}Os/^{188}Os (**Figure 3.5**), the majority of eucrites with non-chondritic ^{187}Os/^{188}Os ratios plot away from the 4.56 Ga isochron (Smoliar et al., 1996) and several samples trend toward younger apparent ages, as indicated by the 3 Ga, 50 Ma and 10 Ma reference isochrones. This includes a number of samples with < 5 ppm Ni and radiogenic Os-isotope ratios. The Re concentrations in eucrites (ppt level) are comparable to lunar mare basalts, and these low abundances lead to these samples being particularly susceptible to contamination (Day and Walker, 2015). The mobilization of Re (or possibly Os) is considered to have occurred after crystallization of the eucrite samples, as indicated by the younger apparent ages. This may result from neturon fluence from cosmic ray exposure (e.g., Walker, 2012), or weathering of sulfides and metal phases, as observed for lunar meteorites and diogenites (Day and Walker, 2015; Day et al., 2012). The eucrite samples may also have been subject to Os loss, but this is difficult to determine given the fractionated Ir/Os ratios; in most other cases, unfractionated Ir/Os ratios are typically used as indicators of limited mobilization of Os for mafic rocks (Day 2013). The Os/Ir ratios of eucrites are clearly not the result of mobilization, as low Os/Ir occurs across a range of samples with variable ^{187}Os/^{188}Os, so such criterion cannot be used in this instance.

3.4.3 Metal-Silicate Differentiation and Chondrite Mixing

The Os isotope ratios measured in eucrite samples supports a continuum of mixing between chondritic and primary, HED mantle components, as suggested by the HSE relative abundances. This is evident in **Figure 3.6**, where many pristine samples and some low Ni samples exhibit variable and radiogenic ^{187}Os/^{188}Os signatures. Samples with ^{187}Os/^{188}Os values > ~0.2 and low Os concentrations (1 - 10 ppt) likely reflect primary mantle differentiation signatures on the HED parent body and the isotopic variability among these samples may reflect heterogeneous melting and differentiation within the HED parent body. In many respects, these data are analogous to variations seen in some lunar crustal rocks (Day et al., 2010).

The majority of intermediate and high Ni concentration samples, as well as several low Ni samples, exhibit Os isotope ratios that are close to the chondrite value of ^{187}Os/^{188}Os = 0.1270 (Shirey and Walker, 1998). This comparison between Ni and Os concentrations is a more sensitive indicator of impact contamination than previous analyses of Ni and Ir (Warren et al., 2009), because of the strong Ir/Os fractionation that is observed in this study and Dale et al. (2012) and Day et al. (2012), and the lower absolute Os content measured in eucrite samples. Within a limited range of Os isotope ratios, the eucrites exhibit a wide range of Os concentrations (1 to 10,000 pg/g). This can be explained by differential amounts of chondritic impactor contamination, as even minimal addition of this component can compromise the primary Os isotope signatures of the eucrites. The Os isotope ratios are therefore extremely sensitive indicators of impact addition, and reflect this process even for samples with low concentrations, ~10 pg/g Os. This may be the case for two pristine sample, GRO 95533 and NWA 5356, which have ^{187}Os/^{188}Os = 0.1378 and ^{187}Os/^{188}Os = 0.1398, respectively. While these samples exhibit radiogenic Os isotope ratios (> 0.1270), they contrast with the higher values observed for other pristine samples, with ^{187}Os/^{188}Os ~ 0.2 to 0.4. This may be explained by mixing with limited amounts (<0.01% by mass) of chondrite component, as suggested by the proximity of these samples to the mixing line. An alternative explanation may be that heterogeneous melting and differentiation on the HED parent body led to a large range of primary, radiogenic ^{187}Os/^{188}Os signatures, which may have resulted from local differences in temperature, sulfide content and oxidation state and consequent fractionation of Re/Os.

3.4.4 Metal-Silicate Differentiation on the HED Parent Body

The CI chondrite normalized HSE abundances for eucrites classified as ‘pristine’ are presented in **Figure 3.7**, and can be considered to be ‘primary’ mantle signatures of the HED parent body. The most notable feature of the HSE abundances and inter-element fractionations in pristine eucrites are Ir/Os ratios >>1. In these samples, Ir abundances are greater than Os by a factor of ~10^2, and are in the range of the other HSE (Ru, Pt, Pd, Re). There is also a strong relation between the Pt/Os and Ir/Os ratios (**Figure 3.8**) across the entire sample set, which suggests that this inter-element fractionation is a result of underlying partitioning mechanisms and a real effect. Elevated Pt/Os ratios have also been observed for planetary materials, including the HED meterorites, with little to no chondritic component, and have been interpreted to reflect the greater incompatibility of Pt and its consequent enrichment in mantle melts (Dale et al., 2012). The pristine eucrites in this study exhibit higher Pt/Os ratios, from ~ 10^2 to 10^3, which extends the range of these ratios (c.f. Dale et al., 2012) and further reflects the more primitive nature of these samples. There is also a strong correlation between Pt/Os and Ir/Os ratios, and samples with higher Ni content trend toward chondritic values and ratios of unity, indicating a dilution effect with greater impact addition.

The strong depletion in Os can generally be explained by its preferential extraction into metal phases during core formation compared to the other HSE. Such effects are apparent in estimates of Pt/Os ratios up to 10^4 at IW -1 (Brenan et al., 2016), which reflects the low oxygen fugacity of the HED parent body. Although Ir and Os are considered to behave similarly during metal-silicate differentiation, there are some differences in their partitioning behavior under low oxygen and low pressure conditions. While these partitioning data are somewhat limited because of possible metal contamination of experiments at reducing conditions, they indicate a slight difference in valence state of Ir (1+) versus Os (mixture of 1 + and 2+ species; Brenan et al., 2016). This demonstrates the need for examining natural experiments of metal-silicate partitioning, such as that represented by the pristine eucrite samples, given the current analytical limitations. Given the persistence of the Ir/Os fractionation among the eucrite samples measured, as well as agreement with previous studies on HED meteorites (Dale et al., 2012; Day et al., 2012), this signature is suggestive of unique Os and Ir partitioning behavior under low mass, low oxygen fugacity conditions.

3.4.5 Heterogenous Melting and Incomplete Mixing

The HSE relative abundances for the pristine eucrite samples exhibit two general trends in partition of Ru and Pd. The majority of samples show depletions in these elements, but some show slight enrichments or even negligible fractionation from the other HSE. While Ru and Pd compatibility is less than that of Os (Day et al., 2016) these somewhat complementary patterns are indicative of unique primary reservoirs on the HED parent body. This is evident in **Figure 3.3**, where the very low and low Ni eucrites exhibit similar, but different HSE fractionation patterns. This may indicate two modes of primary, distinct metal-silicate partitioning behavior on the HED parent body, one that results in slightly higher Ni contents (up to 5 ppm) in the silicate mantle. A scenario of heterogeneous differentiation and incomplete mixing on the HED parent body can be explained by the small size of this planetesimal that may have experienced a short-lived magma ocean event (Righter & Drake, 1997; Mandler et al., 2013).

3.4.6 Timing of Late Accretion to the HED parent body

The HSE data in this study are characterized by relatively low concentrations and a range of fractionation patterns, including two distinct trends in pristine and low Ni eucrites, as well as chondritic additions to less pristine samples. An important trend in this data is the continuum of late accretion represented by the range of HSE relative abundances in eucrites, evident in **Figures 3.3** and **3.4**. This supports previous conclusions of late accretion to the HED parent body based on HSE and Os isotope measurements in diogenites (Day et al., 2012), namely that late accretion in the early Solar System may have been concomitant with the very early crystallization ages of these samples. Among samples with higher Ni and Os concentrations, there are few that exhibit straightforward chondritic HSE relative abundances. Particularly the variability in Pt and Pd enrichments and depletions could be explained by a late-accretion component, for which less compatible HSE were sometimes incorporated into the silicate mantle. The elevated Ir/Os ratios that are evident even in samples with intermediate Ni may similarly be explained by Os more readily partitioning into segregating metal during differentiation on the HED parent body.

3.5 Conclusions

The new dataset presented herein shows for the first time a rigorous chemical definition for ‘pristinity’ in the unbrecciated eucrites, specifically < 1 ppm Ni and < 10 ppt Os. The first step in this study was to use abundances of Ni to determine the least impact contaminated eucrites. Combined with HSE abundance and Os isotope ratio measurements, these samples reveal unique Ir/Os ratios in HED mantle material, up to Ir/Os ~10^2 by order or magnitude. The Os depletions may represent unique HSE fractionations on low-mass, reduced planetesimals. The data also exhibit a range of absolute and relative HSE abundances, from the most primitive to the most impact contaminated, and support previous suggestions of concurrent late accretion and crystallization on the HED parent body (Day et al., 2012). The pristine eucrite samples are valuable for ascertaining the metal-silicate and late-accretion histories of the HED parent body, and may be further analyzed for planetary evolution signatures such as volatile inventories.

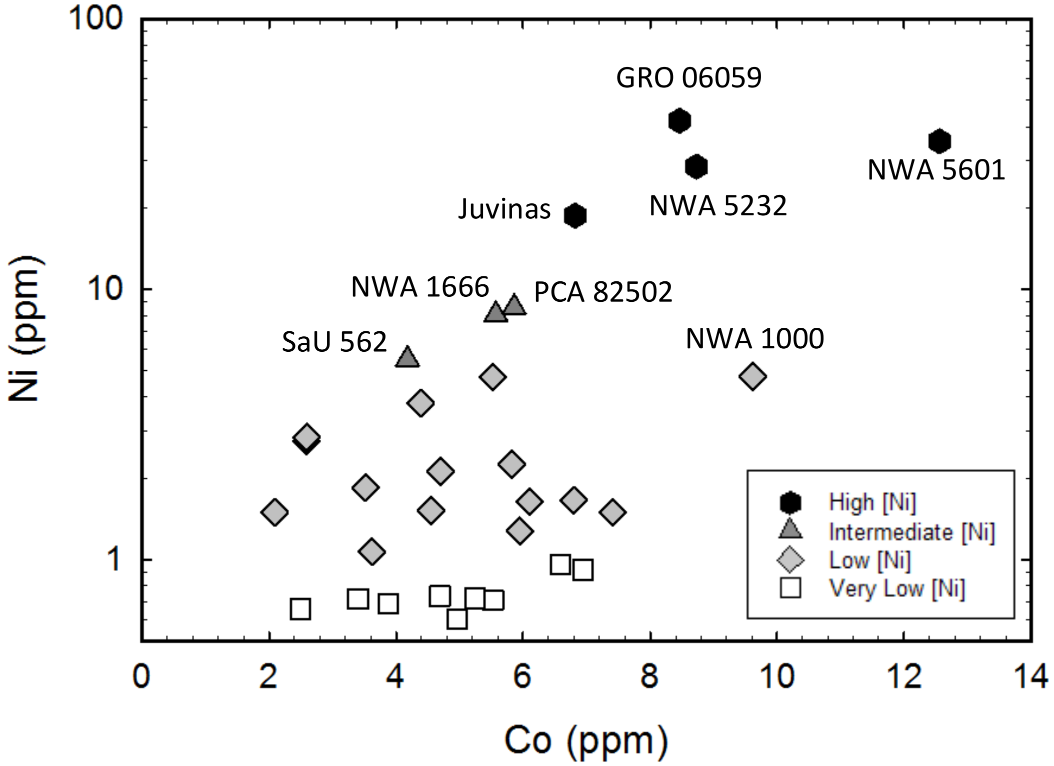

Figure 3.1: Nickel versus Co concentrations for eucrite samples investigated in this study. Samples with Ni concentrations > 8 ppm are considered to reflect impact addition, consistent with petrographic evidence (e.g., Dhaliwal & Day, 2014).

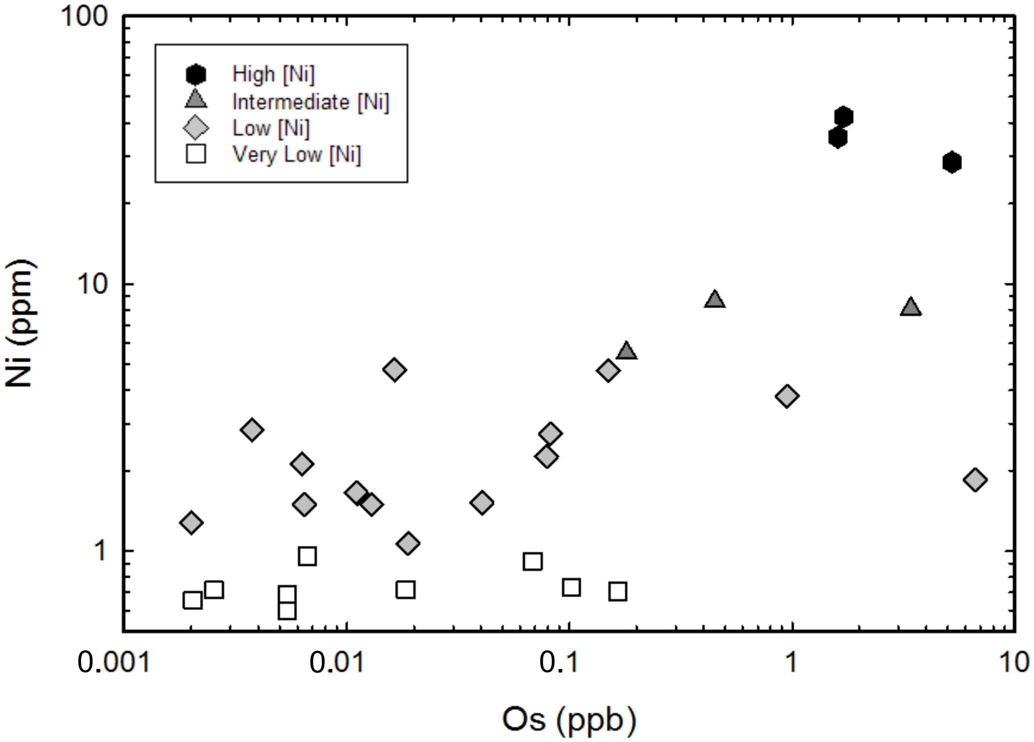

Figure 3.2: Nickel versus Os concentrations for eucrite samples in this study. There is a relationship between increasing Ni and Os content on a logarithmic scale; the linear r^2 = ~0.3.

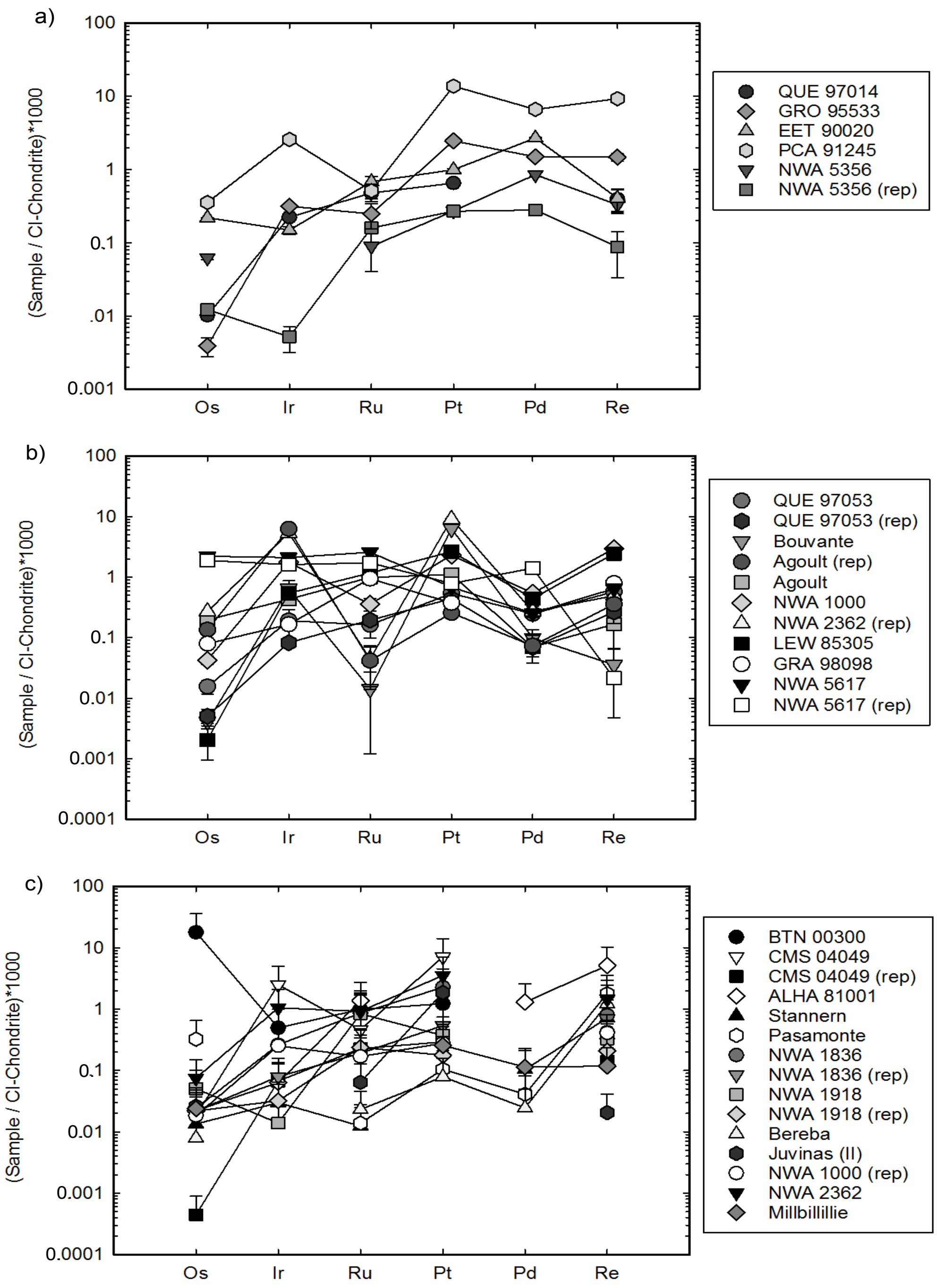

Figure 3.3: HSE relative abundances for eucrite samples with (a) very low Ni concentrations, (b) low Ni concentrations and (c) very low and low Ni content for which abundance data could not be obtained for one or more of the HSE due to relatively high blank to sample ratios and limits of detection. The data are normalized to CI-chondrite (Horan et al., 2003).

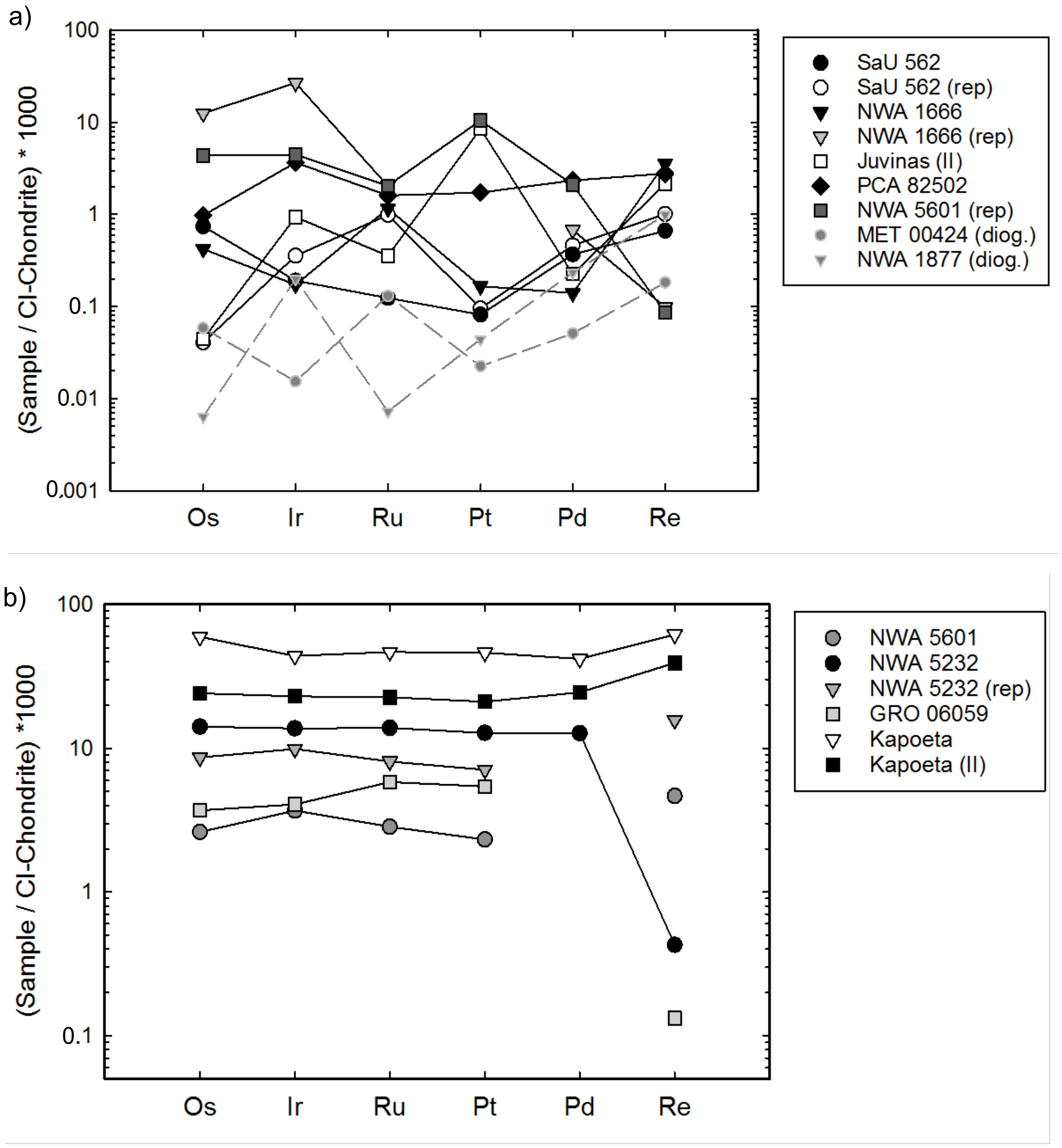

Figure 3.4: Second set of HSE relative abundances for eucrite samples with (a) intermediate Ni content and (b) high Ni content; data for two diogenites with low HSE concentrations from Day et al. (2012) are included in (a). Uncertainties on the measurements are smaller than the plotted symbols. The data are normalized to CI-chondrite (Horan et al., 2003).

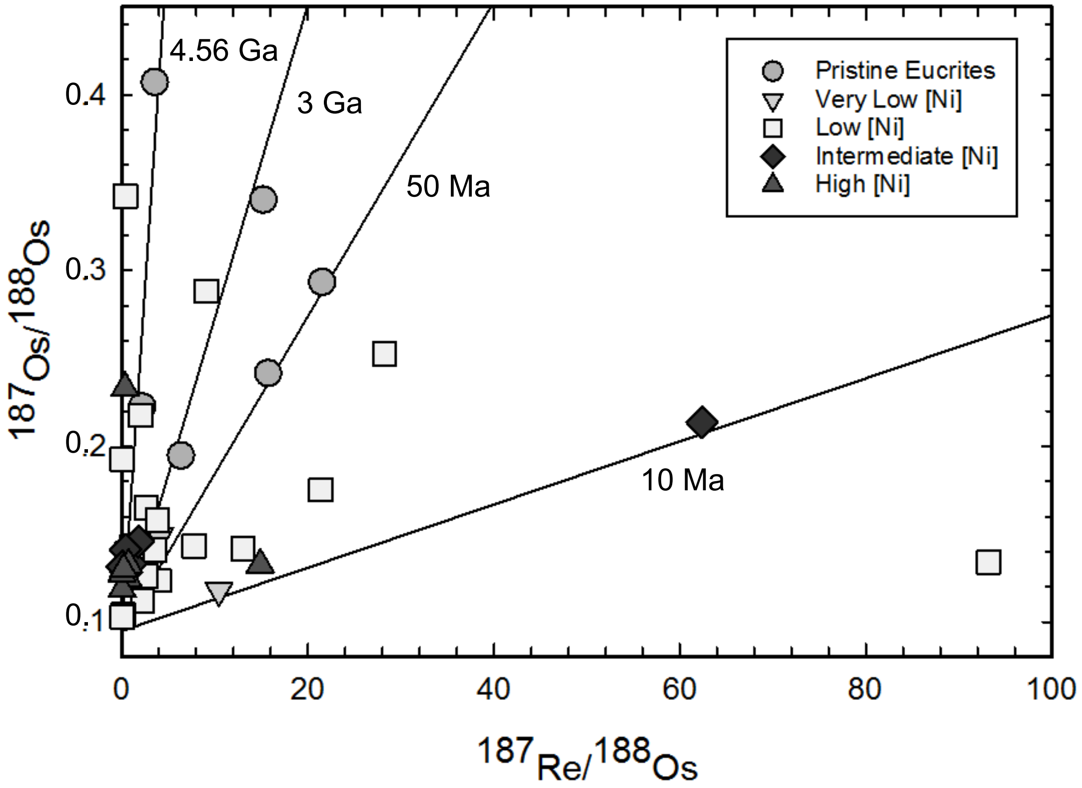

Figure 3.5: ^{187}Re/^{188}Os versus ^{187}Os/^{188}Os for eucrite samples show strong deviation from the 4.56 Ga isochron (Smoliar et al., 1996), with comparative lines for 1 Ga, 50 Ma and 10 Ma isochrons. The apparent young ages of these samples indicates significant disturbance and open system behavior of Re-Os isotope systematics in some samples.

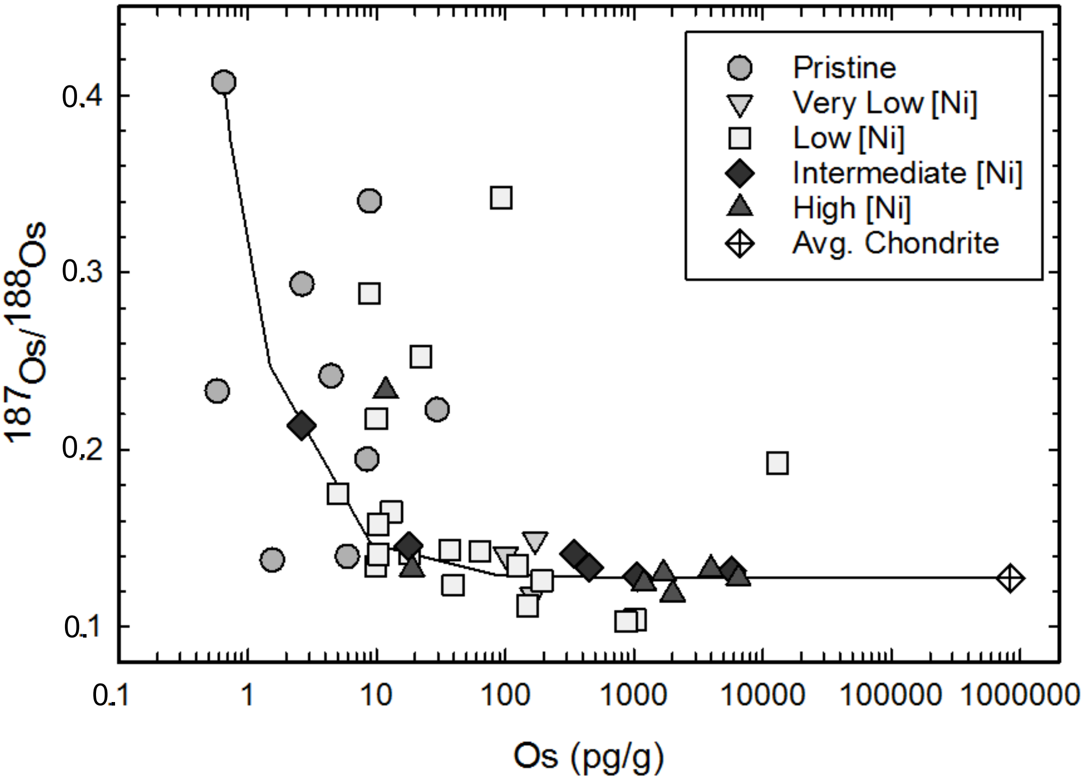

Figure 3.6: Osmium isotope ratios versus Os concentrations for eucrite samples, categorized according to their Ni content. The curve shows mixing between the most radiogenic eucrite sample on the plot (LEW 85305: $^{187}Os/^{188}Os = 0.4275$; Os= 0.934 pg g^{-1}), and an average chondrite composition ($^{187}Os/^{188}Os = 0.1275$; Os = 840,000 pg g^{-1}) and indicates impact contamination for several eucrite samples. Chondrite value is from Horan et al. (2003).

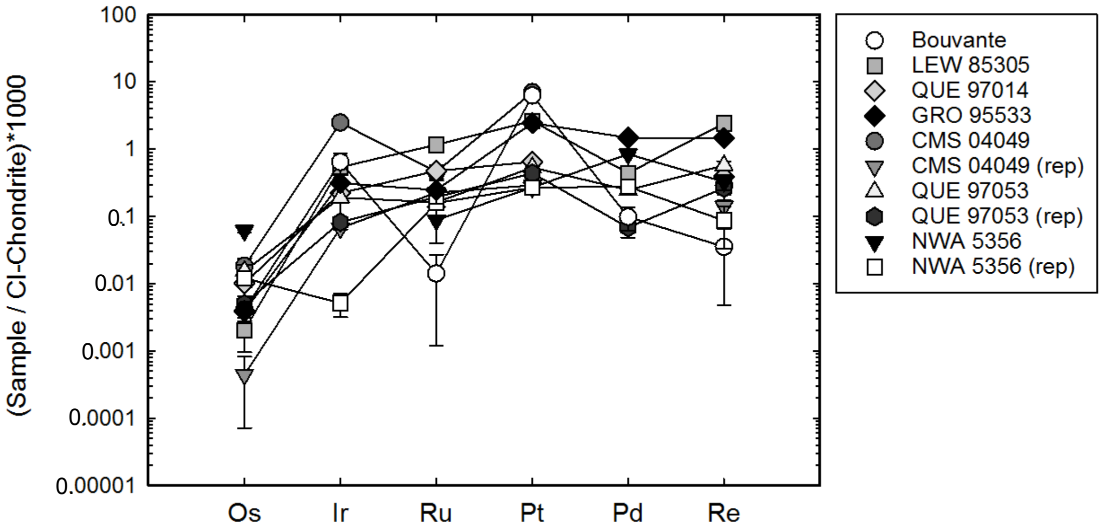

Figure 3.7: HSE relative abundances for the subset of pristine eucrites, considered to generally represent primary signatures of the HED parent body. The data are normalized to CI-chondrite (Horan et al., 2003).

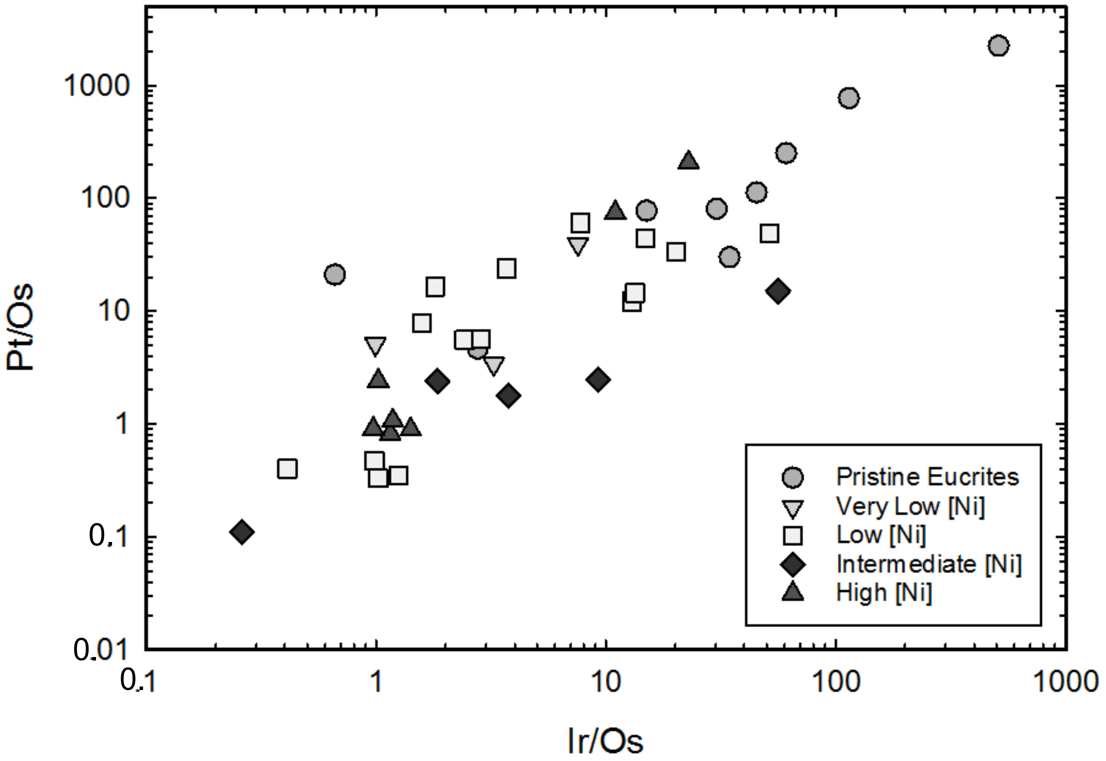

Figure 3.8: Pt/Os versus Ir/OS in eucrite samples show that those with lower Ni content, and therefore less impact contamination, trend toward higher values. This reflects primitive HSE partitioning mechanisms on the HED parent body; high Pt/Os ratios in eucrites are also reported by Dale et al., 2012 but they did not report Ni abundance data.

Table 3.1: Ni and Co abundances in eucrite meteorites (in ppm)

Sample ID	Co	Ni
ALHA 81001	6.80	1.66
BTN 00300	6.59	0.96
CMS 04049	4.96	0.60
EET 90020	4.69	0.73
GRA 98098	4.55	1.52
GRO 95533	3.40	0.72
LEW 85305	5.95	1.28
PCA 82502	5.86	8.59
PCA 91245	5.53	0.71
QUE 97014	3.88	0.69
QUE 97053	2.09	1.49
GRO 06059	8.46	42.08
NWA 1000	9.62	4.76
NWA 1666	5.57	8.08
NWA 1836	7.41	1.50
NWA 1918	3.62	1.07
NWA 1923	3.52	1.84
NWA 2362	2.59	2.75
NWA 5232	8.73	28.50
NWA 5356	5.24	0.72
NWA 5601	12.56	35.30
NWA 5617	4.39	3.79
Agoult	5.82	2.26
Bereba	2.59	2.84
Bouvante	2.49	0.65
Juvinas	6.82	18.75
Juvinas (rep)	6.94	0.92
Millbillillie	6.10	1.64
Oman	4.18	5.51
Pasamonte	5.52	4.73
Stannern	4.70	2.12

Table 3.2 Re-Os isotope and HSE abundance data (in ppb) for eucrite meteorites

Sample	Mass (g)	Sample ID	Re*	Re	±	Os	±	Ir	±	Ru	±	Pt	±	Pd	±	^{187}Re/^{188}Os	±2σ	^{187}Os/^{188}Os	±2σ	GOs[1]	Digestion
Unbrecciated Eucrites																					
ALHA 81001	0.259	JK 15-2	0.002	0.196	0.007	0.010	0.001	0.03	0.007	0.87	0.085			0.74	0.036	93.202	0.039	0.15000	0.00377	-7599	CT
BTN 00300	0.251	JK11-2	2.155	0.016	0.002	8.234	0.004	0.21	0.005	0.63	0.059	1.07	0.024			0.009	0.247	0.18540	0.01064	92	CT
CMS 04049	0.275	JK11-3	0.002	0.011	0.002	0.008	0.003	1.08	0.005	0.30	0.053	6.17	0.024			6.327	0.002	0.18881	0.00697	-423	CT
CMS 04049	0.936	JK 14-3	0.000	0.005	0.003	0.000	0.000	0.03	0.001	0.15	0.011	0.26	0.001			138.592	0.001	0.81468	0.00683	-10636	HPA
EET 90020	0.295	JK 15-3	0.014	0.015	0.005	0.101	0.001	0.06	0.008	0.43	0.077	0.87	0.031	1.54	0.036	0.737	0.004	0.14218	0.00273	-13	CT
GRA 98098	0.272	JK11-4	0.003	0.030	0.002	0.037	0.003	0.07	0.005	0.60	0.059	0.33	0.023			3.978	0.006	0.12414	0.00093	-298	CT
LEW 85305	0.201	JK 15-6	0.001	0.093	0.007	0.001	0.001	0.23	0.009	0.75	0.084	2.30	0.032	0.25	0.033	497.363	0.019	0.42752	0.00669	-40504	CT
PCA 82502	0.221	JK 9-2	0.047	0.087	0.004	0.446	0.004	1.19	0.080	0.72	0.062	1.45	0.014	1.24	0.022	0.946	0.022	0.13216	0.00019	-40	CT
PCA 91245	0.202	JK 15-7	0.011	0.354	0.008	0.164	0.001	1.11	0.009	0.33	0.073	12.04	0.032	3.78	0.037	10.418	0.071	0.11935	0.00124	-832	CT
QUE 97014	0.299	JK 15-5	0.002	0.015	0.005	0.005	0.001	0.10	0.008	0.30	0.072	0.57	0.031			15.702	0.003	0.26696	0.00314	-1112	CT
QUE 97053	0.420	JK 9-3	0.005	0.022	0.003	0.007	0.002	0.08	0.042	0.10	0.041	0.47	0.014	0.14	0.019	15.187	0.004	0.34662	0.00974	-987	CT
QUE 97053	0.970	JK 14-2	0.001	0.010	0.004	0.002	0.001	0.04	0.001	0.12	0.011	0.39	0.001	0.04	0.012	21.510	0.002	0.29071	0.00730	-1564	HPA
SaU 562	0.303	JK 13-6	0.003	0.006	0.004	0.015	0.003	0.09	0.016	0.59	0.013	0.05	0.008	0.20	0.017	1.750	0.001	0.16080	0.00180	-77	CT
SaU 562	0.907	JK 16-8	0.045	0.024	0.001	0.341	0.001	0.02	0.017	0.02	0.015	0.02	0.015	0.17	0.032	0.343	0.011	0.14120	0.00160	19	CT
Monomict Eucrites																					
Bereba	0.606	JK 10-5	0.001	0.047	0.007	0.004	0.000			0.01	0.013	0.07	0.003	0.01	0.010	62.383	0.009	0.19767	0.00155	-5018	HPA
Bouvante	0.501	JK 10-7	0.001	0.001	0.001	0.002	0.000	0.28	0.095	0.01	0.008	5.51	0.004	0.06	0.021	3.504	0.000	0.24163	0.00275	-137	HPA
Juvinas	0.306	JK 13-8	0.027	0.141	0.009	0.169	0.003	0.46	0.018	0.65	0.013	1.07	0.010			4.054	0.029	0.15047	0.00124	-276	CT
Juvinas (II)	0.396	JK 8-2	0.005	0.001	0.001	0.012	0.000			0.04	0.029	1.63	0.014			0.316	0.000	0.23466	0.00790	118	CT
Juvinas (II)	0.448	JK 10-2	0.002	0.062	0.008	0.020	0.000	0.08	0.052	0.01	0.007	7.42	0.004	0.05	0.021	14.852	0.012	0.13437	0.00142	-1180	HPA
Millbillillie	0.613	JK 10-6	0.004	0.005	0.003	0.011	0.000					0.22	0.004	0.06	0.022	1.992	0.001	0.21193	0.00203	-43	HPA
Stannern	0.554	JK 10-4	0.001	0.027	0.007	0.006	0.000	0.01	0.012	0.01	0.007			0.06	0.021	21.371	0.005	0.17177	0.00106	-1677	HPA
Polymict Eucrites																					
NWA 1666	0.296	JK 13-2	0.102	0.099	0.009	1.061	0.003	1.78	0.019	1.76	0.013	4.82	0.010	0.33	0.018	0.448	0.037	0.12857	0.00010	-3	CT
NWA 1666	0.506	JK 16-4	0.605	0.002	0.001	5.761	0.002	1.05	0.050	1.19	0.050	1.19	0.042	0.31	0.035	0.001	0.173	0.13170	0.00141	37	CT
NWA 5601	0.301	JK 8-4	0.101	0.160	0.005	1.202	0.001	1.37	0.061	1.50	0.089	1.98	0.014	1.26	0.046	0.642	0.048	0.12465	0.00009	-23	CT
NWA 5601	0.705	JK 16-2	0.133	0.002	0.001	2.009	0.001	1.84	0.051	1.24	0.050	9.11	0.043	1.15	0.038	0.004	0.060	0.11859	0.00030	23	CT
Pasamonte	0.508	JK 10-3	0.007	0.068	0.008	0.150	0.000			0.01	0.008	0.09	0.003	0.02	0.014	2.192	0.014	0.11227	0.00011	-163	HPA
Anomalous Eucrites																					
NWA 5232	0.204	JK 8-5	0.428	0.572	0.005	3.971	0.001	3.95	0.063	4.69	0.092	6.11	0.014	2.16	0.047	0.695	0.165	0.13266	0.00011	-19	CT
NWA 5232	0.608	Jk 16-3	0.604	0.015	0.001	6.503	0.002	5.82	0.052	8.73	0.052	11.09	0.043	7.20	0.039	0.011	0.195	0.12761	0.00017	32	CT
Eucrites																					
Agoult	0.306	JK 13-4	0.066	0.006	0.004	0.091	0.003	0.19	0.017	0.63	0.013	0.97	0.010	0.04	0.013	0.348	0.003	0.34993	0.05528	235	CT
Agoult	0.707	JK 16-6	0.009	0.014	0.001	0.062	0.001	2.70	0.051	0.03	0.018	0.22	0.036	0.04	0.020	1.061	0.003	0.14352	0.00208	-38	CT
NWA 1000	0.280	JK 9-4	0.008	0.113	0.004	0.020	0.003	0.76	0.077	0.23	0.052	2.02	0.014	0.31	0.021	28.218	0.023	0.24455	0.00312	-2163	CT
NWA 1000	0.992	JK 14-4	0.005	0.016	0.004	0.008	0.001	0.11	0.001	0.11	0.010	0.24	0.001			9.062	0.003	0.28728	0.05623	-546	HPA
NWA 1836	0.284	JK11-7	0.002	0.030	0.002	0.011	0.003	0.11	0.005	0.55	0.058	1.98	0.024			12.994	0.006	0.14724	0.00116	-1014	CT
NWA 1836	0.975	JK 14-7	0.001	0.007	0.003	0.010	0.001	0.03	0.001	0.12	0.011	0.47	0.001			3.554	0.002	0.13566	0.00071	-251	HPA
NWA 1918	0.301	JK11-6	0.005	0.012	0.002	0.023	0.003	0.01	0.003	0.54	0.058	0.33	0.023			2.589	0.003	0.16998	0.00309	-136	CT
NWA 1918	0.955	JK 14-6	0.002	0.008	0.003	0.010	0.001	0.01	0.001	0.15	0.011	0.15	0.001			3.814	0.002	0.15303	0.00161	-254	HPA
NWA 1923	0.298	JK 13-3	0.017	0.103	0.009	0.191	0.003	0.01	0.007	0.70	0.013	0.11	0.009	0.02	0.009	2.586	0.021	0.12712	0.00061	-180	CT
NWA 1923	0.807	JK 16-5	3.697	0.044	0.001	13.108	0.001	0.10	0.035	0.06	0.028	0.06	0.024	0.05	0.021	0.016	0.393	0.19242	0.00368	99	CT
NWA 2362	0.308	JK 13-7	0.005	0.056	0.008	0.035	0.003	0.45	0.018	0.59	0.013	3.09	0.010			7.754	0.011	0.14966	0.00086	-581	CT
NWA 2362	0.907	JK 16-9	0.014	0.019	0.001	0.125	0.001	2.32	0.051	0.03	0.018	7.97	0.043	0.16	0.031	0.729	0.005	0.13485	0.00188	-20	CT
NWA 5356	0.604	JK 9-6	0.010	0.013	0.003	0.028	0.002			0.06	0.031	0.24	0.013	0.48	0.021	2.162	0.003	0.21879	0.00583	-50	CT
NWA 5356	0.974	JK 14-5	0.001	0.003	0.002	0.006	0.001	0.00	0.001	0.10	0.010	0.24	0.001	0.16	0.015	2.863	0.001	0.13008	0.00134	-200	HPA
NWA 5617	0.302	JK 13-5	0.024	0.025	0.007	1.021	0.003	0.91	0.018	1.65	0.013	0.60	0.010	0.15	0.016	0.116	0.031	0.10424	0.00016	-1	CT
NWA 5617	0.508	JK 16-7	0.018	0.001	0.000	0.871	0.002	0.70	0.049	1.10	0.050	0.69	0.041	0.80	0.037	0.004	0.026	0.10305	0.00024	7	CT
Brecciated Eucrites																					
GRO 06059	0.303	JK 8-3	0.171	0.058	0.005	1.700	0.001	1.66	0.061	2.20	0.090	3.40	0.014	2.01	0.047	0.165	0.052	0.13022	0.00011	22	CT
GRO 95533	0.294	JK 15-4	0.001	0.056	0.007	0.002	0.001	0.14	0.008	0.16	0.059	2.15	0.032	0.85	0.036	152.357	0.011	0.21780	0.00557	-12387	CT
Howardite																					
Kapoeta	0.109	JK 8-6	2.454	2.304	0.005	27.384	0.001	18.32	0.063	28.90	0.094	40.22	0.014	23.91	0.048	0.406	0.942	0.12647	0.00011	-2	CT
Kapoeta (II)	0.109	JK 8-7	1.064	1.446	0.005	11.079	0.001	9.31	0.063	13.54	0.094	18.25	0.014	12.92	0.048	0.629	0.441	0.12867	0.00010	-18	CT

[1] DOs (after Fischer-Godde et al. 2010) refers to the combined deviation in the determined ^{187}Os/^{188}Os and ^{187}Re/^{188}Os for a given chondrite sample from the IIIA iron meteorite reference isochron, DOs = 10^4 (^{187}Os/^{188}Os$_{chondrite}$ (0.09524 + 0.07887 × ^{187}Re/^{188}Os$_{chondrite}$)), ^{187}Os/^{188}Os$_{chondrite}$ and ^{187}Re/^{188}Os$_{chondrite}$ are the values determined for chondrites. 0.09524 is the initial ^{187}Os/^{188}Os and 0.07887 is the slope of the IIIA iron meteorite isochron (Smoliar et al., 1996).

References

Amelin, Y., (2008). U–Pb ages of angrites. *Geochimica et Cosmochimica Acta, 72,* 221–232.

Binzel, R. P. & Xu, S., (1993). Chips off of asteroid 4 Vesta: Evidence for the parent body of basaltic achondrite meteorites. *Science, 260,* 186–191.

Birck, J. L., Barman, M. R., & Capmas, F. (1997). Re-Os isotopic measurements at the femtomole level in natural samples. *Geostandards newsletter*, *21*, 19-27.

Borisov, A., & Palme, H. (1997). Experimental determination of the solubility of platinum in silicate melts. *Geochimica et Cosmochimica Acta*, *61*, 4349-4357.

Brenan, J. M., Bennett, N. R., & Zajacz, Z. (2016). Experimental results on fractionation of the highly siderophile elements (HSE) at variable pressures and temperatures during planetary and magmatic differentiation. *Reviews in Mineralogy and Geochemistry*, *81*, 1-87.

Brandon, A. D., Puchtel, I. S., Walker, R. J., Day, J. M.D., Irving, A. J., & Taylor, L. A. (2012). Evolution of the martian mantle inferred from the ^{187}Re–^{187}Os isotope and highly siderophile element abundance systematics of shergottite meteorites. *Geochimica et Cosmochimica Acta*, *76*, 206-235.

Chou, C. L. (1978). Fractionation of siderophile elements in the Earth's upper mantle. In *Lunar and Planetary Science Conference Proceedings, 9*, 219-230.

Cohen, A. S., & Waters, F. G. (1996). Separation of osmium from geological materials by solvent extraction for analysis by thermal ionisation mass spectrometry. *Analytica Chimica Acta*, *332*, 269-275.

Dale, C. W., Burton, K. W., Greenwood, R. C., Gannoun, A., Wade, J., Wood, B. J., & Pearson, D. G. (2012). Late accretion on the earliest planetesimals revealed by the highly siderophile elements. *Science, 336,* 72-75.

Day, J. M.D. , Brandon, A. D., & Walker, R. J. (2016). Highly siderophile elements in Earth, Mars, the Moon, and asteroids. *Reviews in Mineralogy and Geochemistry*, *81*, 161-238.

Day, J.M.D. , Waters, C. L., Schaefer, B. F., Walker, R. J., & Turner, S. (2016b). Use of Hydrofluoric Acid Desilicification in the Determination of Highly Siderophile Element Abundances and Re-Pt-Os Isotope Systematics in Mafic-Ultramafic Rocks. *Geostandards and Geoanalytical Research*, *40*, 49-65.

Day, J. M.D., & Walker, R. J. (2015). Highly siderophile element depletion in the Moon. *Earth and Planetary Science Letters*, *423*, 114-124.

Day, J. M.D., Walker, R. J., Qin, L., & Rumble III, D. (2012). Late accretion as a natural consequence of planetary growth. *Nature Geoscience*, *5*, 614-617.

Day, J. M. D., Walker, R. J., James, O. B., & Puchtel, I. S., (2010). Osmium isotope and highly siderophile element systematics of the lunar crust. *Earth and Planetary Science Letters, 289,* 595–605.

Day, J. M. D., Pearson, D. G., & Taylor, L. A. (2007). Highly siderophile element constraints on accretion and differentiation of the Earth-Moon system. *Science*, *315*, 217-219.

Dhaliwal, J. K, Day, J. M.D., Corder, C. A., Tait, K. T., Marti, K., Assayag, N., Cartigny, P., Rumble III, D. & Taylor, L. A. (in review). Early metal-silicate differentiation during planetesimal formation revealed by acapulcoite and lodranite meteorites.

Dhaliwal, J. K., & Day, J. M. D. (2014). Insights into the Pristinity of Unbrecciated Eucrites. In *Lunar and Planetary Science Conference*, *45,* # 2833.

Fu, R. R., Weiss, B. P., Shuster, D. L., Gattacceca, J., Grove, T. L., Suavet, C., Lima, E.A., Li, L. & Kuan, A. T. (2012). An ancient core dynamo in asteroid Vesta. *Science*, *338*, 238-241.

Greenwood, R. C., Franchi, I. A., Jambon, A., & Buchanan, P. C. (2005). Widespread magma oceans on asteroidal bodies in the early solar system. *Nature*, *435*, 916-918.

Horan, M. F., Walker, R. J., Morgan, J. W., Grossman, J. N., & Rubin, A. E. (2003). Highly siderophile elements in chondrites. *Chemical Geology*, *196*, 27-42.

Jones, J. H., & Drake, M. J. (1986). Geochemical constraints on core formation in the Earth. *Nature, 322*, 221-228.

Kimura, K., Lewis, R. S., & Anders, E. (1974). Distribution of gold and rhenium between nickel-iron and silicate melts: implications for the abundance of siderophile elements on the Earth and Moon. *Geochimica et Cosmochimica Acta*, *38*, 683-701.

Lugmair, G. & Shukolyukov, A., (1998). Early solar system timescales according to ^{53}Mn-^{53}Cr systematics. *Geochimica et Cosmochimica Acta, 62*, 2863–2886.

Mann, U., Frost, D. J., Rubie, D. C., Becker, H., & Audétat, A. (2012). Partitioning of Ru, Rh, Pd, Re, Ir and Pt between liquid metal and silicate at high pressures and high temperatures-Implications for the origin of highly siderophile element concentrations in the Earth's mantle. *Geochimica et Cosmochimica Acta*, *84*, 593-613.

McDonough, W. F., & Sun, S. S. (1995). The composition of the Earth. *Chemical Geology*, *120*, 223-253.

Mandler, B. E. & Elkins-Tanton, L. T. (2013). The origin of eucrites, diogenites, and olivine diogenites: Magma ocean crystallization and shallow magma chamber processes on Vesta. *Meteoritics & Planetary Science 48*, 2333–2349.

Mayne, R., McSween, H., McCoy, T. J., & Gale, A., (2009). Petrology of the unbrecciated eucrites. *Geochimica et Cosmochimica Acta, 73 ,* 794– 819.

McCord, T. B., Adams, J. B. & Johnson, T. V. (1970). Asteroid Vesta: Spectral reflectivity and compositional implications. *Science 168*, 1445– 1447.

McDonough, W. F. & Sun, S., (1995). The composition of the Earth. *Chemical geology, 120,* 223–253.

McSween Jr, H. Y., Mittlefehldt, D. W., Beck, A. W., Mayne, R. G., & McCoy, T. J., (2010). HED meteorites and their relationship to the geology of Vesta and the Dawn mission. In *The Dawn Mission to Minor Planets 4 Vesta and 1 Ceres* (pp. 141-174). Springer New York.

Mittlefehldt, D. W. & Lindstrom, M. M., (1991). Generation of abnormal trace element abundances in Antarctic eucrites by weathering processes. *Geochimica et Cosmochimica Acta, 55*, 77–87.

Paniello, R. C., Moynier, F., Beck, P., Barrat, J.-A., Podosek, F. A., & Pichat, S. (2012). Zinc isotopes in HEDs: Clues to the formation of 4-Vesta, and the unique composition of Pecora Escarpment 82502. *Geochimica et Cosmochimica Acta, 86*, 76 – 87.

Riches, A. J., Day, J. M.D., Walker, R. J., Simonetti, A., Liu, Y., Neal, C. R., & Taylor, L. A. (2012). Rhenium–osmium isotope and highly-siderophile-element abundance systematics of angrite meteorites. *Earth and Planetary Science Letters*, *353*, 208-218.

Righter, K. & Drake, M. J., (1997). A magma ocean on Vesta: Core formation and petrogenesis of eucrites and diogenites. *Meteoritics & Planetary Science, 32*, 929–944.

Righter, K., & Drake, M. J. (1996). Core formation in Earth's moon, Mars, and Vesta. *Icarus*, *124*, 513-529.

Ruzicka, A., Snyder, G. A. & Taylor, L. A., (1997). Vesta as the howardite, eucrite and diogenite parent body: Implications for the size of a core and for large-scale differentiation. *Meteoritics & Planetary Science, 32*, 825–840.

Ryder, G., Norman, M. D. & Score, R. A., (1980). The distinction of pristine from meteorite-contaminated highlands rocks using metal compositions. In *Lunar and Planetary Science Conference Proceedings*, *11*, 471–479.

Sarafian, A. R., Roden, M. F., & Patiño-Douce, A. E. (2013). The volatile content of Vesta: Clues from apatite in eucrites. *Meteoritics & Planetary Science*, *48*, 2135-2154.

Scott, E. R., Greenwood, R. C., Franchi, I. A., & Sanders, I. S., (2009). Oxygen isotopic constraints on the origin and parent bodies of eucrites, diogenites, and howardites. *Geochimica et Cosmochimica Acta, 73*, 5835–5853.

Shirey, S. B., & Walker, R. J. (1998). The Re-Os isotope system in cosmochemistry and high-temperature geochemistry. *Annual Review of Earth and Planetary Sciences*, *26*, 423-500.

Smoliar, M. I., Walker, R. J., & Morgan, J. W. (1996). Re-Os ages of group IIA, IIIA, IVA, and IVB iron meteorites. *Science*, *271*, 1099.

Stolper, E., (1977). Experimental petrology of eucritic meteorites. *Geochimica et Cosmochimica Acta, 41,* 587–611.

Trinquier, A., Birck, J.-L., Allegre, C., G¨opel, C., Ulfbeck, D., (2008). ^{53}Mn–^{53}Cr systematics of the early solar system revisited. *Geochimica et Cosmochimica Acta, 72*, 5146–5163.

Van Acken, D., Brandon, A. D., & Lapen, T. J. (2012). Highly siderophile element and osmium isotope evidence for postcore formation magmatic and impact processes on the aubrite parent body. *Meteoritics & Planetary Science*, *47*, 1606-1623.

Walker, R. J. (2012). Evidence for homogeneous distribution of osmium in the protosolar nebula. *Earth and Planetary Science Letters*, *351*, 36-44.

Walker, R. J. (2009). Highly siderophile elements in the Earth, Moon and Mars: update and implications for planetary accretion and differentiation. *Chemie der Erde-Geochemistry*, *69*, 101-125.

Warren, P. H., & Wasson, J. T. (1977). Pristine nonmare rocks and the nature of the lunar crust. In *Lunar and Planetary Science Conference Proceedings*, *8*, 2215-2235.

Warren, P. H., Kallemeyn, G. W., Huber, H., Ulff-Møller, F., & Choe, W. (2009). Siderophile and other geochemical constraints on mixing relationships among HED-meteoritic breccias. *Geochimica et Cosmochimica Acta, 73*, 5918–5943.

Wiechert, U., Halliday, A., Palme, H., Rumble, D. (2004). Oxygen isotope evidence for rapid mixing of the HED meteorite parent body. *Earth and Planetary Science Letters, 221,* 373–382.

Chapter 4:

Volatile element loss during planetary magma ocean phases

Abstract

Moderately volatile elements are key tracers of volatile depletion in planetary bodies. Zinc is especially useful, because of its generally elevated concentration in planetary basalts (≥mg g^{-1}), and lack of evidence for significant isotopic fractionation under high-temperature igneous processes. Compared with terrestrial basalts, which typically have δ^{66}Zn values (per mille deviation of the ^{66}Zn/^{64}Zn ratio from the JMC-Lyon standard) similar to some chondrite meteorites (+0.15 to +0.3‰), lunar mare basalts yield a mean δ^{66}Zn value of +1.4 ± 0.5‰. These mare basalt samples have Zn concentrations (~2 mg g^{-1}), some 20 to 50 times lower than in typical terrestrial equivalents. Late-stage lunar magmatic products, including ferroan anorthosite, Mg-suite and Alkali suite rocks have even heavier δ^{66}Zn values (+3 to +6‰). Differences in Zn abundance and isotopic compositions between lunar and terrestrial rocks have previously been interpreted to reflect evaporative loss of Zn, either during a giant impact or during a magma ocean phase. To explore the mechanisms and processes under which volatile element loss may have occurred during a lunar magma ocean (LMO) phase, we developed models of Zn isotopic fractionation that are generally applicable to planetary

magma oceans. Our objective was to identify conditions that would yield a Zn isotopic signature of δ^{66}Zn ~ +1.4‰ within the lunar mantle. Simulations were run beginning with a starting composition inherited from the Earth-Moon giant impact, which we presumed has been preserved in the signature of the present-day terrestrial mantle. We developed two models, one that simulates a constant surface Zn isotope composition during LMO crystallization, and a second that allows the Zn isotopic composition to evolve during LMO crystallization. The first model yields a relatively homogenous LMO crystal δ^{66}Zn value, while the second results in a stratification of δ^{66}Zn values within the LMO sequence. The LMO crystal Zn concentrations from these models strongly depend on partition coefficients, and simulations using values from the literature yielded unrealistic Zn abundances. We therefore calculated partition coefficients based on *in situ* analyses of lunar mare basalt samples, 15555 and 12063, and simulations with these values better approximated the extremely low zinc concentrations in mare basalts. Critical to the models are loss mechanisms for volatile elements; we consider hydrodynamic escape and conclude that this was not a dominant process. In contrast, loss of a nascent lunar atmosphere or separation of condensates into a proto-lunar crust, are mechanisms by which volatiles could be separated from the lunar interior. The results do not preclude models that suggest a lunar volatile depletion episode related to a Giant Impact. However, LMO models for volatile loss do not require loss of volatiles prior to lunar formation. Outgassing during planetary magma ocean phases plays a crucial role in setting the volatile inventories of planets. As volatile loss is most effective on low mass bodies under these conditions, a prediction of the model is that planets accreted dominantly from highly differentiated planetesimals were likely to accrete ‘dry’.

4.1 Introduction

Volatile elements and compounds (e.g., H_2O, CH_4, NH_3) play a fundamental role in the differentiation and evolution of planets (e.g., Halliday et al., 2001; Davis, 2006; Albarède, 2009; Day and Moynier, 2014). Under solar nebula conditions, defined as gas pressures of $<10^{-4}$ atmospheres, volatile and moderately volatile elements are defined as those elements for which 50% condensation temperatures are less than 704K and 1290K, respectively (Lodders, 2003). Elements within the range of these condensation temperatures are depleted in the Earth and Mars, and are extremely depleted in some other Solar System planetary bodies, including the Moon and the parent bodies of the howardite-eucrite-diogenite (HED) and angrite meteorites (Wolf and Anders, 1980; Jones and Palme, 2000; Davis, 2006). The baseline volatile inventories of planets in the Solar System are controlled by their position with regard to the 'snow line,' where the temperature falls below the condensation temperature of water in a protoplanetary disk (Lecar et al., 2006). On a large scale, the snow line explains the distinct compositions of the inner Solar System rocky planets (Mercury, Venus, Earth, Mars), compared with the gas giants (Jupiter, Saturn, Neptune, Uranus).

The stable and radiogenic isotopes of moderately volatile elements are particularly powerful for understanding how the volatile inventories of planets have evolved. Of these elements, those with two isotopes or more include Ag, B, Cl, Cu, Ga, Ge, Rb, K, Pb, Sb, Se, Sn, Te and Zn. Studies on isotopic ratios of K, Zn, S, Cl, Cd and Pb (Thode and Rees, 1971; Rees and Thode, 1972; Tatsumoto et al., 1987; Wing and Farquhar, 2015; Humayun and Clayton, 1995; Sands et al., 2001; Schediwy et al., 2006;

Sharp et al., 2010; Paniello et al., 2012a; Kato et al., 2015; Boyce et al., 2015; Wang & Jacobsen, 2016) demonstrate a shift toward elevated relative abundances of the heavy isotopes in the Moon relative to Earth. The geochemical data has been explained by various volatile-loss mechanisms, including early loss of volatile elements by nebula processes (Humayun & Clayton, 1995), during large-scale collisions such as the proposed Earth-Moon Giant Impact (Paniello et al., 2012a; Wang & Jacobsen, 2016), large-scale magma ocean differentiation events (Day & Moynier, 2014; Kato et al., 2015; Boyce et al., 2015), or by lava-flow outgassing at the surface of low gravity bodies (Sharp et al., 2010).

Among the moderately volatile elements, Zn has been studied in the largest number of lunar samples for its isotopic composition, and has also been characterized in a range of planetary materials (e.g., Moynier et al., 2006; 2009; Herzog et al., 2009; Paniello et al., 2012a; 2012b; Kato et al., 2015). Zinc isotopic fractionation is typically expressed in per mille deviation from the JMC-Lyon standard (‰) as: $\delta^{X}Zn = ([^{X}Zn/^{64}Zn)_{sample}/[^{X}Zn/^{64}Zn]_{JMC\text{-}Lyon} - 1) \times 1000$, where x=66, 67, or 68. Since all Zn isotopic variations in planetary materials have been found to be mass-dependent, data are usually reported as $\delta^{66}Zn$; notation that we will also use in this contribution. Lunar samples show significant enrichment in the heavier isotopes of Zn compared to Earth, with both low- and high-Ti mare basalts having an average $\delta^{66}Zn$ value of +1.4 ±0.5‰ (2 s.d.; Kato et al., 2015). The lunar zinc isotopic value is distinct from the average $\delta^{66}Zn$ value for terrestrial lavas ($\delta^{66}Zn$ of +0.28 ±0.05‰; Chen et al., 2013), and for martian basalts ($\delta^{66}Zn$ = +0.25 ±0.03‰; Paniello et al., 2012a) (**Figure 4.1**). Because the low-and high-Ti mare basalts are sourced from distinct reservoirs (e.g., Warren & Taylor, 2014), the similarity in Zn isotope composition between mare basalt suites has been interpreted to reflect global-scale evaporative loss of Zn and consequent preferential enrichment of the heavier isotopes of Zn (Paniello et al., 2012a; Day & Moynier, 2014). The homogeneity of Zn isotopic ratios in lunar mare basalts appears to preclude localized lava flow outgassing (e.g., Sharp et al., 2010), because this effect would be predicted to result in significant Zn isotopic variability among mare basalts from different Apollo sample sites.

The major hypothesis to be examined is that volatile depletion can occur during large-scale magma ocean differentiation processes on planetary bodies. The concept of a magma ocean describes large-scale silicate melting on a planetary body that is subject to convection as it slowly cools and differentiates through fractional crystallization (e.g. Elkins-Tanton, 2012). This process is considered to be widespread in Solar System bodies, including smaller planetesimals such as the howardite-eucrite-diogenite (HED) and the angrite meteorite parent bodies (Greenwood et al., 2005). The hypothesis of magma ocean degassing offers an alternative to volatile depletion following a Giant Impact or in the proto-lunar disk (e.g. Pahlevan and Stevenson, 2007; Visscher and Fegley, 2013). It does not necessarily preclude these models, because volatile depletion observed in the Moon could reflect combined effects from multiple episodes of volatile loss. Nevertheless, a successful model of volatile outgassing during a magma ocean has the potential, on its own, to explain Zn isotopic signatures observed in lunar samples and is more widely applicable to magma ocean processes that may have occurred during the evolution and differentiation on other bodies, including smaller planetesimals.

4.2 Zinc isotopes as a proxy for moderately volatile and volatile elements

Focusing on Zn isotopic ratios as a constraint for volatile depletion currently has advantages over other isotopic systems of volatile or moderately volatile elements. In the first instance, zinc is detectable in most planetary materials (typically >mg $g^{-}1$) and there are now a significant number of high-precision data available on Zn isotope ratios from lunar samples (Moynier et al., 2006; Herzog et al., 2009; Paniello et al., 2012a; Kato et al., 2015). High-precision isotopic data are available for other volatile elements, such as K (Wang & Jacobsen, 2016), but the datasets are currently more limited in scope. Zinc isotopic compositions for lunar samples are also typically reported from homogenized bulk rock aliquots, and results are therefore comparable across different sample sets and lithologies. The Zn isotopic data therefore contrast with Cl isotope ratios, for which measurements have been performed on both bulk rocks and minerals (Sharp et al., 2010; Boyce et al., 2015).

An additional advantage is that Zn is not generally affected by strong partitioning in Zn-rich phases (except for sphalerite in some exceptional lunar samples: e.g., Shearer et al., 2014). Conversely, Cl can be a major constituent of apatite, or S may be affected by metal-silicate equilibration during core formation (e.g., Labidi et al., 2013), with aqueous alteration that can also strongly modify some elements and compounds (e.g., Cl, S, CO_2 and H_2O). Zinc isotope compositions are not affected by secondary effects, such as solar wind spallation or cosmogenic effects (as is the case for the D/H ratio; Greenwood et al., 2011), and all Zn isotopic variations found in lunar samples are mass-dependent (e.g. Herzog et al. 2009, Paniello et al. 2012a), Finally, Zn does not experience significant isotopic fractionation during magmatic differentiation (Chen et al., 2013), and has a single valence state of +II, resulting in negligible effects from variable redox conditions. For these reasons, we have focused on using the available Zn isotope data for lunar samples to examine models for volatile element loss during magma ocean processes.

4.3 Model Description

4.3.1 Conditions

To approximate magmatic mixing conditions during magma ocean degassing, we designed a 1-D model of joint Rayleigh distillation and AIFC. The AIFC and mass balance calculations used in this model are discussed in greater detail in *Supplementary Information*; the model code was developed by the author using equations A25, A30-A33, A38-A48 available in the *Electronic Supplementary Material* from Nishimura (2012).

The model in this study is based on several well-defined assumptions. First, the Moon would have been nearly-completely molten after its formation, leading to a global magma ocean (e.g., Warren & Taylor, 2014). Second, the magma ocean convected vigorously both prior to and during crystallization, resulting in rapid mixing. Third, both degassing and cooling would have occurred at the magma ocean surface, leading to recycling of a degassed and cooled ‘skin’ of material into the lunar magma ocean. We do not explicitly model convective mixing, thermal evolution or the quenched crust, but use these assumptions to develop a magmatic mixing model for the LMO. The model consists of combined Rayleigh distillation calculations for degassing with the assimilation and imperfect fractional crystallization (AIFC) model of Nishimura (2012, based on DePaolo, 1981). The purpose of this is to determine conditions that can yield a δ^{66}Zn = +1.4 ‰ (the value of the source of the mare basalts, Kato et al. 2015) within the LMO crystallization sequence.

The model has two basic components: (1) a thin surface layer that is subject to evaporative fractionation and (2) the bulk magma ocean that mixes with the surface layer and assimilates its signature. It is based on the idea that degassing layers on the lunar surface cool and sink to lower depths, and subsequent mixing results in the assimilation of the surface volatile depletion signature into the bulk LMO. The mixing between these two reservoirs ultimately leads to the dilution of the primary Zn signature in the lunar interior.

The assumed starting composition of the lunar mantle is thought to be the inherited isotopic composition and abundance of Zn in the collided proto-Earth and Moon materials, which can be represented by the present-day bulk silicate Earth (δ^{66}Zn= +0.28‰, Chen et al. 2013). We also explore mechanisms for progressive evaporative fractionation and crystallization that could result in heavier Zn isotopic compositions in late-stage magma ocean products (δ^{66}Zn from +3 to +6 ‰, values for the ferroan anorthosites, Mg- and alkali-suite samples [Kato et al. 2015]).

We explored two models (*Figure 4.S1*). Model 1 uses evaporative fractionation of Zn occurring at the surface prior to LMO mixing and crystallization. In Model 2, the surface evaporation of Zn persisted for at least part of LMO mixing and crystallization. Any models of magma ocean degassing require either a fully molten surface layer, or one with a partially quenched crust that would allow for incomplete degassing (c.f., terrestrial lava lakes). In both models, an early shut-off to evaporative fractionation presumably results from the formation of a 'mechanical boundary layer', such as a stable crust, which led to cessation of degassing at the surface. Below this stable and stagnant lid, the steadily cooling and crystallizing magma bodies would solidify, losing heat through convection within the magma and conduction across the lid.

A 'mechanical boundary layer' is not expected immediately since even a modest insulating atmosphere can maintain temperatures in the LMO above the liquidus initially, and above the solidus for much of the crystallization of the magma ocean (e.g., Abe & Matsui, 1985; Elkins-Tanton, 2008). Furthermore, quenched materials on the surface are predicted to be denser than the magma ocean liquids and would presumably sink shortly after formation (Walker et al. 1980, Spera 1992). Elkins-Tanton (2012) has proposed that the only geologically realistic way to form a relatively complete conductive lid on a planetary-scale magma ocean is by flotation of buoyant mineral phases, which probably occurred on the Moon after significant crystallization to form a plagioclase flotation crust

(>80% e.g., Snyder et al., 1992). Under these conditions, the vaporization of volatile species at the surface of molten or partially molten planetary bodies is possible for nearly the entire duration of magma ocean cooling and crystallization.

The different possible surface layers (molten, quenched, or stagnant lid) are not explicitly modeled, but guide assumptions of at least partial degassing and the subsequent cessation of surface volatile depletion over the course of LMO crystallization. The presence or absence of a transient or quasi-permanent mechanical boundary layer in our models is approximated by (a) assuming a constant surface δ^{66}Zn in the Model 1 and (b) evolving the surface δ^{66}Zn following Rayleigh distillation to variable ranges of F (surface liquid remaining) and M_f (fraction of magma remaining) in Model 2.

4.3.2 Rayleigh Distillation

Mass-dependent fractionation is described by the Rayleigh distillation equation:

$$\delta^{66}Zn_{final} = \delta^{66}Zn_{initial} + \left[(1000 + \delta^{66}Zn_{initial})\left(F^{(\alpha-1)} - a\right)\right] \qquad (1)$$

where α is the isotopic fractionation factor, F is the fraction of liquid remaining and δ^{66}Zn$_{initial}$ is the starting Zn isotopic composition (δ^{66}Zn = 0.28 ‰; Chen et al. 2013). The mass-dependent fractionation is governed by the fractionation factor (α), which depends on the masses of the light and heavy isotopes:

$$\alpha = \sqrt{\frac{m_{light}}{m_{heavy}}} \qquad (2)$$

where m_{light} and m_{heavy} represent zinc compounds, consisting of the ^{64}Zn and ^{66}Zn, respectively.

Values of α for zinc-bearing phases, such as sphalerite (ZnS; α = 0.990) or $ZnCl_2$ (α = 0.993) are large. However, experiments for K (Yu et al., 2003) and natural analogues for evaporation of Zn isotopes (Moynier et al., 2009) imply that alpha values rarely approach these conditions, perhaps due to pressure (Yu et al., 2003) or buffering effects. For the purposes of this work, we used α values of 0.990 to 0.999 to incorporate both theoretically and naturally determined fractionation factors. The starting composition of the lunar mantle is set at a Zn isotopic composition equal to the modern terrestrial mantle, δ^{66}Zn = +0.28 ± 0.05‰ and 55 ppm (McDonough and Sun, 1995). Additional loss mechanisms, such as during the Earth-Moon forming event (e.g. Canup et al., 2015), would reduce the Zn abundance and increase the δ^{66}Zn signature of this starting composition.

4.3.3 Mixing and crystallization in the LMO

Our model for LMO evolution is based on the concept of assimilation and fractional crystallization (AFC; DePaolo, 1981) in which the assimilant is the surface layer that then mixes with the bulk LMO. The LMO is analogous to a magma reservoir because it consists of suspended crystals that eventually settle as it cools and crystallizes.

AFC models have been successful in reproducing assimilation of crust in terrestrial magmas where multiple pulses (e.g., Muskox; Stewart & Depaolo, 1992; Day et al., 2008) and single pulses of magma (e.g., Skaergaard; Stewart & DePaolo, 1990) have occurred.

To properly adapt the specific assimilation and imperfect fractional crystallization (AIFC) model (Nishimura, 2012) to the LMO scenario, major input parameters are based on mass balance calculations of the assimilant surface layer, the crystallizing component and the whole magma ocean. It consists of input parameters that include: the assimilation rate constant (r_a), crystal fraction (ϕ), and the partition coefficient (D) (see also ***Supplementary Materials***). The values of r_a and ϕ remain constant throughout the models, and are based on the relative masses of the surface layer (assimilant) and crystal component compared to the bulk lunar mantle. The Zn partition coefficient changes as a function of the fraction of liquid remaining (M_f) based on the theoretical LMO mineralogy (Snyder et al., 1992) and the initial set of D values are based on studies of Zn partitioning (Dissanayake and Vincent, 1972; Paster et al., 1974; Ewart and Griffin, 1994; Kohn and Schofield, 1994; Klemme et al., 2006). These input parameters are provided in *Table 4.S1*, along with a more detailed discussion of model assumptions for adapting the AIFC model to the LMO scenario. We also obtained empirical Zn partitioning data from Apollo mare basalts 12063 (ilmenite basalt) and 15555 (olivine-normative basalt) using laser-ablation inductively coupled plasma mass spectrometry (*Supplementary Information, Table 4.S2*). These data were used to calculate the set partition coefficients in *Table 4.S3*, which were used for additional LMO simulations as a point of comparison to examine the effects of partitioning behavior on model results.

4.3.4 Model 1 - Constant surface Zn isotopic composition during LMO crystallization

In Model 1, the surface Zn isotopic composition remains constant throughout LMO crystallization, which provides a baseline for understanding the efficiency of assimilation under the more complex, joint Rayleigh-AIFC model. Over multiple simulations, a constant volatile-depleted surface signature is assimilated into the crystallizing LMO. For Model 1, we specifically seek the Zn surface signatures that eventually yield a bulk lunar mantle Zn composition that approximates the average lunar mare basalt signature (δ^{66}Zn ~ +1.4‰), by kinetic, evaporative fractionation of Zn at the surface. For each unique simulation, the assimilant concentration (C_a) and isotopic signature (ε_a) were set equal to random values along curves calculated using the Rayleigh distillation equation (Equation 1) for a range of α values: 0.990 to 0.999. These provided the input parameters for the assimilant in the AIFC model and remained constant throughout the simulation of a full LMO crystallization sequence.

A set of 1000 random-seeded simulations of surface composition were performed for surface Zn isotopic composition from $+0.28‰ < \delta^{66}$Zn $< +7‰$, with intervals of 0.1‰. This range of isotopic compositions was used to narrow down the values of C_a and ε_a that yielded Zn isotopic compositions of the lunar mantle in the range of $1.3 ‰ < \delta^{66}$Zn $< 1.5 ‰$. These simulations indicate that the surface Zn isotopic composition and the bulk LMO signature follow a ~1:1 relation, indicating efficient mixing and assimilation using the AIFC model, as described below (see also *Figure 4.S2*). The AIFC model was run for the full LMO crystallization sequence, defined by the fraction of magma remaining (M_f = 1 to 0.05). The LMO sequence consisted of stepped calculations, where the interval of M_f is 0.001 for M_f = 1 to 0.6 and 0.005 for M_f = 0.59 to 0.05, which represent 0 to 40% LMO crystallization and 41 to 99.5% LMO crystallization, respectively. Although the anorthositic crust forms at ~80% LMO crystallization (Snyder et al., 1992), the late-stage lithologies continue to crystallize from the remaining liquid, and so this model operates for the full LMO crystallization sequence.

4.3.5 Model 2 - Concurrent evolution of surface Zn isotopic signature and LMO crystallization

In Model 2, the Zn isotopic composition of the surface continues to evolve as the magma ocean crystallizes. This concurrent evolution is achieved by calculating the Rayleigh distillation curve (δ^{66}Zn of the residual melt versus F) for a given fractionation factor (α), and allowing the surface assimilant concentration and isotopic signature to evolve along this curve as LMO crystallization proceeds. The extent of surface volatile depletion is sensitive to both fractionation factor (α) and the fraction of liquid remaining at the surface (F). Simulations were run for fractionation factors (α) from 0.990 to 0.999 (stepped by 0.001) and variable ranges of F (lower limit: 0.9 to 0.19). The evolving surface volatile depletion signature was additionally indexed to M_f (fraction of magma remaining), to indicate the point in LMO crystallization when surface volatile depletion ceased. After a given value of M_f, the assimilant concentration and isotopic signature were set constant to their most evolved (minimum) values for the remainder of LMO crystallization. For example, if the surface evolved at α = 0.999 for F = 1 to 0.6 (surface liquid remaining) up to M_f = 0.4 (40% magma remaining), then the most evolved values for the surface isotopic ratio (δ^{66}Zn = +0.8‰) and concentration ([Zn] = 33 ppm) were used as the constant assimilant signature for M_f = 0.4 to 0.005. Indexing the extent of surface depletion to a point along the LMO crystallization sequence is an important aspect of this model, because it regulates the extent to which a progressively depleted surface Zn isotopic signature is assimilated into the bulk lunar mantle.

Model 2 builds on the earlier simulations of constant assimilation composition (Model 1), and so utilizes values for the evolving surface Zn isotopic composition (δ^{66}Zn ~ +0.28‰ to +7‰). This range encompasses a terrestrial-like composition to the most enriched Zn isotopic signatures measured in a single Mg-suite rock (δ^{66}Zn = +6.3‰). It specifically tests the effects of progressive surface volatile depletion on assimilation during LMO crystallization for a range of fractionation factors (α = 0.990 to 0.999) and surface liquid remaining (F = 0.9 to 0.19), with cessation during different points in LMO crystallization (M_f = 1 to 0.005). The remainder of the AIFC model input parameters, namely $r_{a,}$ ϕ and D, were identical to the first model (*Table 4.S1*).

4.4 Results

Both constant (Model 1) and concurrent (Model 2) evolution of the surface Zn isotope signature can reproduce the present bulk isotopic signature observed in lunar mare basalts with δ^{66}Zn ~ +1.4‰. However, the final Zn concentration observed in lunar samples (~2 ppm) cannot be fully simulated and presumably requires a starting Zn concentration less than terrestrial values (< 55 ppm). Given the lack of constraints for the initial conditions of the LMO, and to avoid over-interpretation of model results, we maintain a terrestrial-like zinc composition in our model. For Model 1, the input parameters result in simulated zinc concentrations that converge to < 10 ppm (**Figure 4.2b**, black lines), which is within a factor of five of ~2 ppm Zn observed in mare basalts, but still outside the range of measured Zn concentrations (Paniello et al., 2012a; Kato et al., 2015). Model 2, however, results in late-stage values that are considerably higher, at ~10 to 25 ppm (**Figure 4.2d**, black lines), and there is an increase in Zn concentration toward the end of LMO crystallization ($M_f \sim 0.2$).

As a point of comparison, simulations for partition coefficients calculated from *in situ* measurements of lunar mare basalt samples yield more realistic Zn concentrations across the LMO sequence that converge to ~5 ppm Zn after 40% crystallization (**Figure 4.2b, 4.2d**, colored lines). The two sets of partition coefficients do not yield any significant differences for crystal Zn isotopic composition, which demonstrates that this aspect of the model is more strongly controlled by efficient mixing and assimilation across the LMO sequence than D values.

4.4.1 Constant surface Zn isotope composition during LMO crystallization (Model 1)

Simulations for Model 1 consistently yielded relatively homogenous lunar mantle Zn isotopic compositions across the LMO crystallization sequence (**Figure 4.2a**). The simulations were run for the input parameters in *Table 4.S1* and *4.S3* with surface crystallization values of +0.28‰ < δ^{66}Zn < +7‰. The results yielded δ^{66}Zn values ~ +1.4‰ in the bulk lunar mantle for surface composition of δ^{66}Zn values ~ +1.4‰, demonstrating an approximately 1:1 relation between the surface and LMO crystal zinc compositions (see *Figure 4.S2*). The fact that different partition coefficient values yield similar Zn isotopic compositions reflects the efficiency of the AIFC model. At the point of maximum efficiency (~M_f ~0.6; see **Figure 4.2a**), the isotopic signature of the LMO crystal approximately converges to the surface zinc composition for the remainder of the crystallization sequence. This behavior is likely governed by differences in intervals of M_f across the LMO sequence, which are smaller up to 60% (by 0.001) compared to 59% to 5% magma remaining (by 0.005).

4.2.1 Concurrent evolution of surface Zn isotopic signature and LMO crystallization (Model 2)

A joint Rayleigh-AIFC model (Model 2) yields a lunar mantle more stratified in Zn concentrations and isotopic compositions than in Model 1, with the isotopically heaviest composition forming last in the crystallization sequence **(Figure 4.2c).** The concurrence of volatile depletion of Zn on the lunar surface and LMO crystallization results in a more gradual gradient across the LMO sequence compared to the sudden convergence to surface values in Model 1. A more gentle gradient occurs because the surface composition evolves and is efficiently assimilated into the lunar mantle, leading to LMO crystallization 'capturing' the progressive volatile depletion of the surface. The major control on this phenomenon is the degree of volatile depletion on the surface, which is strongly mediated by α, and to a lesser degree, the fraction of surface liquid remaining (F) and the point at which this ceases along the LMO crystallization sequence (represented by M_f, fraction of magma remaining). Specific model results for a range of alpha values where only 40% of the surface liquid is lost (F = 0.6) are reported in **Figure 4.2c**. The evaporative fractionation is also halted at 75% LMO crystallization (M_f = 0.25), in order to account for limited volatile depletion following the formation of the anorthositic crust. At this point, the LMO crystal composition efficiently converges to the maximum surface signature once surface volatile depletion ceases, which is similar to the behavior of Model 1. As expected, the most enriched zinc signature results for $\alpha = 0.990$, and the isotopic enrichment becomes less marked as the fractionation factor approaches unity.

4.5 Discussion

4.5.1 Constraints for Zn partition coefficients

The joint Rayleigh-LMO model exhibits a strong dependence on literature partition coefficient values (*Table 4.S1*) during the evolution of the crystallization sequence, evident in the elevated Zn concentrations in the late stage lithologies toward the end of LMO crystallization for Model 2 (**Figure 4.2d**). In order to further examine this issue using geochemical constraints, we performed *in situ* laser-ablation analyses of mineral phases in lunar mare basalt samples, 15555 and 12063 (see supplemental information for more detail). The calculated partition coefficients from this analysis yielded significant differences for olivine ($D_{Zn} \sim 2.4 - 5.1$), pyroxene ($D_{Zn} \sim 0.2 - 0.3$) and plagioclase ($D_{Zn} \sim 0.3 - 1$) compared to the values from the literature (olivine: D_{Zn} ~0.9, Kohn and Schofield, 1994; pyroxene: D_{Zn} ~2.1, Klemme et al., 2006; plagioclase: D_{Zn} ~0.17, Ewart and Griffin, 1994). The value for ilmenite ($D_{Zn} \sim 7$) is comparable to experimental data, however ($D_{Zn} \sim 11$; Klemme et al., 2006).

These calculated partition coefficients were used for simulations of both Models 1 and 2, and except for the partition coefficients, the inputs for the model runs were identical, including the initial 55 ppm Zn concentration. For both Models 1 and 2, the two sets of partition coefficients (*Tables 4.S1, 4.S3*) yield unique crystal Zn concentration profiles. For the literature values (*Table 4.S1*) in Model 1 (**Figures 4.2b**, black lines**)** the Zn abundances decrease gradually and do not result in sharp increases in zinc toward the end of the LMO crystallization. For Model 1, the calculated values (*Table 4.S3*, this study) largely remain at ~5 ppm Zn for LMO crystallization after 60% magma remaining (**Figures 4.2b**, colored lines**)**. Over multiple simulations, the most extreme cases exhibit excursions of ~12 ppm at 20% magma remaining, and up to ~15 ppm at 5% magma remaining. Compared to literature partition coefficients, the calculated values yield lower values ($D \leq 1$) for lithologies later in the LMO sequence, which presumably leads to higher Zn concentrations in the late-stage magma reservoir that rapidly crystallize into late-stage products. Zinc enrichment in the remaining magma liquid is also observed for literature partition coefficients under Model 2 (**Figure 4.2d**, black line). These outcomes demonstrate that the concurrent case of volatile depletion and LMO crystallization is more sensitive to partition coefficients than Model 1, which does not exhibit Zn abundance enrichment in late stage crystallization products for the same D values (**Figure 4.2b**, black lines). The calculated partition coefficients exhibit similar behavior in Model 2 (**Figure 4.2d**, colored line) as Model 1, including the excursion with higher Zn concentrations, and show almost opposite behavior to the literature values for the last 20% of LMO crystallization **(Figure 4.2d**, black line).

Across both models, the most significant difference between the two sets of partition coefficients is between 60% and 25% magma remaining, where the calculated values consistently yield ~5 ppm zinc while the literature values do not result in similar concentrations until 25% magma remaining. This is likely the result of higher partition coefficients for olivine in these simulations ($D_{Zn} = 3.75$ compared to $D_{Zn} = 0.9$; Kohn and Schofield, 1994), which leads to higher Zn concentrations for the deeper lunar mantle. Conversely, the lower D_{Zn} for olivine from the literature results in a molten magma fraction that becomes increasingly enriched in Zn concentrations, and is then forced to crystallize later in the LMO sequence (see *Supplementary Information* for more details on the model). For the set of partition coefficients assembled from previous studies (*Table 4.S1*), the crystal Zn concentration is also more sensitive to the initial concentration of the magma. With *Table 4.S1* values, lower initial zinc concentrations (< 55 ppm) yield lower overall zinc concentrations values across the LMO, but still exhibit similar and sudden increases in concentration as observed at $M_f \sim 0.2$ (**Figure 4.2d**). These simulations demonstrate the sensitivity of Zn concentration in these models to partition coefficients, and the need to better constrain these values for more robust estimates of LMO crystallization Zn compositions.

4.5.2 Comparisons of the models

On a large scale, our modeling results show that a surface volatile depletion signature can be assimilated into the bulk lunar mantle. Model 1, with a constant surface signature, demonstrates that the target value of δ^{66}Zn ~ +1.4 ‰ can be achieved in this way under a wide range of α and F values. The constant surface composition (Model 1), however, does not explain the isotopic variability observed in samples of low Zn content alkali suite (δ^{66}Zn = +3 ‰), Mg-suite (δ^{66}Zn = +6.3 ‰) and ferroan anorthosite (δ^{66}Zn = +4.2 ‰) samples (Kato et al., 2015). Under conditions for Model 1, the strong heavy isotope enrichment in these rocks could indicate depletion during the later stages of LMO crystallization.

Results of concurrent evaporative fractionation (Model 2) indicate that the target zinc isotopic compositions are achievable for a wide range of fractionation factors (α = 0.990 – 0.999), by adjusting the value of surface liquid remaining (F). For a given value of F (0.6 in the case of **Figure 4.2c**), the effect of the α value becomes apparent. Fractionation factors closer to unity result in much more gradual volatile depletion and attain Zn isotopic enrichments much later in the LMO crystallization sequence. For example, α < 0.997 does not reach the target δ^{66}Zn signature of ~1.4‰, while α ~ 0.990 attains the target value at 15% crystallization (M_f = 0.85) and results in a strongly stratified LMO up to +5.4‰. Such strong enrichment signatures may potentially explain the heavier isotopic enrichments observed in alkali suite and Mg-suite lunar rocks (Kato et al., 2015). The model behavior indicates that if volatile depletion on the lunar surface was efficient and close to ideal Rayleigh distillation (α = 0.990 for ZnS and α = 0.993 for $ZnCl_2$), it presumably occurred for shorter durations, e.g. α = 0.990 - 0.993 up to ~ 30% LMO crystallization. In contrast, if Rayleigh distillation was non-ideal for these phases (α ~ ≤1), then it suggests a lunar surface that was molten for a longer period of time (greater liquid loss) or that evaporative fractionation persisted longer during LMO crystallization, with up to only 25% magma remaining.

Model 2 can explain preliminary measurements of late stage LMO, but it raises the issue of Zn isotopic enrichment in the late-forming ilmenite layer, which is an important component in high-Ti basalts (up to 13% of the source; Taylor et al., 1991). In this case, ilmenite would crystallize from late-stage liquids increasingly enriched in the heavy isotopes of Zn, and ilmenite overturn may have then resulted in significant differences in heavy zinc isotopic enrichment between low-Ti and high-Ti basalts. The partition coefficients of Zn into ilmenite range from as high as D = 11 under reducing, low-pressure conditions, to as low as D = 0.6 at elevated pressures (Klemme et al., 2006); the partition coefficient calculated from *in situ* measurements in this study is D = 7 (see *Supplementary Information*). Assuming a deep mare basalt source with a composition of δ^{66}Zn ~ +1.4‰ and 2 ppm Zn (as suggested by the observational data), an addition of 7% ilmenite with δ^{66}Zn ~ +5.4‰ (where $\alpha > 0.990$) and up to 10 ppm Zn (the upper limits of Zn concentrations in model outputs) would result in a final source composition of δ^{66}Zn ~ +1.7‰ and ~ 2.5 ppm. This is within the error of the bulk average of Zn isotopes in lunar mare basalts, +1.4 ±0.5‰ (Kato et al., 2015), and for less enriched ilmenite components < +3.4‰ (where $\alpha > 0.993$) with lower Zn abundances <10 ppm, the ilmenite contribution would be even less and yield mare basalt samples closer to δ^{66}Zn ~ +1.4‰. Therefore, a small addition of a moderately enriched ilmenite component would still maintain homogeneity of Zn isotopic signatures across the low-Ti and high-Ti mare basalts.

The LMO model by Snyder et al. (1992) proposes fractional crystallization of high-Ti basalts from trapped instantaneous residual liquids, after the magma ocean reaches the clinopyroxene liquidus and begins to form plagioclase. This model only requires small-scale convective mixing of the upper tenth of the magma ocean sequence instead of large-scale overturn of the cumulate pile (Snyder et al., 1992). Such late-stage formation for both low-Ti and high-Ti mare basalts would require a signature of δ^{66}Zn ~ +1.4‰ in at least the upper tenth of the LMO sequence. This target value is attainable through progressive Rayleigh distillation (Model 2) with $\alpha \sim 0.997$, or a surface zinc composition of δ^{66}Zn ~ +1.4‰ for the case of a constant zinc surface signature (Model 1). Conversely, large-scale overturn within the LMO (Ringwood and Kesson, 1976; Solomon and Longhi, 1977; Elkins-Tanton et al., 2002) and the possibility of a deep source reservoir for mare basalts (e.g. Green and Ringwood, 1973; Delano and Livi, 1981) would make such an explanation invalid. However, shallow, late-stage crystallization may explain both the petrogenesis and heavy isotopic composition of zinc in lunar basalts (e.g. Binder, 1985).

4.5.3 How is Zn lost from magma oceans?

The isotopic loss of moderately-volatile elements, such as Zn, may be related to a planet's escape velocity (v_e), which is a function of the planet's mass and radius:

$$v_e = \sqrt{\frac{2GM}{r}} \qquad (3)$$

where G is the gravitational constant, M is the mass of the body, and r is radius. Escape velocity differences may explain the heavier zinc isotope enrichment of the unbrecciated eucrite samples from the HED parent body (δ^{66}Zn = +4.3 ± 1.1 ‰, Paniello et al., 2012b), compared with the Moon. The HED parent body has a lower escape velocity (0.35 km/sec) than the Moon (2.38 km/sec), which has been suggested as a possible explanation for the greater isotopic enrichment observed in eucrite samples (Day & Moynier, 2014). Mars and Earth, which have higher escape velocities of 5.03 km/sec and 11.19 km/sec respectively, exhibit limited Zn isotopic fractionation. The relationship between escape velocity and Zn isotopic fractionation suggests that more zinc atoms are lost by some mechanism from smaller planetary bodies relative to larger planets. One such mechanism that has been proposed would require the speed of the individual atoms or compounds to exceed the escape velocity, which can be evaluated using the Maxwell-Boltzmann distribution.

The Maxwell-Boltzmann distribution describes the probability distribution of speed for an atomic or compound species in an ideal gas and is a function of particle mass, speed and temperature (see equation in supplement). Maxwell distributions are shown in **Figure 4.3** for individual volatile and moderately-volatile elements (H, O, Cl, Zn) and zinc compounds (ZnO, ZnS, $ZnCl_2$), where an increase in temperature leads to a greater magnitude and range of possible particle speeds. At 2000 K and 4500 K, the mean speed distribution for atomic zinc is below 2000 m/sec (2 km/sec) and is significantly lower than that of hydrogen. These calculated speeds suggest that the loss of zinc to space cannot explain the significant zinc depletion on the Moon.

Hydrodynamic escape, which describes the loss of heavier elements in the drag forces of faster-moving, lighter elements, is another possible loss mechanism for Zn from the lunar atmosphere. Recent studies, however, indicate that hydrodynamic escape is not the dominant process (Nakajima and Stevenson, 2014). Calculations of Zn mass fractionation and loss during hydrodynamic escape further indicate that it cannot explain the bulk Zn depletion and isotopic ratios in lunar samples (see *Supplementary Information*, Hunten et al., 1987; Zahnle and Kasting, 1986; Zahnle et al. 1990).

A related explanation for zinc loss may be atmospheric blowoff during a large impact, which can result from global ground motion excited by shock waves in the planet's interior (Genda and Abe, 2003). Atmospheric blowoff has been invoked to explain limited volatile depletion of the Earth during the Giant Impact (e.g. Tucker and Mukhopadhyay, 2014; Stewart et al., 2014) because its maximum atmospheric loss is estimated to be 30%, compared to smaller bodies like the Moon that approach 60% (Genda and Abe, 2003). This explanation may be valid for subsequent, large-scale impacts on the Moon, such as the South-Pole Aitken basin impact that is thought to have generated ~2.7×10^{19} J/m^2 (Potter et al., 2012), which far exceeds the ~6.5×10^{11} J/m^2 required for complete atmospheric loss for an Earth-sized protoplanet (Genda and Abe, 2003).

A more robust understanding of zinc vaporization has important implications for ascertaining mechanisms of zinc loss, whether to a transient atmosphere, or through subsequent condensation into the liquid or solid phases that were sequestered into un-sampled regions of the LMO. Herein we focus on the potential for the loss of zinc vapor, although condensation is more probable given the atomic weight of zinc. However, the mechanisms of zinc condensation and sequestration of the light isotopic reservoir are largely unexplored. The feasibility of this model hinges on the potential for zinc to escape from the mantle reservoirs of several lunar magma products (e.g. mare basalts, possibly Mg-suite and alkali-suite rocks), and therefore quantifying the timing, conditions and mechanisms of zinc loss is a key area of research.

4.5.4 The Dry Moon and the LMO applied to planetary magma oceans

The magma ocean concept was first suggested for the Moon by Wood (1970) and Smith et al. (1970) based on the various lunar lithologies, and similar concepts for the Earth (Ringwood, 1966). It has since evolved to include geophysical, thermal and chemical modeling (e.g. Elkins-Tanton et al., 2011), and has been extended to asteroidal bodies (Norman and Taylor, 1992), including the HED (Ruzicka et al., 1997; Righter and Drake, 1997; Mandler and Elkins-Tanton, 2013) and angrite parent bodies (Greenwood et al., 2005). Magma oceans may, in fact, be an important step in the differentiation of planets and planetesimals, as hypothesized for the Earth, Moon, Mars and Vesta (Elkins-Tanton, 2012).

Studies that examine the effect of magma oceans on the volatile inventories of planets indicate the loss of elements such as Ne (Tucker and Mukhopadhyay, 2014) and outgassing of H_2O and CO_2 (Zahnle et al., 2007; Elkins-Tanton, 2008). The extension of this idea to moderately volatile element depletion, including large-scale mixing within a magma ocean, can explain the aggregate volatile depletion observed in planetary bodies (e.g. Rb/Sr ratios; Halliday and Porcelli, 2001). Magma ocean phases may therefore act as a 'drying out' mechanism for planets, planetesimals and planetary precursor material, especially for low-mass bodies with low escape velocities and subject to debris loss (e.g. Sarid and Stewart, 2015). Such a 'drying out' mechanism is particularly applicable to the Moon, which exhibits large-scale volatile element depletion as seen in lower Zn/Fe, K/U and Rb/Ba ratios compared to the Earth (Albarède et al., 2015). The effect of the LMO would also be valid in the case of incomplete, heterogeneous accretion following the Giant Impact (Canup et al., 2015), because it can explain how the Moon became dry although it formed from the more volatile-rich Earth (the volatile composition of the impactor, Theia, is unknown).

The case of lunar differentiation is further applicable to magma oceans on planetary bodies such as Vesta, and the angrite parent bodies that show evidence of large-scale mixing (Greenwood et al., 2005). The 'drying out' mechanism is also more broadly applicable to the evolution of terrestrial planetesimals, particularly those with long-lived magma oceans that are subject to desiccation (Hamano et al., 2013). Conditions for these planetesimals are more poorly known than for the Moon, but our model results can be scaled down and applied to smaller bodies. In the case of shallower magma oceans, we would expect greater heterogeneity in the mantle reservoirs and resulting melt products. Such behavior is reflected in model simulations from F = 1.0 to 0.6, when the mantle composition is continually changing, reflecting short time-scale mixing and more rapid changes between mineralogy and partition coefficients. Assuming the case for the Moon, for which iterative mixing over the entire magma ocean sequence leads to homogenous sections in the LMO, the crystal compositions set earlier in the LMO sequence are more applicable to smaller bodies or shallower magma oceans. Recent work on Zn isotopes in eucrite samples supports this idea, because these samples show a large range of volatile depleted signatures that exceed lunar values (Paniello et al., 2012b). The greater range in Zn composition in eucrite samples may be a function of smaller, localized mixing among mantle reservoirs, and the lower escape velocity of the HED parent body.

The potentially pervasive nature of magma oceans on planetary bodies (Greenwood et al., 2005), including shallow magma oceans (Tonks and Melosh, 1993) and locally impact-generated melting (Cintala and Grieve, 1998), suggests that it is a fundamental mechanism in setting the volatile inventories of planetary bodies. In particular, magma ocean degassing may have affected the planetary precursor material prior to accretion, thereby explaining volatile depletion in large bodies with relatively high escape velocities (e.g. Day and Moynier, 2014).

4.5.5 Limitations of the models

The models examine lunar volatile depletion in the context of the lunar magma ocean, and therefore do not depend on initial conditions of the Moon-forming impact or the subsequent proto-lunar disk. The models are therefore valuable because they provide a possible mechanism and timing for lunar volatile depletion independent of conditions of lunar formation (e.g., giant impact, co-accretion models). In contrast, the models rely on prior studies and models of the LMO (Solomon and Longhi, 1977; Snyder et al., 1992; Elkins-Tanton et al., 2011), but they can readily be adapted to new advances in our understanding of LMO mixing and overturn.

Our results particularly highlight the importance of constraining partition coefficients under low-pressure and low oxygen fugacity conditions, and determining the composition and location of lunar mantle reservoirs. Further experimental studies on trace element partitioning in lunar compositional melts are required (e.g. Kohn and Schofield, 1994; Klemme et al., 2006), with attention to unique lunar lithologies such as anorthosites and late-stage intrusive rocks (e.g. Phinney, 1992). Such studies would provide more robust zinc partition coefficients for model parameterization, because at present they have been estimated from a small number of studies under lunar-like conditions, extrapolation from terrestrial studies (see *Table 4.S1* and references therein) and limited *in situ* analyses of lunar samples (this study; *Table 4.S3*).

4.6 Conclusions

Models of volatile depletion during a lunar magma ocean phase demonstrate that evaporative fractionation of Zn may have occurred shortly before or during LMO crystallization. The surface volatile depletion signature can be efficiently assimilated into the bulk lunar mantle, which is evident both for a constant surface Zn signature, as well as for an evolving surface zinc isotopic ratio where progressive Rayleigh distillation occurs during LMO crystallization. Alternative models that explore volatile depletion in the proto-lunar disk (e.g. Visscher and Fegley, 2013), or in the aftermath of the Giant

Impact (e.g. Canup et al., 2015) remain valid, but are specific to the canonical Moon origin hypothesis. We explore a viable mechanism of lunar volatile depletion that is both complementary to existing models but may also be applicable to alternative lunar formation mechanisms. A δ^{66}Zn ~ +1.4 ‰ readily develops in the bulk lunar mantle, and can explain the heavy Zn enrichment observed in both high-Ti and low-Ti mare basalts. The interpretation of this model in the context of late-stage lithologies such as the ferroan anorthosites, Mg-suite and alkali suite rocks is more complex but suggest further late-stage loss of Zn. We conclude that the baseline δ^{66}Zn ~ +1.4‰ for mare basalt source regions is achievable through surface evaporative fractionation during the lunar magma ocean phase, and subsequent assimilation into the bulk lunar mantle. The conditions for this mechanism, however, remain non-unique and require more experimental and observational constraints of small-scale vaporization (and possibly subsequent re-condensation) of volatile and moderately-volatile elements. Experimental studies of zinc partitioning into distinct mineral phases under low oxygen fugacity conditions would be further valuable to constrain the evolution of zinc concentrations within the LMO. Additional work to better understand the pressure and temperature conditions of lunar petrogenesis may provide more robust constraints for the depth of source reservoirs for lunar mantle lithologies, and therefore the expected profile of Zn abundances during LMO crystallization.

Acknowledgements

We are grateful to the NASA Emerging Worlds program for support (NNX15AL74G).

Chapter 4, in full, is a reprint of material submitted to *Icarus*, 2016, Dhaliwal, Jasmeet K.; Day, James M. D.; Moynier, Frederic. The dissertation author was the primary investigator and author of these this paper.

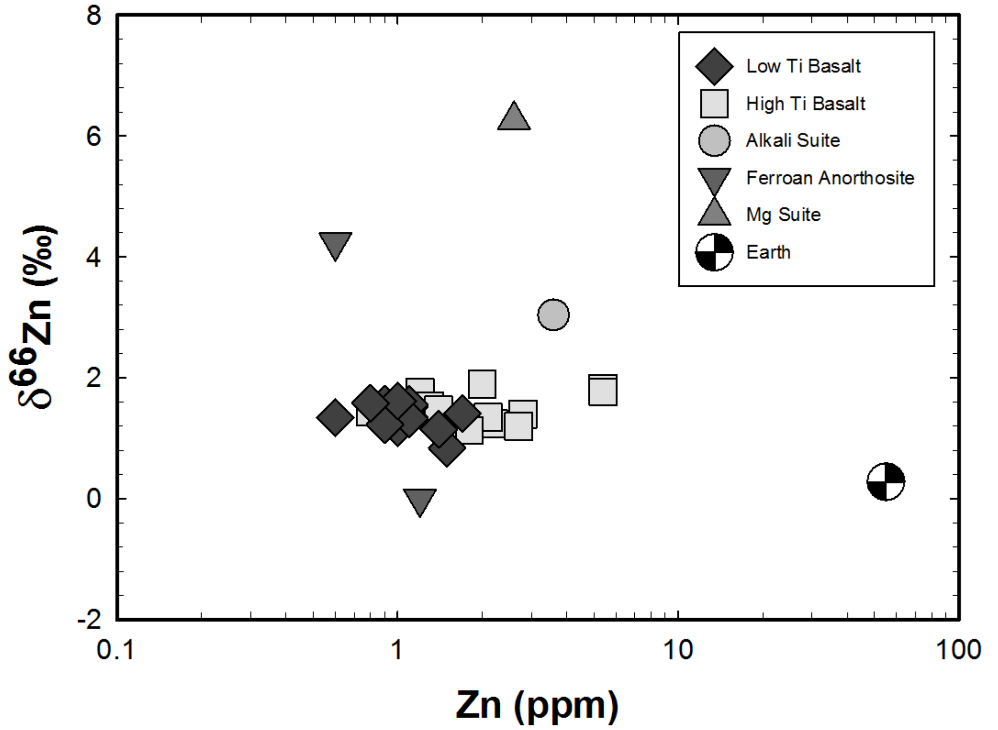

Figure 4.1: Zinc isotope versus Zn abundance data for lunar samples demonstrating that Zn is enriched in the heavy isotopes in lunar mare basalt sources (δ^{66}Zn = +1.4 ± 0.5‰; Paniello et al., 2012a; Kato et al., 2015), compared with the average for the Earth (δ^{66}Zn = +0.28 ± 0.05‰; Chen et al., 2013) and assuming a terrestrial Zn concentration of 55 ppm (McDonough and Sun, 1995). Some lunar samples, including ferroan anorthosite, high-magnesian and alkaline suite rocks, have δ^{66}Zn ranging from +3 to +6 ‰ (Kato et al., 2015). The low δ^{66}Zn values, such as those observed in a few of the mare basalts, has been explained by condensation of isotopically light vapour after degassing (Paniello et al., 2012a; Day & Moynier, 2014). Data are from Paniello et al., 2012a and Kato et al., 2015.

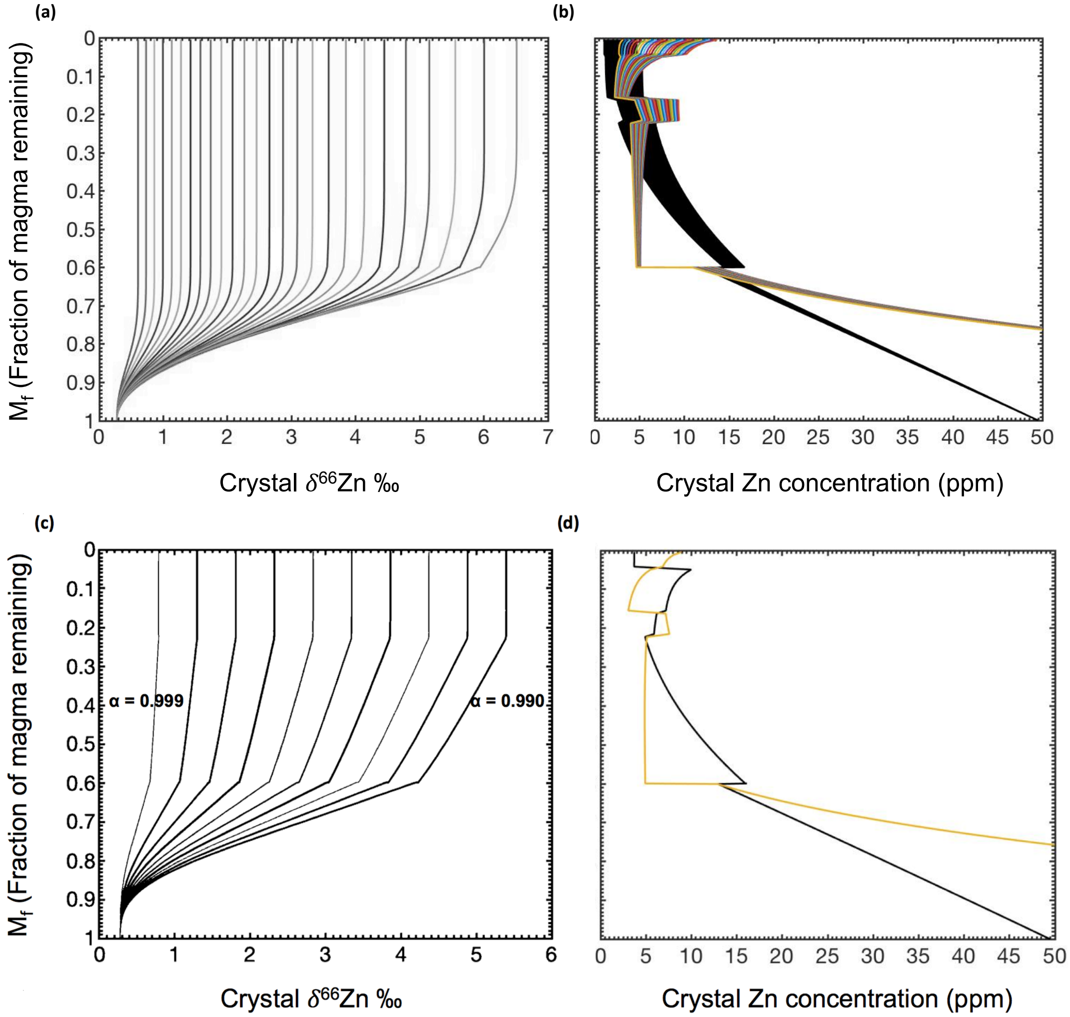

Figure 4.2: The modeled crystal zinc isotopic composition (left) and concentration (right) for the constant surface volatile depletion signature in Model 1 (a, b) and the evolving surface depletion signature in Model 2 (c, d). The black and grey lines in all diagrams are model outputs for literature partition coefficient (*Table 4.S1*). The colored lines in (b) and (d) are modeled crystal zinc concentrations for calculated partition coefficients based on *in situ* measurements in lunar samples (*Table 4.S3*, this study).

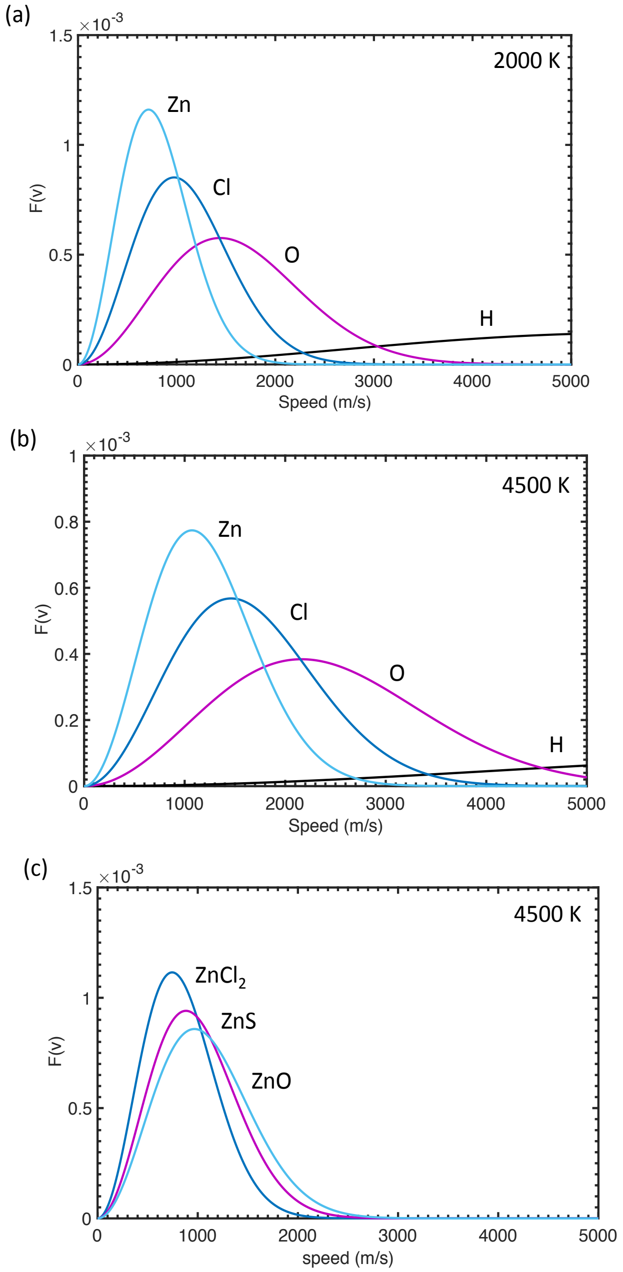

Figure 4.3: The Maxwell-Boltzmann distributions of zinc and volatile elements at 2000K (a) and 4500K (b) and zinc compounds at 4500K (c) demonstrate that atmospheric loss of Zn from the Moon can only occur for elemental Zn at ~ 4500K, based on a lunar escape velocity of ~2.4 km/sec. Speeds greater than 2400 m/sec only hold for the upper tail of the distribution, and so atmospheric loss of zinc to space would only be possible for a small percentage of vaporized zinc atoms in this scenario.

Supplementary Information

Development of the AFC-LMO Model

The process of assimilation and concomitant fractionation crystallization (AFC) describes the evolution of trace element concentrations and isotopic ratios in a magma reservoir as a result of wall-rock assimilation and fractional crystallization. Recent work by Nishimura (2012) extends the traditional AFC model (DePaolo, 1981) to consider re-equilibration of suspended crystals with the surrounding liquid, resulting in *imperfect* fractional crystallization. For assimilation and imperfect fractional crystallization (AIFC), the original mass balance differential equation from DePaolo (1981):

$$M_a C_a - M_c D C_m = C_m \frac{dM_m}{dt} + M_m \frac{dC_m}{dt}$$

is modified to explicitly include the liquid composition in the second term, if $C_l \neq C_m$:

$$M_a C_a - M_c D C_l = C_m \frac{dM_m}{dt} + M_m \frac{dC_m}{dt}$$

where M_m is the mass of the magma, M_a (mass/unit time) is the rate of wall rock assimilation, M_c (mass/unit time) is the rate at which crystals separate from the magma, D is the bulk solid/liquid partition coefficient, C_a is the elemental concentration of the wall rock (assimilant), C_m is the elemental concentration in the magma, and C_l is the elemental concentration in the liquid (Nishimura, 2012).

The elemental concentration in the liquid is related to the concentration in the magma by the following equation:

$$C_l = \frac{C_m}{1-\phi+\phi D}$$

where the crystal fraction, ϕ, is the weight fraction of the suspended crystals in the magma body (Nishimura, 2012).

The introduction of ϕ represents an important development from the original AFC model (DePaolo, 1981), which is equivalent to the case for ϕ=0, and so the crystal composition does not evolve uniquely and remains in perfect equilibrium with the magma. As discussed below, the crystal fraction in this study is low (ϕ = 0.0031) and therefore approaches this condition, but it is still modeled using the AIFC model by Nishimura (2012).

Here, we consider the AIFC model to be analogous to mixing and assimilation during the LMO event, where the assimilant is an isolated, molten surface layer and the magma is the bulk lunar mantle. The convective regime of the lunar magma ocean has been characterized by (Elkins-Tanton et al., 2011) and describes the cooling and sinking of surface layers with the deeper lunar mantle. While our models do not consider temperature, heat flow or convection, they consider mixing between the surface layers and the bulk mantle during the LMO event to be subject to chemical equilibrium and assimilation as described by DePaolo (1981) and Nishimura (2012). The AIFC model has been adjusted for this study explicitly to model the LMO, but contains baselines assumptions appropriate for magma chambers. An important caveat in drawing this analogy is that the LMO is a fully closed system, and therefore magma re-charge and theoretically unlimited assimilation of wall rock do not apply (c.f., singular magma pulses – Skaergaard Intrusion).

We use the analytical solutions derived by Nishimura (2012) that assume the conditions where $C_l \neq C_m$ (Eq. 5). These solutions describe two separate cases (*Figure 4.S3*): (1) assimilation, perfect equilibrium crystallization and partial settling (2) assimilation, surface equilibrium crystallization and partial settling (Nishimura, 2012). In the first case, the suspended crystals are homogenous, in perfect chemical equilibrium with the surrounding liquid, and identical in elemental concentration and isotopic composition to the bulk magma. In the second case, the suspended crystals are zoned because only their surfaces are in equilibrium with the surrounding liquid, resulting in elemental concentrations and isotopic compositions distinct from the surrounding liquid or bulk magma (see Figure S3; after Nishimura, 2012). These two cases were modeled in this analysis, but the differences were negligible within the error of the observed zinc isotopic ratios (0.5‰). For α=0.990, the final LMO zinc composition differed by 0.01‰ and this decreased to 0.001‰ for an alpha value of 0.999.

Input parameters for the AIFC model specific to the LMO crystallization sequence are provided in *Table 4.S1*. These consist of the assimilation rate constant (r_a), crystal fraction (ϕ), partition coefficient (D) and the fraction of magma liquid remaining (M_f). The assimilation rate (r_a) is a constant ratio of the assimilation rate to the rate of crystal fractionation: $r_a = M_a/M_c$ where M_a and M_c are the same as defined for Eq. 4 (DePaolo, 1981; Nishimura, 2012). The crystal fraction (ϕ) is the mass fraction of suspended crystals in the magma: $\phi = M_x/M_m$ where M_x and M_m are the masses of the crystal and magma, respectively. The partition coefficient (D) describes the partitioning of zinc between the fractionating crystal and bulk magma phases and the values used in this study are provided in *Table 4.S1* (and references therein) and *Table 4.S3* (this study). The fraction of magma (M_f) is defined as the ratio of the mass of the magma remaining to the initial mass of the magma: $M_f = M_m / M_m^0$.

In order to properly parametrize this AIFC model for the lunar magma ocean, the assimilation rate constant and crystal fraction remained constant over the course of LMO crystallization. These values were calculated assuming a magma ocean depth of 400 km, a total surface layer 25 km deep, the radius of the Moon (1738.1 km), and corresponding densities of 3.4 g/cm^3 for the bulk mantle and 2.9 g/cm^3 for the crust (Wood et al., 1970). The interval for the fraction of magma remaining (M_f = 1 to 0.6 by 0.001 and M_f= 0.59 to 0.05 by 0.005) resulted in 350 steps, and this index value was used to divide the surface layer into equal 'assimilant packages,' and the total mantle mass into equal 'crystallizing components.' Therefore, the 350 stepped calculations result in both the complete assimilation of the surface layer and full crystallization of the LMO sequence.

Over the course of magma ocean crystallization, the full surface layer represented

6.7 % of the bulk lunar mantle. The crystal fraction in each step is 0.31% of the total mass of the lunar mantle, represented by $\phi = 0.0031$. For each step, the mass of the assimilant is $M_a = 7.7503\times10^{21}$g and the mass of the crystal is $M_c = 1.1293\times10^{23}$g resulting in a constant assimilant rate constant of $r_a = 0.0686$.

The constant values for ϕ and r_a represent a simplified assumption because the LMO presumably had variable rates of convection and crystallization as it cooled. However, it is adequate for modeling chemical and isotopic equilibrium, and also limits uncertainty because it maintains the AFC assumptions of constant assimilation rate and crystal fraction (DePaolo, 1981; Nishimura, 2012).

The partition coefficient, however, does change within discrete sections along the LMO crystallization sequence as a consequence of the changing mineralogy as defined by Snyder et al. (1992). These D values for zinc are from experimental and observational phenocryst-matrix studies (*Table 4.S1*, Dissanayake and Vincent, 1972; Paster et al., 1974; Ewart and Griffin, 1994; Kohn and Schofield, 1994; Klemme et al., 2006), as well as those calculated from zinc abundance measurements from *in situ* analyses of lunar samples (*Table 4.S2, 4.S3*).

Analyses of Zinc Partitioning

Laser ablation ICP-MS analyses of mineral phases was performed using a *New Wave Research* UP213 (213 nm) laser-ablation system coupled to a *ThermoScientific iCAPq* C Inductively Coupled Plasma-Mass Spectrometer at the Scripps Isotope

Geochemistry Laboratory (SIGL). Analyses were done using spots with a 150 μm beam diameter, a laser repetition rate of 5 Hz, and a photon fluence of 3.5 J/cm2. Ablation analysis took place in a 3 cm^3 ablation cell. The cell was flushed with a He-gas flow to enhance production and transport of fine aerosols, and was mixed with an Ar carrier-gas flow of ~1 L/min before reaching the torch. Each analysis consisted of ~60 s data collection. Backgrounds on the sample gas were collected for ~20 s followed by ~40 s of laser ablation. Washout time between analyses was >120 s. Data were collected in time-resolved mode so effects of inclusions, mineral zoning and possible penetration of the laser beam to underlying phases could be evaluated. Plots of counts per second versus time were examined for each analysis, and integration intervals for the gas background and the sample analysis were selected. Standardization was performed using the NIST 610 glass. External reproducibility on the Zn abundance was 8% (2 RSD), with values for BCR-2g and BHVO-2g, run as unknowns of 134 and 156 ppm, respectively.

Citing of Zn within lunar mare basalts 15555 and 12063 occurs mainly within oxide grains and olivine in the order: spinel ≥ ilmenite > olivine > plagioclase > pyroxene. Assuming the bulk-rock represents the parental melt composition, an approximate partitioning for spinel is 5-10, ilmenite is 7, olivine is 2.4-5.1, plagioclase is 0.3-1 and pyroxene is 0.2-0.3. These estimated KD values are similar to experimental values for spinel and ilmenite, are higher for olivine and plagioclase, but are lower for pyroxene by as much as a factor of 10. Experimental KDs are required for lunar conditions.

Equilibrium Fractionation of Zinc

The conditions of the LMO are poorly constrained and evaporative loss of Zn could have theoretically proceeded through either equilibrium or kinetic fractionation. *Table 4.S4* displays the mass (M), reduced mass (μ), vibrational frequency (u) and equilibrium constant (K_{eq}) for equilibrium isotopic exchange reactions of zinc in ZnO, $ZnCl_2$ and ZnS:

$$^{64}ZnO + {}^{66}Zn \rightarrow {}^{66}ZnO + {}^{64}Zn$$

$$^{64}ZnS + {}^{66}Zn \rightarrow {}^{66}ZnS + {}^{64}Zn$$

$$^{64}ZnCl_2 + {}^{66}Zn \rightarrow {}^{66}ZnCl_2 + {}^{64}Zn$$

The masses of these isotopes are a sum of ^{64}Zn and the respective mass of the dominant isotope of the other species (O: 16 amu, S: 32 amu, Cl: 35 amu). For a species in the form of M_1M_2 (e.g. for ZnO, Zn is M_1 and O is M_2), the reduced mass is equivalent to: $\mu = (M_1 \times M_2)/(M_1+M_2)$. The vibrational frequency is estimated at 3×10^{12} cm^{-1} for all compounds, which is a simplification, but adequate for the demonstrating the effect of masses on equilibrium exchange constants (based on values for ZnS, Zach and Ziurys, 2009). The calculations are based on physical chemistry calculations (e.g. Young et al., 2002) and the exchange reactions are between a zinc compound and an elemental zinc isotope in the solid phase.

Using the general form of the equations above, $m_a + m_b \rightarrow m_c + m_d$, with reduced mass equivalents (e.g. μ_a for m_a), the translational (K_{tr}), rotational (K_{rot}) and vibrational (K_{vib}) constants can be calculated as follows:

$$K_{tr} = (m_c \times m_d)/(\, m_a \times m_b)^{(3/2)}$$

$$K_{rot} = 1(\mu_c \times \mu_d)/(\mu_a \times \mu_b)^{(3/2)}$$

$$K_{vib} = 1 + (h/2 \times k_b \times T) \times (u - u(\mu_c - \mu_a)^{(1/2)}) - (u - u(\mu_b - \mu_d)^{(1/2)})$$

The constant for equilibrium isotope exchange is then calculated using the following equation:

$$K_{eq} = K_{tr} \times K_{rot} \times K_{vib}$$

The equilibrium constants (K_{eq}) are comparable to the kinetic fractionation factors (α), and are less than the theoretical value of $\alpha = 0.990$ (for ZnS). The values of K_{eq} approach unity as the mass increases, but these theoretical K_{eq} values strongly deviate from the kinetic fractionation factor that best fits Model 2, $0.998 > \alpha > 0.997$. These calculations support kinetic evaporative fractionation of zinc on the Moon and indicates that any equilibrium exchange reactions between solid and vapor zinc phases had a negligible effect.

Hydrodynamic Escape of Zinc

Work by Zahnle and Kasting (1986), Hunten et al. (1987) and Zahnle et al. (1990) describes the conditions of mass fractionation during hydrodynamic escape as related to noble gases and the loss of water on planetary bodies. This model is applied to the case of Zn loss and mass fractionation through hydrodynamic escape. The initial conditions are as follows and based on Hunten et al. (1987) and Vaniman et al. (1991): ambient atmospheric pressure, $p = 10^{-10}$ to 10^{-6} Pa; height of atmosphere, $r_0 = 120$ km; and absolute temperature, T = 400 to 4500 K.

The inventory of molecules in the atmosphere is based on the ideal gas law, $PV = nkT$ where k is the Boltzmann constant. Subsequently dividing by the total volume yields the number density (in molecules / area): $n/V = P/kT$. The number density is dependent on the ambient pressure, and to a lesser degree, the temperature. The current lunar atmospheric pressure is approximately 10^{-9} Pa, and so the given ranges of 10^{-10} to 10^{-6} Pa are reasonable estimates for ambient pressure at the time of the lunar magma ocean. It is assumed that hydrogen comprises 80% of this total number density (n_a), and the zinc content varies between 0.1 and 5%. In this version of the Hunten et al. (1987) model, the total number of zinc atoms does not affect the magnitude of its loss during hydrodynamic escape. The threshold of atomic mass (crossover mass) subject to hydrodynamic escape is the dominant control. This value largely depends on initial conditions of pressure, temperature and hydrogen number density.

The major inputs of mass, number density and radii of the major (H) and minor (Zn) species are as follows: $m_{\mathrm{H}} = 1$ amu, $n_{\mathrm{H}} = 10^4$ to 10^8 atoms/cm^2, $r_{\mathrm{H}} = 50$ pm; $m_{\mathrm{Zn}} = 64$ amu, $n_{\mathrm{Zn}} = 10^2$ to 10^6 atoms/cm^2, $r_{\mathrm{H}} = 134$ pm. These parameters are then used to calculate the following physical chemistry constraints:

Mean speed of Maxwell distribution: $v_{ave} = \sqrt{\frac{8kT}{\pi m_i}}$

Diffusion parameter: $b = dn_{\mathrm{a}}$

where k is the Boltzmann constant, m_i is the mass of a given atomic species

d is the diffusion coefficient: $d = \frac{1}{3} v_{ave}\lambda$

n_{a} is the total number density: $n_{\mathrm{a}} = n_{\mathrm{H}} + n_{\mathrm{Zn}}$

λ is the mean free path: $\lambda = \frac{kT}{pA_n}\frac{1}{\sqrt{2}\sigma}$

σ is the collisional radius: $\sigma = \pi(r_H r_{Zn})^2$

The vertical flux of hydrogen is defined as follows: $F_H = n_H v_H$

The hydrogen flux is taken to be constant over time, which is the simplest case. The total inventory of hydrogen atoms, N_{H}, is the number density (n_H) multiplied by the volume of the lunar atmosphere. This number decreases over time as a function of the vertical flux of hydrogen, $N_H(t) = N_H - F_H t$

The evolution of hydrogen atoms over time is defined by a ratio of $N_H(t) / N_H$, where N_H represents the initial inventory of hydrogen atoms. The hydrogen flux (F_H) is also used to calculate the crossover mass (m_c), which is the smallest mass for which the flux is 0 during hydrodynamic escape. The equation for m_c is as follows, where g is the lunar gravity (1.622 m/s^2) and $X_H = n_H / n_a = 0.8$:

$$m_c = \frac{kTF_H}{bgX_H} + m_H$$

Within the given range of pressure ($p = 10^{-10}$ to 10^{-6} Pa), the crossover mass varies between 1.02 amu and 168.5 amu. At values greater than 10^{-6} Pa, the crossover mass is 1676 amu, indicating that all species can potentially escape. At pressures lower than 10^{-10} Pa, the crossover mass is 1 amu, suggesting that even H cannot escape at these pressures. These values result from the fact that lower pressures are associated with a lower number of atoms and so fewer collisions. Conversely, higher pressures theoretically result in a higher number of collisions, exciting more atoms to higher velocities. The effects of temperature across the range of 400 to 4500 K are negligible on the resulting crossover mass, as pressure is a more dominant control.

In combination with the ratio of hydrogen atoms over time ($N_H(t)$ / N_H), and under conditions of Rayleigh fractionation, the crossover mass is used to determine the ratio of zinc atoms over time ($N_{Zn}(t)$ / N_{Zn}), using the following equation:

$$\frac{N_{Zn}(t)}{N_{Zn}} = \frac{N_H(t)}{N_H}^{\frac{m_c - m_{Zn}}{m_c - m_H}}$$

The hydrogen and zinc ratios of $N(t):N_0$ (inventory at time, t: initial inventory) from hydrodynamic escape are provided below for a temperature range of 400 to 4500 K and an atmospheric pressure of 10^{-6} Pa. This pressure represents a critical value because for lower pressures (10^{-7} to 10^{-10}), the crossover mass is less than 64 amu and therefore results in no loss of zinc.

These hydrodynamic escape calculations (*Table 4.S5*) examine the issue of zinc vapor loss subsequent to surface evaporative fractionation. Under these conditions, there is increased loss of zinc at higher temperatures. The greatest loss of zinc through hydrodynamic escape occurs at 4500 K and 10^{-6} Pa, but this is still less than 4%. At higher pressures (10^{-5} to 10^{10} Pa), where the crossover mass is the order of 10^3 amu or greater, the ratio of zinc remaining reaches a stable limit of 0.9399, with a loss of ~6% of lunar zinc. However, this value is far too low to explain the zinc concentration in lunar mare basalts, ~2, which reflect a loss of ~95% assuming an initial terrestrial-like zinc abundance of 55 ppm.

At 4500 K and 10^{-6} Pa, the zinc loss ratios for the major zinc isotopes, ^{64}Zn, ^{66}Zn and ^{68}Zn, are 0.9621, 0.9628, 0.9635, respectively. For a total zinc loss of ~4%, this is equivalent to a δ^{66}Zn ~ +0.7 ‰. This isotopic ratio approaches that observed in lunar mare basalts (δ^{66}Zn ~ +1.4 ‰), but it cannot explain the large-scale decrease in zinc concentrations, and so the δ^{66}Zn signature of ~ +0.7 ‰ was likely dampened by 96% zinc vapor retention.

These calculations demonstrate that, while some zinc loss can be attributed to hydrodynamic escape, it was not a dominant process in stripping away zinc from the transient lunar atmosphere. In the absence of a large atmospheric blow off or large-scale ionization of the metallic vapor by the young solar wind, this further supports the condensation of the fractionated, light isotopic enriched zinc vapor onto lunar surface reservoirs.

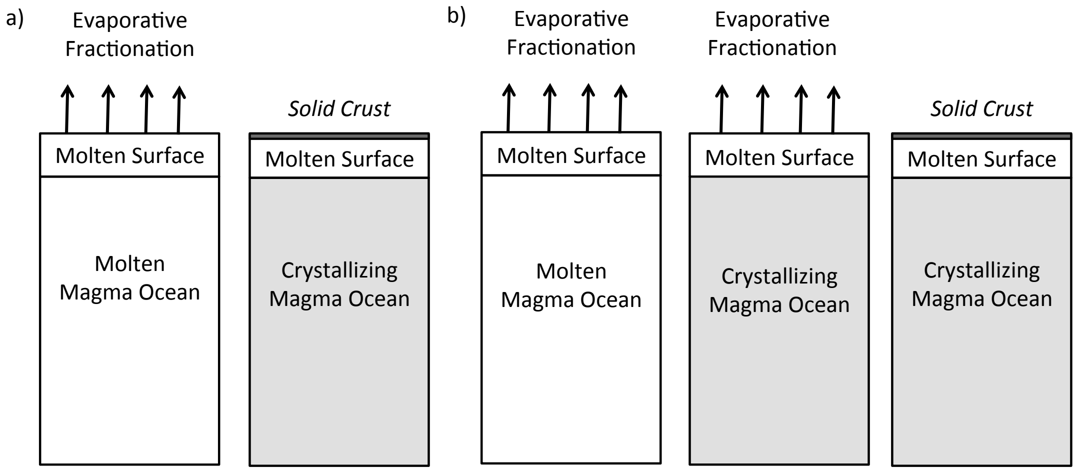

Figure 4.S1: Schematic diagrams of the two models presented in the coupled Rayleigh-AIFC model. (a) *Model 1:* Evaporative fractionation of zinc on the surface ends before LMO assimilation and crystallization, due to a solid boundary layer. (b) *Model 2:* Evaporative fractionation of zinc on the lunar surface is concurrent with LMO assimilation and crystallization, and is later shut-off due to a late-stage boundary layer.

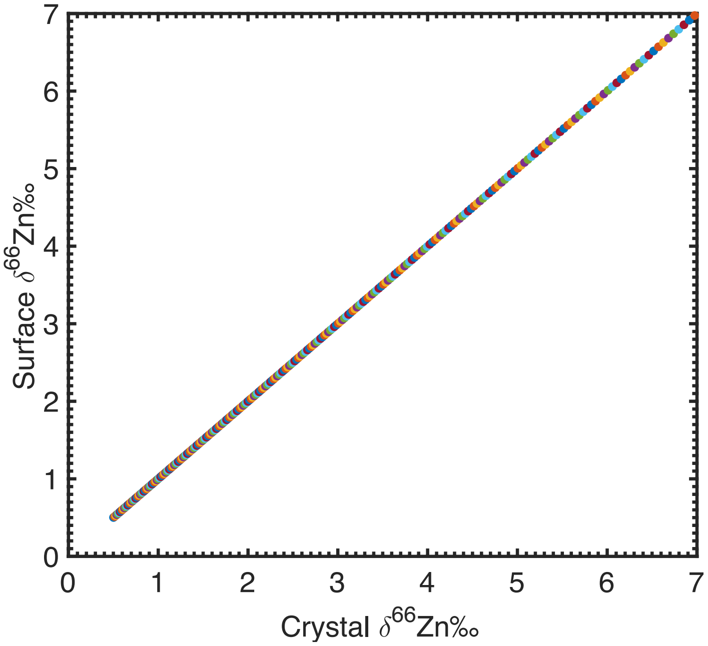

Figure 4.S2: The ~ 1:1 relation observed between the surface and LMO crystal zinc isotopic compositions for both Models 1 and 2, demonstrating efficiency and rapid assimilation of the volatile depleted surface signature into the bulk lunar mantle using the combined Rayleigh-AIFC model.

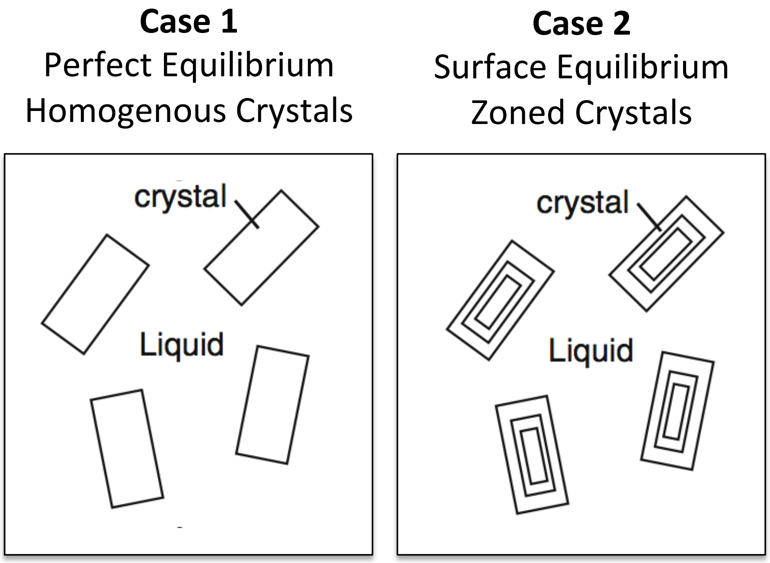

Figure 4.S3: Schematic after Nishimura (2012) showing (Case 1) perfect equilibrium with crystal compositions identical to the surrounding liquid and (Case 2) surface equilibrium resulting in zoned crystals. The combined Rayleigh-AIFC model was simulated for both cases, but over the course of LMO crystallization, there was no significant difference between the two. This indicates that these small-scale effects do not have a pronounced aggregate affect on the zinc isotopic composition of the crystallized LMO.

Table 4.S1: LMO Crystallization Input Parameters

M_f	r_a	ϕ	D	Ref (for D)	Pressure	Temp (C)	Buffer/log(fO_2)
1 - 0.6	0.069	0.003	0.9	Kohn and Schofield, 1994	1 atm	1400	N/A (air)
			*Olivine				
0.6 - 0.21	0.069	0.003	2.1	Klemme et al., 2006	1 Gpa	1200	C-CO buffer
			*Orthopyroxene				
0.22 - 0.15	0.069	0.003	1.8	Ewart and Griffin, 1994	N/A (Phenocryst-Matrix)		
			*Plagioclase: D = 0.17 (53%); Olivine: D = 0.9 (25%); Pigeonite: D = 6.6 (22%)				
0.16 - 0.05	0.069	0.003	2.7	Ewart and Griffin, 1994	N/A (Phenocryst-Matrix)		
				Dissanayake and Vincent, 1972	N/A (Phenocryst-Matrix)		
				Paster et al., 1974	N/A (Phenocryst-Matrix)		
			* Clinopyroxene: D = 0.5 (26%); Plagioclase: D = 0.17 (36%); Pigeonite: D = 6.6 (38%)				
0.05 - 0.005	0.069	0.003	3.6	Klemme et al., 2006	1 atm	1100	-11.6
			* Pigeonite: D = 6.6 (34%); Plagioclase: D = 0.17 (31%); Clinopyroxene: D = 0.5 (24%); Ilmenite: D = 11 (11%)				

*Mineralogy based on Snyder et al., (1992)

Table 4.S2: Zn abundances in mineral phases in lunar mare basalt samples

	12063 - Ilmenite Basalt					15555 - Olivine Normative Basalt			
	Modal % [1]	**n**	**Zn (ppm)**	**1 σ**		**Modal % [1]**	**n**	**Zn (ppm)**	**1 σ**
Plagioclase	0.22	4	1.4	1.3		0.24	4	2.9	1.2
Spinel	0.03	2	50.3	4.600		0.04	2	15.3	8.600
Olivine	0.03	2	25.8	6.000		0.15	4	7.1	2.000
Ilmnite	0.05	3	37.2	16.300					
Pyroxene	0.65	4	1	0.200		0.53	11	1	1.000
Calc WR			5.1					2.9	
Measured Wr			4.5	0.975				1.1	

[1] Modal data and measured whole-rock data are from the lunar compendium.
WR : whole rock

Table 4.S3: LMO Crystallization Input Parameters for *in situ* Partition Coefficients (this study)

M_f	r_a	ϕ	D	Ref (for D)
1 - 0.6	0.069	0.003	3.8	this study (Phenocryst-Matrix)
			**Olivine*	
0.6 - 0.21	0.069	0.003	0.25	this study (Phenocryst-Matrix)
			**Orthopyroxene*	
0.22 - 0.15	0.069	0.003	1.3	this study (Phenocryst-Matrix)
			**Plagioclase: D = 0.65 (53%); Olivine: D = 3.75 (25%); Pigeonite: D = 0.25 (22%)*	
0.16 - 0.05	0.069	0.003	0.3	this study (Phenocryst-Matrix)
			** Clinopyroxene: D = 0.25 (26%); Plagioclase: D = 0.65 (36%); Pigeonite: D = 0.25 (38%)*	
0.05 - 0.005	0.069	0.003	1.0	this study (Phenocryst-Matrix)
			** Pigeonite: D = 0.25 (34%); Plagioclase: D = 0.65 (31%); Clinopyroxene: D = 0.25 (24%); Ilmenite: D = 7 (11%)*	

*Mineralogy based on Snyder et al., (1992)

Table 4.S4: Constants for Equilibrium Fractionation at 2400 K

Species	M (amu)	μ (amu)	v (sec^{-1})	K_{eq}
^{64}ZnO	80	12.8	3.00×10^{12}	0.957
^{64}ZnS	96	21.3	3.00×10^{12}	0.960
$^{64}ZnCl_2$	134	22.6	3.00×10^{12}	0.975

Table 4.S5: Results for Hydrodynamic Escape Modeling of Zn

Temp (K)	P (pa)	m_c (amu)	H Ratio	Zn Ratio
400	1.00E-06	168.5	0.982	0.989
1000	1.00E-06	168.5	0.972	0.982
1500	1.00E-06	168.5	0.965	0.978
2000	1.00E-06	168.5	0.96	0.975
2500	1.00E-06	168.5	0.955	0.972
3000	1.00E-06	168.5	0.951	0.969
3500	1.00E-06	168.5	0.947	0.967
4000	1.00E-06	168.5	0.943	0.964
4500	1.00E-06	168.5	0.94	0.962

References

Abe, Y., & Matsui, T. (1985). The formation of an impact-generated H2O atmosphere and its implications for the early thermal history of the Earth. In *Lunar and Planetary Science Conference Proceedings*, *15*, C545-C559.

Albarède, F. (2009). Volatile accretion history of the terrestrial planets and dynamic implications. *Nature*, *461*, 1227-1233.

Albarède, F., Albalat, E., & Lee, C. T. A. (2015). An intrinsic volatility scale relevant to the Earth and Moon and the status of water in the Moon. *Meteoritics & Planetary Science, 50*, 568-577.

Binder, A. B. (1985). The depths of the mare basalt source region. In *Lunar and Planetary Science Conference Proceedings*, *15*, C396-C404.

Boyce, J.W., Treiman, A.H., Guan, Y., Ma, C., Eiler, J.M., Gross, J., Greenwood, J.P. & Stolper, E.M. (2015). The chlorine isotope fingerprint of the lunar magma ocean. *Science advances*, *1*, e1500380.

Brett, R. (1976). Reduction of mare basalts by sulfur loss. *Geochimica et Cosmochimica Acta*, *40*, 997-1004.

Canup, R. M., Visscher, C., Salmon, J., & Fegley Jr, B. (2015). Lunar volatile depletion due to incomplete accretion within an impact-generated disk. *Nature Geoscience*, *8*, 918-921.

Chen, H., Savage, P. S., Teng, F. Z., Helz, R. T., & Moynier, F. (2013). Zinc isotope fractionation during magmatic differentiation and the isotopic composition of the bulk Earth. *Earth and Planetary Science Letters*, *369*, 34-42.

Cintala, M. J., & Grieve, R. A. (1998). Scaling impact melting and crater dimensions: Implications for the lunar cratering record. *Meteoritics & Planetary Science*, *33,* 889-912.

Davis, A. M. (2006). Volatile evolution and loss. *Meteorites and the early solar system II*, 295-307.

Day, J.M.D., & Moynier, F. (2014). Evaporative fractionation of volatile stable isotopes and their bearing on the origin of the Moon. *Philosophical Transactions of the Royal Society of London A: Mathematical, Physical and Engineering Sciences*, *372*, 20130259.

Day, J.M.D., Pearson, D. G., & Hulbert, L. J. (2008). Rhenium–osmium isotope and platinum-group element constraints on the origin and evolution of the 1· 27 Ga Muskox layered intrusion. *Journal of Petrology*, *49*, 1255-1295.

Delano, J. W., & Livi, K. (1981). Lunar volcanic glasses and their constraints on mare petrogenesis. *Geochimica et Cosmochimica Acta*, *45*, 2137-2149.

DePaolo, D. J. (1981). Trace element and isotopic effects of combined wallrock assimilation and fractional crystallization. *Earth and planetary science letters*, *53*, 189-202.

Dissanayake, C. B., & Vincent, E. A. (1972). Zinc in rocks and minerals from the Skaergaard intrusion, east Greenland. *Chemical Geology*, *9*, 285-297.

Elkins-Tanton, L. T. (2012). Magma oceans in the inner solar system. *Annual Review of Earth and Planetary Sciences*, *40*, 113-139.

Elkins-Tanton, L. T., Burgess, S., & Yin, Q. Z. (2011). The lunar magma ocean: Reconciling the solidification process with lunar petrology and geochronology. *Earth and Planetary Science Letters*, *304*, 326-336.

Elkins-Tanton, L. T. (2008). Linked magma ocean solidification and atmospheric growth for Earth and Mars. *Earth and Planetary Science Letters*, *271*, 181-191.

Elins-Tanton, L. T., Van Orman, J. A., Hager, B. H., & Grove, T. L. (2002). Re-examination of the lunar magma ocean cumulate overturn hypothesis: melting or mixing is required. *Earth and Planetary Science Letters*, *196*, 239-249.

Ewart, A., & Griffin, W. L. (1994). Application of proton-microprobe data to trace-element partitioning in volcanic rocks. *Chemical Geology*, *117*, 251-284.

Ewart, A., & Griffin, W. L. (1994). Application of proton-microprobe data to trace-element partitioning in volcanic rocks. *Chemical Geology*, *117*, 251-284.

Genda, H., & Abe, Y. (2003). Survival of a proto-atmosphere through the stage of giant impacts: the mechanical aspects. *Icarus*, *164*, 149-162.

Gibson Jr, E. K., Brett, R., & Andrawes, F. (1977). Sulfur in lunar mare basalts as a function of bulk composition. In *Lunar and Planetary Science Conference Proceedings, 8*, 1417-1428.

Green, D. H., & Ringwood, A. E. (1973). Significance of a primitive lunar basaltic composition present in Apollo 15 soils and breccias. *Earth and Planetary Science Letters*, *19*, 1-8.

Greenwood, J. P., Itoh, S., Sakamoto, N., Warren, P., Taylor, L., & Yurimoto, H. (2011). Hydrogen isotope ratios in lunar rocks indicate delivery of cometary water to the Moon. *Nature Geoscience*, *4*, 79-82.

Greenwood, R. C., Franchi, I. A., Jambon, A., & Buchanan, P. C. (2005). Widespread magma oceans on asteroidal bodies in the early solar system. *Nature*, *435*, 916-918.

Halliday, A. N., Lee, D. C., Porcelli, D., Wiechert, U., Schönbächler, M., & Rehkämper, M. (2001). The rates of accretion, core formation and volatile loss in the early Solar System. *Philosophical Transactions of the Royal Society of London A: Mathematical, Physical and Engineering Sciences*, *359*, 2111-2135.

Halliday, A. N., & Porcelli, D. (2001). In search of lost planets–the paleocosmochemistry of the inner solar system. *Earth and Planetary Science Letters*, *192*, 545-559.

Hamano, K., Abe, Y., & Genda, H. (2013). Emergence of two types of terrestrial planet on solidification of magma ocean. *Nature*, *497*, 607-610.

Herzog, G. F., Moynier, F., Albarède, F., & Berezhnoy, A. A. (2009). Isotopic and elemental abundances of copper and zinc in lunar samples, Zagami, Pele's hairs, and a terrestrial basalt. *Geochimica et Cosmochimica Acta*, *73*, 5884-5904.

Humayun, M., & Clayton, R. N. (1995). Potassium isotope cosmochemistry: Genetic implications of volatile element depletion. *Geochimica et Cosmochimica Acta*, *59*, 2131-2148.

Hunten, D. M., Pepin, R. O., & Walker, J. C. (1987). Mass fractionation in hydrodynamic escape. *Icarus*, *69*, 532-549.

Jones, J. H., & Palme, H. (2000). Geochemical constraints on the origin of the Earth and Moon. *Origin of the Earth and Moon*, 197-216.

Kato, C., Moynier, F., Valdes, M. C., Dhaliwal, J. K., & Day, J. M. D. (2015). Extensive volatile loss during formation and differentiation of the Moon. *Nature communications*, *6*, 7617, doi:10.1038/ncomms8617.

Klemme, S., Günther, D., Hametner, K., Prowatke, S., & Zack, T. (2006). The partitioning of trace elements between ilmenite, ulvospinel, armalcolite and silicate melts with implications for the early differentiation of the moon. *Chemical Geology*, *234*, 251-263.

Kohn, S. C., & Schofield, P. F. (1994). The importance of melt composition in controlling trace-element behaviour: an experimental study of Mn and Zn partitioning between forsterite and silicate melts. *Chemical Geology*, *117*, 73-87.

Labidi, J., Cartigny, P., & Moreira, M. (2013). Non-chondritic sulphur isotope composition of the terrestrial mantle. *Nature*, *501*, 208-211.

Lecar, M., Podolak, M., Sasselov, D., & Chiang, E. (2006). On the location of the snow line in a protoplanetary disk. *The Astrophysical Journal*, *640*, 1115-1118.

Lodders, K. (2003). Solar system abundances and condensation temperatures of the elements. *The Astrophysical Journal*, *591*, 1220-1247.

Mandler, B. E., & Elkins-Tanton, L. T. (2013). The origin of eucrites, diogenites, and olivine diogenites: Magma ocean crystallization and shallow magma chamber processes on Vesta. *Meteoritics & Planetary Science*, *48*, 2333-2349.

McDonough, W. F., & Sun, S. S. (1995). The composition of the Earth. *Chemical geology*, *120*, 223-253.

Moynier, F., Albarède, F., & Herzog, G. F. (2006). Isotopic composition of zinc, copper, and iron in lunar samples. *Geochimica et Cosmochimica Acta*, *70*, 6103-6117.

Moynier, F., Beck, P., Jourdan, F., Yin, Q. Z., Reimold, U., & Koeberl, C. (2009). Isotopic fractionation of zinc in tektites. *Earth and Planetary Science Letters*, *277*, 482-489.

Nishimura, K. (2012). A mathematical model of trace element and isotopic behavior during simultaneous assimilation and imperfect fractional crystallization. *Contributions to Mineralogy and Petrology*, *164*, 427-440.

Norman, M. D., & Taylor, S. R. (1992). Geochemistry of lunar crustal rocks from breccia 67016 and the composition of the Moon. *Geochimica et cosmochimica acta*, *56*, 1013-1024.

Pahlevan, K., & Stevenson, D. J. (2007). Equilibration in the aftermath of the lunar-forming giant impact. *Earth and Planetary Science Letters*, *262*, 438-449.

Paniello, R. C., Day, J. M.D., & Moynier, F. (2012). Zinc isotopic evidence for the origin of the Moon. *Nature*, *490*, 376-379.

Paniello, R. C., Moynier, F., Beck, P., Barrat, J. A., Podosek, F. A., & Pichat, S. (2012). Zinc isotopes in HEDs: Clues to the formation of 4-Vesta, and the unique composition of Pecora Escarpment 82502. *Geochimica et Cosmochimica Acta*, *86*, 76-87.

Paster, T. P., Schauwecker, D. S., & Haskin, L. A. (1974). The behavior of some trace elements during solidification of the Skaergaard layered series. *Geochimica et Cosmochimica Acta*, *38*, 1549-1577.

.

Phinney, W. C. (1992). Partition coefficients for iron between plagioclase and basalt as a function of oxygen fugacity: Implications for Archean and lunar anorthosites. *Geochimica et Cosmochimica Acta*, *56*, 1885-1895.

Potter, R. W. K., Kring, D. A., Collins, G. S., Kiefer, W. S., & McGovern, P. J. (2012). Estimating transient crater size using the crustal annular bulge: Insights from numerical modeling of lunar basin-scale impacts. *Geophysical Research Letters*, *39*, L18203.

Rees, C. E., & Thode, H. G. (1972). Sulphur concentrations and isotope ratios in lunar samples. In *Lunar and Planetary Science Conference Proceedings*, 3, 1479 – 1485.

Righter, K., & Drake, M. J. (1997). A magma ocean on Vesta: Core formation and petrogenesis of eucrites and diogenites. *Meteoritics & Planetary Science*, *32*, 929-944.

Ringwood, A. E., & Kesson, S. E. (1976). A dynamic model for mare basalt petrogenesis. In *Lunar and Planetary Science Conference Proceedings*, 7, 1697-1722.

Ringwood, A. E. (1966). Chemical evolution of the terrestrial planets. *Geochimica et Cosmochimica Acta*, *30*, 41-104.

Ruzicka, A., Snyder, G. A., & Taylor, L. A. (1997). Vesta as the howardite, eucrite and diogenite parent body: Implications for the size of a core and for large-scale differentiation. *Meteoritics & Planetary Science*, *32*, 825-840.

Sands, D. G., Rosman, K. J. R., & De Laeter, J. R. (2001). A preliminary study of cadmium mass fractionation in lunar soils. *Earth and Planetary Science Letters*, *186*, 103-111.

Sarid, G., & Stewart, S. T. (2015).. Black Sheep and White Elephants: Compositions of Survivors from Collisions of Differentiated Ice-Rock Bodies. In *Lunar and Planetary Science Conference, 46*, # 2834.

Schediwy, S., Rosman, K. J. R., & De Laeter, J. R. (2006). Isotope fractionation of cadmium in lunar material. *Earth and Planetary Science Letters*, *243*, 326-335.

Sharp, Z. D., Shearer, C. K., McKeegan, K. D., Barnes, J. D., & Wang, Y. Q. (2010). The chlorine isotope composition of the Moon and implications for an anhydrous mantle. *Science*, *329*, 1050-1053.

Shearer, C. K., Sharp, Z. D., Burger, P. V., McCubbin, F. M., Provencio, P. P., Brearley, A. J., & Steele, A. (2014). Chlorine distribution and its isotopic composition in "rusty rock" 66095. Implications for volatile element enrichments of "rusty rock" and lunar soils, origin of "rusty" alteration, and volatile element behavior on the Moon. *Geochimica et Cosmochimica Acta*, *139*, 411-433.

Smith, J.V., Anderson, A.T., Newton, R.C., Olsen, E.J., Crewe, A.V., Isaacson, M.S., Johnson, D. & Wyllie, P.J. (1970). Petrologic history of the moon inferred from petrography, mineralogy and petrogenesis of Apollo 11 rocks. *Geochimica et Cosmochimica Acta Supplement*, 897 - 925.

Snyder, G. A., Taylor, L. A., & Neal, C. R. (1992). A chemical model for generating the sources of mare basalts: Combined equilibrium and fractional crystallization of the lunar magmasphere. *Geochimica et Cosmochimica Acta*, *56*, 3809-3823.

Solomon, S. C., & Longhi, J. (1977). Magma oceanography. I-Thermal evolution. In *Lunar and Planetary Science Conference Proceeding, 8*, 583-599.

Spera, F. J. (1992). Lunar magma transport phenomena. *Geochimica et Cosmochimica Acta*, *56*, 2253-2265.

Stewart, B. W., & DePaolo, D. J. (1990). Isotopic studies of processes in mafic magma chambers: II. The Skaergaard Intrusion, East Greenland. *Contributions to Mineralogy and Petrology*, *104*, 125-141.

Stewart, B. W., & DePaolo, D. J. (1992). Diffusive isotopic contamination of mafic magma by coexisting silicic liquid in the Muskox intrusion. *Science*, *255*, 708-711.

Stewart, S. T., Lock, S. J., & Mukhopadhyay, S. (2014). Atmospheric loss and volatile fractionation during giant impacts. In *Lunar and Planetary Science Conference*, 45, # 2869.

Tatsumoto, M., Premo, W. R., & Unruh, D. M. (1987). Origin of lead from green glass of Apollo 15426: A search for primitive lunar lead. *Journal of Geophysical Research: Solid Earth*, *92*, E361–E371.

Taylor, G. J., Warren, P., Ryder, G., Delano, J., Pieters, C., & Lofgren, G. (1991). Lunar rocks. In *Lunar Sourcebook: a user's guide to the Moon*, 183-284.

Thode, H. G., & Rees, C. E. (1971). Measurement of sulphur concentrations and the isotope ratios $^{33}S/^{32}S$, $^{34}S/^{32}S$ and $^{36}S/^{32}S$ in Apollo 12 samples. *Earth and Planetary Science Letters*, *12*, 434-438.

Tonks, W. B., & Melosh, H. J. (1993). Magma ocean formation due to giant impacts. *Journal of Geophysical Research: Planets*, *98*, 5319-5333.

Tucker, J. M., & Mukhopadhyay, S. (2014). Evidence for multiple magma ocean outgassing and atmospheric loss episodes from mantle noble gases. *Earth and Planetary Science Letters*, *393*, 254-265.

D. Vaniman, R. Reedy, G. Heiken, G. Olhoeft, & W. Mendell (1991). The Lunar Environment. In *Lunar Sourcebook: a user's guide to the Moon*, 27-60.

Visscher, C., & Fegley Jr, B. (2013). Chemistry of impact-generated silicate melt-vapor debris disks. *The Astrophysical Journal Letters*, *767*, L12.

Walker, D., Hager, B. H., & Hayes, J. F. (1980). Mass and heat transport in a lunar magma ocean by sinking blobs. In *Lunar and Planetary Science Conference*, 11, 1196-1198.

Wang, K., & Jacobsen, S. B. (2016). Potassium isotopic evidence for a high-energy giant impact origin of the Moon. *Nature*, *538*, 487-490.

Warren, P.H. & Taylor, G.J. (2014). The Moon. In *Treatise on Geochemistry (Second Edition)*, 2, 213-250.

Wing, B. A., & Farquhar, J. (2015). Sulfur isotope homogeneity of lunar mare basalts. *Geochimica et Cosmochimica Acta*, *170*, 266-280.

Wolf, R., & Anders, E. (1980). Moon and Earth: compositional differences inferred from siderophiles, volatiles, and alkalis in basalts. *Geochimica et Cosmochimica Acta*, *44*, 2111-2124.

Wood, J. A. (1970). Petrology of the lunar soil and geophysical implications. *Journal of Geophysical Research*, *75*, 6497-6513.

Wood, J. A., Dickey Jr, J. S., Marvin, U. B., & Powell, B. N. (1970). Lunar anorthosites and a geophysical model of the moon. In *Proceedings of the Apollo 11 Lunar Science Conference*, 965-988.

Young, E. D., Galy, A., & Nagahara, H. (2002). Kinetic and equilibrium mass-dependent isotope fractionation laws in nature and their geochemical and cosmochemical significance. *Geochimica et Cosmochimica Acta*, *66*, 1095-1104.

Yu, Y., Hewins, R. H., & Wang, J. (2003). Experimental study of evaporation and isotopic mass fractionation of potassium in silicate melts. *Geochimica et Cosmochimica acta*, *67*, 773-786.

Zack, L. N., & Ziurys, L. M. (2009). The pure rotational spectrum of ZnS ($X\ 1\ \Sigma+$). *Journal of Molecular Spectroscopy*, *257*, 213-216.

Zahnle, K. J., & Kasting, J. F. (1986). Mass fractionation during transonic escape and implications for loss of water from Mars and Venus. *Icarus*, *68*, 462-480.

Zahnle, K., Kasting, J. F., & Pollack, J. B. (1990). Mass fractionation of noble gases in diffusion-limited hydrodynamic hydrogen escape. *Icarus*, *84*, 502-527.

Zahnle, K., Arndt, N., Cockell, C., Halliday, A., Nisbet, E., Selsis, F., & Sleep, N. H. (2007). Emergence of a habitable planet. In *Geology and Habitability of Terrestrial Planets* (2007), pp. 35-78.

Chapter 5:

Conclusions

This dissertation focuses on three fundamental stages in planet formation: (1) core formation, (2) magmatic differentiation and (3) volatile depletion. A major theme of this work is using geochemical measurements of diverse meteorite and lunar samples to better understand and elucidate these processes. The first two chapters of this work focus on insights into planetary formation using measurements of highly siderophile element (HSE) abundances and Os isotope ratios. The HSE data for the acapulcoite-lodranite samples (Chapter 2) reveal metal-sulfide partitioning processes during core-formation, while that for eucrite samples (Chapter 3) is valuable for ascertaining both metal-silicate differentiation signatures in pristine eucrite samples, and mixing with chondritic components for impact contaminated samples. The fourth chapter examines volatile depletion using zinc abundance and isotopic data from lunar samples and demonstrates the potential efficiency of wholesale mixing in the lunar magma ocean. These geochemical tracers demonstrate the value of laboratory based observational measurements of extraterrestrial samples in examining aspects of planetary evolution that have been long been overprinted on Earth. The planetary bodies examined in this study may further describe processes that continue to persist within terrestrial reservoirs, albeit on a smaller scale. This cosmochemical data is strongly complemented by examination of terrestrial samples that have characterized mechanisms of partial melting and trace element partitioning, which provide the foundation for understanding other planetary bodies.

The samples in this study derive from planetesimals that have experienced different degrees of melting and differentiation. An important factor in planetary differentiation is the size of the body, and this is presumably reflected in the continuum of metal segregation between the acapulcoite-lodranite body and the Moon. In the case of core formation, the progressive depletion of Pt and Pd in acapulcoite-lodranite samples reflects HSE partitioning during metal segregation in the iron-nickel-sulfide system. The majority of samples reflect metal partitioning from the silicate mantle, but the transitional acapulcoite-lodranite samples may derive from deeper depths closer to the nascent core of the parent body. This is relevant to understanding the control of sulfur during early core formation, including that of Earth, and may also describe processes that occurred near the core-mantle boundary.

The HED parent body is a unique end-member - a fully differentiated, but low-mass planetesimal, and with evidence of marked mantle and crustal heterogeneity that may be a result of its small thermal inertia and limited large-scale mixing. In Chapter 3, analyses of HSE relative abundances in eucrite samples with little to no impact contamination exhibit distinct trends of inter-element fractionation among the HSE. These HSE patterns may be considered to be primary signatures of metal-silicate differentiation on the HED parent body. The differences between these trends therefore suggest that differentiation may have been a hetereogenous process, and was not subject to wholesale mixing and homogenization, as is considered to be the case for larger planets and planetesimals. This incomplete mixing may also be analogous to mantle heterogeneities observed on Earth, including those with more primordial signatures (e.g., Puchtel et al., 2009; Touboul et al., 2012; Peters et al., 2016).

In the case of the Moon (and Earth), these primordial compositional differences were largely homogenized during a putative giant impact (e.g., Hartmann & Davis, 1975) and within a long-lived, global magma ocean. In Chapter 4, modeling of the lunar magma ocean demonstrates the efficient assimilation of a surface volatile depletion into the deeper lunar interior. This explains zinc isotopic ratios and abundances in low- and high-Ti mare basalts, which indicate large scale volatile depletion on the Moon that is reflected in distinct lunar mantle reservoirs. Lunar volatile depletion, which is more extreme than that observed on the Earth, is limited by the Moon's size and escape velocity, indicating that atmospheric blow-off may have been important for both bodies, and can potentially explain Earth's noble gas fractionation (e.g., Tucker and Mukhopadhyay, 2014).

The Earth is the best understood example of planet formation, but studies of meteorites reveal numerous evolutionary trajectories, such as those that led to the wholesale loss of liquid water on Mars or a dry, carbon-dioxide rich atmosphere on Venus. In the context of recently discovered exoplanets, and their diversity of rocky and gas planets, the terrestrial bodies in this Solar System reflect a subset of possible paths in planetary evolution. This highlights the importance of continued research on extraterrestrial samples, because they shed insight into fundamental processes in planetary formation, and act as ‘ground truth’ for distant observations, both in the Solar System and beyond. These data also provide robust constraints as scientists simulate accretionary dynamics, planetary atmospheres and ocean worlds, both past and present. The field of planetary science is at a forefront of technology and as we seek to explore farther into space and time, it is the observational data that will allow us to contextualize and understand newly discovered exoplanets and Solar Systems. This work seeks to contribute to the evolving view of planetary evolution, and it is forever indebted to the prior work of generations of scientists, including the Apollo teams that brought us back dust, glass and rocks from the Moon.

References

Hartmann, W. K., & Davis, D. R. (1975). Satellite-sized planetesimals and lunar origin. *Icarus*, *24*, 504-515.

Peters, B. J., Day, J. M.D., & Taylor, L. A. (2016). Early mantle heterogeneities in the Réunion hotspot source inferred from highly siderophile elements in cumulate xenoliths. *Earth and Planetary Science Letters*, *448*, 150-160.

Puchtel, I. S., Walker, R. J., Anhaeusser, C. R., & Gruau, G. (2009). Re–Os isotope systematics and HSE abundances of the 3.5 Ga Schapenburg komatiites, South Africa: Hydrous melting or prolonged survival of primordial heterogeneities in the mantle?. *Chemical Geology*, *262*, 355-369.

Touboul, M., Puchtel, I. S., & Walker, R. J. (2012). ^{182}W evidence for long-term preservation of early mantle differentiation products. *Science*, *335*, 1065-1069.

Tucker, J. M., & Mukhopadhyay, S. (2014). Evidence for multiple magma ocean outgassing and atmospheric loss episodes from mantle noble gases. *Earth and Planetary Science Letters*, *393*, 254-265.